The Dissertation Committee for Kelli Margaret Rankin Certifies that this is the approved version of the following dissertation:

Novel Solvent Injection and Conformance Control Technologies for Fractured Viscous Oil Reservoirs

Committee:

Quoc P. Nguyen, Supervisor

Hon-Chung Lau

Tadeusz W. Patzek

Gary A. Pope

Sanjay Srinivasan

Novel Solvent Injection and Conformance Control Technologies for Fractured Viscous Oil Reservoirs

by

Kelli Margaret Rankin, B.S.P.E; M.S.E.

Dissertation

Presented to the Faculty of the Graduate School of

The University of Texas at Austin

in Partial Fulfillment

of the Requirements

for the Degree of

Doctor of Philosophy

The University of Texas at Austin

May 2013

Acknowledgements

I would like to express my sincere gratitude and appreciation to Dr. Quoc P. Nguyen for his encouragement and aid on this research project and throughout my time in graduate school. His unending patience and invaluable insights always eased the path. I would also like to extend my thanks to Johan van Dorp, Marco Verlaan, Orlando Castellanos-Diaz, and Thanh Nguyen for engaging discussion and support related to the solvent injection experiments and simulation.

Special thanks are owed to Glen Baum and Gary Miscoe, who always made time to help me when I had lost my way in the lab. Also to Mark Smith and Daryl Nygaard for working so diligently to come up with creative solutions to my unique fabrication needs. And to Dr. Sujeewa for his endless efforts to help me to acquire all that I needed.

I also need to thank Shell Oil Company for their financial support of portions of this research as well as for supplying the oil samples used in the viscous oil experiments.

I was immensely fortunate to have had the help of several excellent assistants – Ashay Agrawal, Markos Freeman, Samuel Lau, Tianyu Li, Kevin Liu, Andreas Michael, Vu Nguyen, and Roshan Pandey – to help me in my experimental work. Two – Bradley Nguyen and Tyler Seay – became my right-hands, and I am glad that they will be continuing the work now that I have left.

To my fellow researchers – Naveed Arsalan, Prince Azom, Shashvaat Doorwar, Bi Nguyen, Luiz Santos, and Himanshu Sharma – for providing friendship and support as only a fellow graduate student could. To my friends who always forgave and understood when I had to cancel because of a "lab emergency" – Cigdem Metin, Alaina Smith, and

Rubia Viegas. And to the one person who I am most glad joined me on this journey – Patrick Adiaheno.

Finally, I would like to thank my parents. My mother for always lending a sympathetic ear, sharing stories of her graduate studies that put my own in perspective, and pointing out that in the end everything works out. My father for serving as my ever-evolving counselor, never letting me wallow in my failures, and reminding me to have some fun outside of work. And to both for always reminding me that as a freshman I said that going to graduate school meant getting on the "loser bus" and pointing out now how wrong I was.

Novel Solvent Injection and Conformance Control Technologies for Fractured Viscous Oil Reservoirs

Kelli Margaret Rankin, PhD

The University of Texas at Austin, 2013

Supervisor: Quoc P. Nguyen

Fractured viscous oil resources hold great potential for continued oil production growth globally. However, many of these resources are not accessible with current commercial technologies using steam injection which limits operations to high temperatures. Several steam-solvent processes have been proposed to decrease steam usage, but they still require operating temperatures too high for many projects. There is a need for a low temperature injection strategy alternative for viscous oil production. This dissertation discusses scoping experimental work for a low temperature solvent injection strategy targeting fractured systems. The strategy combines three production mechanisms – gas-oil gravity drainage, liquid extraction, and film gravity drainage. During the initial heating period when the injected solvent is in the liquid phase, liquid extraction occurs. When the solvent is in the vapor phase, solvent-enhanced film gravity drainage occurs. A preliminary simulation of the experiments was developed to study the impact of parameter uncertainty on the model performance. Additional work on reducing uncertainty for key parameters controlling the two solvent production mechanisms will be necessary.

In a natural fracture network, the solvent would not be injected uniformly throughout the reservoir. Preferential injection into the higher conductivity fracture areas

would result in early breakthrough leaving unswept areas of high oil saturation. Conformance control would be necessary to divert subsequent solvent injection into the unswept zones. A variety of techniques, including polymer and silica gel treatments, have been designed to block flow through the swept zones, but all involve initiating gelation prior to injection. This dissertation also looks at a strategy that uses the salinity gradient between the injected silica nanoparticle dispersion and the in-situ formation water to trigger gelation. First, the equilibrium phase behavior of silica dispersions as a function of sodium chloride and nanoparticle concentration and temperature was determined. The dispersions exhibited three phases – a clear, stable dispersion; gel; and a viscous, unstable dispersion. The gelation time was found to decrease exponentially as a function of silica concentration, salinity, and temperature. During core flood tests under matrix and fracture injection, the in-situ formed gels were shown to provide sufficient conductivity reduction even at low nanoparticle concentration.

Table of Contents

List of Tables

List of Figures

Chapter 1: Introduction

The purpose of this work is two-fold: (1) develop a low temperature production process for viscous fractured reservoirs and (2) study the potential of in-situ generated silica nanoparticle gels for conformance control applications in fractured reservoirs. To achieve these purposes, the work (1) proposes a solvent injection strategy that combines the benefits of liquid extraction, film gravity drainage, and gas-oil gravity drainage (GOGD) to successfully produce viscous oil using low-temperature solvent injection and (2) verifies the gelation potential of silica nanoparticle dispersions in the presence of saline solutions in the bulk phase and in dynamic flow tests.

1.1 Background

Heavy oil and bitumen resources have great potential to meet the future demand for petroleum products as conventional resources are depleted. However, oil recovery from heavy oil (viscosity between 100 and 10,000 cp) and bitumen (viscosity greater than 10,000 cp) reservoirs is complicated because heavy oil or bitumen is partially or completely immobile under reservoir conditions. The Alberta government has estimated that there are 600 billion barrels of stranded oil sand resource that is too deep for mining and too shallow for steam assisted gravity drainage (SAGD) (Braswell 2012). This suggests that low temperature/low pressure in-situ operations are a key target for future development in heavy oil production. Low temperature and pressure operations are also important for developing fractured carbonate reservoirs, which worldwide hold 1.6 trillion barrels oil in place (Briggs, Beck, et al 1992). Several current technologies – from steam floods to solvent injection – have been studied for viscous oil production in fractured reservoirs.

During thermal processes in fractured reservoirs, the fractures transport the heat into the reservoir faster than under matrix injection. Gas-oil gravity drainage holds great potential for production from heavy oil fields because conventional displacement methods are often ineffective in fractured rock because the high fracture permeability prevents significant pressure differentials across the matrix. The density difference between the gas and oil provides the energy for the process without depleting the reservoir pressure (Festoy and van Golf-Racht 1987). Thermally assisted gas-oil-gravity drainage (TA-GOGD), unlike a normal steam flood, uses steam only as a heating agent to enhance the existing drive mechanisms rather than serve as the drive mechanism. The fracture network is used for distribution of heat and recovery of oil (Penney 2005). In the TA-GOGD process, the draining matrix is mostly heated, but remains below steam temperature. As a result, the steam will condense before entering the matrix and heat transfer is through conduction. There are only five published steam pilots in naturally fractured carbonates: Lacq Superior field, France (Sahuquet and Ferrier 1980); Ikiztepe field, Turkey (Nakamura, et al 1995); Yates field, USA (Snell and Close 1999); Qarn Alam field, Oman (Macaulay et al 1995); and Bati Raman field, Turkey (Babadagli, et al 2008). The Lacq Superior, Ikiztepe, and Bati Raman pilots were for the steam flood process. The Yates pilot tested the double displacement process defined as the gas displacement of a water invaded oil column. Only the Qarn Alam pilot used the TA-GOGD process and is the only one to be switched to full field scale application.

There have been many hybrid (steam + solvent) processes proposed for non-fractured, heavy oil reservoirs – Expanding Solvent Steam Assisted Gravity Drainage (ES-SAGD), Solvent Aided Process (SAP), Steam Assisted Gas Push (SAGP), Solvent Assisted Steam Assisted Gravity Drainage (SA-SAGD), and Liquid Addition to Steam

for Enhanced Recovery (LASER). Because all of the processes treat solvent as an additive, the operation temperatures are still near steam saturation conditions.

The Expanding Solvent Steam Assisted Gravity Drainage (ES-SAGD) process entails co-injecting a hydrocarbon additive at low concentration with steam. The hydrocarbon is selected so that its evaporation and condensation properties are the same as water. This allows the solvent to condense at the boundary of the steam chamber where it dilutes the oil and in conjunction with heat, reduces its viscosity. Both field trials of the process were unsuccessful (Nasr, et al 2003; Orr 2009). The Solvent Aided Process (SAP) combines the benefit of heat and solvents by adding a small amount of hydrocarbon solvent to the injected steam during SAGD. The SAP process is operated so that steam rates are relatively unchanged after the start of solvent injection. The only difference from ES-SAGD is that the solvent does not need to match the condensation characteristics of the steam at operating conditions. It is believed that the relaxation in solvent constraint, which allows lighter alkanes to be injected, led to the successful field trial (Gupta and Gittins 2005; Orr 2009). In contrast to SAP, the Solvent Assisted Steam Assisted Gravity Drainage (SA-SAGD) process, currently under field trial, does reduce the rate of steam injection. The Steam and Gas Push (SAGP) process entails the addition of non-condensable gas to the Steam Assisted Gravity Drainage (SAGD) process. The gas accumulates at the top of the reservoir to serve as an insulating layer. During the process, fingers of gas rise within the reservoir increasing the oil pressure, which pushes the oil downward. The gas forms an insulating layer long before the heat reaches the top of the reservoir (Dickson, et al 2011). Liquid Addition to Steam for Enhancing Recovery (LASER) involves injecting liquid hydrocarbon as a steam additive in the cyclic steam stimulation (CSS) mode of operation. The LASER process is applicable in later cycles when the conventional drive mechanisms have reached their limits and gravity drainage

has become more predominant. Completed field trials were a success (Leaute 2002; Leaute and Carey 2000). The Steam Alternating Solvent (SAS) involves injecting steam until the heat loss to the overburden becomes significant and then injecting solvent until the chamber temperature is reduced to uneconomic levels (Zhao 2004).

Several of these processes have also been studied in fractured reservoirs with measured improvement over steam-only processes – SAS (Suat Bagci, Samuel, and Mackay 2007); ES-SAGD (Fatemi, Kharrat, and Bassughi 11) and steam-over-solvent injection in fractured reservoirs (SOS-FR). The SOS-FR process has three cycles: steam injection to heat the reservoir and initiate flow, solvent injection to enhance drainage, and steam injection to recover solvent. During the first steam injection cycle, oil is produced from the matrix through thermal expansion and gravity drainage. During the solvent injection cycle, oil production is enhanced by solvent diffusion into the matrix oil, which upgrades the oil (Al Bahlani and Babadagli 2008, 2009, 2010).

Solvent injection was first proposed by Allen (1974) who patented a "huff and puff" process in which propane or butane was injected in cycles to extract oil from a packed cell. Allen and Redford (1976) proposed the injection of a liquid solvent and non-condensable gas at reservoir temperature and pressure. Nenniger (1979) patented a process using pure gas or mixtures at pressures equal to or lower than the saturation vapor pressure. All these processes used vertical injectors and producers. None of them showed economic potential. The introduction of horizontal wells in the 1980s led to further investigation of solvent extraction methods. Dunn et al (1989) applied the principles of SAGD for theoretical and experimental studies of bitumen recovery by gravity drainage using low-temperature soluble-gas injection. The two solvent processes directly relevant to this work are Vapor Extraction (VAPEX), cold injection of vapor solvent, and N-Solv, heated injection of liquid solvent. The key aspects of N-Solv are

production enhancement due to liquid extraction (advantage), higher gravity drainage rates due to elevated operating temperature (advantage), high solvent mass requirement to fill voided space (disadvantage), and possible excessive asphaltene precipitation (disadvantage). The key aspects of VAPEX are enhanced film drainage (advantage), minimal solvent mass requirement to fill void space (advantage), and no solvent purity requirements (advantage). Extensive laboratory and simulation work has been done for the VAPEX process (Butler and Mokrys 1989; Jiang and Butler 1996; Das and Butler; 1998), but little field study. The major impediment to field operations is adequate understanding of the mechanisms necessary to upscale laboratory results confidently (Yazdani and Maini 2005; Ayub and Tuhinuzzaman 2007; Alkindi, Muggeridge, and Al-Wihaibi 2010). The N-Solv process injects a heated pure solvent into the reservoir. The process is similar to SAGD (same well orientation) except condensing solvent provides heat instead of steam. N-Solv has been studied experimentally, and a pilot is currently in the development phase (Braswell 2012; Nenninger 2012; Fraunfeld, et al 2005). There has been minimal work on solvent processes for fractured reservoirs (Fareneh, et al 2010; Rahnema, Kharrat, and Rastami 2008).

Even when using fractures as a conduit for injected fluids, issues of conformance can occur. In a natural fracture network, some portions of the reservoir will be swept before others leading to early breakthrough from the most conductive fracture paths and leaving behind unswept portions of the reservoir. Conformance control can be used to divert subsequent injection from the swept portion of the fracture network into areas of the reservoir with higher remaining oil saturation. Liu, et al (2006) defines conformance control as "those technologies in which chemical or mechanical methods are used to reduce or block water/gas production resulting from wellbores or high permeability zones/channels/fractures of reservoirs." In situ gelation technology is a proven

economical process for improving oil recovery through conformance control (Vossoughi 2000). These systems, which function by strategic plugging of pores, include polymer gels, polymer microgels, silicates, and colloidal silica.

Polymer gels consist of a polymer network developed by the presence of a crosslinker. Polymer gel treatments have been proven successful as a conformance tool (Purkaple and Summers 1988, Hardy, et al 1999, Moradi-Araghi, Bjornson, and Doe 1993, and Moffitt, et al 1996) but there are still many key issues with the system such as "(1) environmental and safety issues over the heavy metal crosslinking agent chromium, (2) limited penetration depth, (3) polymer shear degradation, (4) polymer absorption on the reservoir surface, (5) lack of polymer gel time control, and (6) polymer precipitation under harsh reservoir conditions (Burns, et al 2008)."

Polymer microgels are an alternative to polymer gels using much lower concentration of polymer and crosslinker resulting in a lower viscosity than the polymer gel network, which allows for deeper placement of the gel and reduced injectivity problems. However, microgels are still susceptible to harsh reservoir conditions and have environmental issues.

Compared to polymer gel and microgel, sodium silicates and colloidal silica can better withstand harsh reservoir conditions and do not have any environmental and safety issues. Sodium silicates are silicate powder (Na_2SiO_3) dissolved in an aqueous solution. Colloidal silica is a stable aqueous dispersion of amorphous silicon dioxide particles. For both systems, the addition of salt results in charge screening which causes gelation (Jurinak, Summers, and Bennett 1991). Colloidal silica provides the best option because it has the environmental benefits of silicates with a more robust gel control and no pH limitations.

A critical issue for opening up production from fractured viscous oil reservoirs is developing a low temperature operating strategy. While steam and steam-solvent processes have been successful in un-fractured viscous oil reservoirs, the processes cannot be modified for low temperature operations because of the high steam saturation temperature requirements. Solvent injection allows for low temperature operations, but no solvent-only process (using vapor or liquid solvent or cold or heated injection) has been successfully field tested despite showing positive lab results. I plan to address this issue by combing several production mechanisms that have individually shown promise – the gas-oil gravity drainage process and liquid and vapor solvent injection – in a heated solvent injection strategy that used the fractures as conduits for the injected solvent. In a natural fracture network, some portions of the reservoir will be swept before others leading to early breakthrough from the most conductive fracture paths leaving behind unswept portions of the reservoir. To address this problem, conformance control is necessary. There are several current conformance technologies that generate gels to provide control. However, they initiate the gelling process prior to injection requiring pre-conditioning of the reservoir. My proposed conformance control technique will use the natural salinity gradient between the injected silica nanoparticle solution and the reservoir brine to initiate gelation in-situ.

1.2 OUTLINE

Chapter two provides a literature review of current viscous oil production and conformance control techniques with a focus on those applicable to fracture reservoirs. Viscous oil production requires a reduction in oil viscosity which can be achieved through an application of heat, mixing with solvent, or a combination of the two. While steam and steam-solvent processes have had great success, the phase behavior of steam

prevents operating at temperatures lower than 100 °C. Therefore, the target for low-temperature operation will be solvent injection which has been done in the vapor and liquid phase. Because of environmental issues with polymers and microgels, colloidal silica is targeted as the most robust gelling agent for conformance control.

Chapter three discusses proof-of-concept experiments of the proposed solvent injection strategy, which were performed in a sand column representing a single matrix-fracture interaction. The process is tested under varying conditions – temperature, permeability, injection rate, and solvent type. Production is dominated by two mechanisms dependent on the solvent phase – liquid extraction (liquid solvent) and solvent-enhanced film gravity drainage (vapor solvent). Analytic solutions can be used to confirm the effect of varying test conditions on each mechanism.

Chapter four describes work with the CMG STARS thermal simulator and CMOST history matching tool to determine the simulation parameters necessary to model the two production mechanisms and study the impact of uncertainty in each parameter on the simulation output.

Chapter five studies the bulk phase behavior and rheology of nanoparticle dispersions in the presence of saline solutions. Phase behavior diagrams, with a focus on gelation windows, are developed over a salinity-nanoparticle concentration space for varying temperatures. Dynamic shear measurements were then used to determine gelation times (for solutions within the gel window) as a function of salinity, nanoparticle concentration, and temperature. The work was used as the foundation to design the conditions for the flow tests of chapter six.

Chapter six explores the potential of the gel of chapter five as a conformance control technique in limestone core. Basic proof-of-concept experiments studying the impact of nanoparticle concentration and salinity gradient are carried out before the

optimal conditions for matrix injection are applied to a fractured core. Gelation is successful at low nanoparticle concentrations and salinity gradient can be used to modify placement depth. The optimum matrix conditions were not as good in the fractured core, but permeability reduction was still achieved.

Chapter seven includes conclusions and future work and highlights the major experimental observations supporting continued study of both processes. Because the work was designed as proof-of-concept only, further work will be necessary to mature the technologies investigated here.

Chapter 2 – Literature Review

This chapter is divided into two main sections – production from viscous oil reservoirs and conformance control methods. The two sections are designed to overview the previous work done in both fields that were used as building blocks for the two new technologies introduced in this dissertation.

2.1 Viscous Oil Production

Viscous oil resources hold great potential for continued oil production growth globally. However, much of these resources are not accessible using currently-used commercial technologies. Canadian tar sands contain 1.6 to 2.5 trillion barrels of hydrocarbon liquids, 90% of which are too deep to mine (Nenniger and Dunn 2008). In Alberta alone, there are an estimated 600 billion barrels of stranded oil sand resource that is too deep for mining and too shallow for steam assisted gravity drainage (SAGD) (Braswell 2012). Viscous carbonate reservoirs hold particular potential for improved technologies. Viscous oil contained in carbonate reservoirs worldwide is estimated at $1.6x10^{12}$ barrels in place (Briggs, Beck, et al 1992). Heavy oil in Middle East fractured carbonate reservoirs account for 25-30% of the total oil in place in the region (Nabipour, et al 2007). The work presented in this dissertation explores a novel, low temperature solvent injection strategy targeting fractured systems. The work builds on three current technologies – Gas-Oil Gravity Drainage (GOGD), Vapor Extraction (VAPEX), and N-Solv. The following section details the current state of these technologies and others relevant to our proposed technology.

2.1.1 Gas-Oil Gravity Drainage

Many production mechanisms contribute to production during the life of a fractured reservoir – expansion, solution-gas drive, oil/water imbibition, and gas gravity

drainage. Gas gravity drainage occurs when gas from the gas-saturated fractures displaces the oil from the matrix. The fracture gas can be gas liberated from the oil, gas from an expanding gas cap, or gas from gas injection. Gas-oil gravity drainage holds great potential for production from heavy oil fields because conventional displacement methods are often ineffective in fractured reservoirs because the high fracture permeability prevents significant pressure differentials across the matrix. The density difference between the gas and oil provides the energy for the process without depleting the reservoir pressure (Festoy and van Golf-Racht 1987). The process has been well studied in light oil reservoirs with varying gases: nitrogen (Thomas, Dixon, et al 1991), methane (Morel, Bourbiaux, et al 1990), and heavier carbon fractions (Firoozabadi and Markeset 1994).

Babadagli (2002) included the process in a review of EOR processes for heavy oil reservoirs. The process yields slower recovery rates than other possible mechanisms but can be enhanced by thermal or miscible gas injection. Steam injection has the added benefit that increased temperatures reduce the oil viscosity. Solvent injection has been thought to be the only possible alternative to thermal methods in carbonates because chemical injection has not been shown to be a promising method for this type of reservoirs. In thermal assisted gas-oil gravity drainage (TA-GOGD), the steam condenses in the fracture when it contacts the matrix providing conductive heating of the matrix. The condensed water then flows down the fracture to the production well. Oil production occurs through oil expansion, viscosity reduction (increased drainage rate), solution gas drive, and stripping effects (requires high temperatures). Of the processes studied by Bychkov, et al (2008), viscous oil production was dominated by oil expansion and viscosity reduction. Solution gas drive and stripping effect are only important for light oils.

Van Heel, et al (2008) studied the heating of and oil recovery from a vertical stack of matrix blocks surrounded by fractures using analytical results and thermal reservoir simulations. Steam was injected at the top and oil recovered at the bottom of the fracture system. The gas gravity drainage rate (Equation 2.1) from a matrix block would be

$$q_{gd}(t) = \frac{1}{L_x}\int_0^{L_x} \frac{kk_r}{\mu(T(x,t))} g\Delta\rho_{og}\, dx \tag{2.1}$$

where L_x = block length in the x-dimension

k = absolute permeability

k_r = oil relative permeability end point

μ = oil viscosity

g = gravitational constant

$\Delta\rho_{og}$ = density difference between the oil and gas phases.

The equation is numeric unless analytic functions are assumed for the parameters such as relative permeability and oil viscosity.

2.1.2 Steam in Fractured Reservoirs

Steam has been extensively studied as a method for secondary recovery method in light oil, fractured carbonate reservoirs. Reis (1990) reviewed the recovery mechanisms for steam injection in naturally fractured light oil reservoirs. Oil recovery from fractured reservoirs occurs in two stages: oil is expelled from matrix blocks and is then produced through the fracture network. The differential hydrostatic head between the fracture vapor and the matrix oil establishes a vertical pressure gradient, which forces oil out of the matrix blocks. However, the gravity head between matrix oil and fracture gas must be sufficient to overcome capillary entry pressure. Capillary imbibition is much more prevalent in water-wet reservoirs. Even at already low viscosities, the further reduction of viscosity at higher steam temperatures will speed the imbibition process. The most

important incremental recovery mechanism for steam injection over waterflooding is the differential thermal expansion between the oil and pore volume. Cyclic steam injection can enhance the process. The reservoir pressure increases during injection and decreases during production. Because the matrix has a delayed response to the pressure change, the condensed water in the matrix will flash to steam during the production phase, which expels oil by gas drive. Dreher, Kenyon, and Iwere (1986) studied steam injection into light oil, fractured carbonates in the laboratory and with a fully implicit simulator. Heat is continuously supplied to the fractures and heat conduction into the matrix is the major force for matrix heating. In laboratory floods of carbonate disks with hot water and steam, oil recovery increased as injection temperature increased because of an increased rate of oil-water imbibition, the primary recovery mechanism. Simulation of a massive dolomite with 50 foot fracture spacing showed that long-term isothermal imbibition followed by steam injection created a significant oil production response.

Production from fractured reservoirs under steam injection is essentially independent of oil gravity, making steam injection equally attractive in light or heavy oil reservoirs. Briggs, Beck, et al (1992) performed a mechanistic study of heavy oil production from dolomite core plugs under steam injection to identify the contribution to production from each production mechanism. The experiments went through four phases: initial heating (thermal expansion), brine injection (imbibition), back pressure reduction (internal gas drive and/or steam flashing), and hot water or steam injection (forced displacement). At the lower temperature test (150 °C), imbibition and depletion produced appreciable oil but forced displacement production was minimal. At the higher temperature (250 °C), results were similar for thermal expansion and imbibition, but depletion was negligible because the gas-drive mechanism was exploited in early production times. Babadagli (2002) looked at the effect of hot water injection on

recovery from water-wet sandstone and oil-wet limestone. For the sandstone sample, the capillary imbibition was improved by reduced oil viscosity resulting in an ultimate recovery exceeding that from thermal expansion alone. The limestone sample saw an accelerated recovery rate, but no change in ultimate recovery because only thermal expansion contributed to oil production.

2.1.3 Thermally Assisted Gas-Oil Gravity Drainage

Thermally assisted gas-oil-gravity drainage (TA-GOGD), unlike a normal steam flood, uses steam only as a heating agent to enhance the existing drive mechanisms rather than serve as the drive mechanism. The fracture network is used for distribution of heat and recovery of oil (Penney 2005). In the thermal GOGD process, oil production results from heat conduction through the fracture and into the matrix and gas cap generation due to thermal volatilization of the oil. A lack of hydrodynamic equilibrium (due to a deeper gas-oil contact in the fracture than the matrix) causes gravity forces to drain the oil through the matrix until it reaches the gas-oil contact. When the pressure of the draining oil in the matrix exceeds the fracture pressure, the oil will flow into the fracture. In the presence of a flow restriction, such as shale stingers or change in lithology, the pressure of the oil will increase above the restriction until is exceeds the capillary pressure of the matrix displacing the oil into the fracture. In heavy oil fields, the cold oil can serves as a barrier to downward flow, forcing the oil out of the matrix into the gas filled fracture. Block-to-block reimbibition will be negligible for heavy oil GOGD due to the inability of the lower blocks to drain at any substantial rate without the addition of heat (Shahin, et al 2006). From Darcy's law the GOGD drainage rate (Equation 2.2) can be derived as

$$q_{GOGD} = \frac{k_v k_{ro} A}{\mu_o}[\Delta\rho g - \frac{dp_c}{dz}] \tag{2.2}$$

Where k_v = vertical permeability

k_{ro} = oil relative permeability end point

A = cross sectional area of drainage

μ_o = oil viscosity

$\Delta\rho$ = density difference between oil and gas phases

g = gravitational constant

$\frac{dp_c}{dz}$ = vertical capillary pressure gradient.

The gas-oil capillary pressure in the matrix opposes the gravity effect. Capillary pressure can be neglected to determine the maximum oil drainage rate. With no vertical flow barriers, the final oil saturation profile will be the gas-oil capillary pressure curve (Ikwumonu, et al 2007).

Unlike typical thermal processes, the oil cools as it drains to the oil rim in the fracture. The high fracture permeability can accommodate the cold flow, which allows a cold production stream for many years. In the TA-GOGD process, the draining matrix is mostly heated, but remains below steam temperature. As a result, the steam will condense before entering the matrix and heat transfer is through conduction. Matrix steam flood and heating via convection will not occur until late in the process when the steam chamber has reached maximum expansion (Penney 2005). Thermal volatilization of the lighter hydrocarbon components of the oil occurs as the matrix blocks heat up. This gas generation increases the matrix gas-oil ratio. When the critical gas saturation is reached, the gas migrates to the fracture increasing the size of the fracture gas-oil contact (Shahin, et al 2006).

Ayyatollahi, et al (2005) studied the thermal gravity drainage process in an unconsolidated sand-packed column with varying wettability – water-wet, oil-wet, and mixed-wet. The experiments were free-fall gravity drainage experiments. The ultimate

oil recovery efficiency by the process deceases as the wettability changes toward oil wet. For the water-wet sand pack, film flow of oil under gravity drainage in the gas invaded zone is responsible for high recovery efficiency. Higher residual oil saturations occur in oil-wet reservoirs because the oil occupies the relatively small pores in the gas-invaded zone. Ikwumonu, et al (2007) studied the impact of fracture spacing on thermal GOGD. For larger fracture spacing, the heat front travels faster because heat loss is less and steam does not condense as much. Heating is concentrated near the source and higher matrix temperatures are achieved quicker with dense fracture spacing. Heat breakthrough is also slower at the producer for denser packed fractures.

Al-Rabaani, et al (2008) studied the rate of heating within a matrix block and its impact on gravity drainage using a combination of analytic solutions for heat conduction into the matrix and detailed numerical simulation of heat transport and gravity drainage. These rates are important because the effectiveness of the TA-GOGD process is primarily a function of the rate at which the rock matrix is heated by the steam and the rate at which oil drains from the matrix. They found that the time to heat the matrix block (Equation 2.4) can be similar or greater than the time for the heated oil to drain (Equation 2.3).

$$t_{GD} = \frac{\phi \mu_o l_z}{\Delta \rho g K_v} \tag{2.3}$$

Where φ = porosity

μ_o = oil viscosity

l_z = height of matrix block

$\Delta\rho$ = density difference between oil and gas phase

g = gravitational constant

K_υ = vertical permeability.

$$t = \frac{-1}{\pi^2 \kappa [\frac{1}{l_x^2} + \frac{1}{l_y^2} + \frac{1}{l_z^2}]} \ln[\frac{\pi^6}{512} \frac{(T_{fi} - \overline{T})}{(T_{fi} - T_{mi})}] \quad (2.4)$$

Where κ = thermal diffusivity

l_i = block dimension in i-direction

T_{fi} = initial fracture temperature

$\overline{T}$ = mean matrix temperature

T_{mi} = initial matrix temperature.

They also developed a simple analytically-derived formula (Equation 2.5) for the critical steam injection rate for TA-GOGD. Below the critical rate, oil recovery increases with the square of steam velocity. Above the critical rate, there is no significant increase in oil recovery with injection rate. The equation assumes that steam is recycled through the reservoir and neglects heat losses to the formation. Therefore, the desired operational rate may need to be higher to achieve the same heating.

$$U_{cr} \approx \frac{2\ell_x \lambda_m}{h\ell_z C_w} \quad (2.5)$$

where l_x = matrix length in x-direction

λ_m = matrix thermal conductivity

h = fracture aperture

C_w = water volumetric heat capacity.

There are only five published steam pilots in naturally fractured carbonates: Lacq Superior field, France (Sahuquet and Ferrier 1980); Ikiztepe field, Turkey (Nakamura, et al 1995); Yates field, USA (Snell and Close 1999); Qarn Alam field, Oman (Macaulay et al 1995); and Bati Raman field, Turkey (Babadagli, et al 2008). The Lacq Superior, Ikiztepe, and Bati Raman pilots were for the steam flood process. The Yates pilot tested the double displacement process defined as the gas displacement of a water invaded oil

column. Only the Qarn Alam pilot used the gas oil gravity drainage mechanism and is the only one to be switched to full field scale application, so it is discussed in further detail.

Because of the strong natural aquifer drive and the oil-wet rock, ultimate recovery under primary recovery from the intensely-fractured carbonate Shuaiba/Kharaib/Lekhwair reservoir in Qarn Alam, Oman will only be 2% of OOIP. Because of the success of steam injection into the Lacq Superieur reservoir, a similar type of reservoir, steam injection was targeted and pursued as an alternative means of increasing the GOGD rate in the Qarn Alam field (Macaulay, et al 1995). Van Wunnik and Wit (1992) explored using steam injection into the gas cap of the reservoir to reduce the oil viscosity to enhance drainage rates. In the heated zone of the reservoir, the recovery mechanisms are oil expansion and gravity drainage. Their analytic investigation showed that the main production mechanism was gravity drainage with one-third from gas-oil gravity drainage and 2/3 from water-oil gravity drainage.

Macaulay, et al (1995) used the TA-GOGD study by van Wunnik and Wit (1992) in their design of a steam pilot for the Qarn Alam field. They found that steam injection rate controls the temperature of the steam/gas mixture at the crest of the reservoir up to the maximum temperature of the mixture. Only one percent of original oil in place will be heated during the five year life of the pilot. The primary recovery methods were expected to be thermal expansion and gas gravity drainage (primarily from reduction in oil viscosity) with distillation if the matrix temperature reaches 240 °C and a possibility of wettability reversal for temperatures between 150 and 200 °C. The MoReS simulator was used for a full-field history match of previous production, which was used to predict the behavior of steam injection. The simulation showed that there is a two to three month

time lag before the entire matrix between the fractures is heated. The steam zone will develop radially and be piston-like in cross section.

The steam pilot commenced in July 1996 with two injection wells 25 m apart at the crest of the field. Temperature was measured at two observations wells. Reservoir saturation tool (RST) logs were run before and during the pilot to monitor fluid saturations changes. The logs could also be used to determine gas/oil and oil/water contacts in the fractures. Seismic methods were used to monitor the heat front in time-lapse mode (al-Shizawi, Denby, et al 1997). The pilot produced oil at a high water cut of both condensed steam and aquifer water, which required significant effort with emulsion breakers and separators (Penney, et al 2005). Twenty-seven percent of the thirty percent incremental recovery from the pilot was viscosity reduction with three percent from thermal expansion (Shahin, et al 2006). The incremental recovery from the pilot as well as successful injection of 1.3 million tons of steam without well failure, reduction of injectivity, or loss of matrix/cap rock integrity justified full field development. Significant fracturing is necessary to supply heat to accelerate oil drainage into the fractures at a sufficient rate. Even though the pilot only tested the highly-fractured crestal zone, fracture scenario modeling has provided sufficient confidence that the project can succeed outside the test area. The Full Field Steam Project received final shareholder approval in 2007 with first steam in 2010 (Penney, et al 2007).

2.1.4 Steam + Solvent Processes

Frauenfeld, Jossy, and Ivory (2009) define a hybrid solvent process as any process that heats injected solvent by co-injecting steam. They looked at lab and field scale simulations to study propane-steam and butane-steam injection. At the lab scale, steam injection (SAGD) produced more oil than propane-steam but less than butane-steam. The

authors' cost objective function, though, showed that propane-steam was the best followed by steam and butane-steam. The function accounts for capital and operating (steam cost, solvent, cost, and solvent recycle cost) costs. At the field scale, steam outperformed propane-steam in oil volume and economics. In contrast, butane-steam outperformed steam at the field scale in terms of oil rate and for lower butane injection rates, economically, as well.

There has been many such hybrid processes proposed for non-fractured, heavy oil reservoirs –Expanding Solvent Steam Assisted Gravity Drainage (ES-SAGD), Solvent Aided Process (SAP), Steam Assisted Gas Push (SAGP), Solvent Enhanced Steam Assisted Gravity Drainage (SA-SAGD), and Liquid Addition to Steam for Enhanced Recovery (LASER). Because all of the processes treat solvent as an additive, the operation temperatures are still near steam saturation conditions.

The ES-SAGD process entails co-injecting a hydrocarbon additive at low concentration with steam. The hydrocarbon is selected so that its evaporation and condensation properties are the same as water. This allows the solvent to condense at the boundary of the steam chamber where it dilutes the oil and in conjunction with heat, reduces its viscosity. The maximum oil drainage rate occurred when the steam temperature matched the solvent vaporization temperature. However, as long as the solvent vaporization temperature was within 50 °C of steam injection temperature, significant oil drainage was observed (Nasr, et al 2003). The ES-SAGD process has been field tested twice. Nexen-OPTI injected Jet B, a winter grade aviator fuel blend composed of heavier petroleum fractions (heptane to dodecane) at Pair 3 of the Long Lake Pilot in 2006. The test was terminated after two months because there was no observed increase in oil rate. The suggested cause for failure was that the solvent was too heavy. Suncor injected naphtha into the Firebag area. No increase in oil production was

observed. Because of the heavy nature of the solvent, it likely condensed prior to the steam (Orr 2009).

The Solvent Aided Process (SAP) combines the benefit of heat and solvents by adding a small amount of hydrocarbon solvent to the injected steam during SAGD. The SAP process is operated so that steam rates are relatively unchanged after the start of solvent injection. The only difference from ES-SAGD is that the solvent does not need to match the condensation characteristics of the steam at operating conditions. This allows lighter alkanes to be injected. EnCana first tested the SAP process with butane at Senlac in 2002 (Gupta and Gittins 2005). The test showed a 50% increase in oil rate. It had to be terminated because of loss of reservoir containment, but over 70% of the solvent was recovered. The encouraging results led to the decision to further testing at Christina Lake where similar improvements in recovery as well as improvement in steam-oil-ratio and API gravity (Orr 2009). Both of the SAP projects were started after peak SAGD rates had been achieved. It is not critical to start at this time, but the authors believe it is advantageous because the chamber has already risen to the top of the reservoir. Modeling of the Christina Lake test suggests that the solvent benefit comes during lateral expansion of the vapor chamber (Gupta and Gittins 2005). Comparison of the ES-SAGD and SAP pilots suggest that lighter solvents are necessary for field success.

Exxon-Mobil and Imperial Oil Resources started a pilot of the SA-SAGD process at Cold Lake, Canada, in the fourth quarter of 2009. The SA-SAGD process injects up to 20 volume percent light hydrocarbon solvent with dry steam in the traditional SAGD well orientation. In contrast to SAP, the SA-SAGD process does reduce the rate of steam injection. Two well pairs were studied in the pilot, which allows for comparison between SAGD and SA-SAGD. When the warm-up phase was completed in June 2010, the producers were switched to steam injection, and the well pairs produced under SAGD

until solvent injection was started in one well pair in October 2010. Results have not yet been published (Dickson, et al 2011).

The Steam and Gas Push (SAGP) process entails the addition of non-condensable gas to the SAGD process. The gas accumulates at the top of the reservoir to serve as an insulating layer. During the process, fingers of gas rise within the reservoir increasing the oil pressure, which pushes the oil downward. The gas forms an insulating layer long before the heat reaches the top of reservoir. Canbolat, Akin, and Polikar (2004) performed six experiments to study the SAGP process with CO_2. The experiment showed reduced steam requirements and reduced steam-oil-ratio. Ultimate recovery increased for the larger vertical well separation but not for the smaller separation. As well pair separation increases, more CO_2 is required to reach SAGP conditions.

Liquid Addition to Steam for Enhancing Recovery (LASER) involves injecting liquid hydrocarbon as a steam additive in the cyclic steam stimulation (CSS) mode of operation. In the CSS process, the next cycle is started when the drive mechanisms loose sufficient energy and can no longer provide economic production. The LASER process is applicable in later cycles when the conventional drive mechanisms have reached their limits and gravity drainage has become more predominant. Lab results showed a 40 percent increase in bitumen productivity across 7 cycles. Based on the encouraging lab results, a field trial was performed at the Cold Lake reservoir. The field pilot design was based on a 33% improvement in oil-steam ratio (OSR) and diluent recovery of 66% using 6 volume percent diluent. Diluent injection began in April 2002 scheduled to last two years (seven cycles) at Cold Lake (Leaute 2002). The diluent recovery (80%) exceeded original expectations and is similar in composition to the injected diluent. The increase in OSR was consistent with original expectations (Leaute and Carey 2007).

The Steam Alternating Solvent (SAS) involves injecting steam until the heat loss to the overburden becomes significant and then injecting solvent until the chamber temperature is reduced to uneconomic levels. The higher viscosity of oil along the chamber boundary during solvent injection is compensated by higher relative oil permeability; the lower relative oil permeability during steam injection is compensated by the lower oil viscosity along the chamber boundary (Zhao 2004).

2.1.5 Steam + Solvent Processes in Fractured Reservoirs

The Steam-Alternating-Solvent (SAS) process was also studied in a fractured reservoir numerically by Suat Bagci, Samuel, and Mackay (2007). Their simulations showed that the SAS process (propane) outperformed the SAGD process with best SAS performance for a one year steam/six month solvent injection cycle. In fractured reservoirs, thermal processes have the advantage that thermal conduction can heat areas that are not in contact with the steam. The solvent chamber can inhibit heat transfer from subsequent steam injection. No difference in oil production occurred with differing fracture orientations. At higher pressures where the solvent may condense, the SAGD process outperforms SAS. The SAS process could be improved by finding a way to maintain reservoir temperature during solvent injection.

Fatemi, Kharrat, and Vossughi (2011) numerically investigated the SAGD and ES-SAGD process in fractured reservoirs. The ES-SAGD process had higher oil rates and ultimate recovery than SAGD in traditional and fractured reservoirs. The chamber was more uniform for the ES-SAGD process, which shows better depletion in the non-fractured part of the model.

Al Bahlani and Babadagli (2008) performed static imbibition experiments on Berea sandstone and carbonate cores to study the Steam-over-Solvent Injection in

Fractured Reservoirs (SOS-FR) process. The process has three cycles: steam injection to heat the reservoir and initiate flow, solvent injection to enhance drainage, and steam injection to recover solvent. During the first steam injection cycle, oil is produced from the matrix through thermal expansion and gravity drainage. During the solvent injection cycle, oil production is enhanced by solvent diffusion into the matrix oil, which upgrades the oil. The experiments were conducted in imbibition cells at 90 °C to mimic matrix-fracture interactions in steam condensation zones. Heptane was selected as the solvent for its high boiling point. The cores were immersed in 90 °C distilled water and left in a constant temperature oven until no additional recovery was observed. Then, the cores were allowed to cool in a water bath before being immersed in cold solvent. The cooling period is meant to mimic the cooling time between steam and solvent injection in the field. The cooling period was also used to introduce water into the system, which would improve recovery by spontaneous imbibition of solvent displacing water during phase two. Finally, the cores were immersed again in a 90 °C water bath to retrieve solvent and possibly additional oil. In the water-wet cores, most of the oil production occurred in phase one. In the oil-wet cores, most of the oil production occurred in phase two.

Al Bahlani and Babadagli (2009) expanded their earlier work on the SOS-FR process by running static tests with different solvents (heptane, kerosene, decane, and light crude), dynamic tests with heptane, and similar experiments in glass models. For the dynamic tests, each core was artificially fractured by cutting it through the middle. The core holder was wrapped in heating tape to keep a constant temperature. The impact of solvent injection rate was also studied. The glass models were oil-wet, but light oil was used for better visualization and to eliminate the possibility of asphaltene precipitation. The static tests showed that the higher the solvent molecular weight, the lower the heavy-oil recovery. Lower molecular weight solvents, though, do result in a

higher amount of asphaltene precipitation. No incremental late-time recovery was observed during the decane static test, which was allowed to soak in the solvent longer.

The SOS-FR process can be done in the field as cyclic or continuous injection. However, the authors believe that cyclic injection may not supply enough solvent. They found that if the solvent injection rate was too high, there was not sufficient time for diffusion and the solvent was basically recycled. The direction of flow is also important. The counter-current experiment showed the best phase one production, but solvent performance was limited because of lower contact area.

Al Bahlani and Abadagli (2009) reported numerical modeling of the dynamic experiment of the SOS-FR process will heptane in an oil-wet Berea core. The simulation was done in STARS with heavy oil PVT values characterized in ECLIPSE. Perforations were placed in the fracture which made it act like a source/sink well. During solvent injection three phases of oil production were observed: fracture oil depletion, diffusion dominated transport, and dispersion dominated transport. The first phase generated a small amount as it was only the recovery of residual oil in the fracture. During the second phase, production rate was controlled by the slow solvent diffusion into the matrix. Finally, once the solvent diffusion into the matrix was complete, production became dominated by solvent dispersion in the fracture. The controlling processes during phase one were thermal expansion coefficient, injection temperature, relative permeability curves, and heat loss parameters. For phase two, the controlling processes were matrix molecular diffusion and matrix-fracture mechanical dispersion. Al Bahlani and Babadagli (2010) used the history-matched reservoir properties from the previous work to create field scale simulations to study the process efficiency and identity optimal injection schemes (continuous v cyclic injection). The simulations showed that oil recovery for steam injection was slightly higher than for continuous injection SOS-FR.

However, the SOS-FR process was more economic. The impact of solvent injection rate was not significant for single matrix case. However, it became more critical for the multiple matrix case. Cyclic SOS-FR showed little improvement over continuous injection SOS-FR for recovery, but the solvent to oil ratio was much lower.

Naderia and Babadagli (2011) explored using carbon dioxide (CO_2) as the solvent in the SOS-FR process under static conditions at different temperatures to achieve oil production and CO_2 storage. Using CO_2 instead of heptane has two advantages – solvent cost reduction and greenhouse gas disposal. Torabi and Asghari (2007) found that for CO_2 huff-and-puff in fractured Berea sandstones, permeability only has an impact below miscible conditions with higher permeability giving a higher production rate. The original SOS-FR tests considered deep reservoirs, so the "steam" phases were less than 100 °C. This work looked at hot water (90 °C) and steam (120/150 °C) conditions. As expected increasing the temperature increased oil production during phase one. Under immiscible conditions, the CO_2 replaces the oil in the matrix. The higher temperatures in phase one resulted in improved oil recovery regardless of wettability. For effective mass transfer, CO_2 interaction time needs to be sufficient. Even after phase three injection, CO_2 was successfully stored in the reservoir. Naderi and Babadagli (2012) used the previous experimental results to build a numeric simulation (STARS) of the CO_2 SOS-FR process. For a field scale model, under continuous injection, CO_2 accumulated at the top of the formation along the vertical fractures. Under cyclic injection, it also diffused along the horizontal fracture with a better concentration in the matrix middle. No effect on recovery from injection rate was observed. They also looked at replacing the phase three steam injection with a draw down phase. The oil recovery was slightly lower, but the cases were more economic because of reduced water costs. For cyclic injection, the soaking period has a huge impact on production. Shorter periods lead to higher oil rates.

In term of CO_2 storage, cyclic injection is more useful because it leaves more CO_2 behind.

2.1.6 Solvent Processes

Solvent injection was first proposed by Allen (1974) who patented a "huff and puff" process in which propane or butane is injected in cycles to extract oil from a packed cell. Allen and Redford (1976) proposed the injection of a liquid solvent and non-condensable gas at reservoir temperature and pressure. Nenniger (1979) patented a process using pure gas or mixtures at pressures equal to or lower than the saturation vapor pressure. All these processes used vertical injectors and producers. None of them showed economic potential. The introduction of horizontal wells in the 1980s led to further investigation of solvent extraction methods. Dunn et al (1989) applied the principles of SAGD for theoretical and experimental studies of bitumen recovery by gravity drainage using low-temperature soluble-gas injection. The two solvent processes directly relevant to this work are VAPEX and N-Solv. The key aspects of N-Solv are production enhancement due to liquid extraction (advantage), higher gravity drainage rates due to elevated operating temperature (advantage), high solvent mass requirement to fill voided space (disadvantage), and possible excessive asphaltene precipitation (disadvantage). The key aspects of VAPEX are enhanced film drainage (advantage), minimal solvent mass requirement to fill void space (disadvantage), and no solvent purity requirements (advantage).

2.1.6.1 VAPEX

Butler and Mokrys built on Dunn's work with the concept of Vapor Extraction (VAPEX), which entails injecting a vaporized hydrocarbon solvent through a horizontal well and the diluted oil is produced through a lower horizontal well by gravity drainage.

Vaporized solvent, rather than liquid solvent, provides a higher driving force for gravity drainage due to greater density difference (Butler and Mokrys 1989). The two mechanisms for production during VAPEX are reduction of oil viscosity as solvent dissolves into oil and in-situ upgrading due to asphaltene precipitation (Jiang and Butler 1996).

From their Hele-Shaw experiments, Butler and Mokrys (1989) developed an equation for the drainage rate of oil during VAPEX (Equations 2.6 and 2.7).

$$Q = \sqrt{2kg\phi\Delta S_0 N_s h} \tag{2.6}$$

$$N_s = \int_{c_m}^{c_i} \frac{\Delta\rho D_s (1-c_s)}{\mu c_s} dc_s \tag{2.7}$$

with

where Q = oil drainage rate

k = permeability

g = acceleration due to gravity

ø = porosity

S_o = oil saturation

N_s = dimensionless solvent number integral

h = height

$\Delta\rho$ = density difference

D_s = intrinsic diffusivity of solvent

c_s = volume fraction of solvent

μ = absolute viscosity of bitumen solution

For the same process in porous media, the equation for volumetric flow rate from both sides of the VAPEX chamber (Das and Butler 1998), can be modified as

$$Q = 2L\sqrt{2kg\phi^{\Omega}\Delta S_0 N_s H} \tag{2.8}$$

with

$$N_s = \int_{c_{\min}}^{c_{\max}} \frac{\Delta\rho(1-c_s)D_{eff}}{\mu} d\ln c_s \tag{2.9}$$

$$D_{eff} = (A_d / A_f)D_a \tag{2.10}$$

$$D_a = D\phi^{\Omega} \tag{2.11}$$

Where L = horizontal well length

Ω = cementation factor

D_{eff} = effective diffusivity of solvent in bitumen

A_d = interfacial area for diffusion

A_f = area for fluid flow

D = mutual diffusivity of solvent in the bitumen

Das and Butler (1998) studied the VAPEX process in a Hele-Shaw cell and a scaled packed cell. Hele-Shaw experiments were performed with different temperatures, pressure, and crudes: Lloydminster Tangleflags heavy oil and Cold Lake, Peace River, and Athabasca bitumen. Below the saturation pressure of the solvent, extraction rates were higher at higher pressures. When the process was operated near the vapor pressure, deasphalting occurred. In the Hele-Shaw, the solvent dissolves in the bitumen at the interface and diffuses into it. Above a critical solvent concentration, asphaltene precipitation occurs. The diluted, deasphalted oil drains down. In the Hele-Shaw cell, the oil will flow underneath the deposited layer of asphaltene along the interface. The authors also explored the VAPEX process in a packed bed model. The model was packed with Ottawa sand or glass beads using butane as the solvent. For the process, the injected vapor rises above the injection well to form a chamber, spreads sideways once the chamber reaches the cap rock, and then pushes downward when it reaches the lateral

boundary. When it reaches the boundary, the steady rate falls off as the interface of the unextracted oil begins to fall, reducing the gravity head and the production rate.

The production rates in the packed bed are significantly higher than expected from scaling of the Hele-Shaw cell, which is what lead to the original modification to the Butler-Mokrys equation (Equations 2.8 through 2.11) for porous media. In the packed cell, the vapor extraction process takes place in a contact zone where the high-viscosity oil contacts the solvent vapor in the fine capillaries that offer a high interfacial area of contact. The authors proposed several reasons for the increased rate in the packed bed experiments – higher interfacial contact area, increased effective diffusivity, increased solubility, capillary imbibition and surface renewal, transient mass flux at the interface, and film drainage. Because contact does not take place at a simple surface there is increased interfacial contact area. The solvent does not have to penetrate a long distance into the bitumen; therefore, diffusion at the surface is more important than diffusion in the bulk bitumen phase. A decrease in vapor pressure at a curved interface will cause condensation of solvents at lower pressures. The diluted oil occasionally rises up against gravity due to the capillary action in the asphaltene deposited region. Capillary imbibition is aided by the positive spreading coefficient of diluted oil over water in water-wet sand. The diluted oil is drawn away from the interface by the adjacent capillary pore in the extracted sand matrix. In pores where capillary imbibition removes the diluted oil, the interface is periodically renewed. These initial transient concentration profiles at the interface lead to a higher mass transfer rate. The original Butler and Mokrys equation can be used or a packed bed, but it will require a higher value of diffusion coefficient to model higher mass rate.

One reason for the under-estimate of oil rate using the Butler-Mokrys (B-M) equation in porous medium is that the equation ignores the convective component of

solvent dispersion in porous media. Yazdani and Maini (2005) developed equations that account for the increased height dependency of the convective-dispersion contribution observed in their experiment. The authors performed nine VAPEX experiments. They observed that the deviation from the B-M rates increased as the height of the model increased. They surmised that this was from an increasing height dependency. This effect is related to the convective dispersion term. The current empirical correlations for dispersion coefficient do not account for the height dependency, which means it must be accounted for in the rate correlations. Therefore they developed two correlations (Equations 2.12 and 2.13) to describe their results.

$$\text{Quadratic: } Q = 0.017 h^{1.26} \sqrt{k\phi^m} \tag{2.12}$$

$$\text{Cubic: } Q = 0.0288 h^{1.13} \sqrt{k\phi^m} \tag{2.13}$$

Where Q = oil drainage rate

h = height

k = absolute permeability

ø = porosity

m = cementation factor

The equations have constants that hide the effects of other system variables making the equations only applicable to the specific heavy oil-solvent system studied. However, the correlations can be used for scaling up to field rates with Equation 2.14.

$$\frac{Q_{field}}{Q_{model}} = \left(\frac{h_{field}}{h_{model}}\right)^n \frac{\left(\sqrt{k\phi^m}\right)_{field}}{\left(\sqrt{k\phi^m}\right)_{model}} \tag{2.14}$$

Ayub and Tuhinuzzaman (2007) explored the role of capillarity in the VAPEX process in a transparent visual cell. Capillarity acts in favor of the process by shaping the chamber, reducing free gas production, and increasing drainage rate by increasing effective area for molecular diffusion. Simulation results based on the experiments

showed that for the particular oil sample with butane injection there was a minimum capillarity value below which no effects on VAPEX can be observed.

Alkindi, Muggeridge, and Al-Wahaibi (2010) used experimental results to determine the role of convective dispersion and reservoir thickness on VAPEX drainage rates. The experimental oil rates were higher than those predicted by the Butler-Mokrys analytical model. With these experiments, the authors looked to verify the Butler-Mokrys oil drainage-height dependency. The experiments were done in a 2D linear bead pack with analogue fluids of ethanol (solvent) and glycerol (oil). Because the fluids are first contact miscible only convective dispersion will be responsible for mixing.

There were three phases of oil production in all experiments. The initial transient stage had high oil rates due to miscible displacements due to the imposed pressure drop between the injector and producer. When the pressure drop was eliminated after solvent breakthrough, oil rates declined to a stabilized rate due to gravity as the primary production mechanism. These rates are those predicted by the Butler-Mokyrs equation. Once the solvent chamber reached the outer boundary of the cell, production rates started declining. The authors computed longitudinal and transverse dispersion coefficients from interfacial velocities and substituted them for diffusion only mass transfer coefficients in the B-M equation. Because the equation still under-predicted the oil rates after this improvement, further study was done to explore the effect of height. The authors found a 2/3 relationship rather than the ½ suggested by Butler and Mokrys. Other work studying the effect of height suggested a higher relationship (Karmaker and Maini 2003), but did not account for dispersion coefficients, which is expected because model height also increases the magnitude of convective dispersion. The height dependency is a result of velocity-dependent dispersive mixing. The greater the height, the greater the range of frontal velocity over the interface height leading to more dispersive mixing and higher oil

rates. The authors do caution, though, that this scale-up method while applicable at the lab scale may not apply at the field scale.

Ahmadloo, et al (2011) studied the effects of capillarity and drainage height on drainage rate for ~ 5 Darcy sand packs. In high permeability packs, molecular diffusion was the major drive for mass transfer. At lower permeabilities, drainage height, capillarity, and solvent concentration in the oil phase play more important roles in mass transfer. The experiments (n-butane injection) showed that molecular diffusion was the prominent mixing mechanism with dispersion mixing playing only a minor role in mass transfer. At the microscopic level the interplay of capillary and gravity forces leads to counter-current drainage until swelling, viscosity, and interfacial tension reduction of the heavy oil from dissolution of the solvent into the oil mobilizes the oil. A pressure drop across the system can induce forced oil displacement, which can mask gravity drainage phenomenon at the edge of the vapor chamber. As the absolute permeability and/or the drainage height increased, the penetration depth of n-butane increased.

Moghadam, Nobakht, and Gu (2007) used a sand pack model to study the effect of permeability on the VAPEX process and to determine the extent of asphaltene plugging using Lloydminster oil with propane injection. At lower permeability, the solvent-oil ratio increased so that asphaltene precipitation and deposition became more pronounced because more solvent dissolves into the oil. At lower permeability the pores will also be smaller, which means precipitated particles are more likely to be trapped in pores.

Etminan, Maini, and Kharrat (2007) studied the role of connate water saturation in the VAPEX process. They questioned the assumption of previous experiments that rationalized the absence of connate water saying that it had little effect on oil relative permeability and no effect on mass transfer processes because vaporized solvent does not

dissolve in water. The authors studied the process with butane in a fine Ottawa sand pack. The authors found that contrary to prior assumptions, the connate water impacted the shape of the vapor chamber and the oil drainage rate. The water caused faster lateral spreading of the chamber with a thicker mixing zone due to capillary drive fingering. They observed higher initial rates, but lower rates for the remainder. This was because the water sped up communication between the two wells for faster chamber spreading. Ayub and Tuhinuzzaman (2007) also studied the impact of connate water. They found that connate water in the reservoir creates a curvature at the interface due to capillary pressure enhancing the total available area for mass transfer.

The faster lateral spread of the chamber at the top of the model is due to three-phase relative permeability. In dry cases, the oil drains along the sand grains. In the wet cases, though, there is a thin layer of water between the oil and the sand. Therefore, the oil drains along the water layer, which exerts less drag. For the wet cases, the diluted oil spontaneously imbibes into the solvent vapor. This improves the process by exposing fresh oil to the solvent thus providing a higher concentration gradient at the interface. Also, the oil is now distributed throughout the transition zone, which increases contact area (Etminan, Maini, and Kharrat 2007).

Behrouz, Kharrat, and Ghanzanfari (2007) studied the effect of pore structure on solvent flooding using heptane, octane, and decane in micromodel of different patterns. The pore structure has an effect on oil recovery due to enhancement or detraction of the longitudinal and transverse dispersion in porous medium. Lower solvent injection rates gave more stable displacement fronts. At the lower rates, the transverse diffusion equalizes the concentration in each pore, which reduces viscosity.

Jiang and Butler (1996) studied the impact of lower-permeability layers on the VAPEX process (butane). Experiments with low permeability layers have lower

production rates than those with uniform high permeability packing because the vapor flow into smaller pores is limited by capillarity. This suggests that capillarity is important to the VAPEX process. It is beneficial because it increases contact area between the solvent and oil, but detrimental when it resists the rise of the vapor chamber from a high permeability layer to a low permeability layer. Solvent processes rely on solvent dissolution into the oil, which depends on the area of interfacial contact. The authors feel the inclusion of heterogeneity is necessary to improve the understanding of the process in scaling experimental results to field predictions.

The lowest rates were observed in sand packs with continuous low permeability zones. Production from these packs was much improved when a vertical fracture went through all of the layers. Discontinuous low permeability sand lenses also performed better than continuous low permeability layers. The reduced rates with the low permeability sand inclusion is because no drainage occurs from a low permeability layer into a high permeability layer until the liquid head (height) of the mixed layer is large enough to exceed the capillary pressure between the layers. It is important to note, though, that this impact of capillarity is larger in the model than the field.

Butler and Mokrys (1991) studied improving the VAPEX process by injecting solvent vapor, at or near its dew point, with hot water. This raises the reservoir temperature to 40 to 80 °C. In the VAPEX process, drainage is controlled by molecular diffusion of solvent into the bitumen. The hot water serves two purposes: heats the reservoir to lower oil viscosity and releases propane vapor from draining oil to be circulated back to the top of chamber.

Das and Butler (1995) considered injecting a non-condensable carrier gas with the solvent to increase the operating pressure because pure solvent use requires that the reservoir pressure is at or below the solvent vapor pressure. Under co-injection, the

solvent is injected as a liquid, which the carrier gas vaporizes and carries to the bitumen interface. Liquefied solvent may lead to en masse precipitation of asphaltene. Injection of two solvents is found to have extraction rates between that of the two pure solvents. Therefore, the extraction rates with co-injection of a carrier gas will be less than that of the solvent alone. Also, the production rate depends on the solvent injection rate. There is a minimum amount of solvent required to mobilize the oil. At higher rates, liquid solvent will accumulate in the chamber, which reduces the production rates.

Heated solvent injection has also been studied as an improvement to the cold injection in VAPEX. Ivory, Frauenfeld, and Jossy (2010) performed an experimental and numerical analysis of the thermal solvent reflux process with propane, which involves heating the wellbore during solvent injection with heaters. Heating the wellbore initiated injector-producer communication and increased the rate of diffusion of solvent into oil. Operating temperature were in excess of 100 °C. Compared to cold solvent injection, the reflux process improved oil production by 65%.

Li and Mamora (2010) performed a numeric analysis of replacing steam with high temperature solvent to recover Athabasca oil. In their simulation (STARS), they inject n-hexane at condensing conditions into a SAGD well pair. The hexane reduces the oil viscosity (both by heat and dilution) more effectively than steam and can displace all the original oil. Most of the injected hexane can be recovered. The temperature gradient is less along the hexane chamber front because the latent heat of hexane is much less than that of water. Also, at lower temperatures, hexane's solubility is higher. Finally, liquid solvent will mix with oil more effectively than vapor.

Pathak, Babadagli, and Edmunds (2010) used glass bead packs and Berea cores to study the performance of hot solvent injection (propane and butane) for viscous oil recovery at varying temperatures. The entire set-up was placed inside a convection oven

to keep the process at a constant temperature. Also, the samples were exposed to the solvent vapors for a long time to allow for diffusion. Then, the produced oil was drained into a sample collection system at the end. As a consequence, the results cannot show dynamic production. They observed that increased pressure decreased recovery because the condensation of some of the solvent in the system resulted in slower diffusion. This explanation does not account for an increase in rate due to liquid extraction under condensing conditions. In terms of asphaltene precipitation, butane was more effective. A higher degree of precipitation led to more in-situ upgrading and produced samples with lower asphaltene content.

Rezaei, Mohammadzadeh, and Chatzis (2010) studied the warm VAPEX process (pentane) by exploring the effect of solvent temperature, permeability of porous medium, and viscosity of oil in place. While the process is designed to occur above saturation conditions so that the solvent is in the vapor phase, they did perform one experiment below the saturation temperature with the solvent in the liquid phase. Allowing the solvent to condense provided a modest increase in performance. Asphaltene content analysis did not show significant deposition of asphaltene when condensation did not occur. The experiments were performed in a 2D visualization cell stored inside a heated chamber so that the entire system would be at the target temperature before initiating injection. This ensured that no condensation would occur unless desired.

The authors did not observe appreciable asphaltene precipitation during the VAPEX experiments. However, it did occur for the warm VAPEX experiments. The precipitant was observed near the solvent injection tube binding the glass beads together. The precipitant was concentrated there because there is a decrease in pressure and temperature at the injection point which triggers the precipitation. At higher temperatures, the asphaltene content of the produced oil is higher suggesting that less

precipitation takes place in the glass bead pack. The lower permeability model has a higher amount of asphaltene precipitation. This is explained by longer residence time due to lower drainage rates.

Pathak, Babadagli, and Edmunds (2011) built on their previous results of viscous oil recovery using heated solvent vapors with a study of the effect of temperature, pressure, solvent type (propane and butane), and asphaltene precipitation. The experimental work included six glass bead, two Berea core, and two Hele-Shaw experiments. The glass bead and core experiments were done in the same set-up with heated solvents. The Hele-Shaw set-up was used for cold liquid solvent experiments designed to study the effect of solvent type and asphaltene precipitation.

The authors concluded that diffusion of solvent into heavy oil is the dominant production mechanism based on observed pressure decrease during the core soak period. Cores were allowed to soak in solvent for 10-15 days. They confirmed their previous conclusion that optimal production occurs at a temperature just above the saturation temperature. Increasing the temperature further decreases recovery because at higher temperatures, there is less solvent in the oil phase (Raoult's law). The authors found no height sensitivity to ultimate oil recovery. Increasing height only increased the pore volume meaning more time was required to produce. The authors also used a simulation to study the height dependency. This allowed them to increase the height while keeping the pore volume constant. At heights below 40 cm, increasing height increased recovery. However, above 40 cm, recovery was constant with increasing height. The asphaltene study was done at low and high permeability. For high permeability, asphaltene precipitation does not affect the recovery and in fact accelerates oil displacement because the upgraded oil has a lower viscosity. However under the same precipitation conditions, the impact of upgrading is negated by pore plugging in low permeability environments.

The authors concluded that solvent type was not critical to recovery, so that field solvent use should be determined by reservoir temperature and pressure.

2.1.6.2 N-Solv

The N-Solv process injects a heated pure solvent into the reservoir. The process is similar to SAGD (same well orientation) except condensing solvent provides heat instead of steam. When the solvent condenses, its latent heat is released to the reservoir. The temperatures, unlike SAGD, are not high enough to mobilize the oil. However, the released heat is sufficient to reduce the oil viscosity enough to achieve rapid solvent penetration. The condensing solvent then extracts the low molecular weight components of the oil at the chamber interface. The solvent is recovered, purified, vaporized, and recycled back into the reservoir. The major difference between N-Solv and other solvent processes is the solvent purity requirements of N-Solv. Methane, or any non-condensing component, cannot exit from the chamber, which stifles the solvent extraction process (Braswell 2012). In N-Solv, the solvent is chosen as the most cost effective fluid that can deliver heat at the target reservoir temperature. Because the solvent is mostly contained in the chamber, there is no risk of deep penetration of the solvent into the reservoir (Nenniger and Dunn 2008). Because the oil is never mobilized, precipitated asphaltenes are also immobilized. This leads to a uniform distribution of asphaltenes throughout the solvent chamber meaning they should not block the drainage of fluids (Nenniger 2012).

Hatch, Ltd. And Nenniger Engineering, Inc. employed the Alberta Research Council to perform an experimental study of the N-Solv process (Frauenfeld, Jossy, et al 2005). All experiments used propane with one experiment modeling levels of methane contamination. The experiments were done in a 6 D sand pack contained within an Adiabatic Test System (ATS), which kept the sand pack at near-adiabatic conditions.

The first experiment operated at several temperatures spanning from VAPEX conditions at 11 °C to condensing (N-Solv) conditions at 40 °C. The second experiment repeated operations at 40 °C to verify oil rates from first experiment. The third experiment explored the impact of methane contamination (0.5 and 1.0 mole %) on the process. Oil rates, heat transfer, bitumen yield, effect of pressure and temperature, oil upgrading, and effect of solvent purity were determined from the experimental set. The first experiment showed a 50 fold increase in oil production for N-Solv over VAPEX. High recoveries were obtained for all condensing temperatures with substantial upgrading due to asphaltene deposition, but methane contamination led to significant reduction of oil rates. Nenniger believes N-Solv can access an additional 1,300 billion barrels of Canadian bitumen reserves (Nenniger 2012).

Because of the successful experimental investigations, N-Solv Corp. is building a pilot test of the process at the Dover site near Fort McMurray, Alberta (the site of the original SAGD pilot). The pilot will have a 300 m horizontal well pair. Startup is expected in the first quarter of 2013 (Braswell 2012). One of the major purposes of the field trial is to determine the process solvent holdup. Nenniger (2012) expects it to be twice that of SAGD (~0.2 barrel of solvent per barrel of oil production). Compared to steam processes, commercial N-Solv operations are expected to be economically preferable. The oil is more valuable because it is de-asphalted, and the surface facility is greatly simplified.

2.1.6.3 Solvent Injection in Fractured Reservoirs

Packed cell experiments (Rahnema, Kharrat, and Rostami 2008) showed a significant difference in the pattern of solvent flow in fractured model versus conventional model. Also, the presence of fractures compensated for low matrix

permeability. The experiments were done with Kuh-e-Mond oil and propane just below the saturation pressure of propane. The solvent spreads through the fractures first and then begins to diffuse into the matrix. As the solvent diffuses into matrix it forms an oil chamber as the solvent invades and the oil bank shrinks. The fractures enhance the process by improving the contact area between solvent and oil.

Farzaneh, et al (2010) studied the role of fracture geometry on oil production during solvent flooding. Recovery increases when the fracture spacing, discontinuity, overlap, and distribution increased. Recovery decreased when the orientation angle, discontinuity distribution, and number of fractures increased. Mass transfer is not as pronounced as the viscous ratio in five-spot ratios. As a consequence, even though mass transfer is faster for hexane than decane, but the overall recovery is still higher for decane.

2.1.6.4 Simulation

Nenniger and Dunn (2008) developed an empirical correlation for oil production for solvent based gravity drainage processes applicable for condensing and non-condensing systems suggesting a common rate limiting step in both N-Solv and VAPEX. The correlation resolves the oil rate discrepancy between Hele-Shaw and packed bed VAPEX experiments without employing unphysical diffusion/dispersion coefficients. Under condensing conditions, oil production occurs because the solvent extracts the oil (solvent extraction). This extraction is driven by concentration gradients between pure solvent and pure oil. The authors reported that when a film of Athabasca bitumen sandwiched between two glass disks was placed in a beaker of hexane, the mixing zone occurred as a concentration shock within a few microns of the raw bitumen interface. The packed bed experiments described by Frauenfeld, et al (2005) confirmed that solvent

extraction in packed beds also proceed via a concentration shock mechanism. The shape of the mixing zone is important because solvent extraction occurs when concentration gradients push solvent into the bitumen. Because of the high viscosity of oil at reservoir temperatures, it is very difficult for solvent to penetrate into the raw bitumen. Virtually all the resistance to mass transfer is due to the difficulty of initial solvent penetration into the raw bitumen. Therefore, the authors concluded that these steep concentration gradients, which are accounted for in their correlation, are the cause of unexpectedly high mass flux in VAPEX packed bed experiments.

The correlation (Equation 2.15) accounts for the surface area of the shock front (porosity), limit of solvent penetration rate into the oil (viscosity), and a characteristic distance related to pore size (k*ø).

$$m = 43550 \cdot (\frac{k\phi}{\mu})^{0.51} \tag{2.15}$$

where m = mass flux

k = permeability

μ = initial oil viscosity

φ = porosity.

The lack of solvent type dependency in the correlation supports the authors' view that mass transfer into the bitumen rather than draining of the oil layer is the rate limiting step because solvent type would control the physical characteristics of the draining fluid layer and thus need to be modeled if this step was dominant. However, solvation kinetics are strongly dependent on solvent type, which should be represented in an equation describing the N-Solv process, whose primary mechanism is solvation of the oil. Additionally, the use of the initial oil viscosity eliminates the temperature effect on the

process. While the empirical equation matches reporting values, it does not sufficiently explain the process mechanisms.

Xu, et al (2012) used the history match of a 2D VAPEX experiment to predict the performance of a 3D VAPEX experiment. The 2D and 3D experiments were waterfloods followed by solvent (86 mole% n-butane, 14 mole% methane) injection under the same conditions. The authors first compared the experimental results to three analytic models discussed previously: the Das and Butler (1998) model (Equation 2.8), the Yazdani and Maini (2005) empirical correlations (Equations 2.12 and 2.13), and the Nenniger and Dunn (2008) correlation (Equation 2.15).

The 3D results were underestimated by all of the models, with the closest prediction for the Yazdani and Maini correlation. Therefore, the next step was to study the applicability of numerical simulation (CMG STARS) for scaling solutions. The history match of the 2D experiment was excellent for the waterflooding period, but showed a misfit for cumulative oil production under solvent injection. The two primary discrepancies were lower oil rates and higher water production during the early stage of solvent injection. Using the tuned parameters from the 2D history match to model the 3D model gave a poor predictive performance, though the simulation result were more accurate than the analytic solutions. The authors studied two effects for the difference in the 2D history match: wall effect and solubility. In the physical model, there are high permeability paths along the walls, which can be modeled with a layer of higher permeability grid cells. The solubility is adjusted through the k-values. Modeling of the wall effect made the most improvement in the history match.

Cuthiell and Edmunds (2012) used the VAPEX experiments performed by Maini and his colleagues over the past ten years to study different methods of simulating the method with the semi-compositional simulator Tetrad. Simulations show that even at

higher permeabilities, capillarity plays a significant role because most of the drainage occurs in the capillary transition zone at the edge of the vapor chamber. Due to higher fluid velocities in higher permeability media, mechanical dispersion is expected to play a larger role. However, the contribution of mechanical dispersion compared to molecular diffusion is not as large as expected. The experiments showed a near-linear relationship between oil rate and height and support the square root dependence on permeability. Mixing occurs at the boundary due to molecular diffusion, mechanical dispersion, and capillary fluid re-distribution. The Ns term in the Butler-Mokrys equation captures many aspects of diffusional mixing. The Butler-Mokrys equation, though, does not "embody all of the physics of a vapor phase/porous medium process," specifically mechanical dispersion and capillary effects.

Tetrad has a full tensorial mechanical dispersion model and models solubility using k-values. The authors were surprised to see that produced oil contained very close to the equilibrium amount of solvent. In order to match the smaller solvent volume fractions at lower heights, the authors increased the k-values to match the observed trend with decreasing height. When matching the experimental results, they only focused on the stabilized VAPEX rate period of production.

The simulations showed a square root proportionality between the stabilized rate and the diffusion/dispersion terms. This is consistent with the B-M equation, which shows a square root relationship between rate and the Ns term, which contains the mass transfer terms. The authors explored the effect of capillary pressure by using different capillary pressure scenarios. At higher capillary pressure, oil production was higher with a slower decline to the stabilized rate. They also confirmed that most of the oil drainage occurred within the capillary transition zone. The authors proposed a different view on the discrepancy in height dependence between the B-M equation and experimental data.

They observed an increase in rate and average solvent loading at greater heights. The higher solvent loading suggests increased mixing, which can only enter the model through the Ns term. However, there is not a height term in the Ns term meaning the height-dependent mixing phenomenon can only be represented by adjusting the h exponent. The authors were required to adjust the k-values to match this solvent loading. Under this tuning the height dependence is 1.23. However, when the authors do not used the tuned k-values, the height dependence is only 0.86.

These findings suggest that significant modifications need to be made to the B-M equation for scaling process. The new model would need to address the issues discussed above as well as a velocity-depending dispersion term. The authors suggest that an increased dominance of the mechanical dispersion term at larger heights may be part of the cause for the observed height dependence. Though larger than the diffusion term, the mechanical dispersion term does not completely dominate at smaller heights. At the field scale, permeability will be significantly reduced. This means that mechanical dispersion will also be reduced, but no change in diffusion will occur. This means that in the field molecular diffusion will completely dominate so that dispersion is only important at lab scale. Once pore-scale mixing reaches its maximum, increasing the height above that point does not change the mixing conditions, so the height dependency will not exist. The authors conclude their work with a sentiment shared by many working on the VAPEX process. "Several of our conclusions suggest the need for an improved analytic model of the VAPEX process which accounts for additional pore-scale mechanism, mechanical dispersion and capillary effects. Such a model would be extremely useful in making reliable extrapolations from laboratory results to the field."

2.1.7 Grosmont Formation

The Grosmont Formation is the most promising of Alberta's bitumen resources in carbonate reservoirs, with an original oil in place estimates from 320 (Jiang, et al 2010) to 406 (Yuan, et al 2010) billion bbl. It is discussed here to give an idea of the potential for my proposed technology and show what work has been done to address a specific reservoir within my target reservoir type. Several pilots (cyclic steam stimulation, steam drive, and forward combustion) were undertaken in the late 1970s and early 1980s, but no commercial development occurred. All of these pilots were performed prior to the introduction of the gravity drainage production techniques. Therefore, Edmunds, et al (2009) used the McMurray SAGD performance to get an estimate of the technology's performance in the Grosmont reservoir. Using comparative reservoir properties, such as thickness and permeability, to calculate SAGD rates for the Grosmont reservoir, they expect the SAGD performance in the Grosmont to be comparable to that in the high-quality McMurray reservoirs.

The authors also studied the possibility of cold solvent injection. The fractures and vugs will provide convective transport to about half of the oil-in-place found in the secondary porosity. Within the matrix porosity, molecular diffusion will control solvent transport. Study of Grosmont cores suggest that diffusion need only occur over the distance of a few centimeters. As a consequence, the bitumen in the matrix will absorb the solvent rapidly and swell, forcing much of the oil into the fracture network where it can be drained. An 80 cm Grosmont core was supported inside a core holder so that the injected propane and non-condensable carrier gas mixture could flow freely around the core. This set-up eliminated any pressure gradient, meaning only diffusion, swelling, and gravity drainage recovered oil.

A cold solvent test was performed in the winter of 2007-2008 at a single well in the Saleski field. Two slugs of solvent were injected each followed by a production period. The oil was mobilized, but production was modest because the limited solvent injection volume led to a higher-than-ideal bottom hole viscosity. Another solvent slug was injected in the winter of 2008-2009, but the results were not included. The authors feel that these results suggest cold solvent injection is a credible alternative to SAGD for commercialization at Saleski.

Jiang, et al (2010) expanded the laboratory investigation of solvent processes for the Grosmont with a warm solvent soak test. The injected solvent (butane) was vaporized in the annulus to achieve VAPEX conditions (50 °C and 400 kPa). In comparison to the cold solvent test of Edmunds, et al (2009), the heated solvent test did not require non-condensable gas co-injection. The test showed enhanced diffusivity because of reduced oil viscosity and improved oil rate. Disadvantages included reduced solubility of solvent in the bitumen and additional required energy to heat the solvent. Oil rates were higher in the warm solvent test, especially initial rates. Reduced pressure and increased temperature will improve diffusivity of solvent into bitumen but reduce solubility of solvent in bitumen.

Yuan, et al (2010) created a numerical model of the Grosmont C to explore the commercial viability of the SAGD and SAGD/solvent processes. The two-dimensional SAGD simulation showed promise for the technology. The SAGD/solvent model was based on data from the warm solvent test of Jiang, et al (2010). Initial production is from fracture flow. Matrix flow occurs concurrently, but only becomes dominant at later stage flow. In comparison to oil sands, the fractures enhance the solvent process in the carbonate and are more desirable for the gravity recovery process. Based on the positive

laboratory and simulation results, a SAGD/solvent pilot test was planned to start in late 2010.

2.2 CONFORMANCE CONTROL

Even when using fractures as a conduit for injected fluids, issues of conformance can occur. In a natural fracture network, some portions of the reservoir will be swept before others leading to early breakthrough from the most conductive fracture paths and leaving behind unswept portions of the reservoir. Conformance control can be used to divert subsequent injection from the swept portion of the fracture network and into areas of the reservoir with remaining oil saturation. Liu, et al (2006) defines conformance control as "those technologies in which chemical or mechanical methods are used to reduce or block water/gas production resulting from wellbores or high permeability zones/channels/fractures of reservoirs." In situ gelation technology is a proven economical process for improving oil recovery through conformance control (Vossoughi 2000). These systems, which function by strategic plugging of pores, include polymer gels, polymer microgels, silicates, and colloidal silica.

2.2.1 Polymer Gels

Polymer gels consist of a polymer network developed by the presence of a crosslinker. This network makes the polymer gels much more viscous than uncrosslinked polymer (Sheng 2011). When completely crosslinked, the polymer gel will plug the rock. Ideally, the polymer gelant will only propagate through high permeability channels/zones diverting subsequent flooding to low permeability zones (Seright and Lian 1994). Polymer gel injection can occur as bulk gel injection or sequential injection. In bulk gel injection, high concentrations of polymer and crosslinker are mixed at the surface before

injection. Upon injection, the solution quickly becomes a strong gel. This restricts the application under this injection strategy to near-wellbore treatments. This process often results in weaker gels (Mack and Smith 1994; Coste, et al 2000; Dovan and Hutchings 1987). Sequential injection involves alternating injection of polymer and crosslinker. Because crosslinking cannot occur until both chemicals are present in the formation, this method allows for in-depth placement. The major disadvantage of this process is the potential for loss of control; it is possible for the slugs to not even come in contact if they follow different injection paths (Mack and Smith 1994; Coste et al 2000). Polymer gel treatments have been proven successful as a conformance tool (Purkaple and Summers 1988, Hardy, et al 1999, Moradi-Araghi, Bjornson, and Doe 1993, and Moffitt, et al 1996) but there are still many key issues with the system such as "(1) environmental and safety issues over the heavy metal crosslinking agent chromium, (2) limited penetration depth, (3) polymer shear degradation, (4) polymer absorption on the reservoir surface, (5) lack of polymer gel time control, and (6) polymer precipitation under harsh reservoir conditions (Burns, et al 2008)."

2.2.2 Polymer Microgels

Polymer microgels are an alternative to polymer gels. The primary difference is a result of the concentration of reactants used in each formulation – microgels use a much lower concentration of polymer and crosslinker. The low concentrations result in primarily intramolecular crosslinks as opposed to intermolecular links in polymer gels, resulting in a solution of many separate polymer microgels rather than a continuous gel network. The lack of a continuous network results in a lower viscosity than the polymer gel network, which allows for deeper placement of the gel and reduced injectivity problems. Also, the crosslinking reaction is slower at lower reactant concentrations

(Mack and Smith 1994; Diaz et al 2008, Sheng 2011). Polymer microgels can be divided into four main categories: colloidal dispersion gels (CDGs), preformed particle gels (PPGs), pH sensitive polymers, and Bright Water®.

Mack and Smith (1994) pioneered the use of colloidal dispersion gels (CDGs) in the field. The CDGs are "micro-scale separate gels/colloids that come about from primarily intramolecular forces" that are injected as a gelant that gels in-situ. Mack and Smith recommended the use of polyacrylamide with an aluminum citrate crosslinker at a ratio between 20:1 and 100:1. This is the most common formulation, but others have also been used (Diaz, et al 2008). CDG gelation is triggered when the pressure differential across the gelant drops below a specific "transition pressure." The high pressure differentials near wellbores are typically above the transition pressure allowing for easy injection and in-depth placement (Smith et al 2000).

Chang, et al (2006) compared a CDG flood to a conventional polymer flood using parallel linear core floods. They concluded that the CDG flood performed better because CDG injection occurred preferentially in the higher permeability core diverting subsequent injection into the unswept lower permeability core. Seright (2006) questions these results claiming the results violate Darcy's law because the microgel would instead plug the lower permeability core to a higher degree. He asserts that the faulty results stem from the use of parallel linear cores, which do not adequately model flow through layered reservoirs. Several other authors also argue against the capability of in-depth placement of CDG gels because they observed gel formation primarily at the inlet end of the cores (Seright 1995; Ranganathan 1998, Lu et al 2000; Wang et al 2006). Despite the controversy over the process at the core level, the process has been proven successful in the field. Papers have reported successful field applications in Daqing field, China (Chang, et al 2004), North Rainbow Ranch Unit, Wyoming (Fielding, et al 1994),

Comodoro Rivadavia Formation, Argentina (Muruaga, et al 2008), Loma Alta Sur field, Argentina (Diaz, et al 2008), and the Adon Road field, Wyoming (Smith, et al 1996).

Pre-gelled (PG) particles (a type of preformed particle gel) are dry gels that have been crushed and sieved to create different cuts of gel particles. They swell in water to form a stable suspension. Coste, et al (2000) studied the potential of PG particles for conformance control in water floods. Their target reservoirs were Chinese fields that have high permeability contrast among layers. In the near wellbore region, the pressure gradient is large enough to deform the particles allowing them to pass through pore restrictions. As the pressure gradient decreases away from the well to a value insufficient to deform the particles, they will plug the pore throats and divert flow into unswept zones. Core floods showed that the particles went into the higher permeability layers and created a resistance to water flow. In a pilot test in the Shengli oilfield, PG particles were injected into two injection wells. The injection distribution between layers was more homogenous and the sweep was improved in the lower permeability layers for both wells.

PG particle gel (PPG) treatments have been used for in-depth fluid diversion in the Daqing oilfield, China since 2001. Incremental oil (200,000 tons) averages 2.6 t/d/well and water cut has decreased 2.6% (Bai, et al 2008). Commercially available preformed particle gels (typically mm-sized) can only be injected into fractured rock or extremely permeable porous media because larger pore networks (or fractures) are necessary to allow initial penetration into the formation and prevent the formation of a filter cake. (Bai, et al 2007).

Al-Anazi and Sharma first proposed the use of pH-Sensitive polymers for conformance control in 2002. Hu, et al (2005) expanded the idea to microgel by proposing the use of the polymers in the form of small and elastic microgel globules. Either form uses polyelectrolytes, which are very pH sensitive and capable of swelling by

several orders of magnitude (through water retention) as pH increases. The swelling occurs when the carboxylic groups (-COOH) in the polyacrylic acid are ionized and the resulting negatively charged groups (-COO-) repel each other. This repulsion causes the polymers to stretch and uncoil resulting in swelling and a corresponding viscosity increase. At somewhat neutral pH (around 6), the solution viscosity can increase by three orders of magnitude. They are an attractive technology because polyelectrolytes are very low in cost. Also, the swelling can be reversed by a simple acid wash. The one disadvantage is that an acid pre-flush is necessary to prepare the reservoir for injection so that the solution is at low pH thus low viscosity during injection. After injection, the well must be shut-in to allow the pH to increase due to geochemical reaction between the polymer and carbonate/mineral components. Once the pH is above the gelling pH, the polymer will gel. Lalehrokh, et al (2008) investigated using pH-Sensitive Polymer Microgels in fractured rocks. The main difference from unfractured rocks was that permeability reduction was more dependent on shut-in time. This is because the residence time in the fracture is too small to significantly increase the pH (and thus initiate gelation) without longer shut-in periods. Also, the microgel solution was found to propagate much deeper in the fractured sandstone reservoir than in the fractured carbonate reservoir. The pH increases much faster in carbonates due to reactions with the rock, limiting the depth of placement before gelation is triggered. This means that acid pre-flushes are even more important in carbonates. Overall, though, the process looks promising for fractured reservoirs. Despite the good laboratory results, the pH-Sensitive Polymer Microgels have not been implemented in the field.

Bright Water® is a micron-sized, heat-activated polymer particulate developed by an industry consortium between BP, ChevronTexaco, and Ondeo Nalco Energy Services as a novel technology to improve sweep efficiency in water floods. The Bright Water®

particulates are supplied as a 30% active dispersion in light mineral oil and injected into the water prior to injection (Pritchett, et al 2003). The particles heat up as they flow through the reservoir. The quickest heating occurs in thief zones, where the injected water is sandwiched between two hot, unswept zones. When the particles reach a pre-designed temperature, they expand to block the current flow path and divert the flow into previously unswept zones (Smith 2007).

The first test of the Bright Water® technology was at the Minas field, Sumatra, Indonesia, in November 2001. Forty-two thousand barrels of water with forty five hundred ppm polymer, fifteen hundred ppm surfactant, and caustic soda to control pH were injected over nine days. Pressure data indicated a definitive change in injectivity. The effective permeability to water decreased up to 125 feet from the injection well. Even though the injection response was positive, the Minas team saw little incremental oil gain after the treatment. The oil production decline returned to pre-treatment trends in less than a year. However, operational factors shortly before and during the treatment could have affected the performance (Pritchett, et al 2003).

The BP Milne Point field on the North Slope of Alaska was selected for a commercial trial of the technology in 2004. The pattern water cut had reached 90% at only 20% oil recovery – almost all of the injection was into one of the three productive sands. Fifteen thousand five hundred eighty seven gallons of the particulate at a three hundred thirty ppm active concentration with eight thousand sixty gallons of dispersing surfactant was injected over twenty one days with no change in injectivity. Injectivity decreases were observed nine months after the treatment. Pressure fall-off tests showed a 50% decrease in permeability without significant changes in reservoir pressure and wellbore skin suggesting the treatment affected the permeability deep in the reservoir with little to no plugging near the wellbore. The treatment resulted in 60,000 barrels of

incremental oil at less than $5 per incremental barrel (Ohms, et al 2009). While many microgel technologies have been shown to be very successful conformance control tools, they can still suffer from injectivity and toxicity issues similar to polymer gels.

2.2.3 Silicates

Compared to polymer gel and microgel, sodium silicates and colloidal silica can better withstand harsh reservoir conditions and do not have any environmental and safety issues. Sodium silicates are silicate powder (Na_2SiO_3) dissolved in an aqueous solution. Colloidal silica is a stable aqueous dispersion of amorphous silicon dioxide particles. For both systems, the addition of salt results in charge screening which will cause gelation (Jurinak, Summers, and Bennett 1991). Also, both solutions behave like a Newtonian fluid before gelation, which eliminates the concern for shear degradation allowing higher injection rates to be used. Silicate gels form faster than colloidal silica gel and have a greater ultimate gel strength at a given silica concentration. The ultimate strength of a silicate gel is more dependent on initial reaction conditions. Higher SiO_2 concentrations are required for gelation of colloidal silica than for sodium silicate. Silicate solution pH must be increased to between 9 and 10 to produce gel time comparable to those of colloidal silica at near neutral pH. High pH increases potential interaction with reservoir mineral and residual oil (Jurinak, Summers, and Bennett 1991). Silicates also suffer from accurate gelation control in the field. Therefore, colloidal silica provides the best option because it has the environmental benefits of silicates with a more robust gel control and no pH limitations.

Krumrine and Boyce (1985) reviewed silicate treatments for conformance control. Sodium silicate gels in several forms have been used. Silicate gels form under weakly acidic, neutral, and weakly alkaline pH conditions. The acidic systems are the oldest and

most common technique, with pH ranging from 4 to 6. Alkaline silica gels tend to be softer and weaker than acidic silica gels. Even though they are weaker, alkaline gels can be placed deeper in the reservoir. The silicate injection strategy has been varied to include polymer and silicate, alternating slugs of silicate and various chlorides, and CO2 or surfactant as the activator (Sandiford 1982; Bernard 1972; Sydansk 1981; Andersen, et al 1946; and Christopher, et al 1973). For neutral systems, CO_2 dissolved in the water phase can act as a gelling agent by reducing the solution pH. The hydrophilic nature of the silicates enhances their tendency to seek the high water content zones. Once set, the silicate gels are generally long-lasting and stable under high pressure and sever brine conditions. Hydrofluoric (HF) acid and strongly alkaline solutions, though, will dissolve the gels. Additionally, the gels are not shear sensitive until gelled, which allows flexibility in injection without degrading ultimate strength upon gelation.

Stavland, et al (2011) studied the use of sodium silicate (Krystazil 40) to improve waterflood sweep efficiency. They found that the gelation reaction rate was controlled by formation temperature and silicate concentrations. The authors used pH as the controlling parameter for placement of the silicate gel. The gel system included 4.0 wt % silicate, tap water with 20 ppm calcium, and 2.0 M HCl as the activator. In coreflood experiments, high flow rates gave good injectivity and dynamic reaction rates similar to bulk reaction rates. However, at lower injection rates, gelation times decreased because fines particle transport increased the deposition rate of the silicate resulting in face plugging rather than in-depth gel placement. The injection rate did not impact gel performance for the higher permeability sand pack tests. The authors suggest two ways to initiate the onset of plugging: shutting in the well after placement of the silicate slug or optimizing the preflush volume to allow the silicate and saline formation water to mix at the silicate front.

2.2.4 Colloidal Silica

Our proposed conformance control technique uses colloidal silica (aqueous silica nanoparticle solutions) for a gelling system to address conformance control. The difference between this process and past work on colloidal silica is that no activator is used prior to injection. Rather the salinity of the formation water is used as an in-situ activator. This eliminates the need for a preflush to condition the reservoir.

Jurinak and Summers (1989) looked at using colloidal silica – Du Pont Ludox (7 nm) – for conformance control in the oil field. Laboratory tests showed that fully cured colloidal silica gels could withstand more than 2500 psi/ft without exhibiting any change in permeability. However, at least three times the initial gel time was required for the gel to reach at least 50% of its ultimate stability. The gels were stable to 100 pore volume throughput of neutral brine, resistant to HCl, and stable to temperatures exceeding 350 °F. An ion-exchange preflush is necessary because ion exchange with the injection and reservoir fluids can dramatically reduce silica gel times. The gelation activator is added to the silica solution prior to injection. The injectivity of the solution was lower than expected. In Berea cores, it was one-half that of water. In clay-laden field cores, it was 1/10 of water. But the injectivity was still an order of magnitude better than polymer gel solutions.

For field applications, a preflush slug of at least one-half of the silica application is injected to isolate the silica injection from the in-situ brine. The solution gel time is controlled by the amount of concentrated brine added to the silica solution prior to injection. After injection, the well is shut in for at least three times the minimum gel time to allow the gel to set and cure. The authors report that eleven wells were treated with colloidal silica. One of the four treatments for injection-profile modification was successful. The failed treatments all exceeded parting pressure. Two of the three

production well treatments were technical and economic successes. The remaining cases were casing repair treatments that allowed compliance to be met. The incremental production from the two successful production treatments paid for the cost of the entire program. For the other successful tests, there was no economic improvement despite the technical success. The tests also showed that zones that had previously been hydraulically fractured can be treated successfully.

Jurinak, Summers, and Bennett (1991) expanded on the laboratory work discussed in Jurinak and Summers (1989). For the tests, the silica concentration was diluted to between 6 and 10 weight percent silica solution. Even at equal ionic strengths, use of $CaCl_2$ as the activator resulted in ½ to 1/3 of the gel time compared to NaCl. The near neutral pH of the silica gelling solution used prevented pH fluctuations in the reservoir rock. The authors did not see any effect on permeability reduction in the presence of oil. However, the presence of gas (CO_2) did impact the performance. The dissolution of CO_2 into the silica solution lowered the pH and decreased gel times by as much as 40 percent. However, permeability to CO_2 was still significantly reduced. Compared to bottle tests, silica gel stability was improved in the rock matrix. The gel permeability was constant to a yield point above which the gel permeability increased by an order of magnitude. The gel remained immobile above the yield point. Gel strength increased with increasing silica concentration. Fracture treatments were not as successful because the gel in the fracture yielded at a lower pressure gradient. The authors postulated that the lower yield was because the rock matrix was not present to support the gel.

Seright (1992) studied the effect of permeability and lithology on the performance of various gels, including colloidal silica (10% Ludox SM). The "strongest" gels occupied most of the available pore space. For "weaker" gels, gelation was often less complete than that in a bottle. The cores were saturated with the same brine composition

used in preparing the gelant formulation. Each core was then saturated with many pore volumes of gelant to ensure complete saturation. Consequently, the reported gel properties do not account for mixing effects with the reservoir brine. For colloidal silica gels, the residual resistance factor decreases significantly for lower permeability rock. There was no evidence of gel breakdown even after exposure to pressure gradients up to 1300 psi/ft.

Noll, Bartlett, and Dochat (1992) explored the use of neutralized Ludox colloidal silica gels for reducing the permeability of subsurface formations. The gels were formed from a mixture of 5 wt % LUDOX particles, sodium chloride, and enough hydrochloric acid (HCl) to reduce the pH to 6. These gels were stable over long periods of time when not exposed to solutions with pH below 3 or above 9 and decreased the permeability by four orders of magnitude. Gelation time can be controlled by adjusting pH, salinity, and/or silica concentration. Since other salts will be present in the formation water, it was valuable to learn that, in small amounts, the other ions had no measureable effect on gel time when sodium was the dominant cation. However, aluminum did have a detrimental effect on gel formation because the salt addition rapidly dropped the pH. For charge-equivalent solutions of sodium and calcium, the gel times were similar.

Noll, et al (1993) expanded the previous work with a field-scale pilot study to explore the feasibility of using colloidal silica gel to construct a horizontal containment permeability barrier. The injection batch was mixed for a 72 hour gelation time. After 66 hours of injection, the hydraulic head in the injection well increased indicating the onset of gelation. The authors postulated that the premature gelation was caused by attenuation of the silica, resulting in an effective increase in silica concentration. Increasing silica concentration will cause a decrease in gel time. The other deviation from laboratory conditions was that the chemistry of produced groundwater, used to mix

the silica batch, varied during injection. In order to eliminate the effect of varying groundwater chemistry between batches, the groundwater chemistry would need to be regulated or an alternative source of water for mixing used.

Patil, et al (2011) studied a colloidal silica – sodium chloride brine gelation system for conformance control at temperatures up to 150 °C. The gelation process is activated by the formation temperature, but gelation time is controlled by the amount of sodium chloride brine added prior to injection. The gel remains homogenous and stays in place under confined conditions during core and sand pack floods. As in previous tests, the cores were shut-in to allow the gel to set. The system was stable for at least two months in sandstone and carbonate formations up to 140 °C. Dynamic gelation times, measured with a Brookfield PVS rheometer, were shorter than static gelation times due to higher contact area per unit volume in the rheometer.

2.2.5 Other Systems

There has been other relevant work with systems outside the four main groups discussed above. Huang, Crews, and Johnson (2009) find fault with silicate treatments because the solutions are not compatible with formation waters because they will react with chloride instantly to form gel. They patented a non-aqueous fluid (an oil and/or glycol) with an amount of nanoparticles (from 4 to 2000 nm). When the slurry is injected, it will react with the water to form a solid plug, but does not interact with crude oil or natural gas. This allows the fluid to be used to selectively block off water channels. The particular particle stated in the patent is MgO. The concentration of nanoparticles ranges from 2 to 50 weight percent. Acid can be used to remove the barrier. The authors postulate that the MgO particles have unique particle surface charges that use charge attraction, surface adsorption, and/or other chemistries to join together in the presence of

water, but not oil. Piezoelectric and/or pyroelectric crystals in contact with water display the same solidification behavior.

Castelijns, et al (2007) studied the effect of in situ formed silica gel from gelling solutions of tetra-methyl-ortho-silicate (TMOS) and methanol in water in dry Bentheim sandstone plates. The effect of TMOS concentration and water pH and salinity were studied. Gel permeability decreased with increasing silica content. Acid-catalyzed gels have much lower permeability than base-catalyzed gels. The authors did not systematically measure gel time as a function of the various parameters. However, they did observe that gelation times were quicker at higher pHs. The sandstone plates were immersed in the gelling solution and then allowed to cure outside of the solution. For acid-catalyzed gels, the addition of salt slightly increases the gel permeability with no clear function of concentration. Gel strength was not affected by addition of salt or change in pH of the solution. However, increased curing time did increase gel strength. The authors concluded that even though the gel was not uniformly distributed in the pore space, the gel did adequately block the pores to substantially reduce permeability.

2.3 SUMMARY

The critical issue for opening up production from fractured viscous oil reservoirs is developing a low temperature operating strategy. The gas-oil gravity drainage mechanism is very successful in fractured reservoirs and is enhanced by the injection of steam for viscous reservoirs. Steam and steam-solvent processes have been successful in un-fractured viscous oil reservoirs, but the processes cannot be modified for low temperature operations because of the high steam saturation temperature requirements. Several solvent injection strategies have been developed for low temperature operations spanning from vapor to liquid solvent injection under both cold and heated injected.

However, none have been successfully field tested despite showing positive lab results. This is because up-scaling efforts have proven problematic. I plan to develop a new injection strategy by combining several production mechanisms that have individually shown promise – the gas-oil gravity drainage mechanism and liquid and vapor solvent injection – in a heated solvent injection strategy that uses the fractures as conduits for the injected solvent. In a natural fracture network, some portions of the reservoir will be swept before others leading to early breakthrough from the most conductive fracture paths leaving behind unswept portions of the reservoir. To address this problem, conformance control is necessary. There are several current conformance technologies that generate gels to provide control. However, they initiate the gelling process prior to injection requiring pre-conditioning of the reservoir. My proposed conformance control technique will use the natural salinity gradient between an injected silica nanoparticle solution and the reservoir brine to initiate gelation in-situ.

Chapter 3 – Novel Solvent Injection Strategy for Low-Temperature Production from Fractured Viscous Oil Reservoirs

The Alberta government has estimated that there is 600 billion barrels stranded oil sand resource that is too deep for mining and too shallow for steam assisted gravity drainage (SAGD) (Braswell 2012). This suggests that a key target for future development in viscous oil production is low temperature/low pressure in-situ operations. Low temperature and pressure operations are also important for developing fractured carbonate reservoirs, which worldwide hold 1.6 trillion barrels oil in place (Briggs, Beck, et al 1992). The Grosmont Formation is the most promising of Alberta's fractured resources with original oil in place estimates from 320 (Jiang, et al 2010) to 406 (Yuan, et al 2010) billion bbl. The field has previously been subjected to steam flooding and cyclic steam stimulation. Because of the large resource base and improved technologies, especially in thermal gravity drainage processes since initial field exploration, new technologies have been targeted for the Grosmont. The work presented in this chapter explores a novel, low temperature solvent injection strategy targeting fractured systems.

The works builds on three current technologies – N-Solv, VAPEX, and Gas-Oil Gravity Drainage (GOGD). The N-Solv process injects a heated pure solvent into the reservoir. The process is similar to SAGD (same well orientation) except condensing solvent provides heat instead of steam. When the solvent condenses, its latent heat is released to the reservoir. The temperatures, unlike SAGD, are not high enough to mobilize the oil. However, the released heat is sufficient to reduce the oil viscosity enough to achieve rapid solvent penetration. The condensing solvent then extracts the low molecular weight components of the oil at the chamber interface (Braswell 2012). The other end of the solvent injection spectrum is the VAPEX process, which entails injecting a cold vaporized hydrocarbon solvent to produce oil by gravity drainage (typical

SAGD well orientation). A non-condensable carrier gas is often injected with the solvent to increase the operating pressure because pure solvent use requires that the reservoir pressure is at or below the solvent vapor pressure. Under co-injection, the solvent is injected as a liquid, which the carrier gas vaporizes and carries to the bitumen interface.

The gas-oil gravity drainage (GOGD) process holds great potential for production from fractured viscous oil fields where conventional displacement methods are often ineffective because the high fracture permeability prevents significant pressure differentials across the matrix. The density difference between the gas and oil provides the energy for the process without depleting the reservoir pressure (Festoy and van Golf-Racht 1987). Thermally assisted gas-oil-gravity drainage (TA-GOGD), unlike a normal steam flood, uses the steam as a heating agent to enhance the existing drive mechanisms rather than serve as the drive mechanism. The fracture network is used for distribution of heat and recovery of oil (Penney 2005). The TA-GOGD process, while proven successful at the Qarn Alam field, is not ideal for all reservoirs because steam injection requires high temperature operations.

Steam processes are limited to operating temperatures in excess of 100 °C. Using solvent as a steam additive does not allow for sufficient reduction in operating temperatures. However solvent injection provides sufficient viscosity reduction at much lower temperatures and pressures. This work looks to use the benefits of solvent injection seen in the N-Solv and VAPEX process in the GOGD mechanism. Therefore, I built on the TA-GOGD process by replacing steam injection with warm solvent injection. The proposed technology uses heated solvent in the gas-oil gravity drainage process for a fractured viscous reservoir. The work discussed in this chapter starts with steam and steam-solvent injection experiments to justify the move to solvent-only processes. Then

proof of concept solvent injection sand-pack experiments explore the key parameters affecting the process and the degree to which in-situ upgrading occurs.

3.1 INTRODUCTION

In the new process, production is dominated by two production phases – liquid extraction and solvent-enhanced film gravity drainage. Thermal expansion also contributes a small fraction to oil production. The warm solvent is in the vapor phase when injected into the reservoir but will condense when it contacts the cold oil. At this interface, liquid extraction occurs. The liquid extraction process can be described by mass-transfer coefficients for each phase of the extraction process, which are a function of temperature, solvent type, and concentration gradient at the solvent-oil interface. After the system has reached the target operating temperature, the injected solvent remains in the vapor phase when it contacts the oil. During this phase, production is due to solvent-enhanced film gravity drainage. This differs from traditional bulk gravity drainage because the remaining oil after liquid extraction exists as film, not in bulk. As the oil film drains out of the matrix, the vapor fills the void space further enhancing the GOGD mechanism. The film gravity drainage rates are controlled by permeability, oil viscosity (function of temperature/pressure and solvent concentration in oil), and solvent type. The experiments discussed in this chapter explore the key parameters that influence each production mechanism. The study also looks at the asphaltene content of the residual oil to explore the degree of in-situ upgrading that occurs after solvent injection.

3.2 MATERIALS AND METHODS

The heavy oil is from an un-dewatered sample of crude provided by an industrial collaborator. The viscosity of the oil as a function of temperature was measured with an ARES LS-1 rheometer using a double-walled fixture. Figure 3.1 is the viscosity profile

for the oil used in all experiments. n-Butane is supplied as research grade (99.99% purity) gas by Matheson. The n-pentane is technical grade (95%) purity from Acros Organics. The n-hexane is technical grade (95%) purity from Acros Organics. Two types of sand were used for the experiment: F35 and F50 silica sand purchased from U.S. Silica. Prior to use the sand was run through a stack of sieves so that only a certain distribution of the sand would be used. The F35 sand was run through a stack of sieves including 20, 40, 50, 70, and 100 mesh screens. Only the sand collected on the 40 mesh sieve was used to pack the mesh column with grain sizes ranging from 422 to 853 µm. The F50 sand was run through a stack of sieves including 40, 60, 70, 80, and 100 mesh screens. Only the sand collected on the 80 mesh sieve was used to pack the mesh column with grain sizes ranging from 178 to 211 µm.

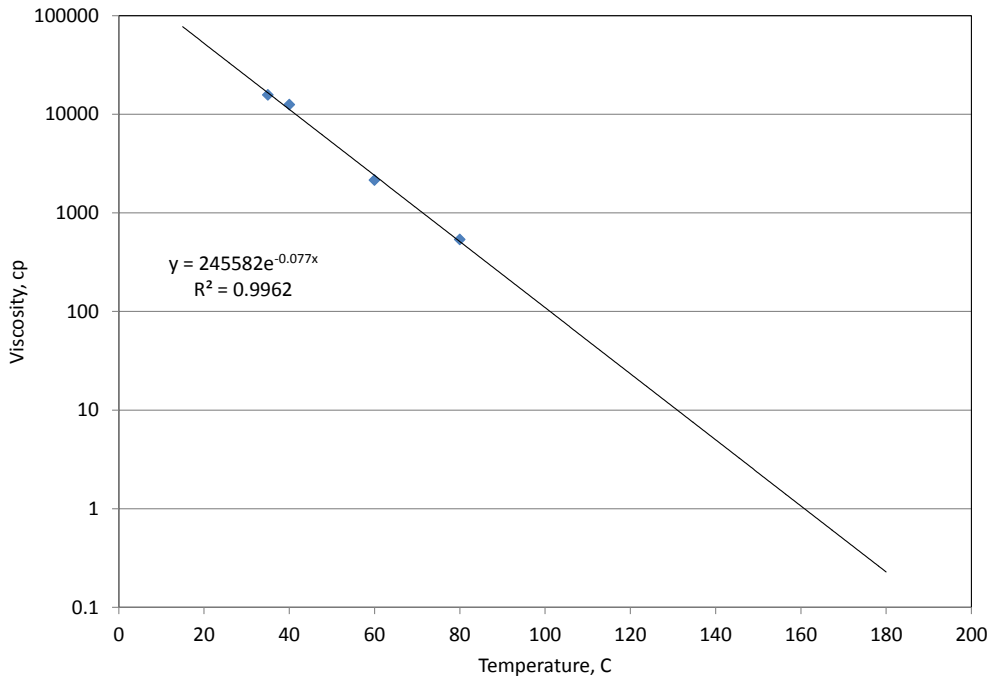

Figure 3.1. Viscosity profile with the trend line from the oil sample measurements.

The experimental set-up is designed to study a single fracture matrix interaction during the process. For ease of description, discussion of the set-up has been divided into sections based on function.

3.2.1 Production System

The first step in the saturation procedure is to pack the mesh column. Custom-designed mesh screen columns, manufactured by Hillshire Wire Mesh Company, were used to hold the sand pack. Each column has two layers of mesh screen welded together to form a cylinder that is one meter long with a five cm diameter. One end (the top) is left open. A mesh end cap is welded onto the other end (the bottom). There is only one layer of mesh for the bottom end cap. The mesh cylinder is then welded to the inside of a metal support frame. The frame consists of three metal rings (top, bottom, middle) connected by four rods that run the length of the cylinder. The size of mesh for each screen is designed to prevent sand production when using a given sand but still allow flow with minimal restrictions. One column used two layers of 60 mesh screen (60-60 column). The second used two layers of 100 mesh screen (100-100 column).

Figure 3.2 is a schematic of the production unit, which consists of the sand pack, outer metal containment tubing, and temperature/pressure measurement devices. The mesh column (2) is placed inside a stainless steel tube 1 m long and 6 cm in diameter (1a). This creates a 5 mm annulus around the mesh column. This allows a single matrix (mesh column)-fracture (annulus) interaction to be studied. The steel tube is fitted with two end caps custom-made by the PGE fabrication shop. Figure 3.3 is a picture of the two end pieces with the top on the left. The top end cap has three ¼" Swagelok male fittings welded on. The central port allows the thermocouple bundle to pass through the cap so that the lead lines can be attached to the digital reader for the thermocouples. The

two edge ports are aligned over the annular space. The port in use during the experiment is attached to a four-way union. One port on the union holds a J-type point thermocouple from Omega Engineering (4) to record the temperature of the injected fluid before it passes through the end cap. One port connects to the steam or solvent injection system. The final port connects to an absolute pressure transducer to measure the inlet pressure. The bottom end cap (1c) has two parts. For both parts there is a ¼" opening in the center with a Swagelok fitting on the bottom part. Two strips of 100 mesh screen overlain so the gridding is offset are glued over the ¼" opening of the bottom part. Then the two parts are epoxied together so that the ¼" openings align. The screen serves as the final barrier to sand production because all produced fluid must pass through the end cap to reach the outlet system. Sand production prevention is vital because even a single grain of sand can scratch the diaphragm of the outlet back pressure regulator (BPR). A scratched diaphragm will not hold pressure, which means that the outlet pressure will not be controlled. In addition to the four point measurements on the thermocouple bundle (3), temperature is measured at points 4, 5a, and 5b. These four points use J-type point thermocouples from Omega Engineering. Point 4 measures the temperature of the injected fluid before it passes through the top end cap and into the annulus. Points 5a and 5b measure the temperature in the annulus at the top and bottom of the column. Pressure is measured at points 6a and 7a using Rosemont absolute pressure transducers (6b and 7b). Point 6a measures the pressure in the annulus at the top of the column. This value can be used in conjunction with the outlet pressure to measure differential pressure along the column. Point 7a measures the pressure at the same point of injection as temperature is measured at point 4. Typically, these two pressure points are similar. A thermocouple bundle (3) runs through the center of the sand pack. The bundle, purchased from Thermometrics, has four J-type point thermocouples cemented together with each tip at a

different depth and encased in a closed tip stainless steel tubing. The bundle is one meter long with the point measurements at 25, 50, 75, and 100 cm from the top. The thermocouple lead lines emerge from the top and are encased in Teflon coating for durability. The lead lines are then connected to the Omega Dual DIN Rail Temperature Transmitter (8), which transmits the digital input from the thermocouples to the LabView software.

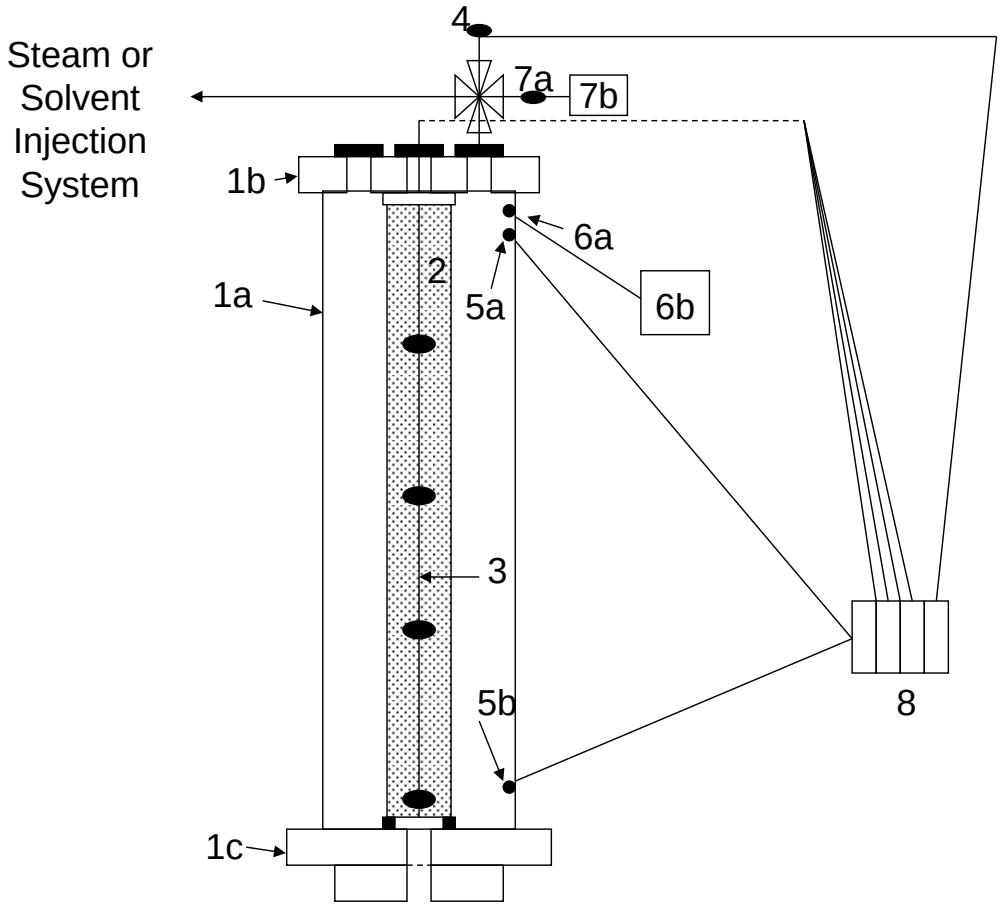

Figure 3.2. Proof-of-concept experiment production system.

Figure 3.3. Stainless steel column end caps.

3.2.2 Steam Injection System

Figure 3.4 shows the schematic for the steam injection system. Two Infinity Fluids inline steam generators were in use. The low rate generator (4) was capable of generating 1-8 cc/min CWE. The high rate generator (3) was capable of 15-50 cc/min. The generators shared the same inlet and outlet, so only one could be in operation at any given time. The generators' operating conditions are set with connected control boxes (3a and 4a). During operation, distilled water (DI) was pumped from a Quizix QX pump (1) through a 500 mL accumulator (always full of DI) and into the generators. The accumulator (2) serves as a buffer between the generators and the pumps. In case of a back flash of steam into the injection line, the heat will be absorbed in the accumulator and not reach the pump. Once inside the generator, the water is vaporized when it passes by a heated coil at the top of the generator resulting in steam output. If the generator is operated at too high a power rating, the entire column of water will vaporize causing the system to overheat. Additionally, the presence of air in the generator will cause the system to overpressure. Because these issues prevent continuous steam injection, the system must be carefully calibrated for the applicable power level for each flow rate (high enough to create high quality steam but low enough to prevent overheating) and ensure that no air is in the injection line. In order to control the power setting of the coil,

it is necessary to operate the generators under manual control. Items 3a and 4a are the power supply and control box for the two generators. The control boxes were designed such that under manual control the target temperature could not be set. Rather, the generators operate at the saturation temperature corresponding to the pressure downstream of the generators. For both steam cases, this pressure was controlled by an Equilibar EB1LE1 BPR (5), which was set at the same pressure as the BPR at the outlet of the column. Before injecting steam into the column, it is first vented through a secondary line to the atmosphere. It can take up to 30 minutes of injection through the generator to reach the target temperature and high quality steady-state steam generation. When the steam has reached steady-state flow, it is diverted into the column. For the steam-solvent case, the solvent is co-mingled with the steam downstream of the BPR before the column inlet.

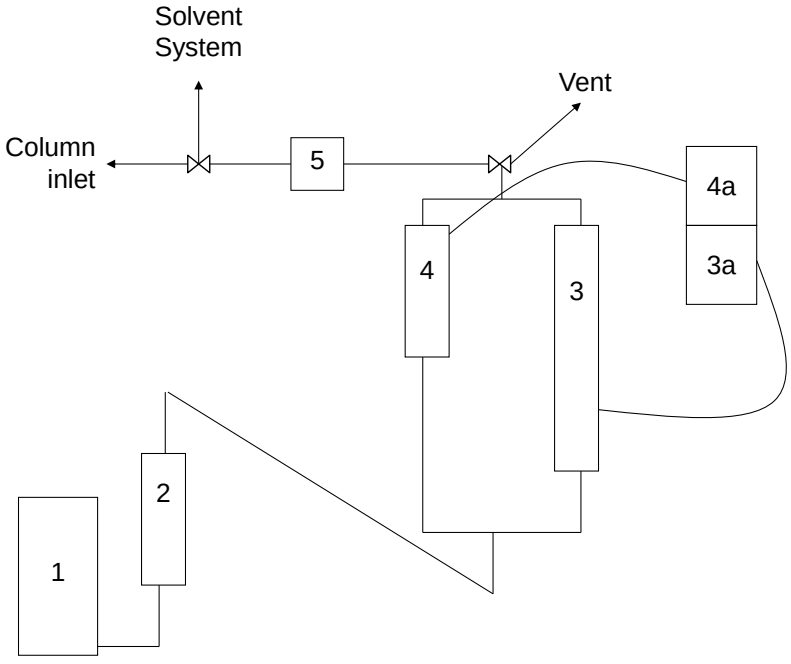

Figure 3.4. Steam injection system.

3.2.3 Solvent Injection System

The solvent injection system consists of two orientations. The injection system can be in refill or injection mode. The solvent is stored in two three-liter stainless steel piston accumulators (3). During an experiment, one accumulator will be in injection mode, and one accumulator will be in refill mode. The refill mode varies dependent on the phase of the solvent at atmospheric conditions. For liquid solvents (n-pentane and n-hexane), the piston is displaced to the bottom by injecting air into the top of the empty accumulator and allowing the water below the piston to be expelled. Once the piston is at the bottom, the top cap is removed, and the liquid solvent is poured into the accumulator. For gaseous solvents, the refill orientation shown in Figure 3.5 is used. The solvent is pumped from the gas tank (1) through a Haskel AGT-4 compressor (2). At the beginning of the refill process, the piston in the accumulator is at the top, which means the entire accumulator below the piston is filled with water that needs to be displaced. The goal of transferring the solvent from the gas tank to the accumulator is to compress it into a liquid. The pressure of the accumulator is controlled by a Mighty Mite BPR (4) that controls the flow of the water out of the accumulator. This forces the gas pressure to exceed the BPR dome pressure in order to displace water and fill the accumulator resulting in an accumulator full of liquid solvent at the desired pressure. Once the piston is completely displaced, the pump is stopped.

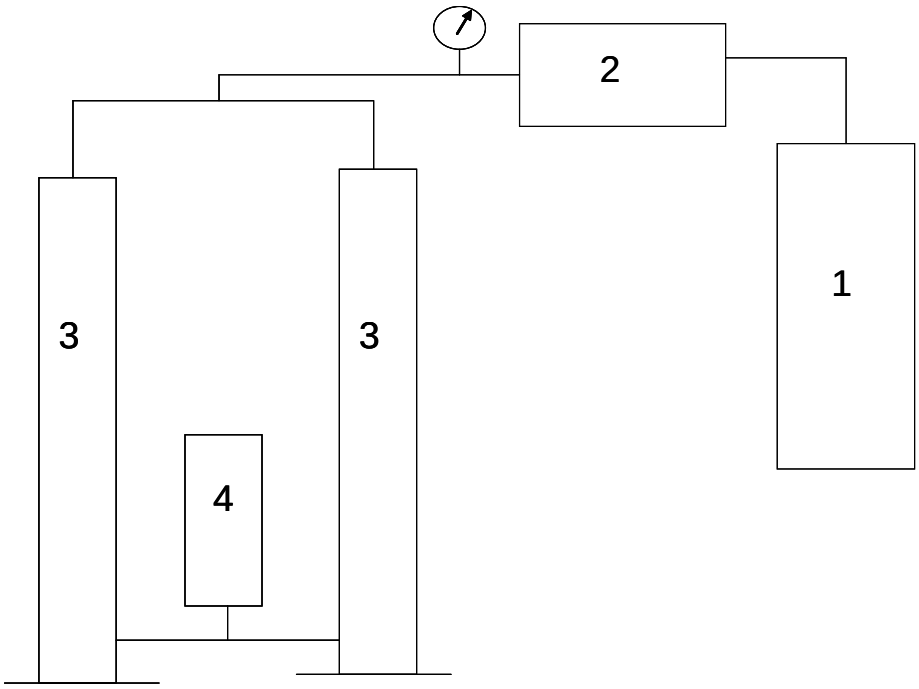

Figure 3.5. Solvent injection system in refill mode for gaseous solvent.

Figure 3.6 shows the solvent system in injection mode. Because the solvent in the accumulator can be considered an incompressible fluid, the amount of water injected beneath the piston equals the amount of solvent injected into the solvent line. A Quizix QX pump (2) is used to inject water into the accumulators (1). Once the solvent leaves the accumulators it enters the solvent line that goes to the oven (4) where it flows through a coiled loop (3). The oven is set at a predetermined temperature to heat the solvent to the desired injection temperature. The solvent injection line pressure is controlled with a BPR (5) set to a pressure 29.0 psia above the outlet BPR dome pressure. All of the lines from the oven outlet to the production column, including the BPR, are wrapped in Briskheat HSTAT or BSAT heating tape so that the solvent does not lose heat after it leaves the oven. For the steam-solvent case, the solvent lines were not preheated.

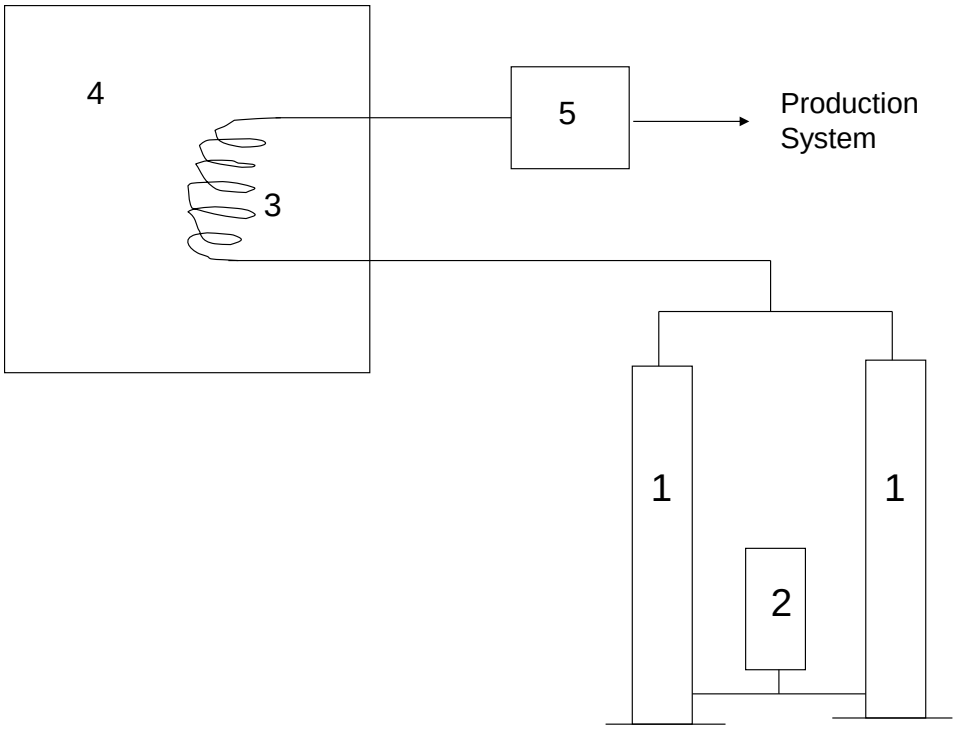

Figure 3.6. Solvent injection system in injection mode.

3.2.4 Pressure Control System

The Equilibar EB1LF1 BPR used at the outlet operates under a dome pressure-diaphragm combination. Air or gas is injected into the dome of the BPR that pushes the diaphragm closed until the inlet pressure of the BPR exceeds the dome pressure. Then the diaphragm is lifted allowing flow through the BPR as long as the inlet pressure stays above the dome pressure. Normally, the dome pressure can be applied prior to the start of the experiment with no maintenance necessary. However, the BPRs at the outlet of the steam generators and the column are exposed to increasing temperatures during generator start-up and the beginning of the experiment. These temperature changes would result in a corresponding increase in dome pressure as the gas was heated because it cannot expand inside the dome. Therefore a pressure control system was devised to maintain the

dome pressures at their set point. To maintain the dome pressure at a constant value during the heating period, a Control Air Type 700 pressure regulator is installed in the gas line between the air supply and the BPRs. The pressure regulator controls the downstream pressure by releasing excess gas from the BPR dome to keep the pressure at the set value even during heating. This control process uses excess air, so the air tanks (dry grade from Matheson Gas) have to be changed as they are depleted throughout the experiment. Control at higher pressure requires more air tanks. The pressure control is not necessary for the solvent injection line BPR because the temperature of this line does not change during the experiment.

3.2.5 Effluent Collection System

The effluent collection system (Figure 3.7) is designed to make the collection of the different produced fluids as easy as possible. After passing through the outlet BPR, the effluent flows into a glass double-walled accumulator (1). The double-walled accumulator is designed to collect oil, oil-solvent mixtures, and water. The double-walled accumulator is kept in excess of 100 °C using ethylene glycol heated by a Brookfield circulating heating bath (2). This temperature ensures that the solvents used will be in the vapor phase in the double-walled accumulator and will then pass through the super condenser (3). The temperature is also high enough to ensure the oil does not stick to the walls of the accumulator and will flow when removed from the accumulator. The accumulator has a 1000 mL capacity, but the inlet line from the column connects with the accumulator at the 500 mL level. This is necessary because if the inlet line was put at the top of the accumulator a pressure surge would blow oil into the super condenser. The lower level does limit volume retention, but prevents any oil from getting into the super condenser in case of pressure surge. Fluid is collected from the bottom of

the accumulator through a stopcock. Because the heating does not reach the stopcock, it often has to be heated using a BriskHeat HSTAT heating tape to promote flow during sample collection. Any parts of the effluent that are in the vapor phase at the double-walled accumulator conditions will go through the super condenser (3). The condenser is an Aldrich® super condenser that combines a cold-finger, coiled, Liebig, and Vigreux condenser into one unit with a forced spiral path that has 820 cm^2 of cooling area. The condenser is cooled using ethylene glycol. The ethylene glycol is cooled with a Fisher Isotemp 3013S circulating bath (4) chilled to -5 °C. This temperature was chosen because it will condense all solvents. The condensed solvent will then be collected in the single-walled glass accumulator (5). The liquid solvent is collected using the stopcock at the bottom of the accumulator. The n-butane revaporizes after leaving the condenser and continues to flow through to the Elster American Meter wet test meter (6). The wet test meter records the flow rate of the gas before it is exhausted into a fume hood.

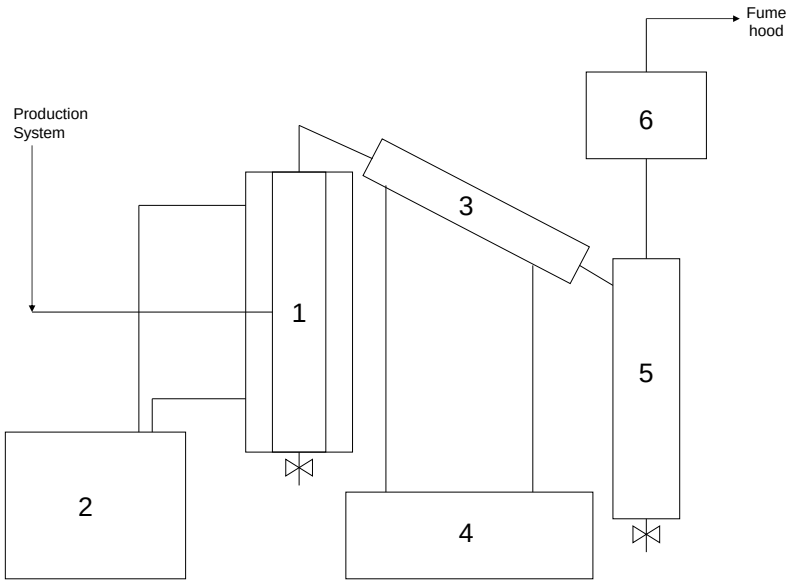

Figure 3.7. Effluent collection system.

3.2.6 Saturation Procedure

The first step in the saturation process is to pack the mesh screen column. To pack the column with sand, the mesh column is attached to a metal frame resting on the floor. A Vibco vibrator is also attached to the metal frame. The vibrator is turned on at 40% which vibrates the frame and correspondingly the mesh column. An aluminum cut-out piece is placed at the bottom of the screen (see Figure 3.8, left piece). The piece serves as a centralizer for the thermocouple bundle. The piece's outside diameter is equal to the screen internal diameter and has a ¼" hole in the center. The thermocouple bundle is inserted into the ¼" hole. This piece remains in the screen during the experiment. At the top of the column a second centralizer is used (see Figure 3.8, right piece). This piece is designed to rest on the top of the column during saturation. Again, it has a ¼" hole in the center. These two pieces guarantee that the thermocouple bundle remains centralized during the sand packing process. Once the thermocouple bundle is in place, the vibrator is turned on. The sand is poured into the column for five seconds every two minutes. This timing allows each new addition of sand to settle before the next is added, preventing layering and providing homogeneity in the sand pack. Once the sand has reached the top of the mesh screen column, the top stabilizer is removed and replaced with a Teflon plug. The Teflon plug accommodates the pass-through of the thermocouple bundle. It has a Viton o-ring on its top, which seals against the top cap of the steel tube in the experiment. The purpose of this plug is to guarantee that no sand is produced from the top of the sand pack into the annular space during the experiment. Any space between the plug and the thermocouple bundle and the plug and the mesh screen column not filled with sand is filled with glass wool (Supelco, silane-treated).

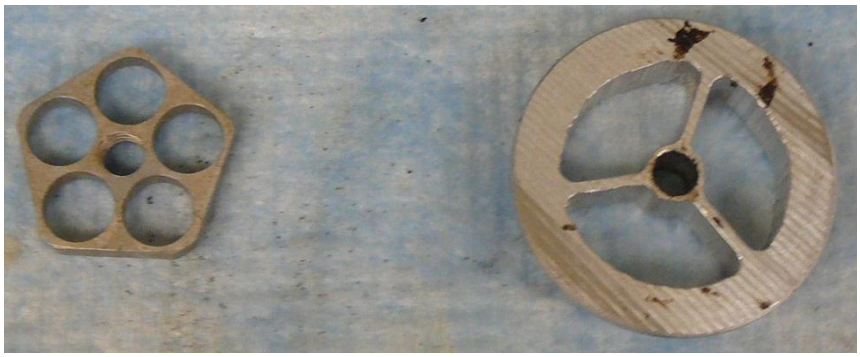

Figure 3.8. Thermocouple stabilizers for mesh screen.

Figure 3.9 shows the saturation set-up. Once the mesh column has been packed with sand, the column is weighed prior to being placed in the saturation cell. The saturation cell (4) is a clear tube with Teflon end caps. Each end cap has a recess that ensures the mesh column is centered inside of the saturation cell because the cell has a larger diameter than the mesh screen. The bottom end cap has a fitting on the side that allows oil to be injected at the bottom of the screen. The top end cap has a t-fitting that allows the thermocouple bundle to pass through and has an outlet port for oil production at breakthrough and to be used to pull an initial vacuum on the system. Because of the high viscosity of the oil, the saturation must take place inside an oven at 85 °C to ensure sufficiently low viscosity for the process. Oil is stored in three double-ended accumulators – one 1000 ml (2) and two 500 ml (3). It is necessary to preheat the system for four hours before the saturation begins to ensure that the oil is at the target temperature. During this time, a vacuum is pulled on the system. However the vacuum is released before saturation begins because the vacuum will result in boiling oil at the set oven temperature. Distilled water is injected with a pump (1) into the bottom of the accumulators to displace the oil into the saturation cell. Pressure build-up in each accumulator due to expansion of the oil is released before each accumulator is switched

to the saturation cell to avoid a pressure surge. For the 40 mesh sand packs, the saturation is done over a 24 hour period (1.166 cc/min). For the 80 mesh sand packs, the saturation is done over a 48 hour period (0.583 cc/min). These rates are used to ensure a quality saturation with no channeling. The bottom-up saturation method is used to ensure no trapped air bubbles. Once saturation has been completed, the saturation cell is removed from the oven and allowed to cool. The saturated sand pack can remain in the cell until the start of the experiment with no loss of mass or change in properties. It is necessary to keep the mesh column in the saturation cell until the start of the experiment because once the column is removed from the cell, oil will begin to drain out through the mesh.

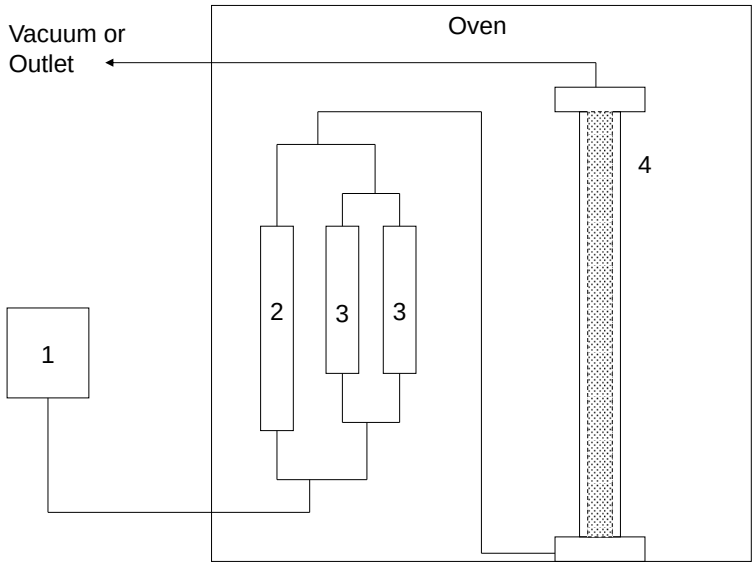

Figure 3.9. Saturation set-up for proof of concept experiments.

Because of the nature of our experimental set-up, the permeability of the sand packs cannot be measured using the mesh columns. Therefore, the permeability of a representative 40 mesh and 80 mesh sand pack was measured using an auxiliary flow set-

up (Figure 3.10). The set-up consisted of a 40 cm long glass column with 2 cm diameter (1), Rosemont differential pressure transducer (2), Flom KP-22 HPLC pump (3), and distilled water reservoir (4). The same procedure used to pack the mesh column was used to pack the glass column. Then, distilled water was injected into the glass column at different rates, and the corresponding pressure drops were recorded. The filters on the end caps of the glass column provided a base resistance to flow. Therefore, the pressure drops in the column when it was only full of distilled water were measured at various rates. The pressure drop was subtracted from the pressure drop recorded during flow through the sand pack to determine the actual pressure drop due to the sand pack. Using Darcy's law (Equation 3.1), the permeability of the pack could be measured.

$$q = -\frac{k}{\mu} A \frac{\Delta P}{L} \tag{3.1}$$

Where q = volumetric flow rate

k = absolute permeability

μ = viscosity

A = area perpendicular to flow

ΔP = pressure drop

L = length

Figure 3.11 shows the injection test for the 40 mesh sand pack. The calculated permeability for the sand pack was 129.7 D. Figure 3.12 shows the injection test for the 80 mesh sand pack. Only the final curve used to calculate permeability is shown. The permeability is 35.6 D.

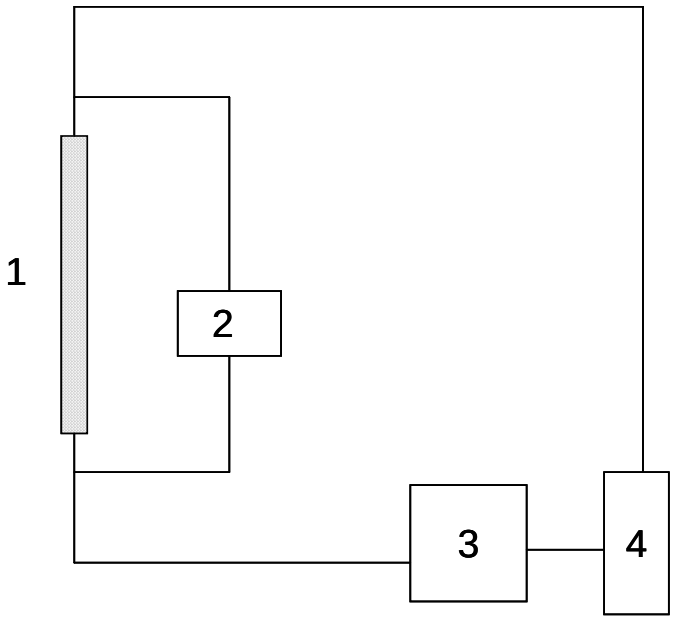

Figure 3.10. Schematic of the flow loop for permeability measurements.

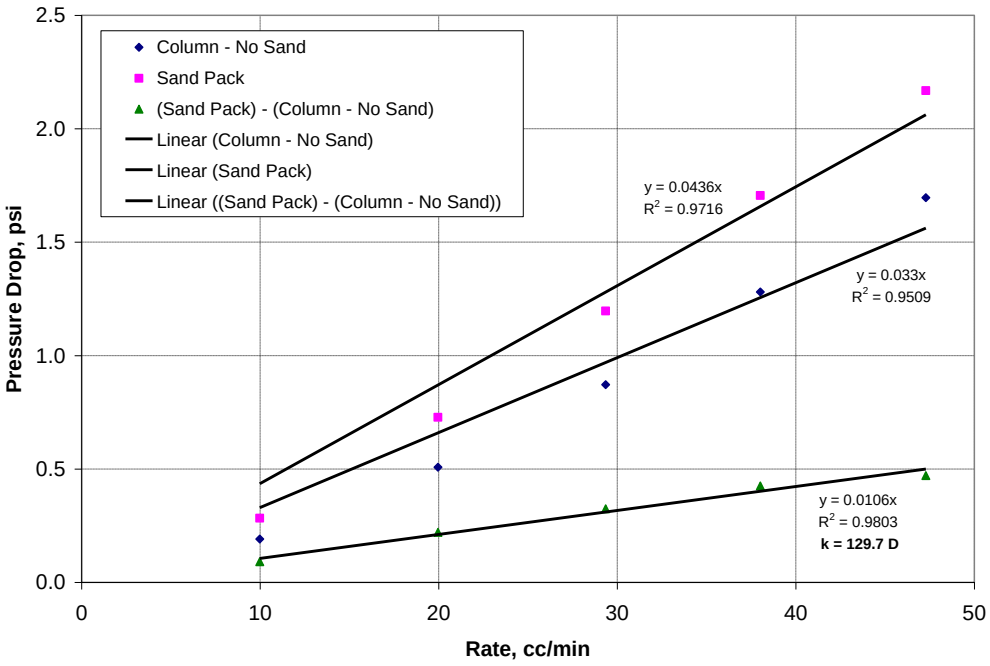

Figure 3.11. Determination of the 40 mesh sand pack permeability using the glass column flow loop.

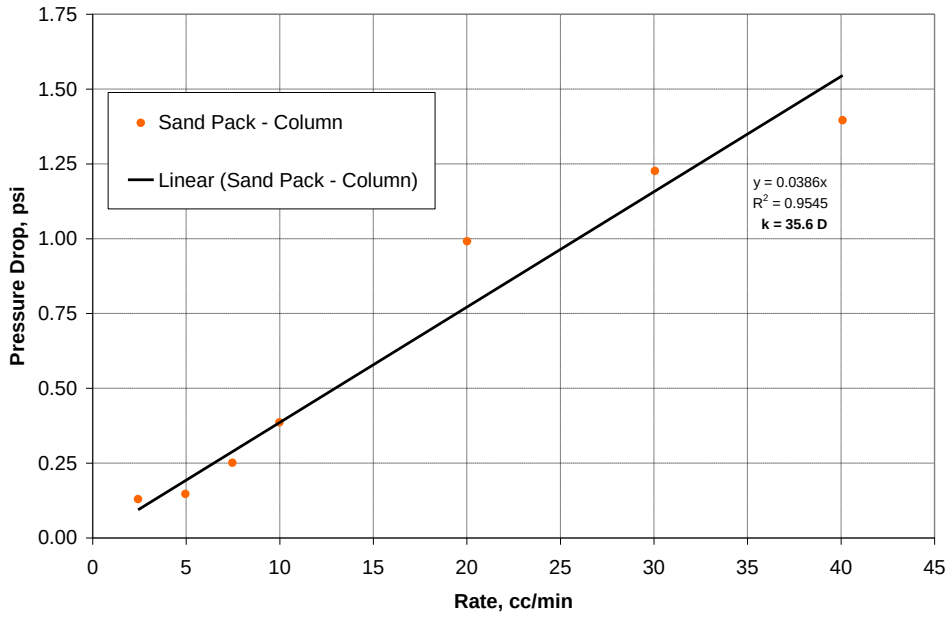

Figure 3.12. Determination of the 80 mesh sand pack permeability using the glass column flow loop.

3.2.7 Injection Preparation

Prior to an experiment, the mesh column has to be transferred from the saturation cell to the steel tubing that is part of the experimental set-up. At room temperature, the oil is still viscous enough to significantly seep through the mesh sides of the column. This can result in significant loss of oil mass before the injection is initiated, which make subsequent data unreliable. Therefore, the entire saturation cell is placed in an ice bath for at least 4 hours before removal of the mesh column. This cools the oil to a sufficient temperature to impede seepage so that oil mass loss is negligible during transfer. Once the mesh column has been removed, excess oil on the outside is removed and the column is weighed. The difference between this weight and the dry weight prior to saturation is used to determine the mass of oil in the column. After weighing, a tab is attached to each of the four posts on the mesh column's metal frame. These tabs work to centralize the

column inside the metal tubing without affecting annular flow. The column is then transferred to the production system and the top cap of the metal tubing is secured. The final step before the experiment begins is to saturate the annular space with water. To do this water is injected through the bottom end cap at a high rate until breakthrough at the top. Once breakthrough occurs, injection of the desired test fluids from the top can be initiated.

3.2.8 Steam and Steam-Solvent Effluent Analysis

The cases involving steam injection required additional work to determine the oil rate because much of the oil was produced as an oil-in-water emulsion. During the steam and steam-solvent cases, the oil was produced as three phases – a heavy pure oil phase, a light oil phase with some trapped water, and an oil-in-water emulsion. After the initial high rate of production, the oil was primarily in the emulsion form. This meant that the emulsion needed to be broken before the oil rate could be calculated. The original samples, if all three oil phases were present, had three layers: light oil phase, emulsion, and heavy oil phase. To break the emulsion, a 40 wt % CaCl solution was added to the samples. The samples were allowed to equilibrate until the emulsion was fully broken and the emulsion phase was clear with only suspended oil particles remaining. At this point the oil could be collected for analysis. The first step was to collect the top layer of oil by scooping it out of the jar into a vial. This oil composed of some original light oil layer and some of the oil from the broken emulsion. Once this oil had been removed, the water layer was extracted and run through P5 grade filter paper (Fisher). This was done to quantify the amount of oil suspended in the water. Finally, the remaining heavy bottom oil was removed. The total mass from all three layers was used for calculation of the recovery curves. For some of the first samples analyzed, the top layer of oil was

removed before the salt solution was added to break the emulsions. This resulted in some water trapped in the collected oil. In order to remove this water, the vials were heated to 85 °C to aid phase separation and then placed in a centrifuge immediately upon removal from the oven. Any water separated from the oil during this process was removed from the vial with the use of a syringe. Despite these secondary removal processes, some water still remained trapped in the oil.

3.2.9 Residual Oil Analysis

At the end of each solvent-only experiment, the mesh screen column is removed promptly, and the sand is collected for residual oil analysis. To remove the sand from the mesh column, it is necessary to use a heat gun to loosen the sand from the mesh wall. The sand is divided into four sections and stored in an air tight container until oil removal. Some of the sand/oil mixture sticks to the wall of the screen and cannot be removed mechanically without damaging the mesh. As a result, the residual oil saturation cannot be determined from our analysis. However, the removed oil is considered a good representative sample of each section for asphaltene content analysis. After removal from the screen, each sand section is washed with toluene to remove the oil. The sand is placed in a filter-lined funnel during the washing process, which allows the sand-free liquid to be collected. Once all of the oil has been extracted from a sand section, it exists as a toluene-oil mixture. The next step is to remove the toluene from the mixture. This is done with the aid of a Büchi Rotavapor R-114 rotary evaporator. After the mixture has been run through the rotary evaporator, the pure oil can be used for asphaltene analysis.

The ASTM recommended procedure for separating asphaltenes from cured oil (ASTM D2007-80) was followed. The process is summarized below.

1. Determine the volume of the oil sample. The standard recommends 20 mL of oil, but none of the samples produced this much oil. Therefore, the target was reduced to 10 mL.
2. Add forty times the oil volume of n-heptane to the oil sample.
3. Seal the container and allow the mixture to equilibrate for two days.
4. Use a funnel filter assembly to separate asphaltenes from the oil/precipitant mixture.
    a. Weigh a 0.22 μm filter and place on the funnel cup.
    b. Pour ~ 100 mL of the mixture into the funnel cup and seal with aluminum foil.
    c. Connect the funnel filter assembly to the vacuum to begin filtration.
    d. Repeat a-c until all of the mixture has been filtered.
5. Continue to pull a vacuum until the deposited asphaltene dries enough to form cracks.
6. Remove and weigh the filter paper to determine asphaltene weight.

The asphaltene weight can then be compared to the weight of the oil sample to determine the asphaltene content of the residual oil.

3.3 Results and Discussion

The experimental set-up for this work explores the behavior of a single matrix-fracture interaction. A meter long sand pack (matrix) is placed inside a stainless steel column leaving a five millimeter annulus (fracture) between the pack and the column. The first experiment looked at high temperature steam injection, which is considered the

base technology for viscous oil production. Then, a 96-4 mole% mixture of steam and n-hexane was injected at the same temperature to study the impact of solvent addition on steam performance. These experiments served as justification to move to low temperature solvent processes. Therefore, the bulk of this work focused on the solvent proof of concept experiments. The experiments in this phase (Table 3.1) were designed to study the effects of permeability, temperature/pressure, in-situ injection rate, and solvent type on the two primary production mechanisms.

	Case Name	Solvent	Permeability, D	Temperature, °C	Pressure, psia	In-Situ Rate, cc/min
1	Base	n-butane	129	60	91.4	1583
2	Permeability Effect	n-butane	36	60	87.0	1583
3	Temperature Effect	n-butane	36	40	52.2	1583
4	Temperature + Rate Effect	n-butane	36	40	52.2	2592
5	Solvent Type Effect	n-pentane	36	60	29.0	4193

Table 3.1. Proof-of-concept experimental grid.

The base case (Experiment 1) is n-butane injection at 60 °C in a 129 D reservoir. Experiment 2 is designed to study the impact of permeability. The primary impact of decreasing permeability is a decrease in film gravity drainage rate. Experiment 3 was designed to study the impact of temperature. Temperature should slow the solvation kinetics during the liquid extraction phase and decrease the drainage rate during the film gravity drainage phase. Experiment 4 was designed to look at the impact of temperature and in-situ injection rate. Increasing the injection rate leads to improved liquid extraction because of higher concentration gradient in the solvent rich liquid phase at the oil-solvent interface. The final experiment (5) looked at the effect of solvent type (n-pentane), which impacts the production rates during both phases. A heavier solvent should result in

improved liquid extraction. Additionally, the use of a different solvent type will change the nature and amount of asphaltene precipitation.

3.3.1 Steam Case

The steam experiment injects steam at 188 °C and 160 psia into the 129 D sand pack. The 40 mesh sand was used with original oil in place of 546.5 g for a porosity of 27.8%. The steam was injected at 25 cc/min cold water equivalent (CWE). Figure 3.13 is the pressure profiles for the first two hours of the experiment. In the steam cases, the only pressures recorded were the outlet pressure and the dome pressure of the outlet BPR. Outlet pressure is downstream of the column, but upstream of the BPR. The dome pressure remains constant around 160 psia throughout the experiment as it is controlled by the pressure regulator. The peak in the outlet pressure running from 0.45 hours (27 minutes) to 0.7 hours (42 minutes) is due to plugging in the outlet line. During the initial production period before steam breakthrough, the draining oil collects in the annulus between the cold water and steam. When the oil arrives at the outlet, it begins to cool as it travels through the cooler production lines to the BPR. As a consequence, it does not flow through the BPR resulting in the observed pressure increase until the hot steam channels through the oil bank and arrives at the outlet at 0.53 hours (32 minutes). The steam arrival manifests as a sudden burst of oil and steam at the double-walled accumulator and a corresponding decrease in pressure. There were secondary peaks at 0.8 hours (48 minutes) and from 0.87 to 1.2 hours (52 to 72 minutes). These are subsequent minor disturbances as the outlet completely stabilized. The dome pressure was temporarily decreased at 1.3 hours to promote the final passage of the oil plug. When stabilization was reached the dome pressure was returned to its original value.

Figure 3.14 shows the entire pressure profile for the 48 hour experiment. The pressures remain stable for the duration of the experiment.

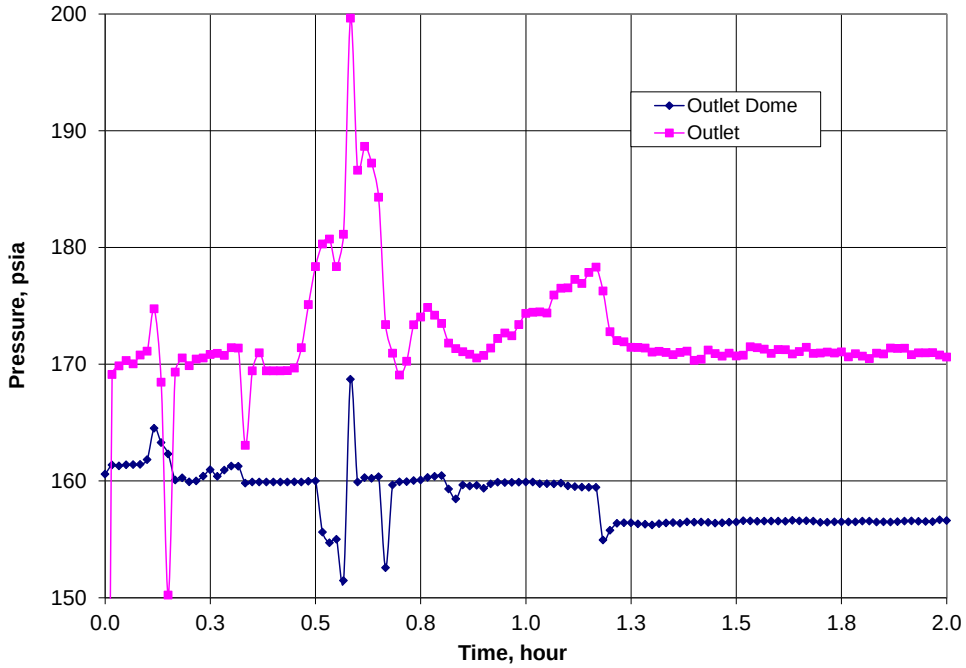

Figure 3.13. Early pressure profiles for steam cases.

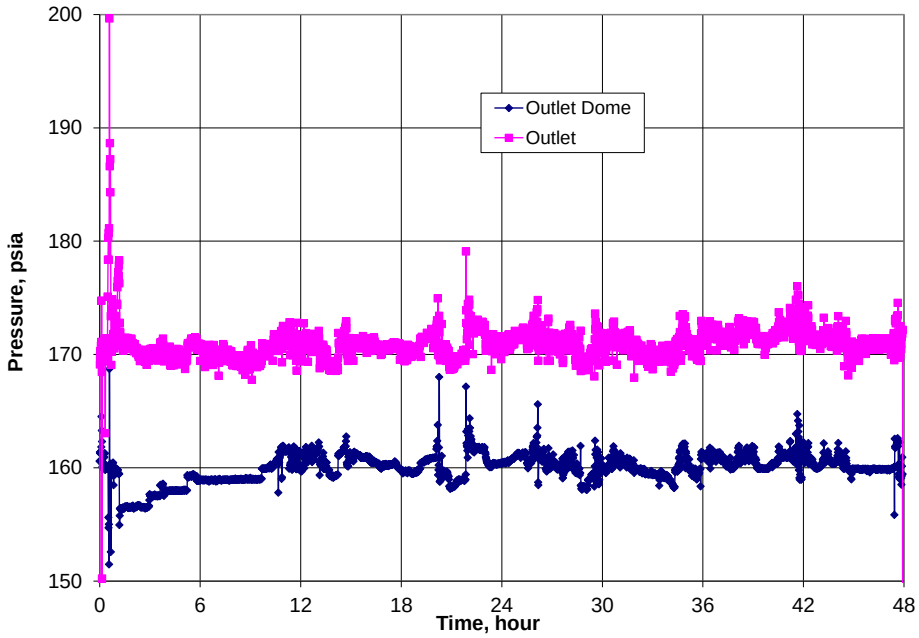

Figure 3.14. Steam case pressure profiles for the entire experiment.

Figure 3.15 shows the temperature profiles for the first hour of the experiment. Temperature is measured at two points in the annulus and four points at the center of the sand pack. The annulus measurements are made at the inlet and outlet. The sand pack measurements are 25, 50, 75 and 100 cm for the top of the pack at the center of the pack. The heat front moves vertically downward at 3.5 cc/min. Radial propagation of the heat front proceeds at 1.39 cc/min. Vertical propagation is calculated by determining the arrival times of a certain temperature at two adjacent column measurement points. Radial propagation is calculated from the arrival time difference between the Annulus-Outlet and Column-100 cm points, since they are at the same vertical position in the system. After the initial arrival of the heat front at a given location (sharp increase in temperature), the temperature continues to gradually increase to the steady-state temperature. The values slightly overshoot before settling at their stabilized values. The

overshoot occurs because the system overheats due to the increase in outlet pressure during the blockage periods. The effect of the outlet plugging can clearly be seen in the temperature profiles of the annulus-outlet and column-100 cm. When the pressure at the outlet begins to increase it corresponds with the temperature arrival at the outlet. However, the temperature increase is arrested around 0.47 hours (28 minutes), which corresponds with the significant increase in pressure The pressure build prevents the propagation of the heat front until the bank is produced allowing the pressure to decrease. The pressure peak corresponds with the time that the temperature profiles continue their upward progression. Once the temperatures have reached their stabilized values, the pressure has completely restabilized indicating that the outlet blockage has been removed. Figure 3.16 shows the temperature profile for the entire experiment. After the initial heating period, all of the temperatures remain at their stabilized values.

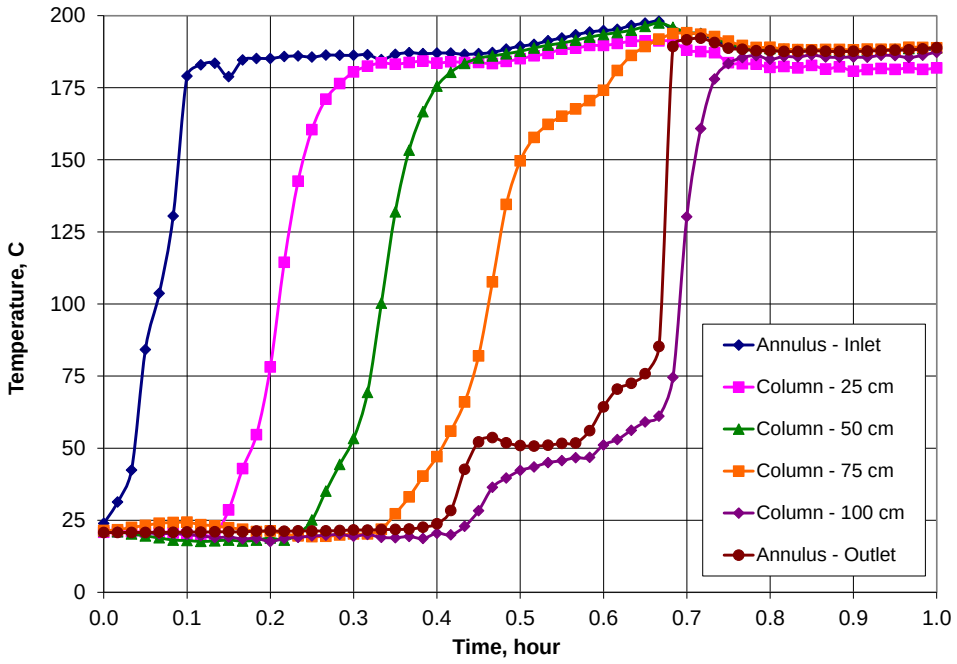

Figure 3.15. Early temperature profiles for the steam case.

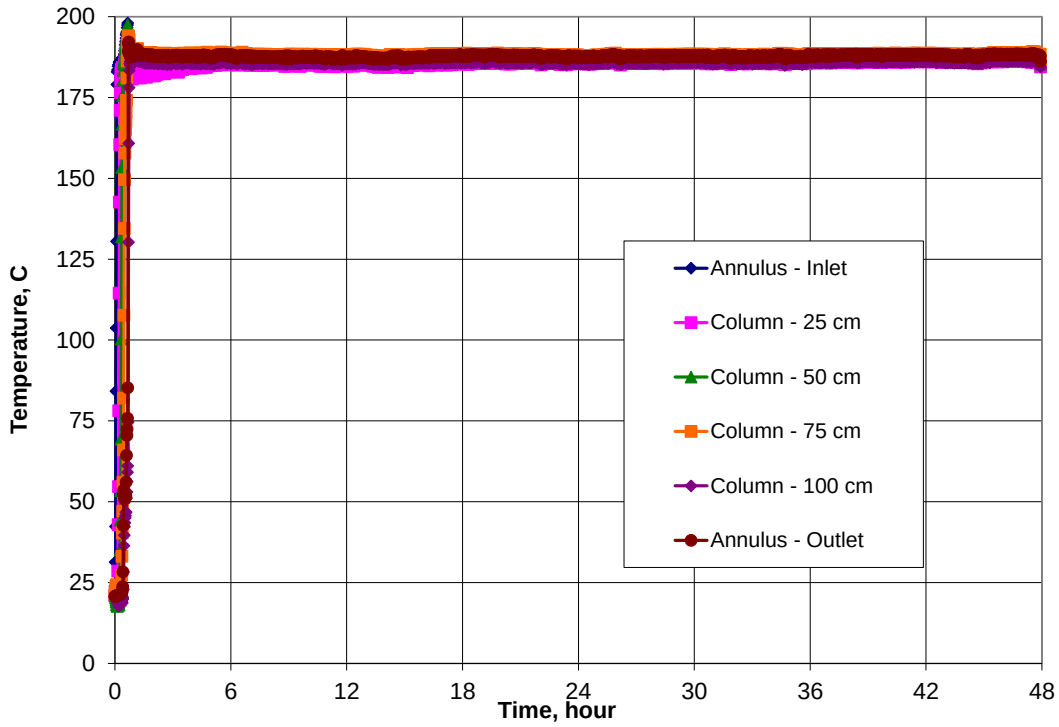

Figure 3.16. After initial heating, the system temperature remains constant for the entire steam only case.

Figures 3.17 and 3.18 show the cumulative oil and oil rate, respectively. Production did not occur until 0.42 hours (25 minutes). This is due to the outlet blockage discussed earlier. As a result, all of the oil produced from the start to burst was produced during the period from this to 0.75 hours (45 minutes) during which the burst occurred. This period of production accounts for 430 g of the production, which is 76% of the total oil produced. Thermal expansion should account for approximately 10% of the initial oil in place at these temperatures – 54.65 g. From the oil rate graph, it appears that oil production goes into decline immediately and there is no plateau production. There should be a bulk gravity drainage rate of 18.7 cc/min for the experiment (Equation 2, Corrêa and Firoozabadi 1996). This rate is not observed because all of the oil produced

from bulk gravity drainage is produced and stored in the annulus until the outlet is unblocked and then produced in a single burst.

$$q_{\max} = \frac{kA}{\mu}\Delta\rho g \tag{3.2}$$

where k = absolute permeability

A = cross-sectional flow area

μ = oil viscosity at injection temperature

Δρ = density difference between oil and injected fluid

g = gravity constant

The ultimate oil production is 563 g, which is higher than the original oil in place. The excess volume is assumed to be measurement error and trapped water in the samples. However, these errors do not overshadow that high recovery can be achieved by high-temperature steam injection into a fracture.

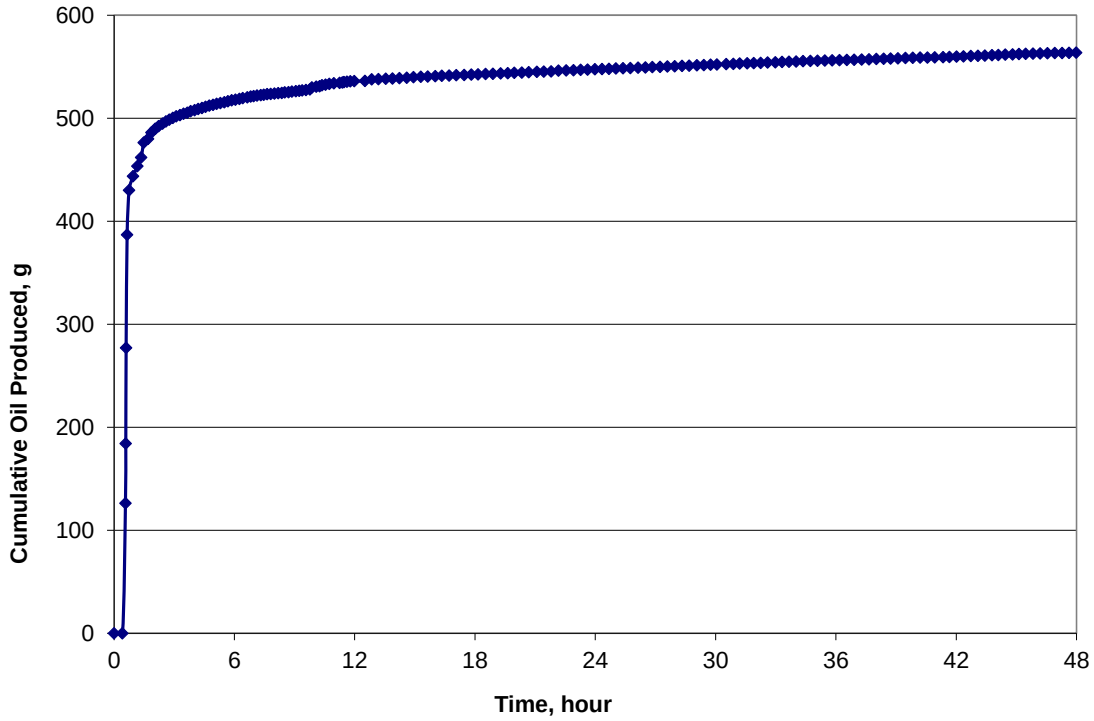

Figure 3.17. Cumulative oil production for the steam case.

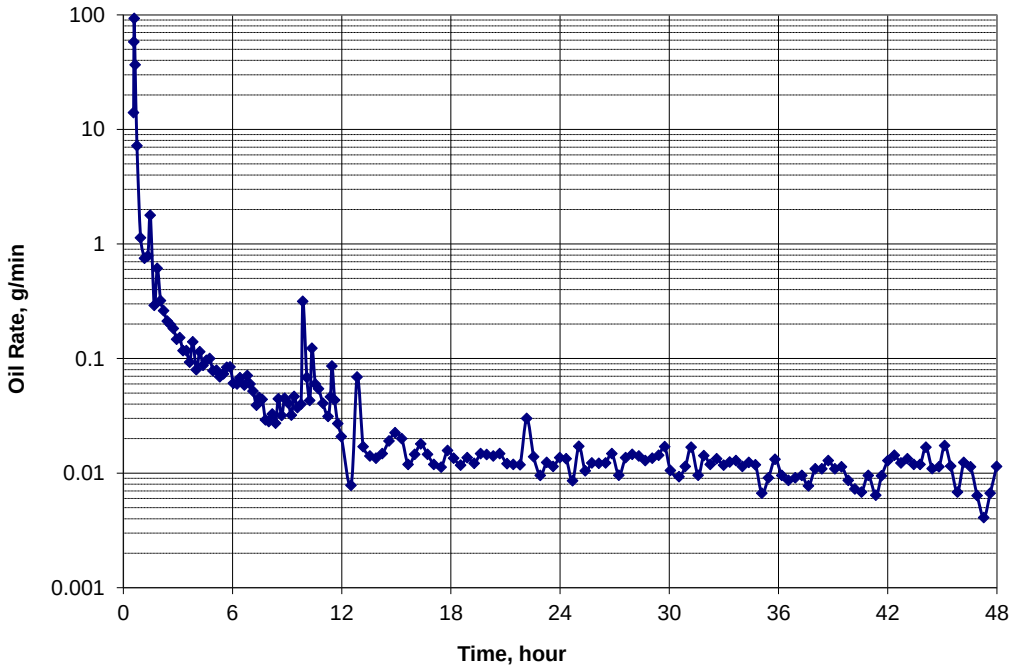

Figure 3.18. Oil rate for the steam case.

3.3.2 Steam + Solvent Case

The high recovery of the steam injection case suggests that there is little room for improvement with the addition of solvent at the same operating temperature. Solvent addition aids oil production through viscosity reduction due to solvent dissolution into the oil. However, the viscosity at such high temperatures is already sufficient for oil production minimizing the benefit of solvent addition. However, since steam-solvent processes are highly touted in literature mainly to reduce the steam requirement, I ran a case injecting a 96-4 mole% mixture of steam and n-hexane to study the process. The 40 mesh sand was used with an original oil in place of 594 g for a porosity of 30.3%. The steam-solvent mixture was injected in the 129 D sand pack at 186 °C and 160 psia. The solvent injection line was not heated. The latent heat of the water was thought to be sufficient to heat the solvent to the target temperature. However, the injection

temperature never reached the 186 °C target but rather slowly increased throughout the experiment from 176 to 181 °C. This was still sufficient temperature to ensure complete vaporization of the injected mixture (greater than 175 °C). To achieve the desired mole ratio in the vapor, steam was injected at 25 cc/min CWE and n-hexane at 8 cc/min.

Figure 3.19 is the pressure profiles for the first hour of the experiment. Again, only the outlet BPR dome pressure and the outlet pressure are recorded. The dome pressure remains at 160 psia as designed. The outlet pressure again shows the build and release cycles seen in the steam case due to plugging at the outlet. The major peak occurs from 0.42 hours (25 minutes) to 0.52 hours (31 minutes) with a subsequent peak from 0.62 hours (37 minutes) to 0.78 hours (47 minutes). After this peak, the outlet pressure stabilized around 169 psia until 1.2 hours when it jumped to 172 psia, which was the stabilized pressure for the remainder of the experiment. Figure 3.20 shows the pressure profiles for the entire experiment. The only significant features are the temporary losses of pressure that occurred during the short stop of solvent injection each time the accumulators were switched.

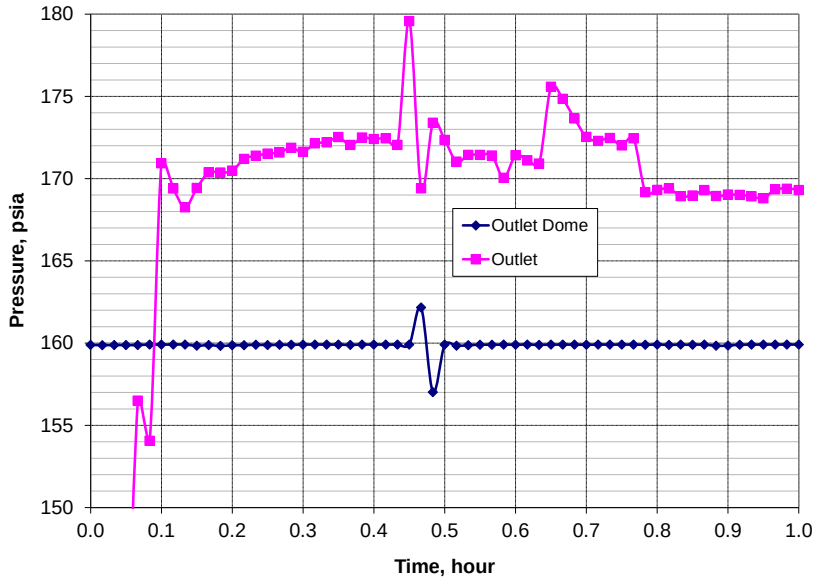

Figure 3.19. Pressure profiles for the first hour of the steam-solvent case.

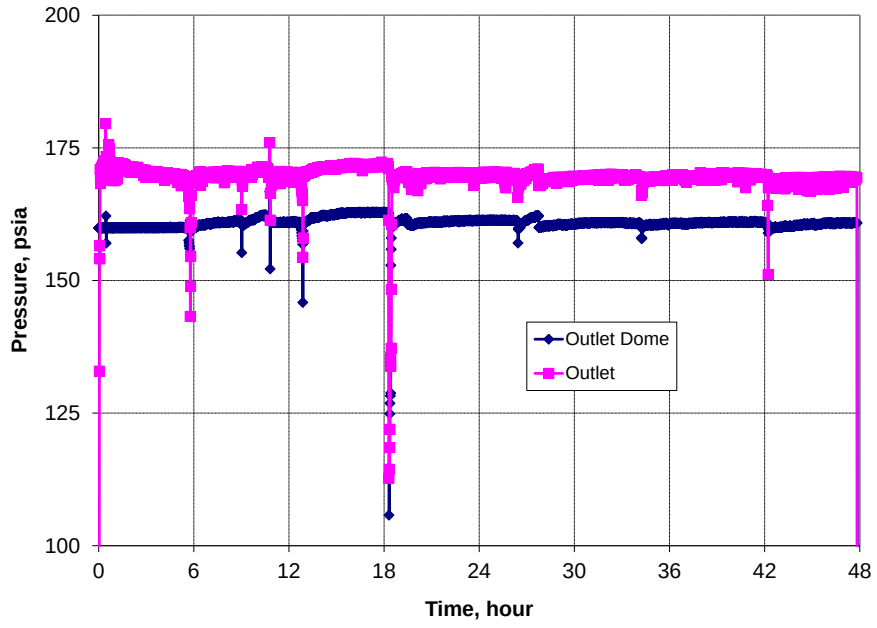

Figure 3.20. Pressure profile for the entire steam-solvent case.

Figure 3.21 shows the temperature profiles for the first hour of the experiment. The temperature measurements are at the same points as in the steam case. The heat front moves vertically downward at 3.2 cc/min. Radial propagation of the heat front proceeds at 1.39 cc/min. The values are very similar to those for the steam injection case. The slightly slower vertical rate is justifiable as some of the steam condenses to vaporize the n-hexane thus decreasing the vapor growth. The same radial rate is expected as this transfer is conduction-dominated – controlled by the thermal properties of the sand pack and oil, which are the same for both experiments. After the heat front arrives at each point, the temperature increases quickly to its stabilized value around 176 °C. The only deviation in this behavior occurs at the Annulus-Outlet data point. For this point the temperature shows some instability and plateau behavior from 0.42 hours (25 minutes) to 0.52 hours (31 minutes). This coincides with the steam arrival at the outlet and subsequent surge of oil production as the oil block was removed. Once this behavior ends, the temperature profile stabilizes and follows the same pattern as observed at the other points. Figure 3.22 shows the temperature profiles for the entire experiment. The temperatures initially stabilize around 176 °C and then start to rise around 20.5 hours to reach a final temperature of 181 °C by the end of the experiment. The sharp peaks after the initial heating period correspond to the pressure drops when solvent injection was interrupted.

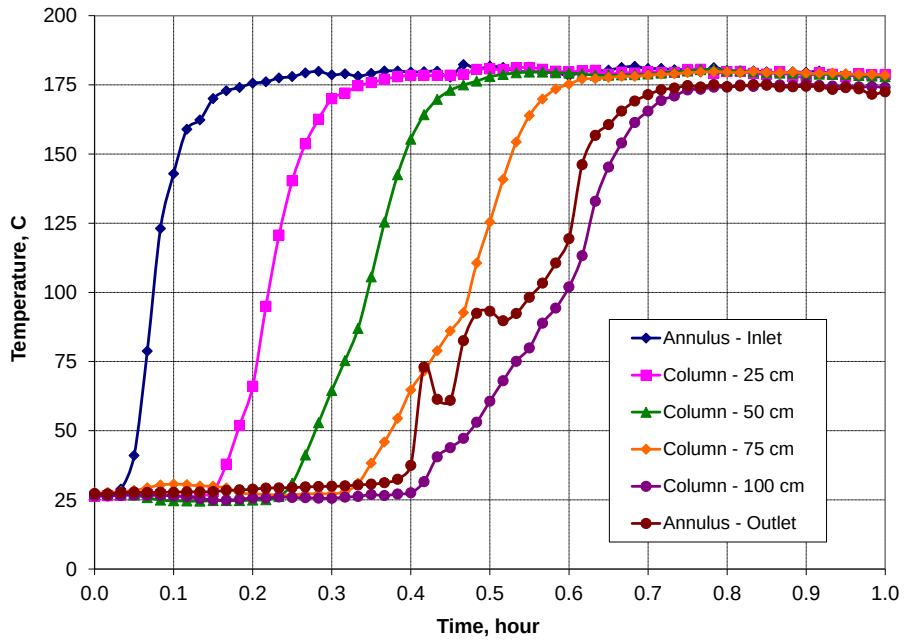

Figure 3.21. Early temperature behavior during the heating phase of the steam-solvent case.

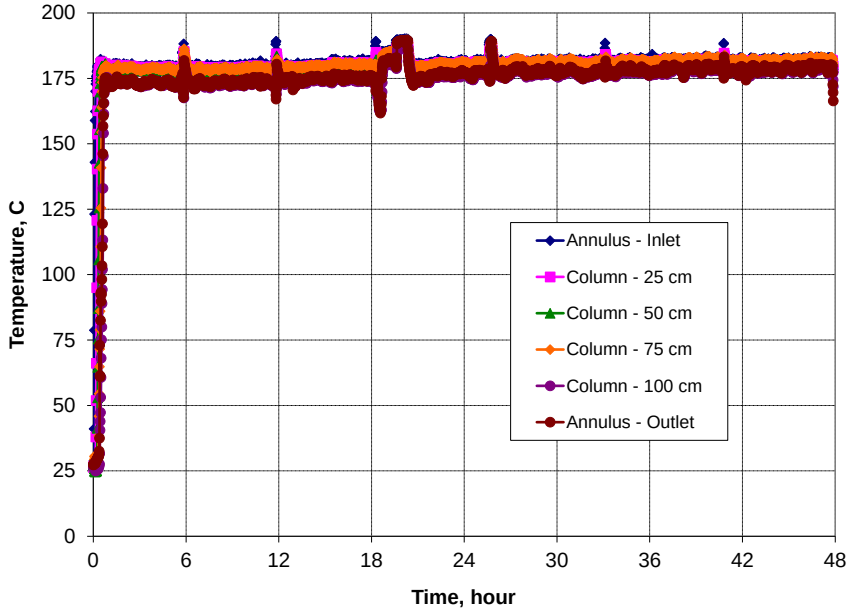

Figure 3.22. Temperature profile for the entire steam-solvent case.

Figures 3.23 and 3.24 show the cumulative oil and oil rate, respectively. Production did not occur until 0.42 hours (25 minutes). Again the production delay is caused by the outlet blockage due to cold oil drainage. The oil produced during this shut-in is produced from 0.42 (25 minutes) to 0.78 hour (47 minutes) while the outlet pressure is stabilizing as the oil block is cleared. During this period 304 g is produced, which is 43% of the total production. An additional 282 cc is produced during the next hour bringing the cumulative recovery to 586 g, 87% of the total production. Thermal expansion accounts for about 60 g of this production. The remaining 89 g are then produced over the remaining 46.25 hours of the experiment. The oil rate graph shows a brief plateau around 4 cc/min before going into decline and producing at ~0.01 cc/min for most of the experiment. The bulk gravity drainage rate at breakthrough for a steam-only process at 176 °C using Equation 3.2 would be 14.4 cc/min, assuming an oil viscosity of 10.8 cp. This value is lower than that for the steam case, which is expected since the operating temperature for this experiment is lower. However, they are still very high and leave little improvement for further viscosity reduction by solvent dissolution.

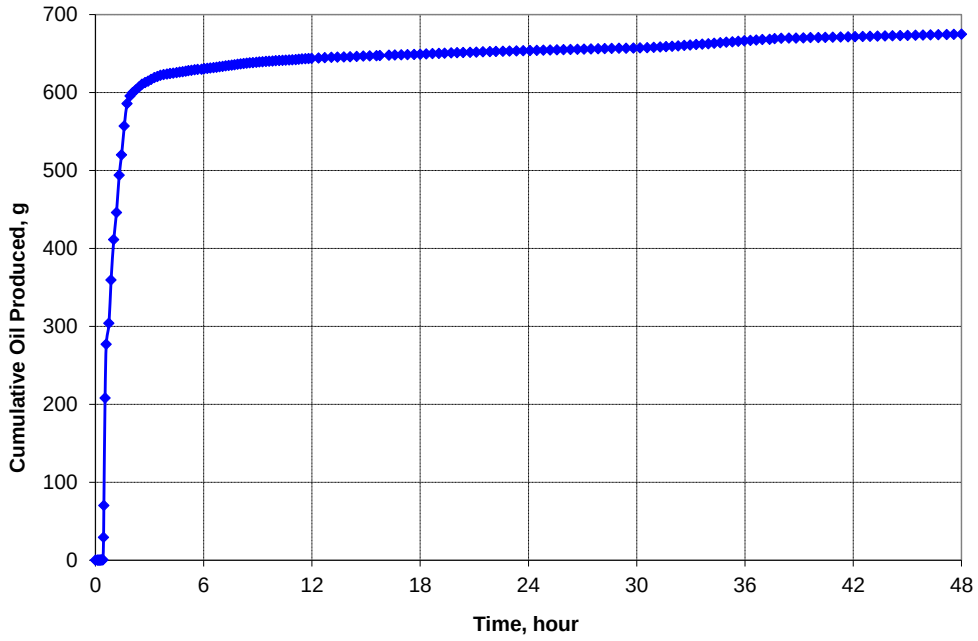

Figure 3.23. Cumulative oil production for the steam-solvent case.

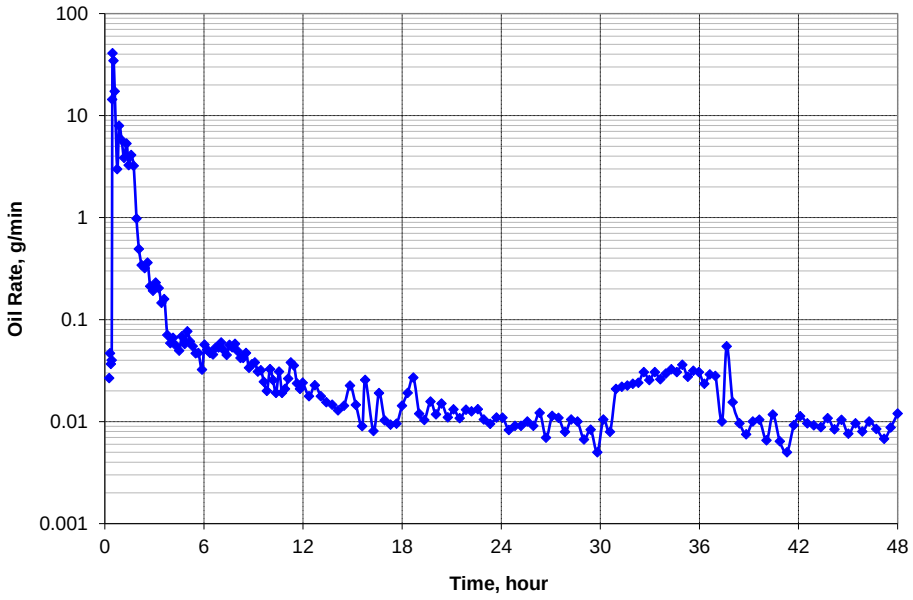

Figure 3.24. Oil rate for the steam-solvent case.

For this experiment the cumulative oil production is greater than the original oil in place. I believe that some n-hexane that remained dissolved in the oil accounts for this excess production. The separation methods for this experiment did not include hexane-oil separation. Again, the high temperature injection was very effective at producing oil. Figures 3.25 through 3.33 are photographs of select effluent collection samples. The evolution of the oil phase discussed earlier can clearly be seen as time progresses. Sample 9 in Figure 3.26 has all three oil phases. Bottom oil is not produced after sample 42 (5.67 hours - Figure 3.28). The top oil stops after sample 110 (20.77 hours – Figure 3.31) even though significant top oil production ended at sample 55 (7.88 hours – Figure 3.30). The remaining samples only have emulsion oil. The decrease in oil volume in the emulsion as time progresses manifests as an increase in opaqueness of the samples.

Figure 3.25. Samples 1 through 6 show the water production as the annulus is displaced by the steam and n-hexane injection (Start to 24 minutes).

Figure 3.26. First oil arrival at sample 8 (24 minutes to 45 minutes).

Figure 3.27. Samples 13 through 18 (45 minutes through 1 hour 35 minutes).

Figure 3.28. Samples 37 through 42 (4 hour 40 minutes through 5 hour 40 minutes).

Figure 3.29. Samples 43 through 48 (5 hour 40 minutes through 6 hour 35 minutes).

Figure 3.30. Samples 55 through 60 (7 hour 43 minutes through 8 hour 44 minutes).

Figure 3.31. Samples 108 through 113 (23 hours 35 minutes through 24 hour 50 minutes).

Figure 3.32. Samples 144 through 149 (35 hours 38 minutes through 37 hour 39 minutes).

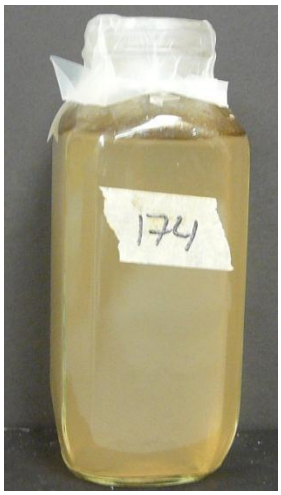

Figure 3.33. Sample 174 (48 hours).

The final graph of interest is the n-hexane production history curve (Figure 3.34). Production averages 6-8 cc/min, which is justifiable given the 8 cc/min injection rate and some retained hexane in the oil, which was not included in this calculation. These values suggest that little, if any, n-hexane was retained in the sand pack.

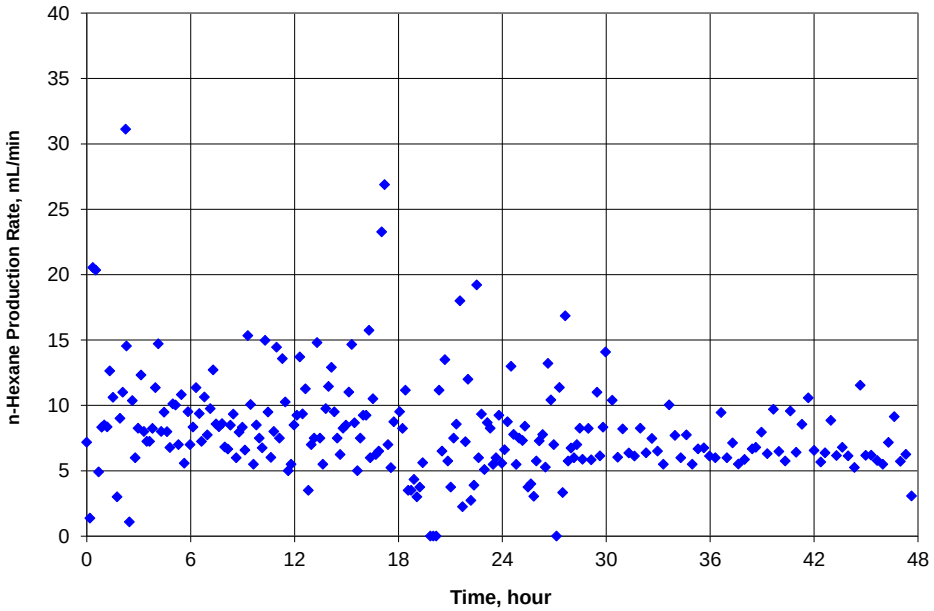

Figure 3.34. n-Hexane production suggests that little retention occurred in the sand pack.

Both the steam and steam-solvent cases have high recoveries due mostly to the reduction in oil viscosity at the higher operating temperature. The incremental reduction in oil viscosity due to hexane dissolution is minimal at high temperatures. While the addition of solvents to steam injection allows the injection temperature to be reduced without significantly sacrificing viscosity reduction, the temperature reduction is limited to the steam saturation temperature at reservoir conditions. This limits the use of steam or steam-solvent processes to high temperature operations, so other injectants must be used for low temperature operations.

3.3.3 Solvent Base Case

The remaining experiments were run to study the proposed low temperature injection strategy. The base case experiment injects butane at 60 °C and 87.0 psia into the 129 D sand pack. The 40 mesh sand pack was used with an original oil in place of

574.5 g for a porosity of 29.3%. For the first 40 minutes, butane was injected at 40 cc/min liquid rate (22 °C, 87.0 psia), which corresponds to a vapor rate of 1492 cc/min at 60 °C and 87.0 psia. Then the injection rate was decreased to 15 cc/min liquid rate (560 cc/min vapor rate). These rates correspond to 4.2 and 1.6 PV/hr (pore volume per hour). These rates were not chosen for economic efficiency. Instead the high rates were intended to minimize heat loss during the initial heating of the system and to control the mass transfer rate at the solvent-oil interface to better isolate and study each mechanism. Figure 3.35 is the pressure profiles for the first two hours of the experiment. The outlet and outlet dome pressures are in the same location as in the steam cases. The solvent line pressure is downstream of the solvent line BPR at the exit of the oven. It is however significantly upstream of the column inlet. The dome pressure remains constant throughout the experiment. As in the steam cases, the produced oil gathers in a bank between the cold water and injected solvent until solvent breakthrough at the outlet. The major difference though is that the oil bank in the solvent case contains dissolved solvent. This means that when the oil bank arrives at the outlet lines, the reduction in temperature does not impact the flow properties as much. As a result, the early pressure fluctuations are not as severe for the solvent cases. In this experiment the first pressure increase starts at 0.17 hours (10 minutes). The initial burst of oil and butane occurs at 0.41 hours (25 minutes), which releases the pressure. There are two subsequent major and one minor pressure cycles after the initial burst until the outlet becomes stabilized. Even though the pressure cycling is due to the arrival of the oil bank at the outlet, it also affects the solvent line pressure because any pressure disturbance at the outlet propagates back through the system to the solvent line BPR. The outlet pressure stabilizes at 93 psia with the solvent line at 94.5 psia (see Figure 3.36 for full pressure profiles). As mentioned earlier the solvent line pressure is significantly upstream of the column so that the difference

between the pressures should not be interpreted as a differential pressure along the length of the column. For future experiments, a pressure tap was included in the solvent injection line just upstream of the inlet cap and another in the annulus at the top of the column.

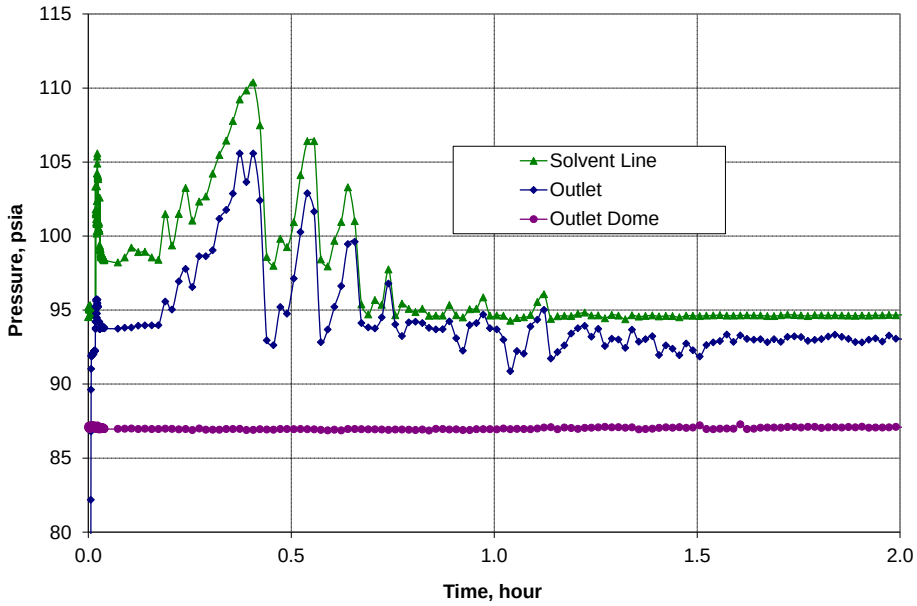

Figure 3.35. Early pressure behavior for the C4 base case experiment.

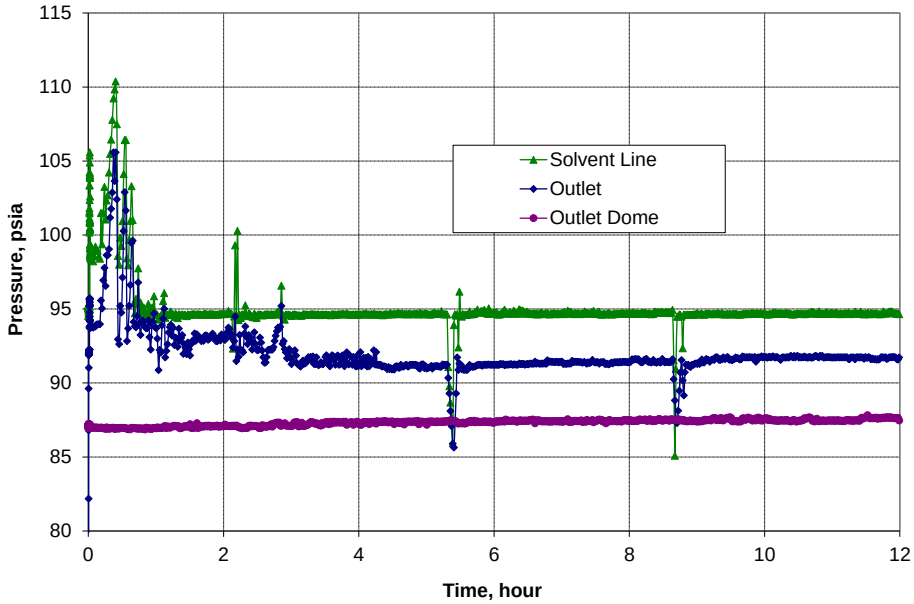

Figure 3.36. Long-term pressure profiles for the n-butane base case.

Figure 3.37 shows the temperature profile for the first hour of the experiment. The heat front moves vertically down the system at 6 cm/min. Radial propagation of the heat front proceeds at 1.39 cm/min. The vertical propagation is higher than in the steam cases because the heat loss is less significant for the low temperature solvent cases. Radial propagation is similar because the conductive properties of the system remain the same.

The n-butane phase map based on the outlet pressure and outlet-annulus temperature is overlain on Figure 3.37. Temperatures above the solid black line indicate n-butane vapor conditions at that measurement point. After the initial arrival of the heat front at a given location (sharp increase in temperature), the temperature continues to gradually increase to the steady-state temperature. This is a result of initial heat losses to the outer stainless steel column, mesh screen, and end caps. The system is enclosed in fiber-glass insulation, which minimizes heat loss and allows the system to reach

equilibrium. The transition point from the liquid extraction to the film gravity drainage production regime is indicated by the vertical dashed line in Figure 3.37. The transition is defined as the time at which the entire sand pack has reached vapor conditions. Therefore, this experiment is under liquid extraction for the first 0.47 hours (28 minutes). The annulus conditions are still at liquid conditions, but this does not impact the dominant production mechanism. Even when a majority of the column is at vapor conditions, the liquid extraction mechanism is dominant, which is why the transition was selected at the point when the entire column has reached vapor conditions. Once the column is under vapor conditions, the primary production mechanism is solvent-enhanced film gravity drainage.

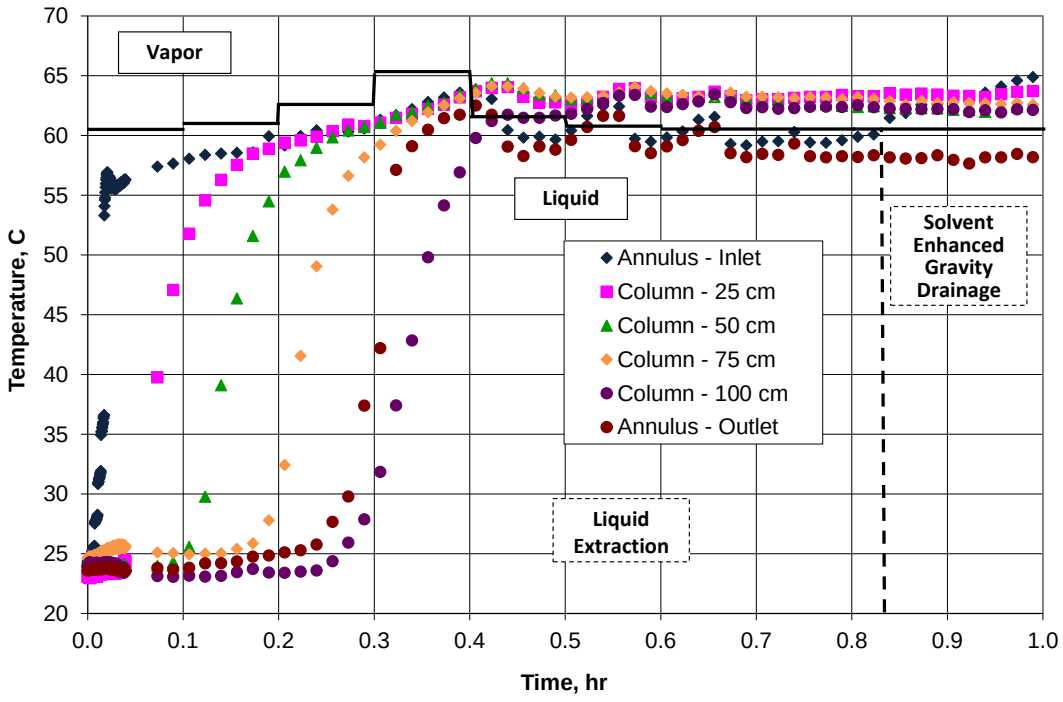

Figure 3.37. Early temperature profile overlain with the n-butane phase map with dominant production mechanisms indicated.

Figure 3.38 shows the temperature profile for the entire experiment. When the injection rate is decreased, the solvent line heating condition is kept the same. Under the same heating conditions lower rates results in high injection temperatures. This increase in injection temperature, which is not quantified for this experiment, causes the increase in temperature at the Annulus-Inlet and the Column - 25 cm measurement points. This temperature does not progress any further down the column because heat losses retard its propagation. The higher operating temperatures do not affect which production mechanism is dominant because the entire column is still vapor. They would have an impact on oil viscosity profile across the column, which can impact oil rate.

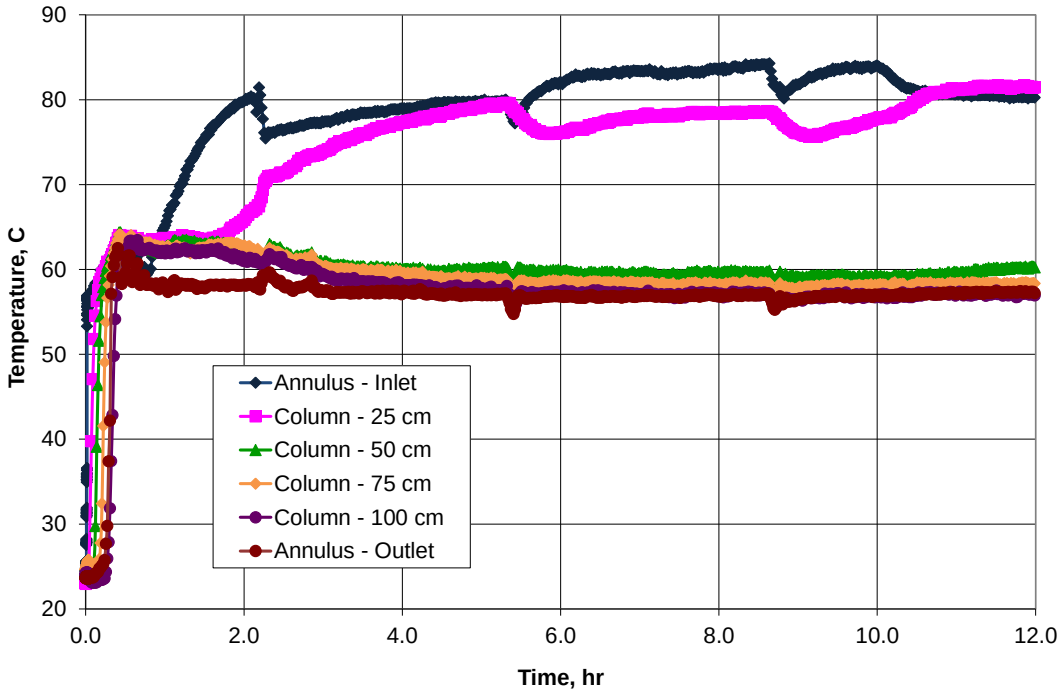

Figure 3.38. Temperature profile for the n-butane base case.

Figures 3.39 and 3.40 show the cumulative oil and oil rate, respectively. For all cases, production is show as mass or volume versus time rather than in dimensionless terms of pore volume produced versus pore volume injected because the purpose of these experiments was to study the kinetics of each solvent mechanism, typically expressed as a mass or volume per time. Production did not occur until 0.22 hours (13 minutes). This is due to the outlet line blocking discussed earlier. As a result, all of the oil produced from start to burst is produced in a single slug once the blockage is cleared. The cumulative oil graph can also be used to determine the transition between the phases. The slope change that occurs at 0.47 hours indicates when the system transitions from liquid extraction to gravity drainage. The much steeper slope, during the liquid extraction period indicates that it is a faster production mechanism than film gravity drainage. After 2.82 hours, essentially no more oil is produced, and the butane is just cycling through the system. There are two background effects that need to be extracted to determine the rate and cumulative production for the liquid extraction period. The two processes are thermal expansion (3.7% at 60 °C = 21.4 cc of oil) and the underlying film drainage (using the stabilized rate of 2 cc/min = 56.4 cc). Once these impacts are subtracted, total production from liquid extraction is 222 cc, which equates to 7.9 cc/min. A comparison of this rate to the film drainage rate verifies that liquid extraction is the dominant mechanism when the solvent is in the liquid phase.

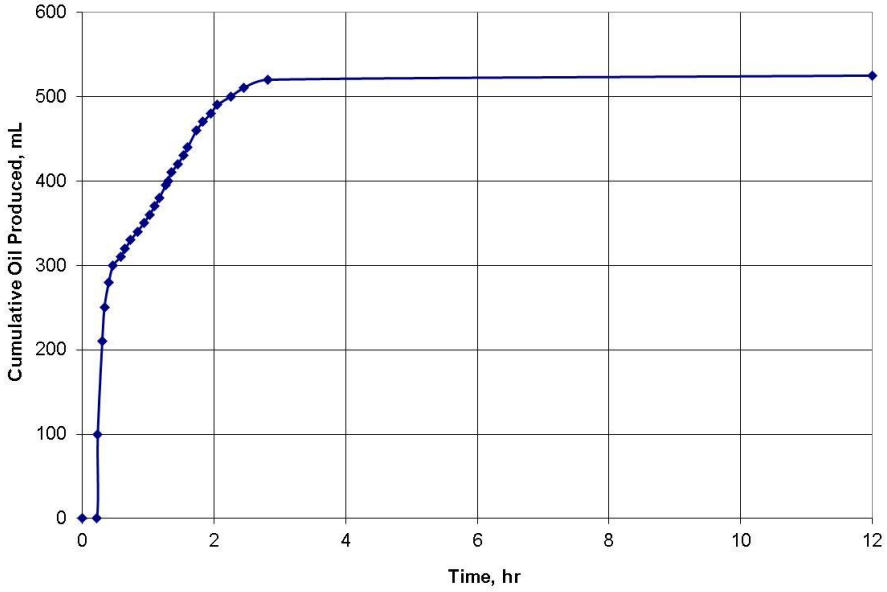

Figure 3.39. Cumulative oil recovery for the n-butane base case.

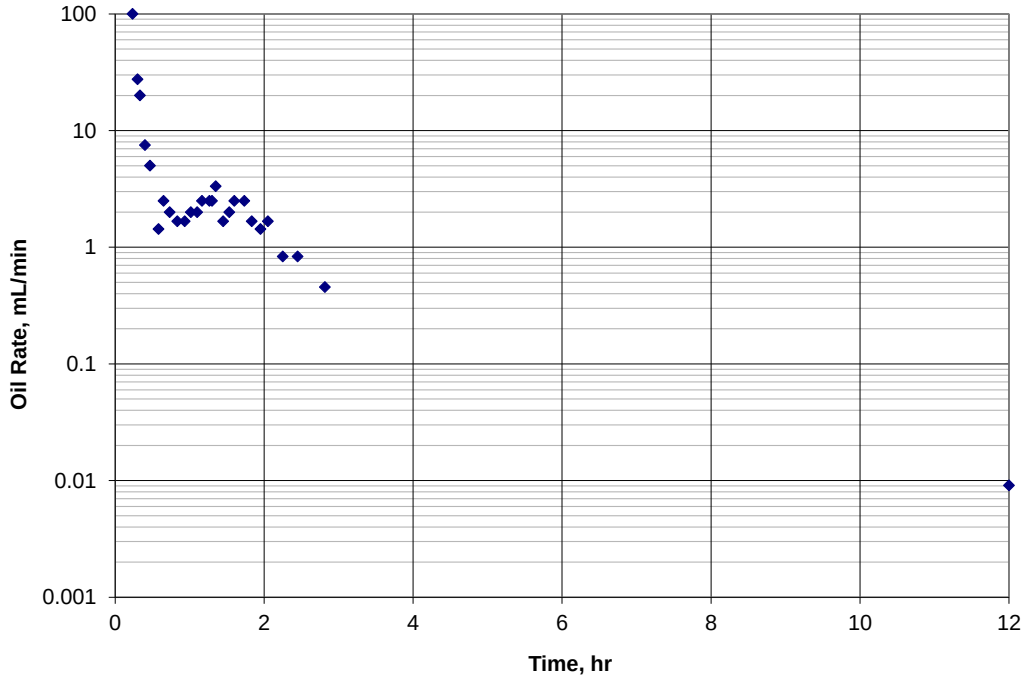

Figure 3.40. Oil rate for the n-butane base case.

Patricelli, et al (1979) developed a kinetic model for liquid extraction describing the process through two phases – a washing phase and a diffusion phase (Equation 3.3).

$$\rho_t = \rho_e - (\rho_e^w)e^{-k_w t} - (\rho_e^d)e^{-k_d t} \tag{3.3}$$

Where ρ_t = total yield

ρ_t = yield at equilibrium

ρ_e^w = yield due to the washing phase

k_w = mass transfer coefficient for washing phase

ρ_e^d = yield due to diffusion phase

k_d = mass transfer coefficient for diffusion phase

t = time

Yields can be substituted with cumulative production. The washing process is responsible for the initial steep production curve. Because of the short length that the column undergoes liquid extraction, the primary extraction process is the washing mechanism as the solvent initially washes over the sand grains. As a consequence, the early production can be matched using the first two terms in Equation 3.3. Using simple regression, the match gives a mass transfer coefficient of 0.251 min^{-1}.

The total production during film gravity drainage is 220 cc produced over 2.35 hours at an average rate of 2 cc/min. There were only 5 more cc of oil produced for the remaining 9 hours of the experiment suggesting that there is little to be gained from additional butane injection after film gravity drainage plateaus. Total production was 525 cc, which equates to 91.4% recovery at termination. The oil production mechanisms during the solvent-enhanced film gravity drainage phase are similar to those in the VAPEX process. However, whereas the VAPEX process includes bulk and film drainage, this strategy only involves film drainage. During VAPEX, the vapor solvent diffuses into the viscous oil, which generates a film of live oil draining between the bulk

viscous oil and the vapor solvent. This film has been estimated to be a few pores deep (James, Rezaei, and Chatzis 2008). The live oil begins to drain when its velocity exceeds the buoyant forces of the trapped vapor. The draining film can inhibit the diffusion of the solvent directly into the viscous oil, but enhances mixing through pore-scale drainage. However, solvent diffusion through the oil is not the limiting factor for solvent dissolution. Butane and pentane have diffusion coefficients on the order of 1e-5 to 1e-6 m^2/sec (Wen, Kantza, and Wang 2004; James and Chatzis 2004) in viscous oils, which lead to diffusion times on the order of minutes. Rather, the limiting factor is the liquid-gas equilibrium controlled by the frequency of gas molecules striking the oil surface. Only a small percentage of the molecules that strike the surface will have enough energy to penetrate. At higher temperature, more particles will have enough kinetic energy to penetrate (Chemistry 2013). This equilibrium can be describe by Henry's law, which states that the solubility of a gas in a liquid is directly proportion to the partial pressure of the gas above the liquid. More commonly, though, it is represented in numeric simulation as the k-value, the ratio of the mole fraction of vapor to the mole fraction of liquid of a specific component at a given pressure and temperature.

The final graph of importance is Figure 3.41, which shows the butane production rate at room conditions (22 °C and atmospheric pressure). Any deviation from 9444 cc/min during the first 40 minutes and 3542 cc/min for the remainder of the experiment indicates retention of the butane in the oil or set-up. The initial high rates are due to the blockage event resulting in high rate bursts of butane as the blockage cleared. The momentary drops in rate at 2.16, 5.37, and 8.81 hours were due to brief interruptions in injection during changes between accumulators. The gradual decrease after 4 hours is not indicative of retention, but rather an issue with the pump which decreased the injection

rate. There was no way to quantify the decrease. Overall, it appears that butane retention was minimal.

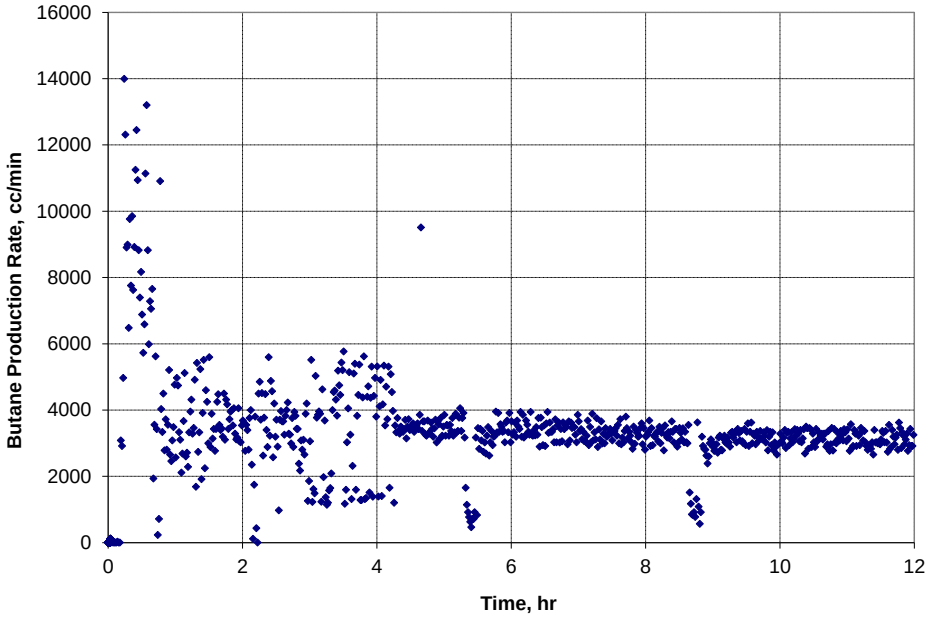

Figure 3.41. n-Butane production rate shows little retention in the n-butane base case.

3.3.4 Permeability Effect

The next experiment was designed to study the effect of permeability on each production mechanism. In the experiment, butane is injected at 60 °C and 87.0 psia into the 36 D sand pack. The 80 mesh sand was used with an original oil in place of 564.9 g for a porosity of 28.8%. Some changes were made to the solvent injection line for this and subsequent experiments. A pressure and temperature measurement point was added just upstream of the inlet cap. The solvent injection line pressure point was moved upstream of the solvent BPR. These changes allow the true injection temperature and pressure to be recorded. Also, the solvent BPR is now set at 116 psia (29 psia above the outlet pressure) to ensure that the solvent is in the vapor phase at the injection point.

Also, moving the solvent line pressure upstream of the BPR means that the measurement point is not affected by the column conditions. Finally, an inlet annulus pressure measurement point was added so that the true pressure differential along the column could be measured. For the first 40 minutes, n-butane was injected at 40 cc/min. Then the injection rate was dropped to 15 cc/min. However, at this lower rate, the system pressure began to decrease. In order to regain pressure the injection rate was increased to 25 cc/min 30 minutes after the initial rate change (70 minutes after the start of the experiment).

Figure 3.42 shows the pressure profile for the first four hours of the experiment. The new inlet and inlet annulus measurement points can be compared to the outlet pressure to see that there is essentially no pressure drop along the column. By design, the solvent line is operated 29 psia higher than the column. After 0.18 hours (11 minutes), the pressure of the column starts to increase until an initial burst occurs at 0.25 hours (15 minutes). However, the pressure rises again until the primary burst occurs at 0.50 hours (30 minutes). The pressure temporarily stabilizes at 90 psia before the injection rate was decreased leading to a loss of pressure. At 1.18 hours, the injection rate was increased to stop the pressure decline. This somewhat stabilized the system until the pressure returned to the designed operating condition of 87 psia at 2.6 hours. After the first 40 minutes, the solvent line showed fluctuating pressure with a stable pressure of 110 psia starting at 4.0 hours (see Figure 3.43 for pressure profiles for the entire experiment). At 6.0 hours, the solvent line pressure drops to around 107 psia. At 4.0 hours, there is a second temporary pressure loss at the outlet that lasts around 30 minutes but corrected itself without requiring a change in injection rate. After this the outlet pressure maintained for the remainder of the experiment.

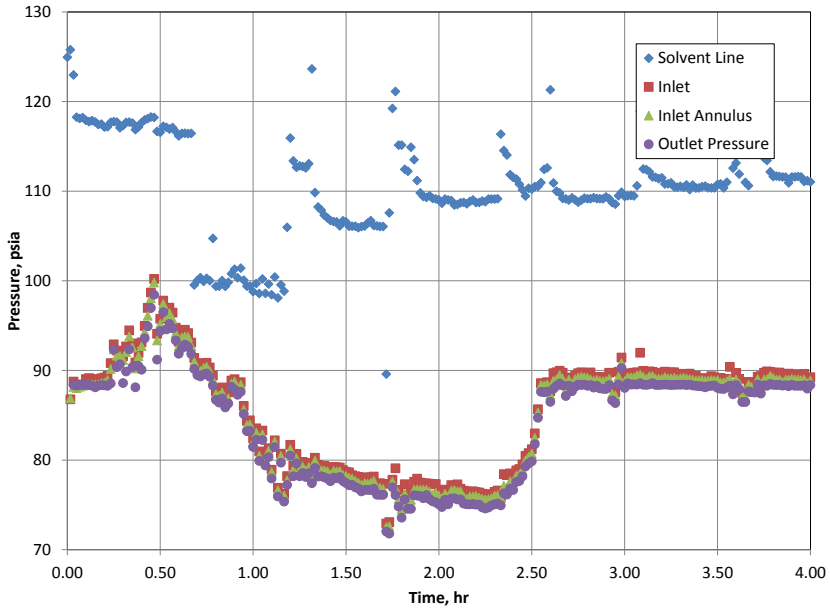

Figure 3.42. Early pressure profile for the n-butane permeability effect case (experiment two).

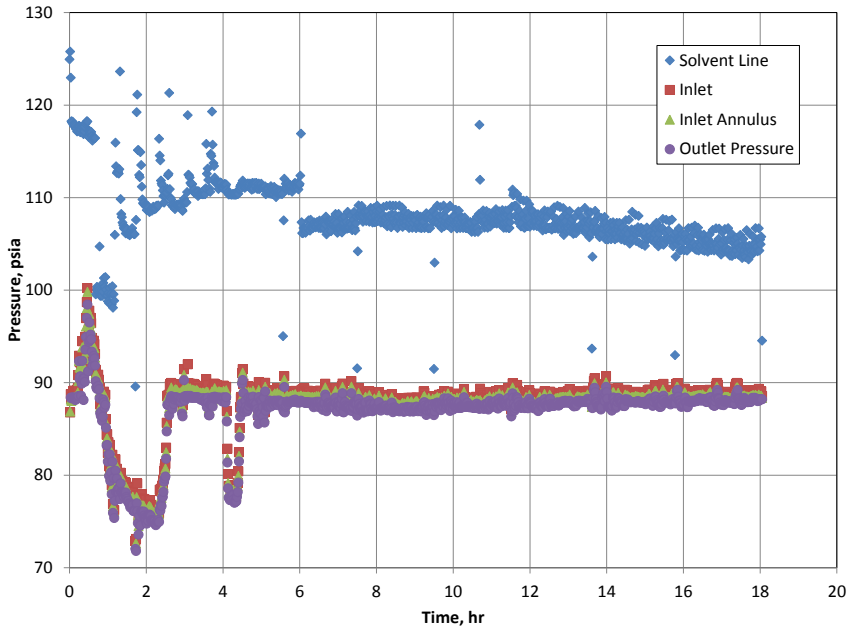

Figure 3.43. Full pressure profile for the n-butane permeability effect case (experiment two).

Figure 3.44 shows the temperature profiles for the first hour of the experiment. The heat front progresses vertically at a rate of 5.2 cc/cm. Radial propagation occurs at 1.0 cc/min. The vertical propagation is similar to the first experiment which is to be expected since the vertical propagation is controlled by the annular flow rate, which was not changed. The radial propagation is also similar. The n-butane phase map is overlain on Figure 3.44. Temperatures above the solid black line indicate vapor conditions at that measurement point. After the initial arrival of the heat front at a given location, the temperature continues to gradually increase to the steady-state temperature. This behavior is consistent with the effect of heat loss experienced in the first experiment. The transition point from liquid extraction is indicated by the dashed vertical line in Figure 3.44. For this experiment, liquid extraction occurs for the first 0.60 hours (36 minutes). After this time, the entire system is in vapor conditions, and production is dominated by film gravity drainage. Figure 3.45 shows the temperature profiles for the entire duration of the experiment. Even during the pressure loss, the system remains in the vapor state because the temperature drops with the pressure to remain at saturation conditions. The only deviation is that the temperature at the Annulus – Inlet and Column – 25 cm points increased as expected when the injection rate was decreased. Eventually, the Column – 50 cm point also felt the effect of the increased injection rate. For the other measurement points, the stabilized temperature is 58 °C. The most glaring anomaly in the temperature is that the temperature at the Column – 25 cm is greater than the Annulus – Inlet. This can be explained by heat loss. Despite our best effort at insulation, the top end cap experiences greater heat loss due to the modifications required to measure pressure and temperature at the inlet. This leads to the lower temperature despite being closer to the injection point at the top of the column.

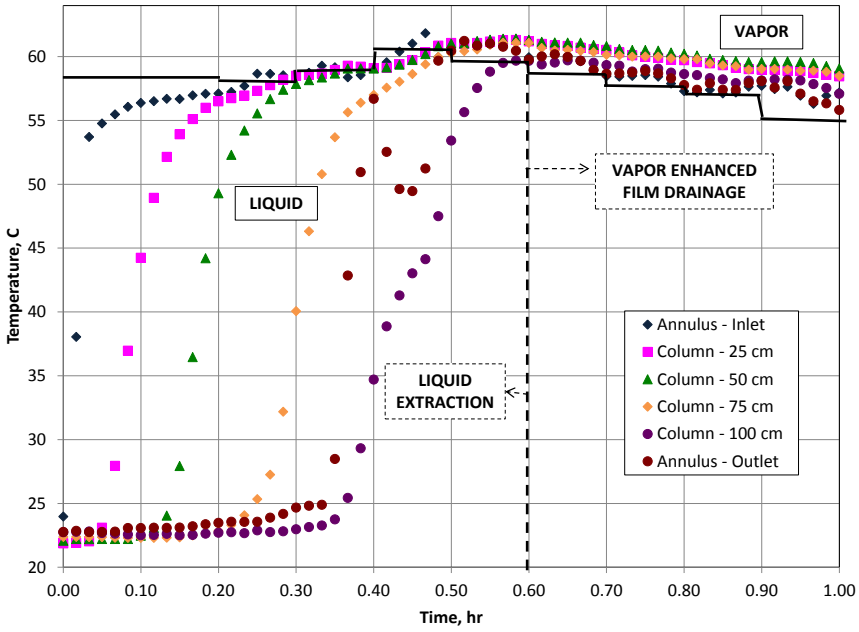

Figure 3.44. Early temperature profile overlain with the n-butane phase map with dominant production mechanisms indicated.

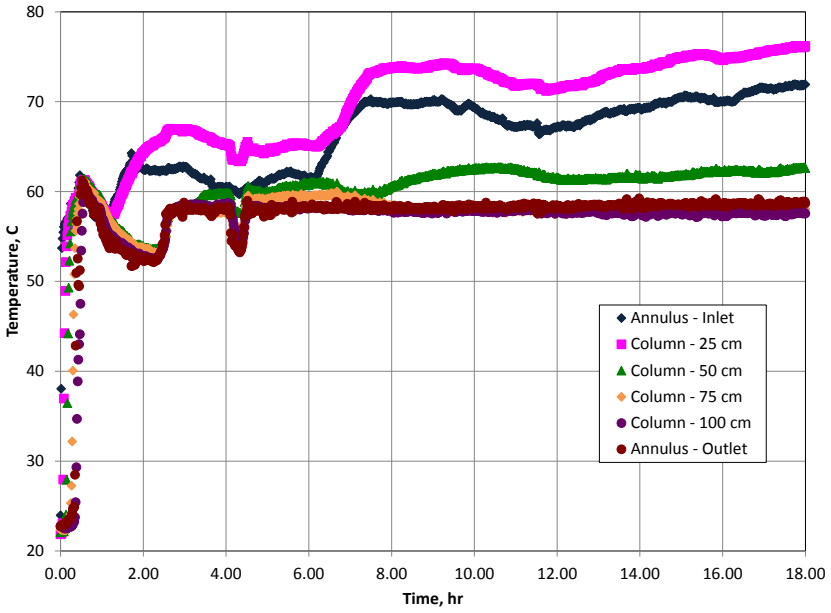

Figure 3.45. Full temperature profiles for the n-butane permeability effect case (experiment two).

Figures 3.46 and 3.47 show the cumulative oil and oil rate, respectively. Production did not occur until 0.23 hours (14 minutes), similar to the breakthrough time in the base case. Again this delay is a result of the oil bank arrival at the outlet. As a result, all of the oil is produced in a single burst. Again the change in slope indicates the transition from liquid extraction to gravity drainage, which occurs at 0.63 hours (38 minutes). The production at this point is 200 cc. Accounting for production from thermal expansion (21.1 cc) and gravity drainage (13.4 cc based on average drainage rate of 0.56 cc/min), total liquid extraction production is 165 cc for an average rate of 4.6 cc/min. Using the first two terms of Equation 3.3, this production can be matched giving a mass transfer coefficient of 0.225 min^{-1}. This value is comparable to that for the base case suggesting that permeability does not significantly impact the liquid extraction process. The total production during film gravity drainage is 260 cc over 7.72 hours, which averages as 0.56 cc/min. This is a reduction by a factor of 3.6 for film gravity drainage rate. The reduction is due to the lower permeability sand pack. Between the experiments, the permeability was reduced by a factor of 3.6. This agrees with the analytic model for gravity drainage rate (Equation 3.2) that suggests drainage rates are proportional to permeability verifying that film gravity drainage is the dominant production mechanism during the second production phase. After this period, 21 cc more were produced for the remaining 10.6 hours. The tail end of production is longer and less abrupt than the base case, which is also a function of the lower permeability. However, again, once the plateau is reached (at 11.48 hours), no significant incremental oil is gained meaning that continued butane injection is inefficient. In the end, 471 cc of oil is recovered, which is a recovery factor of 83.4%. This is eight percentage units lower than for the high permeability case, which is expected because residual oil typically increases with decreasing permeability.

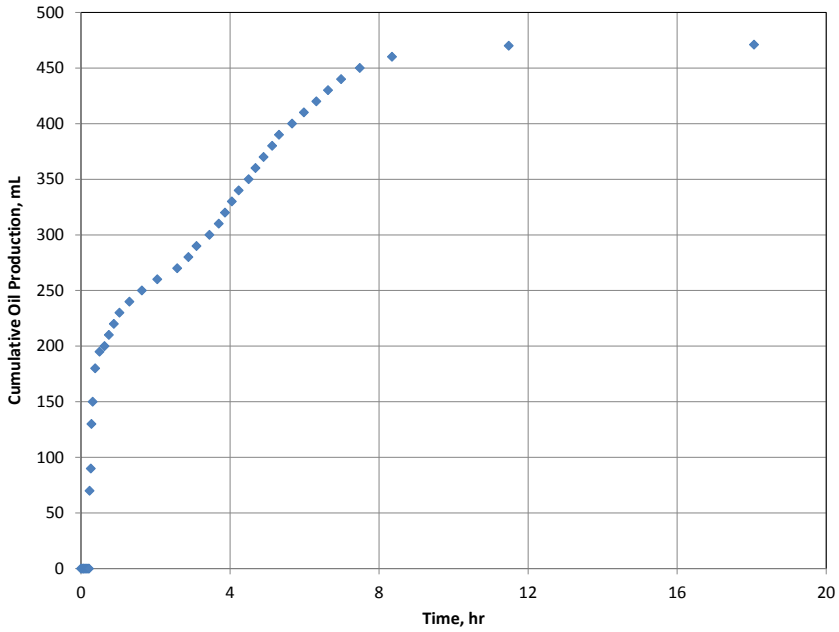

Figure 3.46. Cumulative oil production for the n-butane permeability effect case (experiment two).

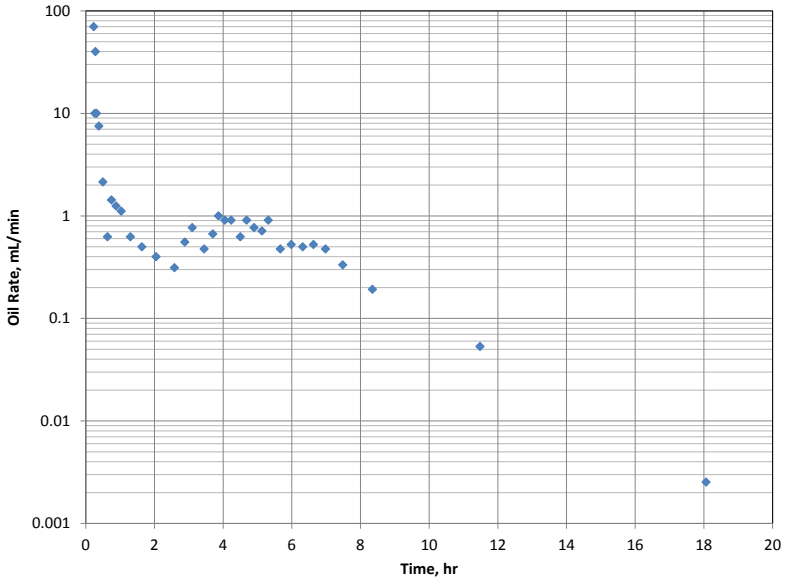

Figure 3.47. Oil rate for the n-butane permeability effect case (experiment two).

Figure 3.48 shows the butane production rate at room conditions (22 °C and atmospheric pressure). This graph is very similar to Figure 3.41 because the same injection strategy was used and permeability would have little impact on butane production. The gradual reduction in production rate beginning around 11 hours is not due to butane retention. Rather, it is a result, again, of a gradual reduction in injection rate as the percentage of air in the injection line from the pump to the solvent accumulators increased.

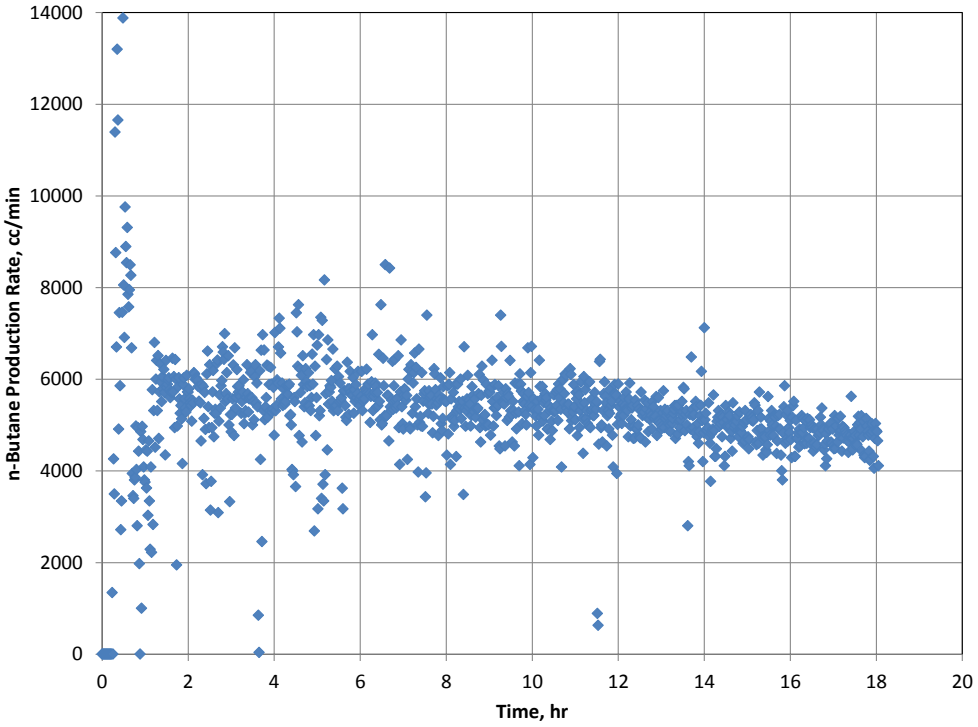

Figure 3.48. n-Butane production rate for the permeability effect case (experiment two).

3.3.5 Temperature and Rate Sensitivity

Cases three and four from Table 3.1 are discussed in this section. Both experiments are run in the 36 D sand pack at 40 °C. Case four (section 3.3.5.1) looks at

the impact of both temperature and increased in-situ injection rate. Case three (section 3.3.5.2) isolates the temperature effect.

3.3.5.1 Temperature and Rate Effect

This experiment was designed to study the effect of temperature and in-situ injection rate on the process. Change in temperature should result in a decrease in production rate for both production mechanisms. In the experiment, butane is injected at 40 °C and 52.2 psia. The decreased pressure was necessary to ensure that the system would be under vapor conditions at the reduced target temperature. The solvent line back pressure regulator dome pressure was set at 81.2 psia. Original oil in place was 576.7 g for a porosity of 29.4%. For the first 40 minutes, butane was injected at 40 cc/min. The injection rate was decreased to 25 cc/min for the next 10.5 hours and then 20 cc/min for the remainder. The decrease from 25 cc/min to 20 cc/min was required so that the refill time for the accumulators would not exceed the injection time for each accumulator. At the reduced operating pressure, these pump rates correspond to 2592 cc/min and 1620 cc/min in-situ compared to 1583 cc/min and 990 c/min in the second experiment. So in addition to the decrease in temperature compared to experiment two, this case also increased the in-situ injection rate.

Figure 3.49 shows the pressure profile for the first hour of the experiment. The first pressure increase started at 0.12 hour (7 minutes) with an initial oil burst at 0.15 hour (9 minutes). The time to burst is significantly reduced from the previous experiment, which showed the first burst at 0.25 hours (15 minutes). There were secondary bursts at 0.2, 0.32, 0.43, 0.55, and 0.68 hours (12, 19, 26, 33, and 41 minutes) before the system stabilized around 53 psia. Figure 3.50 shows the pressure profiles for the entire experiment. Throughout the experiment, there is about a 1.5 psia pressure drop across

the column. In the previous experiment, the pressure drop was only 1.0 psia. The increased pressure drop is due to the increased in-situ vapor flow rate which increases the viscous drag within the sand pack.

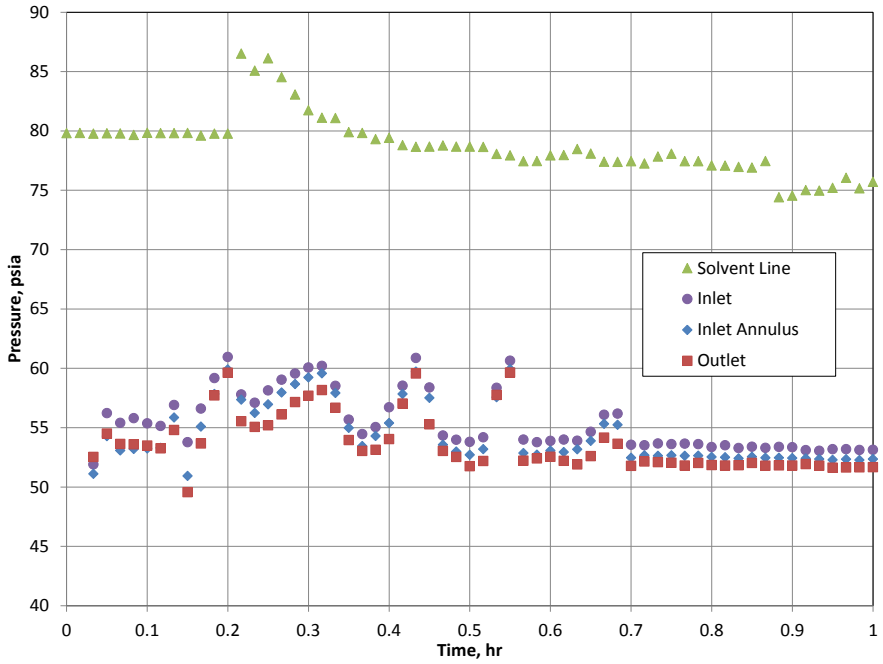

Figure 3.49. Early pressure profiles for the n-butane temperature and rate effect case (experiment four).

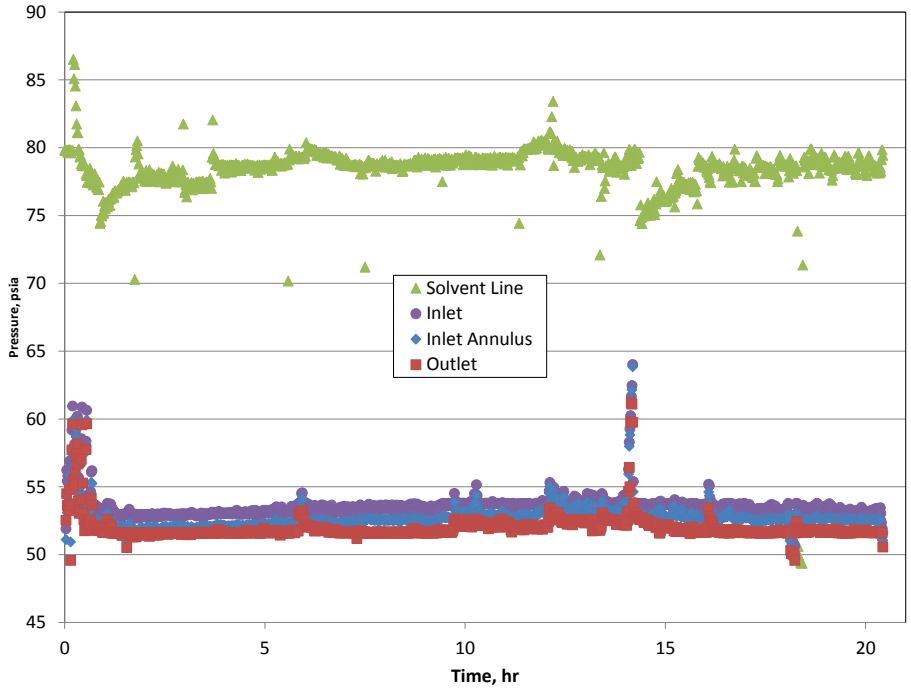

Figure 3.50. Full pressure profiles for the n-butane temperature and rate case (experiment four).

Figure 3.51 shows the temperature profiles for the first hour of the experiment. As can be calculated from the profiles, the vertical propagation of the heat front occurs at 16.67 cm/min. The radial propagation occurs at 0.83 cc/min. The radial propagation is similar to the previous experiment whereas the vertical propagation is significantly faster. This is a result of the much higher in-situ injection rate. The vertical propagation is controlled primarily by convection in the annulus, which would be impacted by increased vapor rate. So a faster rate is expected at the lower pressure. However, radial propagation is dominated by conduction, which would not significantly be affected by a change in injection rate. The n-butane phase map is overlain on Figure 3.51. Temperatures above the solid horizontal line represent the vapor phase. Again, the temperature at each measurement point experiences a quick increase at arrival and then

gradual increase as heat loss reaches equilibrium. A secondary effect of the higher vertical heat propagation is that the heat front arrives at the outlet in the annulus when it is only at 50 cm in the sand pack. The transition point from liquid extraction is indicated by the dashed vertical line in the figure. For this experiment, liquid extraction occurs for only 0.25 hours (15 minutes). After this time, the entire system is exposed to gaseous n-butane, and production is dominated by film gravity drainage. Figure 3.52 shows the temperature profiles for the entire experiment. For this experiment, the increase in injected heat caused by dropping the injection rate affects all of the measurement points except those at the outlet. Again, the inlet shows a lower temperature than the column at 25 cm due to heat losses at the end cap. As the temperatures began to rise, they started to get closer to the target temperature for the second experiment than the current experiment. Because the purpose of the experiment was to study the impact of temperature, the oven temperature was decreased at 11.5 hours to reduce the supplied energy to the system and keep the temperature within an acceptable range of the target temperature. After the adjustment, the temperature stabilized.

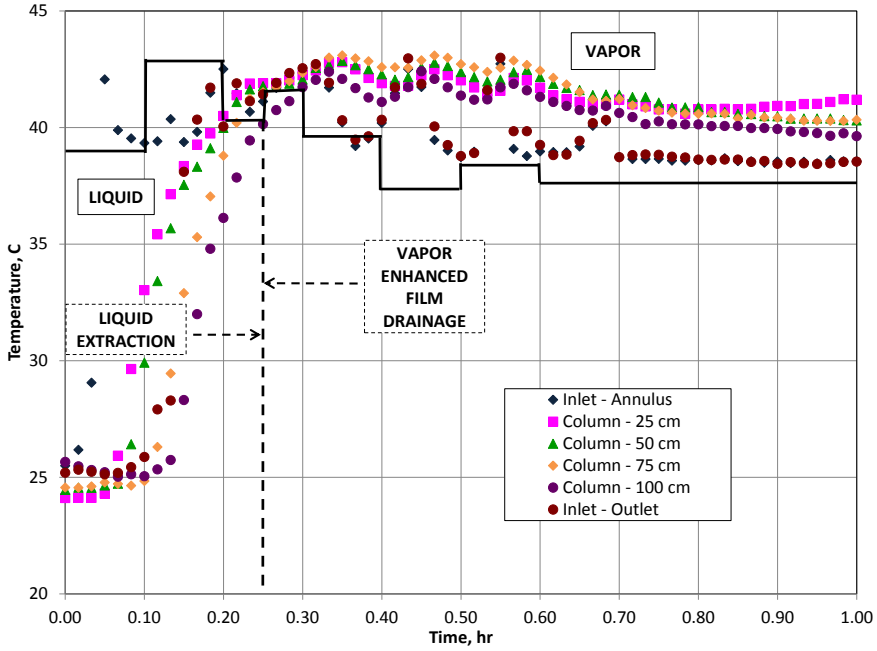

Figure 3.51. Early temperature profile overlain with the n-butane phase map with dominant production mechanisms indicated.

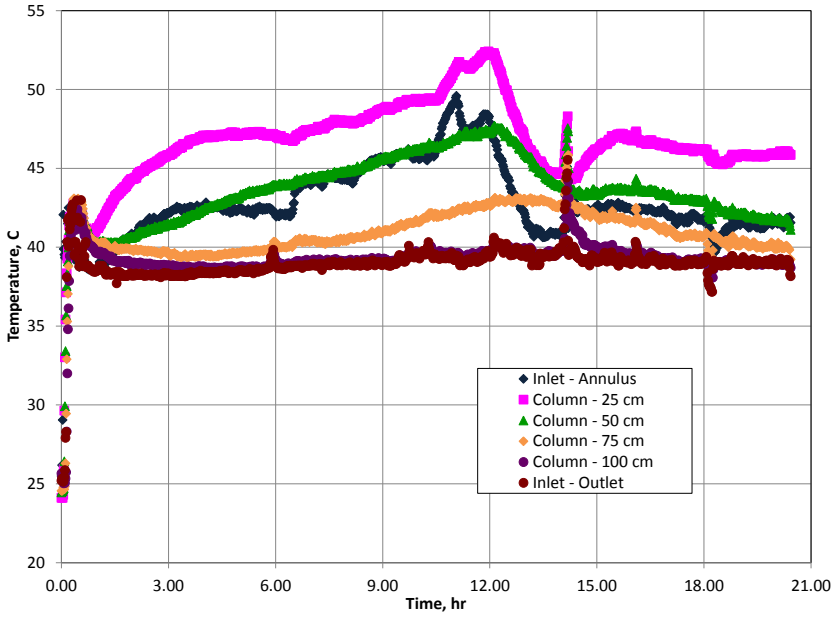

Figure 3.52. Full temperature profiles for the n-butane temperature and rate effect case (experiment four).

Figures 3.53 and 3.54 show the cumulative oil and oil rate, respectively. Production did not occur until 0.15 hours. The start of production, corresponding to the initial burst, is a function of vapor rate, so the earlier production is expected. Liquid extraction lasts for 0.25 hours (15 minutes) indicated by the slope change. Subtracting the thermal expansion production (2.3 % at 40 °C = 13.1 cc) and gravity drainage (5.9 cc), total liquid extraction is 156 cc. This is an average production rate of 10.4 cc/min. The production data can be matched using Equation 3.3 to produce a mass transfer coefficient of 1.415 min^{-1}. This value is an order of magnitude higher than that for the base (experiment one) and permeability sensitivity (experiment two) cases. The higher in-situ butane rates lead to faster replenishment of pure butane at the solvent-oil interface resulting in higher concentration gradients in the solvent rich phase at the interface enhancing the liquid extraction process. While the solvation kinetics should be decreased at the lower temperature, the impact of the higher rate was more significant leading to an overall improvement of the process.

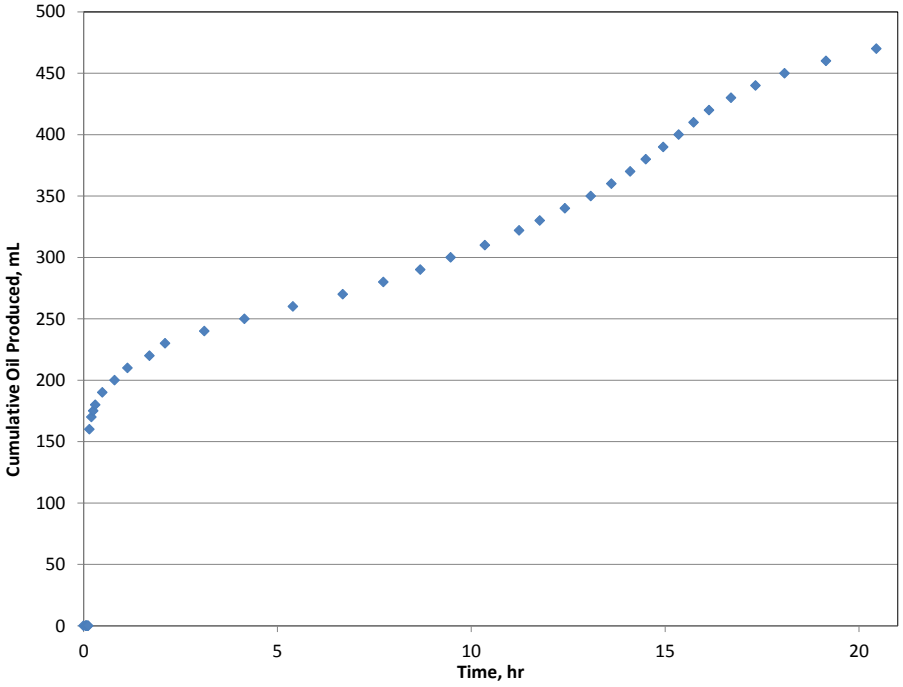

Figure 3.53. Cumulative oil recovery for the n-butane temperature and rate effect case (experiment four).

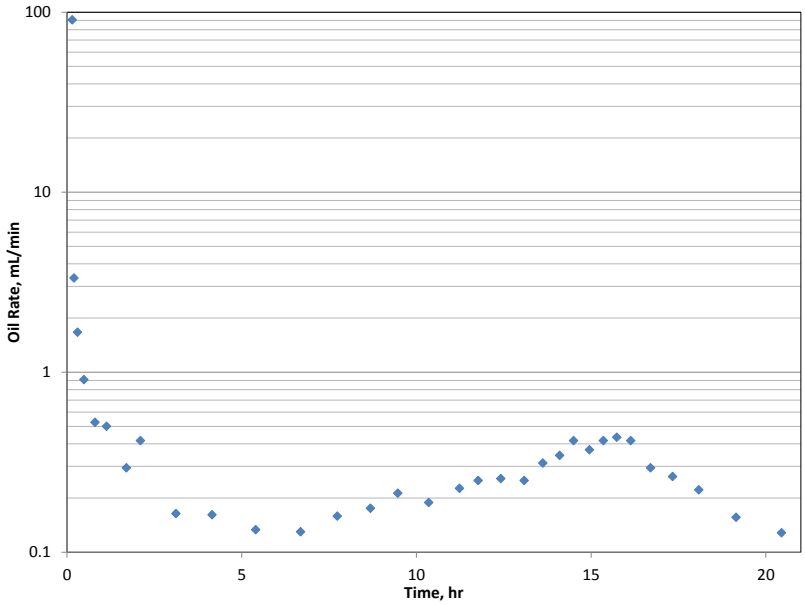

Figure 3.54. Oil rate for the n-butane temperature and rate effect case (experiment four).

This conclusion is supported by Meziane and Kadi (2008) who discuss the effect of both concentration gradient and temperature on the liquid extraction process. They studied the kinetics of oil extraction from olive cake by using 96% ethanol. The amount of oil extracted increased with the solvent-to-solids ratio, which is expected because increased ratios mean larger concentration gradients at the oil-ethanol interface. The increase in driving force manifested as an increase in the mass transfer coefficient for each stage of production. For the three ratios studied, the relationship between mass transfer coefficient and solvent-to-solids ratio was linear. The increase in coefficient was most significant for the washing phase, which makes sense because increased concentration gradient would impact surface processes more. While the authors manipulated solvent-solids ratio to increase the concentration gradient, any parameter that affects the concentration gradient would have the same affect. In this experiment, the increased viscous drag at the solvent-oil interface due to the higher rates lead to faster drainage exposing fresh oil to solvent thus increasing the concentration gradient in the solvent rich phase near the interface compared to the previous experiment. The authors also studied the impact of temperature on the process from 20 to 50 °C. An increase in temperature results in an increased oil yield because higher temperatures increase the solubility and facility of diffusion of the oil while decreasing the viscosity. An increase in temperature leads to higher mass transfer coefficients for each phase. Temperature changes have a more significant effect on the diffusion properties than the concentration gradient in the solvent rich phase at the interface so the increase in mass transfer coefficient was more significant for the two diffusion phases. Because liquid extraction in my experiment is dominated by the interfacial concentration gradient affect, the impact of changing both temperature and in-situ injection rate should be dominated by the rate change.

The total production at the termination of the experiment was 470 cc. As can be seen in Figure 3.55, the production had just begun to bend over but was not in true plateau at this time. This is because the experiment had to be terminated prior to the terminal point due to a forced evacuation of the laboratory during a bomb threat. Even though it does not reflect the ultimate recovery, the recovery factor at termination was 81.5%, which is similar to the previous case suggesting decreased temperature will not significantly affect ultimate recovery, just oil rate and consequently recovery time. The data is also still useful to determine gravity drainage rate as it appears that minimal additional oil would have been produced under continued injection. The gravity drainage production was 470 cc over 20.2 hours for an average rate of 0.39 cc/min. As seen in Equation 3.2, there is no direct relationship between drainage rates and temperature. However, the impact of changing temperature is represented in the viscosity term, which is a function of temperature. The viscosity term is also a function of solvent concentration during solvent-assisted gravity drainage. Dead oil viscosity is 2148.6 and 12530 cp at 60 °C and 40 °C, respectively. Because these are solvent-free viscosities, their ratio cannot be used in comparison to the oil rate ratios. The viscosity that needs to be compared is the in-situ viscosity of the oil-solvent mixture at operating temperature. Because our effluent collection method was designed to separate the butane from the oil mixture at a different temperature than the operating temperature, I did not have the necessary viscosity measurements to confirm that the temperature effect during the second stage of production is primarily the result of gravity drainage. However, our results do follow the overall trend that oil rate decreases as temperature decreases.

Figure 3.55 shows the butane production rate at room conditions (22 °C and atmospheric pressure). As before, the change in process parameter did not appear to impact butane retention as the production is equivalent to injection with slight

deterioration as a result of increased air percentage in the injection line from pump to solvent accumulators. The sudden drop at 11.5 hours is due to the decrease in injection rate from 25 to 20 cc/min.

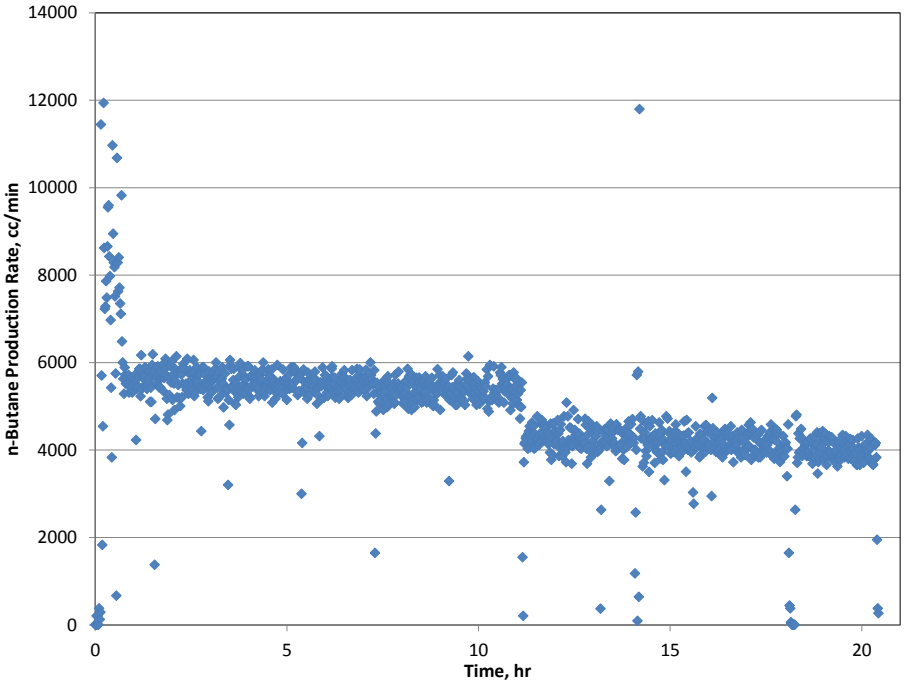

Figure 3.55. n-Butane production for the temperature and rate effect case (experiment four).

3.3.5.2 Temperature Effect

This experiment was designed to isolate the temperature effect from the rate effect. The primary effect of this change is for the analysis of the liquid extraction period. Therefore, the same parameters were used as in the previous experiment except the rates were dropped from 40 cc/min and 15 cc/min to 24.32 cc/min and 9.12 cc/min. This allows for the same vapor rate during liquid extraction as the permeability effect case (experiment two) even at the lower operating conditions (40 °C and 52.2 psia). The 36 D sand pack was used with an original oil in place of 566.5 g for a porosity of 28.9%.

For the first 40 minutes, n-butane was injected at 24.32 cc/min. Then the rate was lowered to 9.12 cc/min for the remainder of the experiment. When the first switch between solvent accumulators was made at 4.2 hours, the temperature of the system dropped from 40 °C to 32 °C. Also, at this time the production of n-butane went to essentially zero. Efforts to regain the target temperature (increasing injection rate; increasing heating of solvent injection lines) were unsuccessful. At the set operating pressure, the lower temperature results in liquid butane in the column. Therefore, the outlet dome pressure was reduced to 43.2 psia at 7.57 hours so that the column would be under vapor conditions even at the reduced temperature. The experiment was run under these conditions (32 °C and 43.2 psia) for the remainder of the experiment. The butane production did not return to normal production rates (~ 2000 cc/min) until the accumulators were switched again at 8.15 hours.

Due to a recording error with Lab View, the pressure, temperature, and butane production data were not recorded until 5.33 hours into the experiment. This unfortunately means that the early time pressure and temperature data cannot be used to determine the transition time between liquid extraction and solvent-enhanced film gravity drainage. Also, the exact pressure and temperature history at the time of the injection disturbance cannot be studied. What follows is an approximation of the early time temperature (and pressure) profile based on previous experience, memory, and production data. The initial burst of oil occurred at 0.18 hours (11 minutes). At this point the temperature at the inlet-annulus, column – 25 cm, column – 50 cm, and column – 75 cm thermocouple had all shown a sharp increase to ~ 40 °C. At the time of the first burst, the outlet-annulus temperature began to increase followed shortly by the column – 100 cm temperature. After the initial burst, the temperature at the last two thermocouples plateaued at their current temperatures until the second burst occurred at 0.22 hours (13

minutes). After this burst, the final two temperatures continued their climb to ~ 40 °C. I do not remember the pressure trends, but I can assume from previous experience that each of the bursts was preceded by a pressure increase and that after the final burst, the outlet pressure stabilized. The lack of data means that I cannot compare the pressure drop along the column to the previous experiments to determine if the same viscous drag occurred for both experiments.

Figures 3.56 and 3.57 show the temperature and pressure profiles, respectively, from 5.33 hours to the end of the experiment. The data from 5.33 to 8.50 hours is during the injection disturbance. During this time, the outlet dome and column pressure are at the original value, but the solvent line is well below the set value of 81.2 psia. Even though the dome pressure was decreased at 7.57 hours, the solvent injection line did not return to the set point until the accumulators were switched at 8.15 hours. After that switch, the column and outlet/inlet pressures stabilized. The solvent line shows a gradual decrease throughout the remainder of the experiment. The temperature profiles prior to 8.15 hours can be ignored because they just show the temperature decrease during the incident until 8.15 hours. Then, the values jump up once typical solvent injection is resumed. It should be noted that the column – 75 cm curve is missing because of a malfunction in the thermocouple. Because the column conditions had been changed, the predetermined solvent line heating design was not ideal. This is why the inlet-annulus temperature increases throughout the experiment. This increase also affects the column – 25 cm point around 29 hours. The column – 50 cm, column – 100 cm, and outlet-annulus temperatures remain relatively constant. The change in experimental parameters leads to a high variability in temperature along the length of the core.

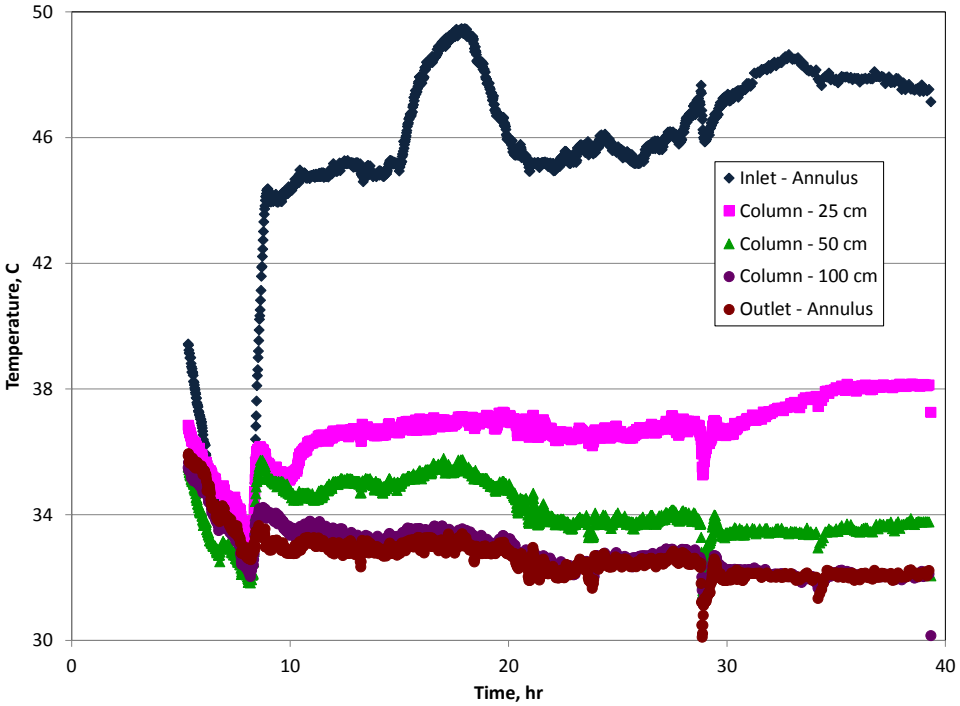

Figure 3.56. Temperature profiles for the temperature effect case (experiment three).

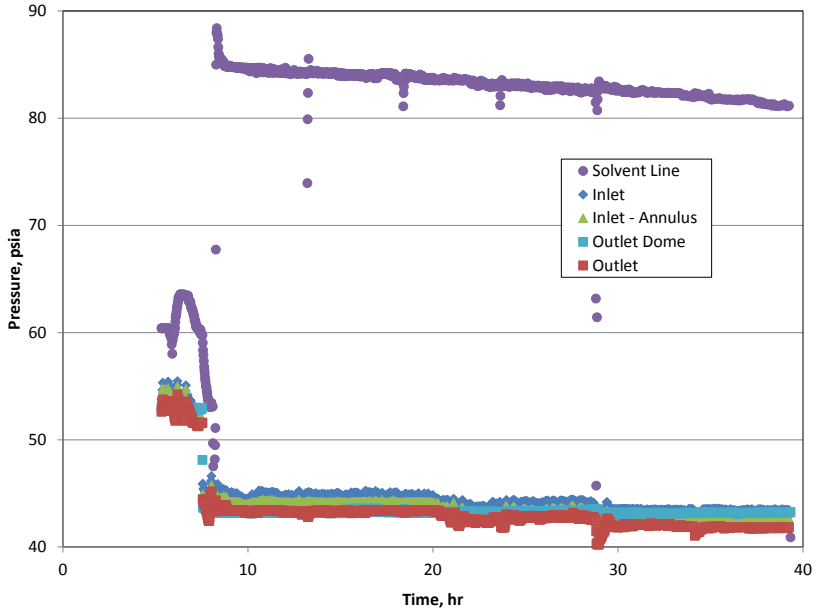

Figure 3.57. Pressure profiles for the temperature effect case (experiment three).

Figures 3.58 and 3.59 show the cumulative oil and oil rate, respectively. Production did not occur until 0.18 hours (11 minutes). This is slightly longer than in the previous case, but not as long as in the permeability effect case (experiment two) suggesting that the vertical propagation of the heat front would be more in line with the previous experiment. Even though the transition from liquid extraction to film gravity drainage cannot be determined from the temperature and pressure profiles, it can be determined from the cumulative production curve. The previous experiments have shown that the transition point coincides with the change in slope on the cumulative curve. For this experiment that occurs at 0.45 hours (29 minutes). Subtracting the thermal expansion (13.1 cc) and gravity drainage (5.67 cc from an average of 0.21 cc/min) production, the total oil produced from liquid extraction was 121.2 cc. This is a 4.5 cc/min production rate. Both the cumulative production and rate during the liquid extraction period are less than in the previous experiment. The rate is comparable to the permeability effect case (experiment two). Because I do not have the pressure profiles, I cannot claim to have removed the effect of concentration gradient entirely, but the reduced values suggest its impact was reduced. Matching the liquid extraction data with Equation 3.3 gives a mass transfer coefficient of 0.25 min^{-1}. The mass transfer coefficient is significantly reduced compared to the previous experiment suggesting that the concentration gradient in the interfacial region is the dominant effect compared to temperature. Furthermore, the value is comparable to the permeability effect case (experiment two) (0.23 min^{-1}) run at 60 °C suggesting that the solvation kinetics for this experiment are not a strong function of temperature. The similar values also suggest that the liquid extraction process will not be significantly impacted at lower temperatures. The experiment was terminated at 39.35 hours when the cumulative production curve had plateaued. The film gravity drainage period lasts from 0.45 hours to 17.35 hours. During

this time, 210 cc was produced for an average rate of 0.21 cc/min. After this time, production went into decline and produced an additional 54 cc. At termination, 404 cc had been produced which is 71.3% recovery. This is the lowest recovery achieved. This is because the operating temperature was the lowest meaning a much longer time at ever lower oil rates would be required to achieve similar recoveries to the previous cases. Assuming an average temperature of 35 °C, this equates to a dead-oil viscosity of 15689 cp. The oil rate is lower than the previous experiment, which follows the general trend of decreasing rate with decreasing temperature (increasing viscosity). The drainage rate equation proposed for the VAPEX process by Butler and Mokrys (1989 - Equation 2.6) suggests an inverse proportionality to the square-root of viscosity. While I cannot quantitatively confirm this relationship, the results do qualitatively agree. Furthermore, it is likely that our process has some difference in description from VAPEX because the process only includes film gravity drainage.

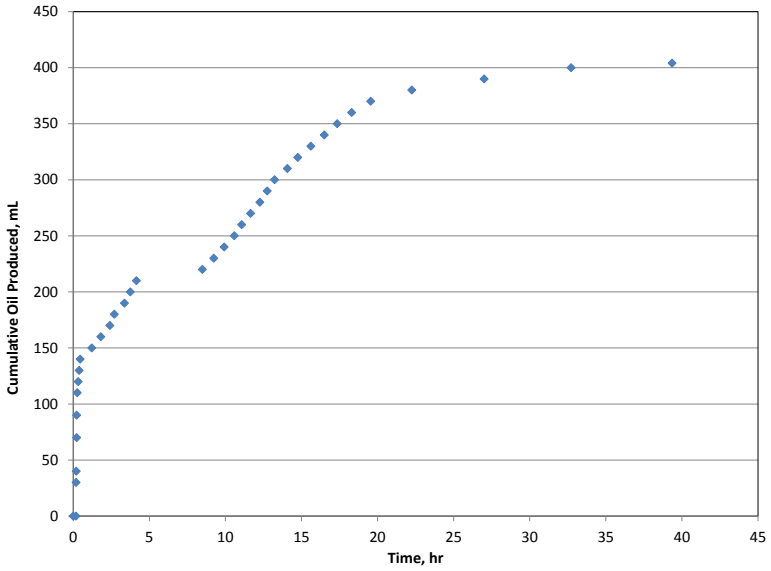

Figure 3.58. Cumulative oil production for the temperature effect case (experiment three).

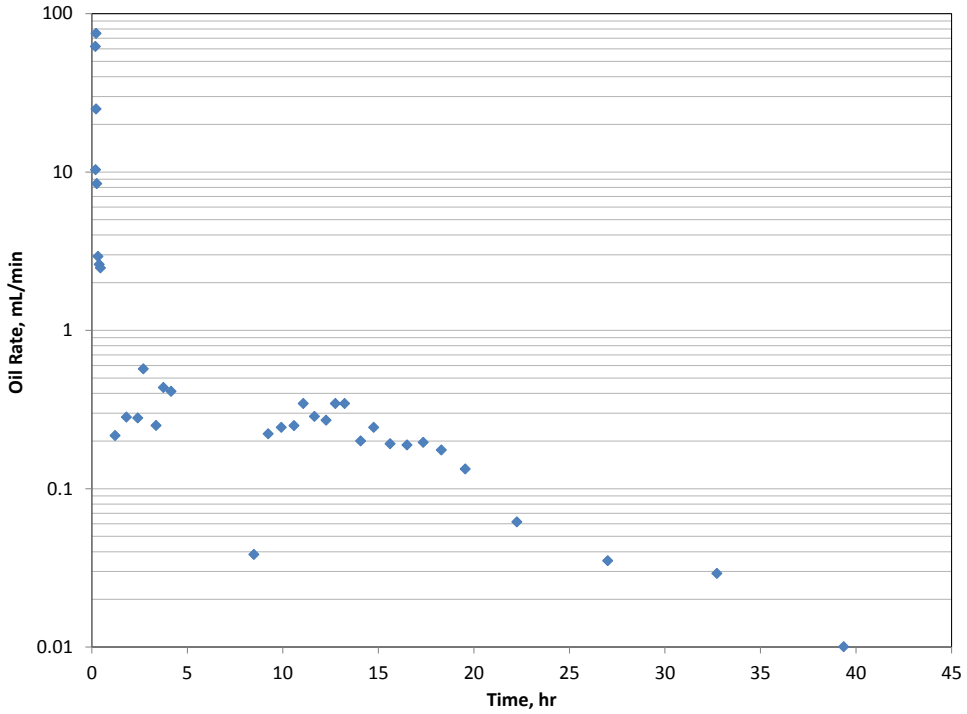

Figure 3.59. Oil rate for the temperature effect case (experiment three).

Figure 3.60 shows the butane production rate at room conditions (22 °C and atmospheric pressure). As mentioned previously, the butane rate during the injection disturbance was almost zero (~ 90 cc/min). This suggests that the incident was a result of having vapor, not liquid, butane in the accumulator. Once normal operations were resumed, the butane rate averaged ~ 2000 cc/min. There is no gradual decrease in production rate as observed in the previous experiments. This is because the air intake in the pump is only significant at higher rates. The constant rate supports our previous determination that there is no significant retention of butane in the sand pack.

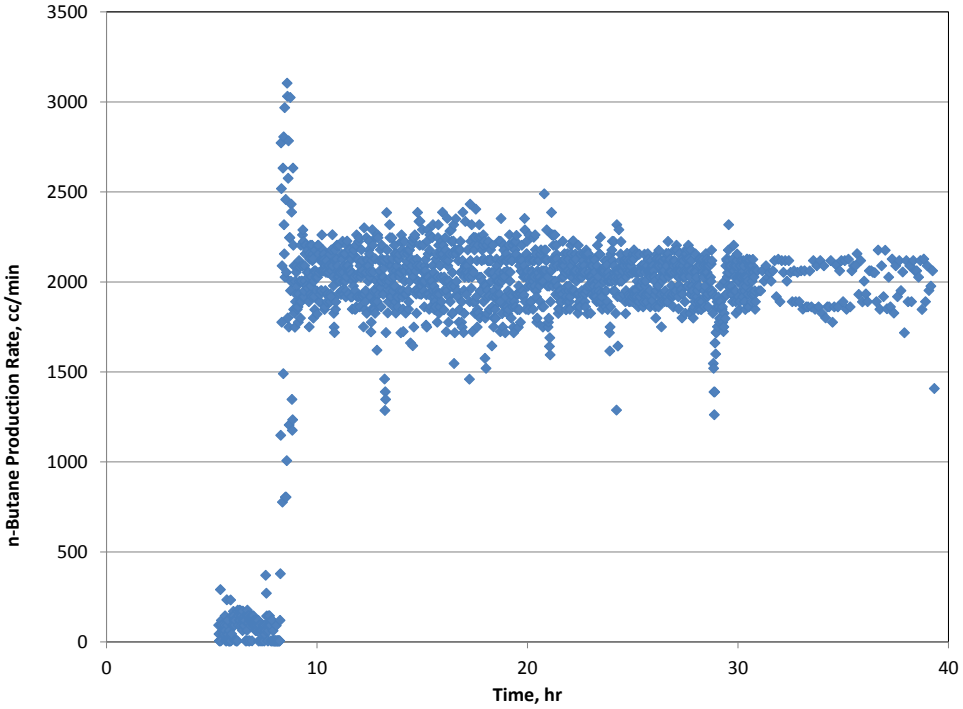

Figure 3.60. n-Butane production for the temperature effect case (experiment three)

3.3.6 Solvent Type Effect

The final experiment was designed to test the effect of solvent type on solvation kinetics. n-Pentane was injected into the 36 D sand pack with an original oil in place of 562.3 g for a porosity of 28.6%. The outlet BPR dome pressure was set at 29.0 psia. This was designed so that the pentane, injected at 60 °C, would be under vapor conditions at equilibrium conditions. The solvent line back pressure regulator was set at 58.0 psia (29.0 psia above the outlet pressure). For the first 72 minutes, pentane was injected at 40 cc/min (liquid at 58.0 psia, 22 °C). The higher injection rate was used for a longer period of time because at 40 minutes the entire system had not reached the target temperature. After 72 minutes, the injection rate was decreased to 15 cc/min for the remainder of the experiment.

Figure 3.61 shows the pressure profile for the first 1.5 hours. The first pressure build started at 0.27 hour (16 minutes) with release at 0.32 hour (19 minutes). However, immediately upon return to the original pressure, the pressure began to build again. This pattern continued to occur with longer times for each subsequent cycle. Oil breakthrough coincided with the first increase. Subsequent oil/pentane mixture bursts occurred at 0.5 and 0.9 hours (30 and 54 minutes). After the burst at 0.9 hours, the outlet pressure did not return to the original pressure; rather, it stabilized around 34 psia. Figure 3.62 shows the pressure profiles for the entire experiment. There is significant fluctuations in the inlet and inlet-annulus pressures, but the outlet remains relatively constant until 15 hours when the pressure decreases to 30 psia and then again at 18.6 hours to 29 psia. The higher pressures for the first 15 hours mean that the system is beyond the design parameters resulting in liquid conditions even after the system has reached the target temperature. The higher inlet pressure means that there is a significant pressure differential along the column (~ 7 psia).

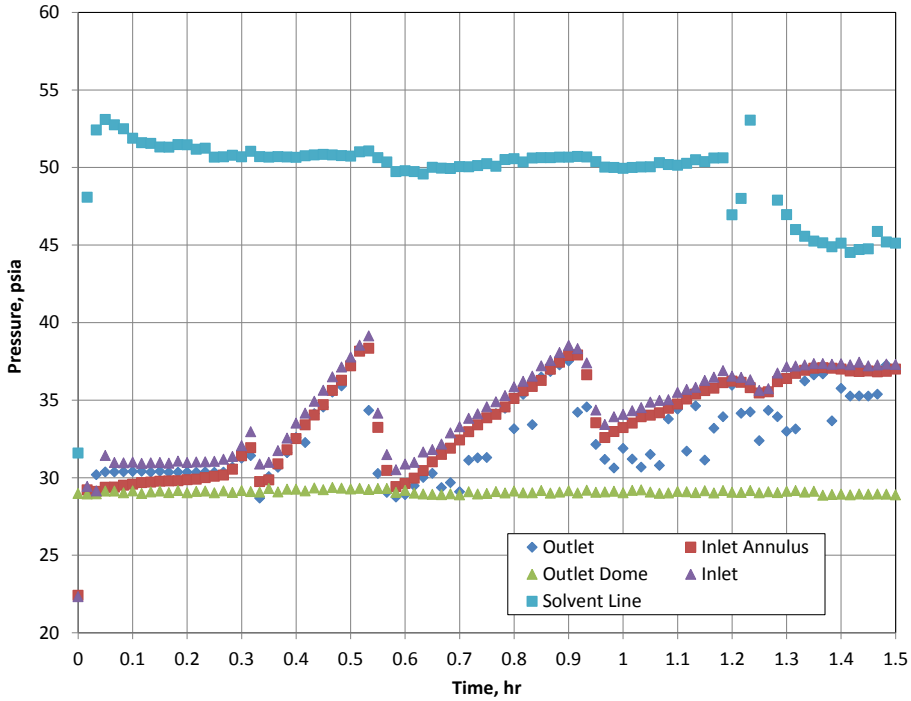

Figure 3.61. Early pressure profiles for the solvent type effect case (experiment five).

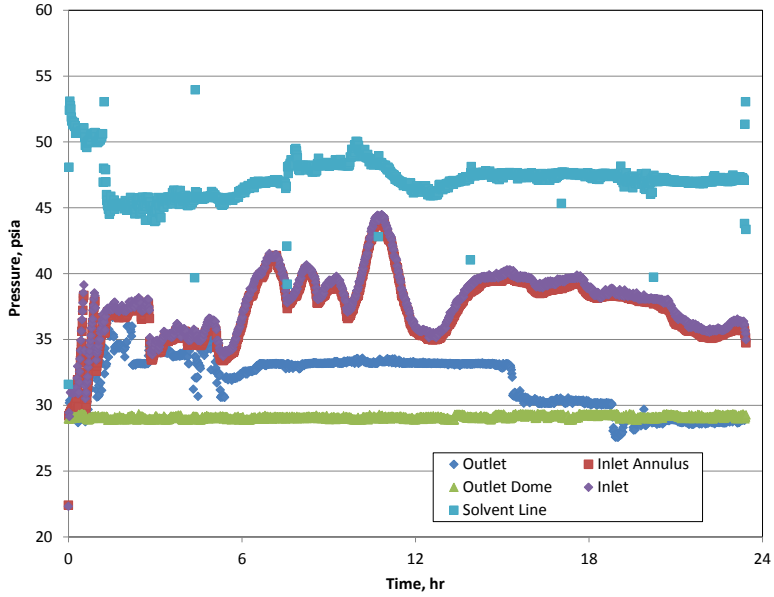

Figure 3.62. Full pressure profiles for the solvent type effect case (experiment five).

Figure 3.63 shows the temperature profiles for the first 1.5 hours. As calculated from the profiles, the vertical propagation rate is 3.1 cc/min. This is the slowest propagation of all of the cases despite the fact that the in-situ rate should have been the highest for this case. However, the pentane never vaporized, which meant it was only flowing in the liquid phase. Based on a 40 cc/min injection rate, the annular velocity of the liquid would be 4.6 cc/min. The lower observed rate is due to hold-up from the outlet blocking. The radial heat propagation is 0.83 cc/min, which is again in line with previous experiments because the conductive properties remain the same. The inlet annulus, column – 25 cm, and column – 50 cm temperature profiles were similar to previous experiments. The other points went into a low temperature plateau after initial increase before finally increasing to their stabilized temperatures. The "plateau" for column – 75 cm lasted from 0.4 to 0.55 hours (24 to 33 minutes). This coincides with first major pressure increase. During this time, no oil production occurs, which is why the temperature propagation is retarded during this period. The next plateau occurred from 0.63 to 0.9 hours (38 to 54 minutes) for the column – 100 cm and annulus – outlet points, which again coincides with a pressure increase and subsequent stop of production until the blockage was cleared. The severe pressure spikes and more significant blockages occurred because solid asphaltene was being produced along with the oil-pentane mixture, which will be discussed in more detail in the next section. After the final major blockage was cleared, the temperature profiles all reached their stable values. Figure 3.64 shows the temperature profiles for the entire experiment. In previous experiments, when the injection rate was decreased the temperature increased because the heating scenario for the solvent line was not changed. For this experiment, when the injection rate was dropped, the temperature of the oven housing the solvent line coil was decreased to maintain the target temperature at the inlet. The practice was successful as there was

no major increase in temperatures after the rate change. The only significant features in the pressure profiles were the fluctuations in the outlet – annulus and column – 100 cm from 5. 4 to 15.4 hours. These are a result of fluctuation in the column conditions. The phase behavior diagram for n-pentane is overlain on Figures 3.62 and 3.63. The vertical dashed line in Figure 3.63 indicates the transition from liquid extraction to gravity drainage at 16 hours. Normally this transition occurs when the entire system reaches the target temperature. However, since the system remained at an elevated pressure, it remained in the liquid phase until the system pressure decreased close enough to the set pressure at 16 hours to transition to the vapor phase. For the remaining seven hours, the n-pentane is in the vapor phase resulting in film gravity drainage dominated production.

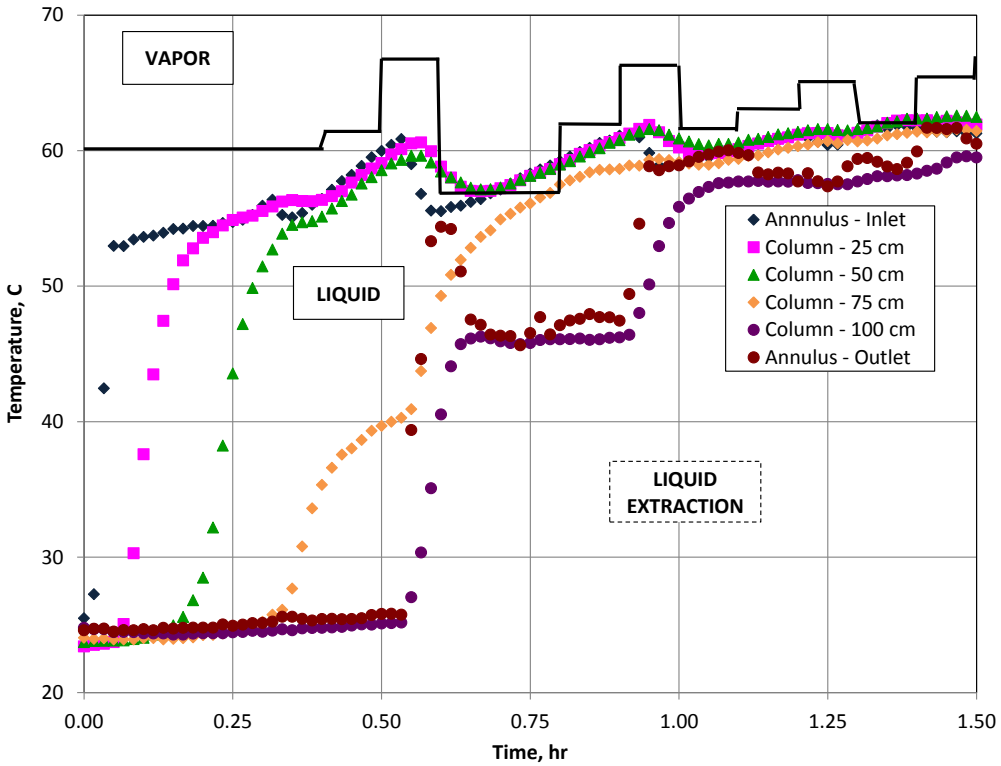

Figure 3.63. Initial heating of the system during solvent type effect case (experiment five).

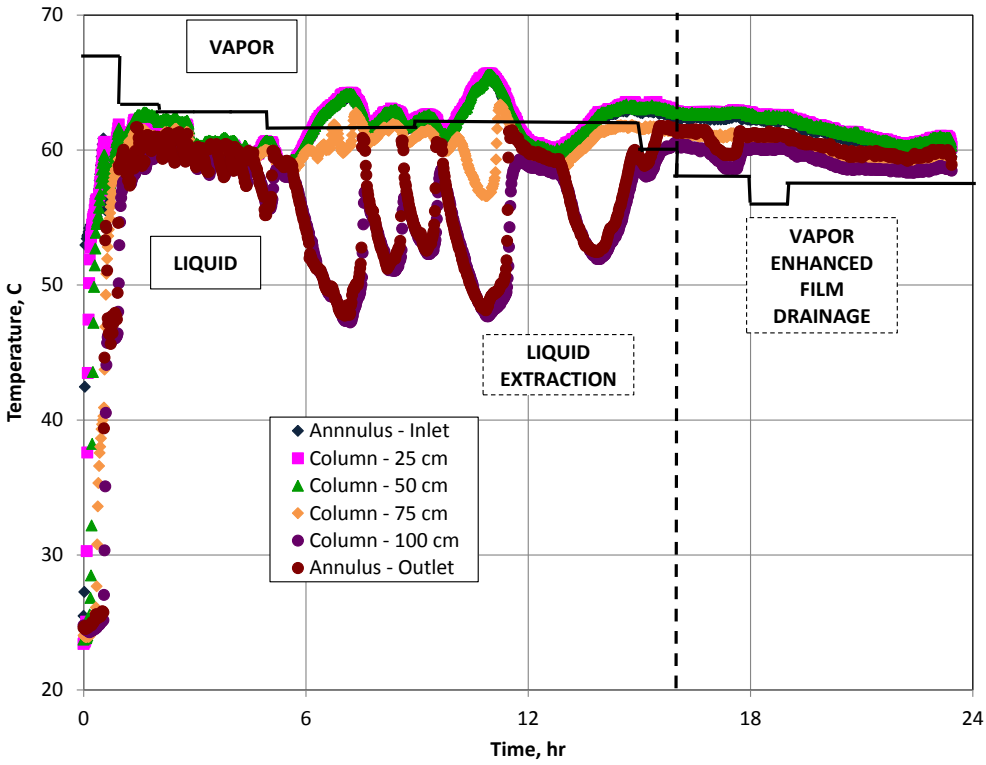

Figure 3.64. Full pressure profile and dominant production mechanisms for the solvent type effect case (experiment five).

Figures 3.65 and 3.66 show the cumulative oil and oil rate, respectively. Oil production did not occur until 0.28 hours (17 minutes). This coincides with the first breakthrough of oil and pentane. Because liquid extraction lasts beyond the initial washing phase, all the terms in Equation 3.3 can be used to match the liquid extraction process. Before matching, the thermal expansion production (21 cc) was removed. The resulting match (see Figure 3.67) gives mass transfer coefficients of .00485 min^{-1} and .0671 min^{-1} for the washing and diffusion phases, respectively. The cumulative production for each phase was 284.47 cc for washing and 127.52 cc for diffusion. The washing phase coefficient for this experiment is two orders of magnitude smaller than the

value calculated for the n-butane base case. Even though the asphaltene precipitation was more noticeable for this case, the lower mass transfer coefficients are in-line with work showing that n-butane induces more precipitation. Akbarzadeh, et al (2004) explored the onset and amount of asphaltene precipitation from Athabasca bitumen in the presence of n-alkanes including n-pentane and n-butane. Figure 3.68, from their work, shows that for a given solvent-to-bitumen ratio, dissolution of n-butane generates more precipitants than n-pentane. Also, precipitation onset occurs at a smaller ratio for n-butane than n-pentane (0.7 wt % versus 0.8 wt %). Liquid extraction accounted for 431 cc over the first 16 hours. After 16 hours, the primary production mechanism is film gravity drainage. The production during this period is 27 cc, which is 0.06 cc/min. This rate is not comparable to the average rates for the previous processes because it occurs at the tail-end of production when the previous cases had already started to reach plateau behavior on the cumulative curve. This is why no drainage rate was subtracted from the cumulative curve used to fit the liquid extraction period. Some of the production during that period was probably contributed by gravity drainage, but since it could not be quantified it was not subtracted. This is an acceptable omission because when liquid extraction is the dominant production mechanism, gravity drainage's contribution to production is probably insignificant. The production performance of the butane base case (experiment one) and this case were similar. The liquid extraction rates were 4.6 cc/min and 4.96 cc/min for the butane and pentane cases, respectively. The liquid extraction period only lasted 17 minutes for the butane case compared to 38 minutes for the initial high rate liquid extraction for the pentane case. The ultimate recovery for butane (471 cc) was higher than for pentane (458), but this is largely due to the lack of long-term solvent-enhanced film gravity drainage during the pentane case. The pentane performance shows

that the transition from liquid to vapor solvent does enhance production. Figure 3.69 shows the comparison of the cumulative oil curves for both cases.

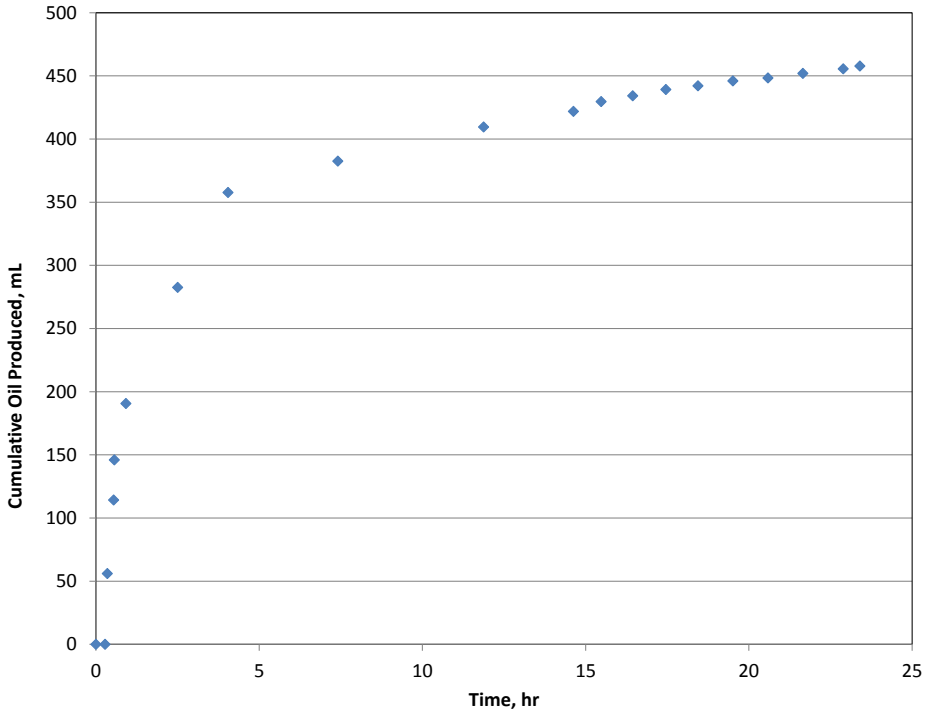

Figure 3.65. Cumulative oil production for the solvent type effect case (experiment five).

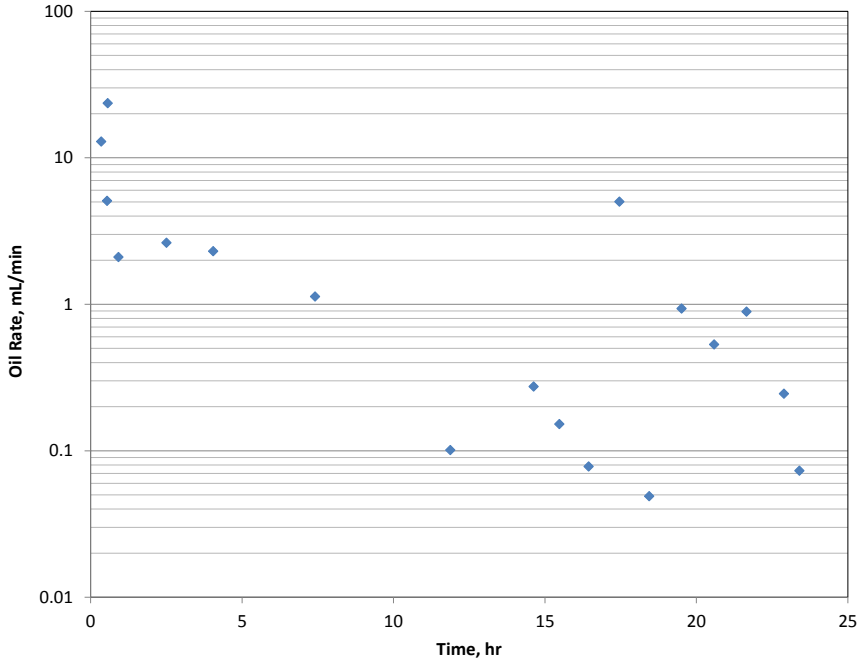

Figure 3.66. Oil rate for the solvent type effect case (experiment five).

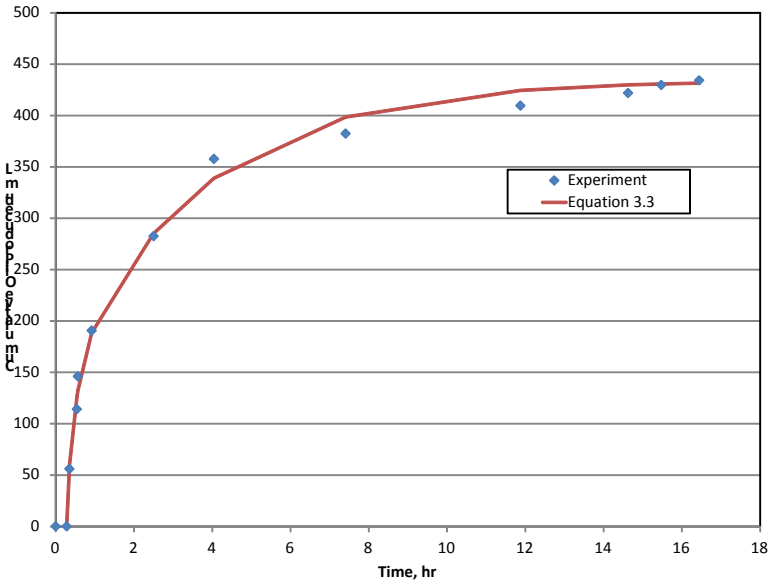

Figure 3.67. Model of liquid extraction process matches the n-pentane cumulative production data.

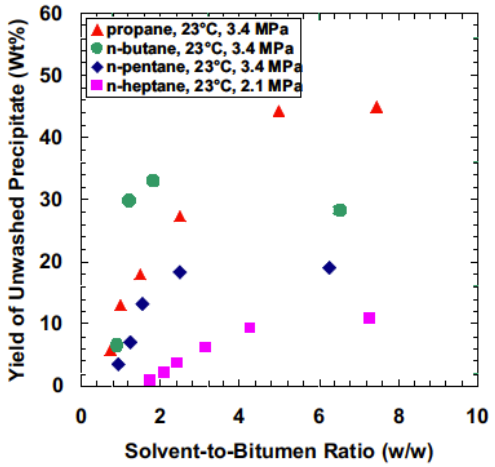

Figure 3.68. Asphaltene precipitation increases with lighter n-alkanes (Akbarzadeh, et al 2004).

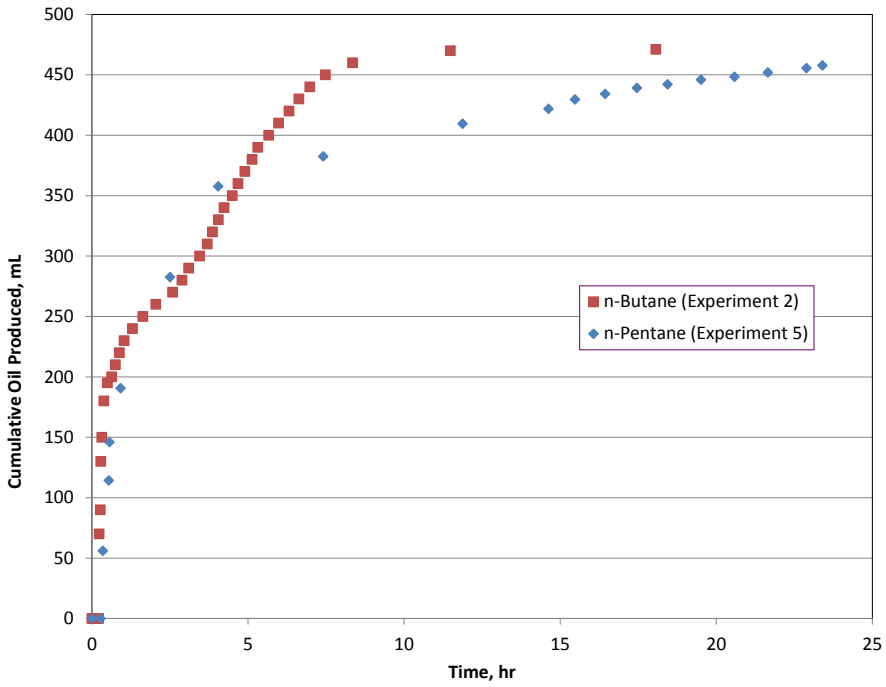

Figure 3.69. Comparison of oil production during butane and pentane injection.

Figure 3.70 shows the pentane production rate at room conditions (22 °C and atmospheric data). The data is fairly scattered, but there does seem to be a concentration around 15 cc/min until 15 hours. After 15 hours, the rate appears to drop to around 10 cc/min. This could be a sign of some later-stage pentane storage in the sand pack as the pentane fills the void space.

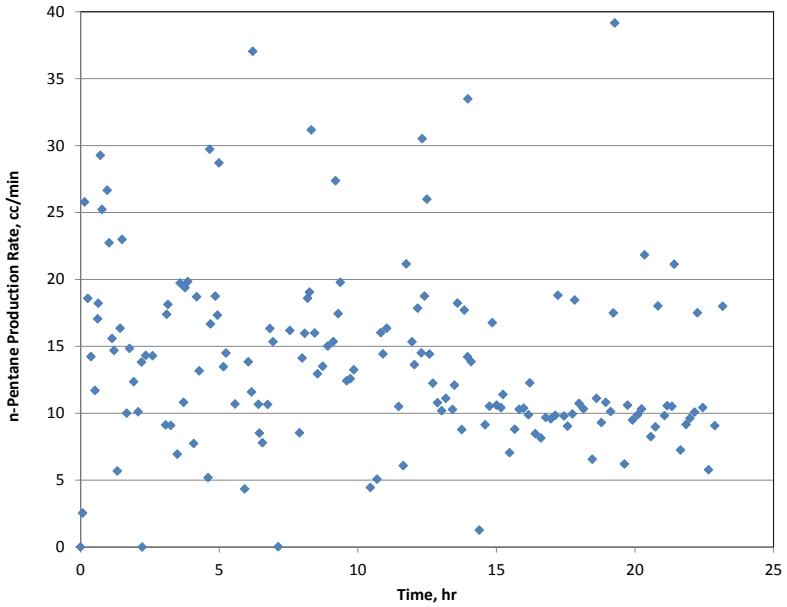

Figure 3.70. n-Pentane production for the solvent type case.

3.3.7 Residual Oil Asphaltene Content

All viscous oils have a significant fraction of asphaltenes in their make-up. The oil used in these experiments is 14.5 wt% asphaltene. In the absence of solvents, the asphaltenes are stable. When the oil is mixed with the oil, though, the asphaltene thermodynamic equilibrium is disturbed causing the asphaltenes to accumulate and form flocs. Flocculation is a double-edged sword. On the plus-side, it reduces the viscosity of the oil (often referred to as in-situ upgrading). On the down-side it can lead to

asphaltene precipitation and subsequent deposition, which can reduce permeability. It is the balance between these two occurrences that determine the net effect of asphaltene precipitation. It is widely been shown that the viscosity reduction dominated in the high-permeability packs commonly used in experimental models (Das and Butler 1994; Butler and Mokrys 1994; Cavallaro, et al 2005). However, at more realistic permeabilities comparable to field values, the permeability impairment caused by deposition negates the benefits from reduced viscosity (Lou, et al 2008; Haghighat and Maini 2008). Since our experiments were done in high permeability sand packs, I did not expect to see any permeability impairment due to asphaltene deposition even though I expected to see precipitation because the oil is exposed to a liquid solvent (Nenninger and Dunn 2008). What I did not account for was the issues caused by mobile asphaltenes in the production line.

The asphaltene content of the residual oil for each solvent experiment was calculated to determine the degree of in-situ upgrading that occurred. The residual oil was collected in four sections from the sand pack: Section 1 = 0 – 25 cm from the top, Section 2 = 26 – 50 cm, Section 3 = 51 – 75 cm, and Section 4 = 76 – 100 cm. Figures 3.71 through 3.75 are pictures of the removed sand for each experiment. The top of the column is at the top left of the photo; the bottom is at the bottom right. For all of the n-butane cases (experiments one through four), there is evidence of sequestered asphaltenes – the darker spots seen in the sand sections. The overall color of the sand can be qualitatively used to compare the residual oil saturation. The darker the sample is the higher the residual oil saturation is. The darkest samples are the two 40 °C cases (experiments three and four), which supports this qualitative analysis as they have the lowest recovery factors. It is important to not use color to compare asphaltene content as the darkest samples have the lowest asphaltene content. The n-pentane sections

(experiment five) are noticeably lighter than the n-butane cases. This is because the precipitated asphaltenes were mobile and much were either produced or trapped in a filter cake that formed on the inside wall of the mesh column. Unlike the butane cases, which required the application of heat to loosen the sand from the mesh column wall, the sand in the solvent type effect case (experiment five) was removed without the addition of heat. After sand removal, a thin filter cake of asphaltenes and sand was found coating the inner wall of the mesh screen. The filter cake could not be removed mechanically without risking damage to the screen, so its contribution to asphaltene content was not included in the analysis.

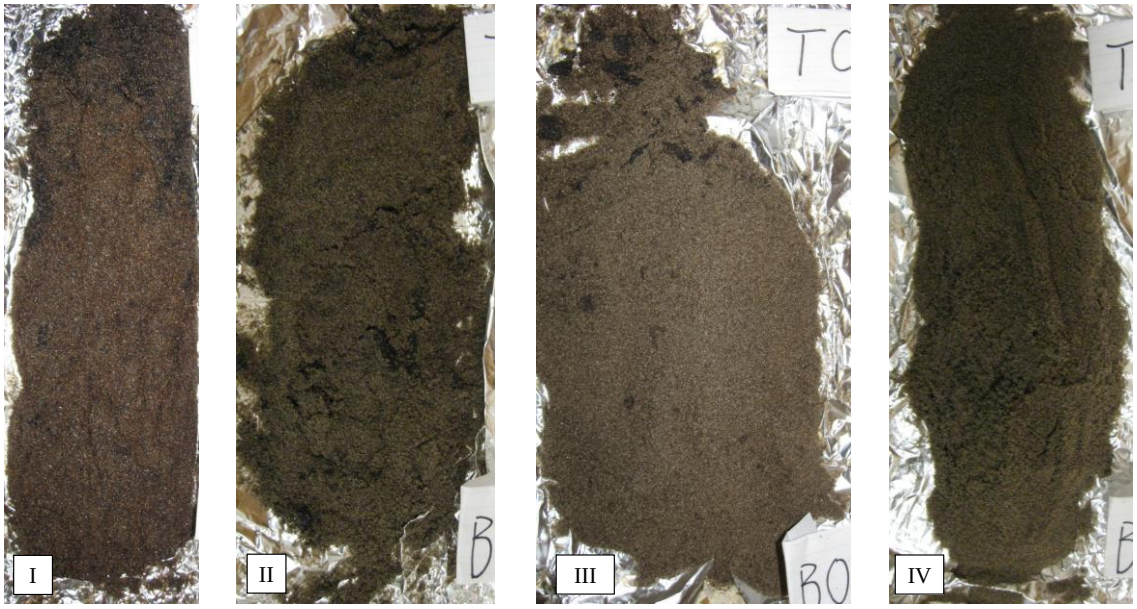

Figure 3.71. Sand pack after the base case (experiment one).

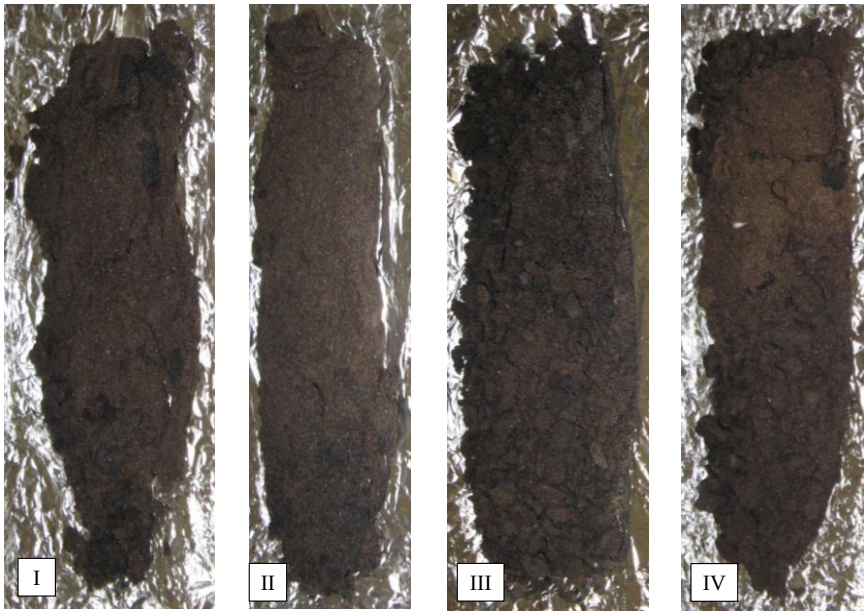

Figure 3.72. Sand pack after the permeability effect case (experiment two).

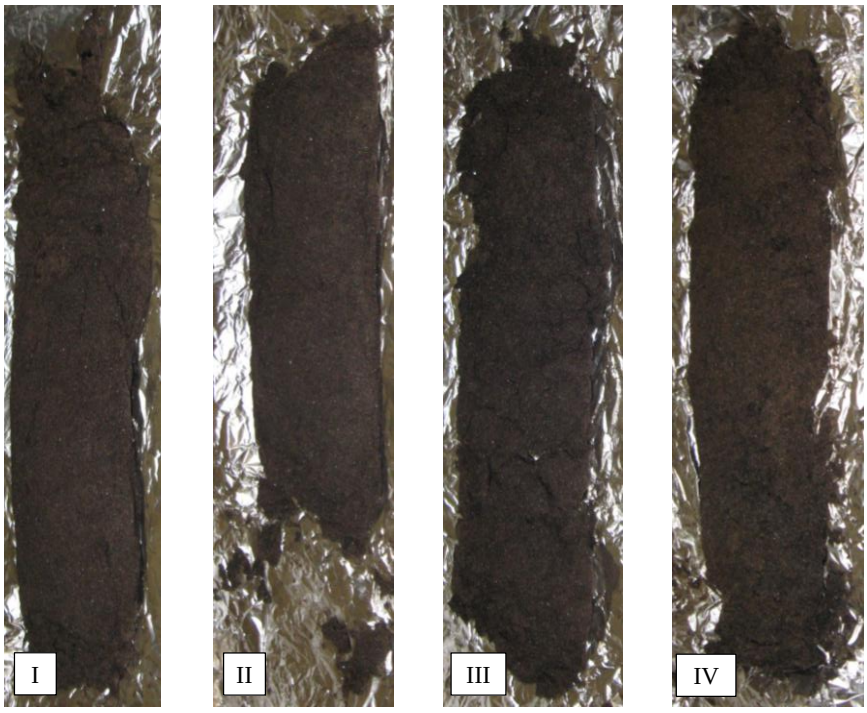

Figure 3.73. Sand pack after the temperature and rate effect case (experiment four).

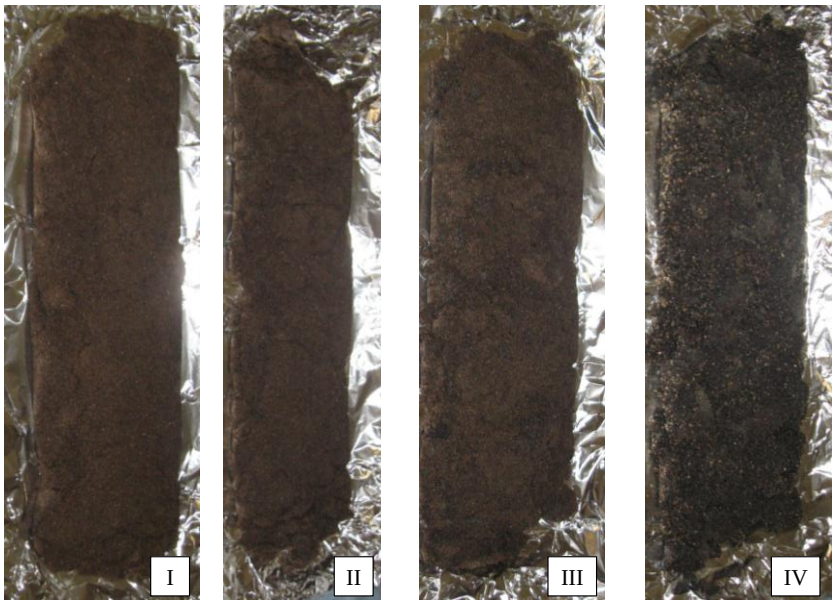

Figure 3.74. Sand pack after the temperature effect case (experiment three).

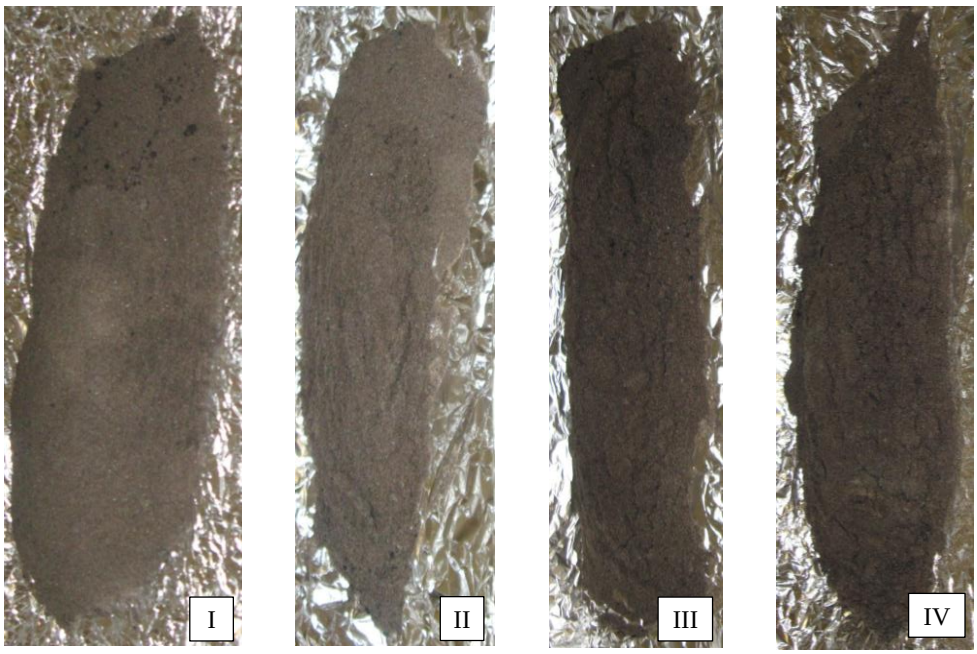

Figure 3.75. Sand pack after the solvent effect case (experiment five).

Figure 3.76 compares the average asphaltene content in the residual oil for each experiment. The original oil has an asphaltene content of 14.5%. It can be seen that all experiments experience significant in-situ upgrading with the highest degree seen for the solvent type (experiment five) and permeability effect (experiment two) cases. The reason that the solvent type effect case (experiment five) has comparable or greater values than the n-butane cases is that the liquid extraction, during which asphaltene precipitation is more severe, lasted longer allowing larger flocs to form, which were trapped in the sand pack. Regardless, the comparable contents show that asphaltene precipitation is only helpful in terms of in-situ upgrading if the asphaltenes remain sequestered meaning that solvents that mobilize the asphaltenes might be less desirable, in terms of operations, even if their liquid extraction properties are better. The liquid extraction process is the biggest contributor to in-situ upgrading. Therefore, longer extraction periods or higher mass transfer coefficients will result in more in-situ upgrading, and thus higher asphaltene contents in the residual oil.

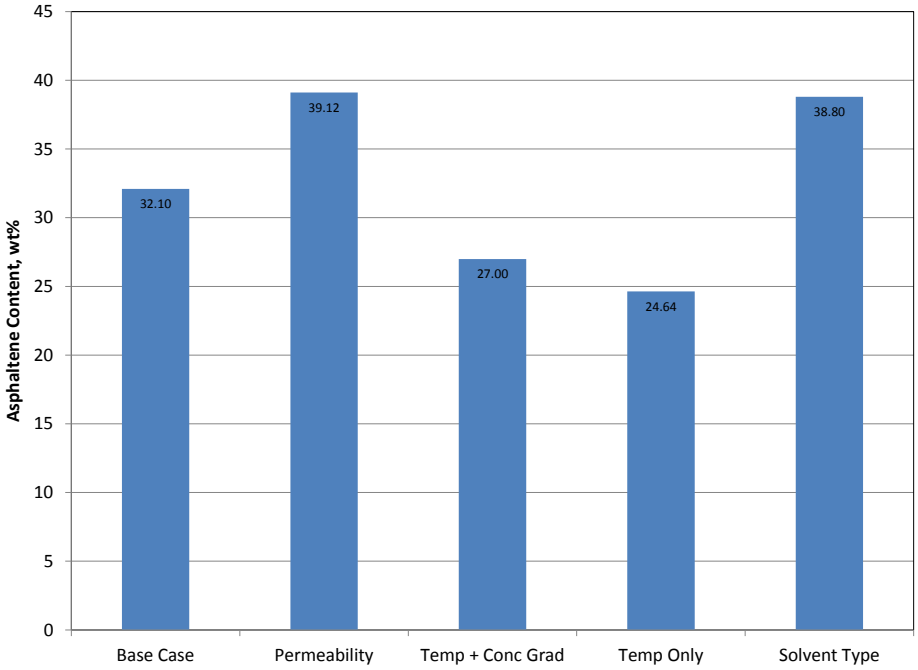

Figure 3.76. Average asphaltene content of the residual oil for all experiments.

The higher asphaltene content in the permeability effect case (experiment two) compared to the base case is because a lower permeability pack is more likely to trap the precipitated asphaltene. Also, the lower drainage rates for this case lead to higher residence times for the solvent in the sand pack. This increased exposure time leads to more precipitation. Lower permeability reservoirs are more likely to benefit from in-situ upgrading during n-butane injection. The two cases at 40 °C have the lowest asphaltene concentration (i.e. least degree of in-situ upgrading). At lower temperatures, asphaltene precipitation is less severe resulting in a lower degree of extraction. Because the temperature case is also lower than the base case, it suggests that the reduction in precipitation at lower temperatures outweighs the increased sequestration capabilities of a lower permeability sand pack. The temperature effect case (experiment four) has the

lowest asphaltene content among the n-butane case, which would be predicted from a comparison of the mass transfer coefficients.

Figure 3.77 compares the section-by-section asphaltene content in the residual oil for each experiment. The asphaltene content variability among sections for a single experiment is a function of inconsistencies in the sand collection process. Some of the samples had less than 10 mL of oil, which can lead to values with larger errors. The extremely high values for the solvent type effect case (experiment five) – section 2 might be a result of this error source because it had less than 3 mL of oil collected. Without this point, the average asphaltene content for the solvent type effect case (experiment five) would be 32.5%, which is comparable to the base n-butane case. This is probably a truer value, which makes it even clearer that in-situ upgrading is only valuable if the asphaltenes remain sequestered. The section-by-section is included for completeness, but the clearest picture of the in-situ upgrading effect comes from the average value graph.

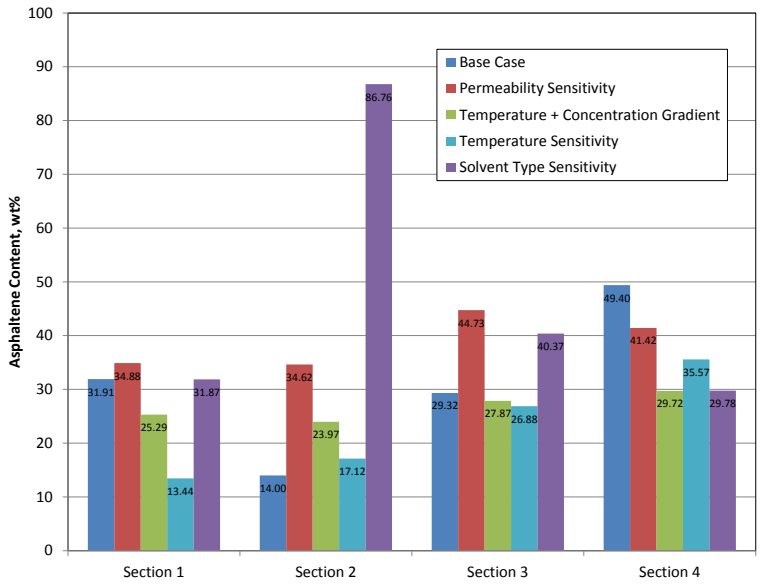

Figure 3.77. Residual oil asphaltene content for each section of the sand pack.

3.4 CONCLUSIONS

This preliminary work showed that high-temperature steam injection was an efficient oil production processes for a single fracture-matrix interaction. However, the goal of this work was to target low temperature production techniques. The addition of solvent to the steam injection process does not allow the operating temperature to be decreased significantly. Additionally, at higher temperatures, the additional viscosity reduction generated by solvent dissolution is not significant. Finally, the oil-in-water emulsions generated during steam or steam-solvent injection are not ideal and would require additional handling in the field. Therefore, the preliminary work confirms the consistency of my experimental set-up with previous observations and verifies the current issues with steam and steam-solvent injection for low temperature strategies.

The solvent proof of concept experiments showed that production from a single fracture-matrix interaction is dominated by two production mechanisms. When the injected solvent is in the liquid phase, liquid extraction occurs. Production during this phase can be well described using the equation developed by Patricelli, et al (1979) for liquid extraction kinetics. When the injected solvent is in the vapor phase, solvent-enhanced film gravity drainage occurs.

The key parameters explored were permeability, temperature, in-situ injection rate, and solvent type. Permeability does not have a significant impact on the liquid extraction process but is proportionally related to oil rate during film gravity drainage. Temperature affects both phases of production. Increased temperature leads to lower oil viscosities and higher film gravity drainage rates. Increases in temperature have a minimal impact on the solvation kinetics of the liquid extraction phase. The in-situ injection rate controls the concentration gradient in the solvent rich liquid phase at the oil-solvent interface during the liquid extraction phase. Higher concentration gradients

lead to higher mass transfer coefficients, with a more significant impact during the washing phase. Finally, solvent type can have a significant impact on both processes. The most striking impact observed when n-butane was replaced with n-pentane was the production of solid asphaltenes. While in-situ upgrading is desirable, its benefit is negated if the asphaltenes become mobile rather than being trapped in the residual oil as was the case in the n-butane experiments. Consequently, the same residual oil asphaltene content (measure of degree of in-situ upgrading) was achieved for the n-pentane (experiment five) and permeability effect (n-butane – experiment two) cases.

The major impact of this work is introducing a new solvent injection strategy combining the best mechanisms from previously proposed techniques to achieve good production at low temperatures. The production rates, heating profiles, and solvent usage are specific to the experimental set-up used. However, the process would generate the same production mechanism at any scale as long as the injection was designed to go from liquid to vapor solvent injection. The solvent usage for these experiments was excessive by design to control the process. However, preliminary work underway in core floods show that the mechanisms are the same even at reduced injection rates. These core floods are being used to study the process under more realistic field conditions and show a solvent to oil ratio less than two for the liquid extraction process.

The single fracture-matrix interaction is not representative of field behavior, but is sufficient to study the process mechanisms at the lab scale. In the field, there would be a small bank of condensing solvent in the matrix being pushed by vapor solvent. This large-scale feature is not captured in my set-up. Rather, my set-up is designed to study the behavior at a given point in the reservoir as it transitions from exposure to liquid to vapor solvent. The best process performance can be achieved with solvent that have better solvation properties during liquid extraction. However, these solvation properties

are only useful if they do not also result in asphaltene precipitation which can reduce the reservoir permeability or, if mobile, cause problems in the production lines. Finally, because these experiments only encompasses a small data set of variables there is still significant uncertainty associated with the effect of parameters on each mechanism.

Chapter 4 – Process Modeling through Numeric Simulation

4.1 INTRODUCTION

The ultimate goal for this new process would be commercial field-scale deployment. The first step in taking the process form the lab to the field would be reliable and accurate upscaling. This requires a numeric simulation capable of capturing the primary mechanism of the process – liquid extraction of the oil by the liquid solvent and diffusion of the vapor solvent into the oil. It is also necessary to understand the impact of uncertainty in experimental parameters when matching results with simulation. The intent of this chapter is to use the CMG STARS thermal simulator and CMOST history matching tool to determine the simulation parameters necessary to model the two production mechanisms and study the impact of uncertainty in each parameter on the simulation output. The STARS simulator was chosen because it is commercially available, commonly used for thermal viscous oil simulations, and has a user-friendly history-matching tool (CMOST) that allows for sensitivity analysis. A good history-match is not the desired output of this work. Rather, the sensitivity analysis and history-match are tools to identify and evaluate the significance of physical process parameters as well as the adequacy of thermodynamic and transport property models available in STARS related to the description of our process.

4.2 MODEL DESCRIPTION

The model needs to capture both the thermodynamic and transport properties of the production mechanisms and the physical and thermal properties of the experiment set-up. The same base design is used for all simulations. The grid was developed to accurately represent the sand column and the stainless steel experimental vessel. The oil and solvent properties were provided by an industrial collaborator.

4.2.1 Grid and Reservoir Properties

The 2D model is a cylinder with 27 grid blocks in the r-direction and 53 grid blocks in the z-direction. The sand column extends from r=1 to r=25 (each 1 mm thick) and z=2 to z=51 (each 2 cm thick). The annulus between the sand column and the stainless steel column extends from r=26 (5 mm thick) and z=2 to z=52 (each 2 cm thick). The gap between the bottom of the sand column and the bottom endcap extends from r=1 to r=25 (each 1 mm thick) and z=52 (5 mm thick). The stainless steel column extends from r=27 (3.175 mm thick) and z=2 to z=52 (each 2 cm thick). The top endcap extends from r=1 to r=27 (total thickness = 3.3175 cm) and z=1 (2.42 cm thick); the bottom endcap extends from r=1 to r=27 (total thickness = 3.3175 cm) and z=53 (4.43 cm thick).

Three sets of thermal properties were used to describe the parts of the model. Table 4.1 summarizes the base case values for each set. Set one has the sand column properties. Set two has the annulus properties. Set three has the stainless steel (column and endcaps) properties. For set one, the porosity is that measured during the experiment (29.3%). The permeability is that measured for the sand pack in the auxiliary flow set-up (126 D). The thermal properties (heat capacity and thermal conductivity) are the typical values for each component – silica sand, water, oil, and n-butane. The purpose of rock type two is to trick the simulation into thinking the "rock" in the annulus grid blocks is not there. To do this, the rock thermal properties are given the values of the gas. The annulus porosity is 50%; the value is not made higher for numerical stability reasons. The annulus permeability is set at 500 D to eliminate any resistance to flow to represent the pipe flow that is actually occurring. Set three covers all the grid blocks that are modeling the steel components of the experimental vessel. All of the component thermal properties are set to equal the values for 316L stainless steel. A zero heat loss boundary is

used for all external faces. While this is not representative of the experiment, I chose to not model the heat losses from the system. Figure 4.1 is the r-z profile showing the different rock-type assignments – brown = sand pack; blue = annulus; gray = stainless steel. The gap indicates missing grid blocks in the z-direction.

Set	$c_{p,rock}$ (J/cm^3-C)	k_r (J/cm-min-C)	k_w (J/cm-min-C)	k_o (J/cm-min-C)	k_g (J/cm-min-C)
Sand Column (1)	2.2048	1.08	0.372	0.079	0.00816
Annulus (2)	4.415E-3	0.00816	0.372	0.079	0.00816
Stainless Steel (3)	3.995	9.72	0.372	9.72	9.72

Table 4.1. Thermal properties summary for each rock type.

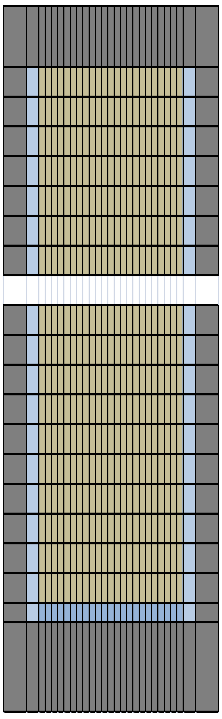

Figure 4.1. Vertical cross-section of the model showing rock-type assignments - brown = sand column (1); blue = annulus (2); gray = stainless steel (3).

4.2.2 Fluid Properties

The fluid system is represented through three components: 'WATER,' 'OIL,' and 'C4.' The 'WATER' component uses STARS default values. The 'OIL' component properties were supplied by an industrial collaborator. 'OIL' is a pseudo-component with representative values for the actual multi-component oil. Because of the non-volatile nature of the viscous oil, it is acceptable to use a single pseudo-component. The 'C4' component properties are those for n-butane. Because STARS is not a compositional simulator, gas-liquid equilibrium is represented through the mass transfer coefficient, k, rather than an equation-of-state. The k-value is defined as the ratio of vapor mole fraction to liquid mole fraction of a component at a given pressure and temperature. The k-values are represented in color plots, Figures 4.2 and 4.3, over the pressure and temperature range supplied to the simulation for the 'OIL' and 'C4' components, respectively. The k-values are essential to modeling the solvent-enhanced film gravity drainage period because the butane k-value controls the diffusion of oil into the oil film. The 'OIL' and 'C4' component viscosity varies with temperature. The viscosity measurements for the oil sample were extended to cover a wider range for use in the simulation (Figure 4.4). The STARS default fluid enthalpies for water, oil, and gas components were used because they gave the correct injected enthalpy rate for the n-butane stream. The 'OIL' component diffusivities were set as constant values of 10^{-9} and 10^{-5} m^2/sec, for the oil and gas phases, respectively. The 'C4' component diffusivities are functions of temperature and viscosity described by Equation 4.1 (STARS Manual).

$$D^* = D * \frac{T}{T_{ref}} * (\frac{\mu_{ref}}{\mu})^{\beta} \qquad (4.1)$$

Where D* = diffusion coefficient

D = reference value of diffusion coefficient

T = temperature

T_{ref} = reference temperature

μ = viscosity

μ_{ref} = viscosity

β = proportionality exponent.

The reference value for the diffusion coefficient in the gas and liquid phases were 10^{-5} and 10^{-9} m^2/sec, respectively. The reference temperature is 25 °C. The reference viscosity was 35824 cp, the oil viscosity at 25 °C. Finally, the proportionality exponent was set to a value of 0.545, which was calculated by Das and Butler (1996) for propane and bitumen in Peace River Oil.

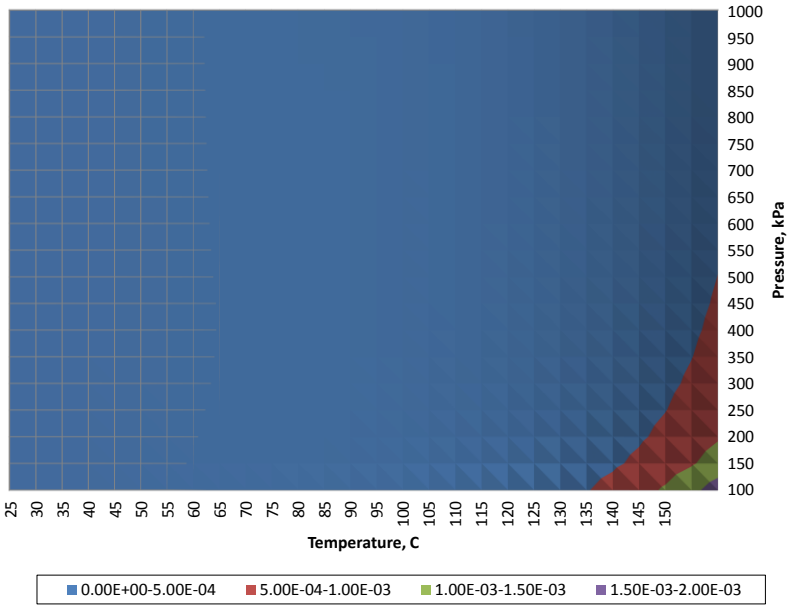

Figure 4.2. k-Values for the 'OIL' component.

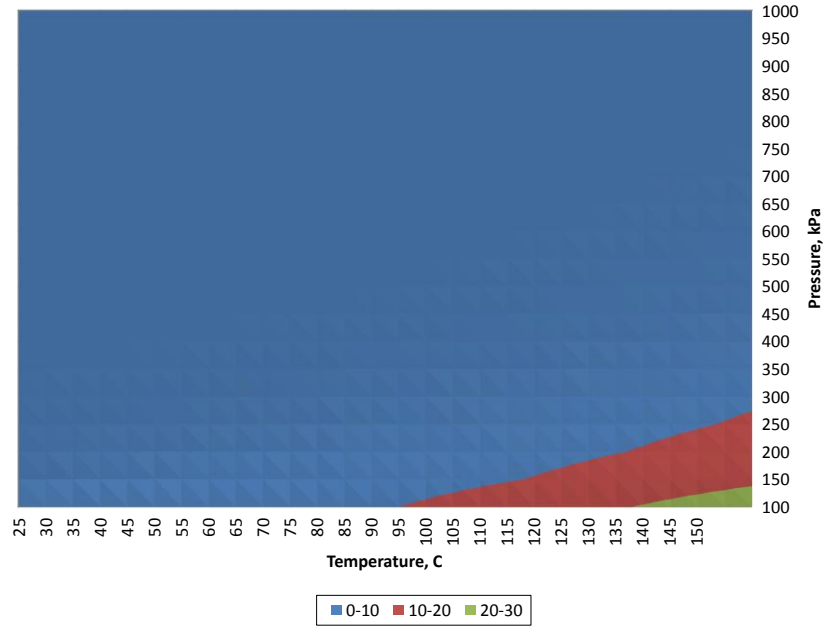

Figure 4.3. k-Values for the 'C4' component.

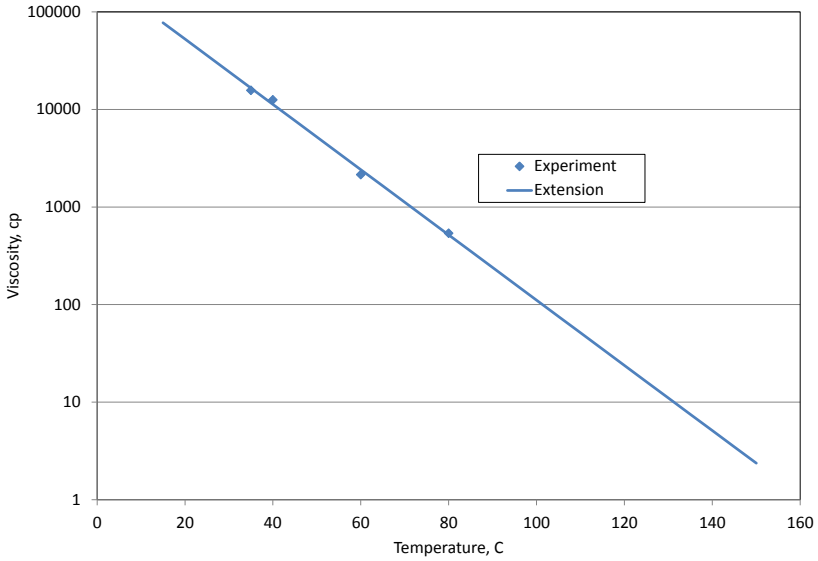

Figure 4.4. 'OIL' component viscosity curve extended from lab measurements.

4.2.3 Rock-Fluid Properties

The relative permeability curves for the sand column are shown in Figures 4.5 and 4.6. Corey-type curves were used with water and oil-water exponents of three, oil-gas exponent of 4, and gas exponent of 1. Straight-line relative permeability curves (saturation = relative permeability) were used for the annulus to mimic fracture flow. These curves were also applied to the stainless steel grid blocks.

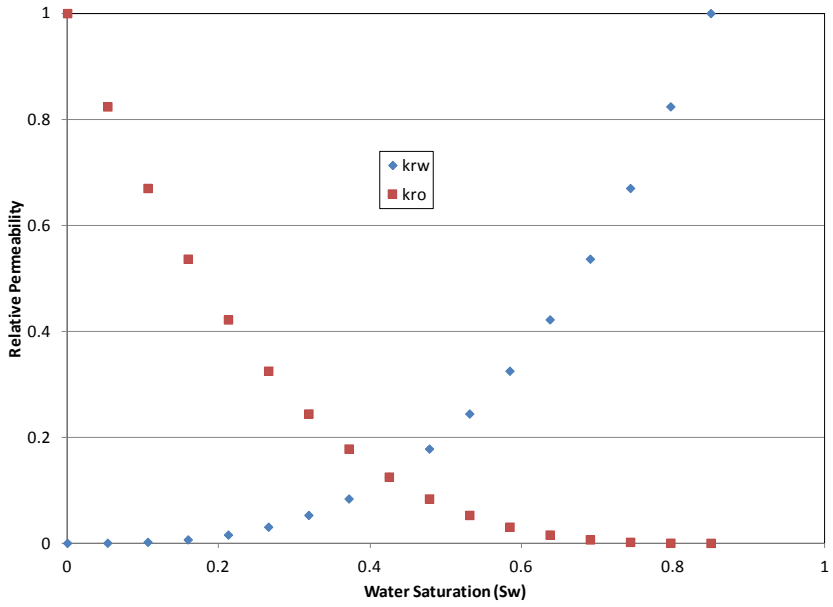

Figure 4.5. Sand column oil-water relative permeability curves.

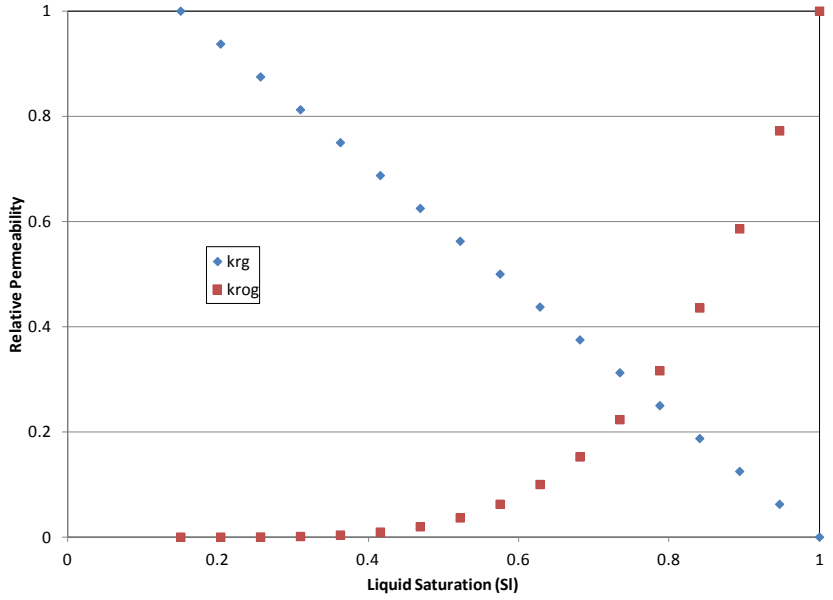

Figure 4.6. Sand column liquid-gas relative permeability curves.

4.2.4 Initialization

As was the case in the experiment, the sand-pack was originally 100% oil-saturated, and the annulus was 100% water-saturated. Because only 50% porosity was used for the annulus, only half the actual water was modeled. The initial temperature and pressure were 22 °C and 101 kPa.

4.2.5 Injection and production lines

The injection line was represented as a single injection point in the top-most annular grid block. The injection line from the pumps through the oven and to the end-cap was not modeled because the exact boundary conditions, especially with respect to heat loss, were not quantified. Furthermore, I measured the pressure and temperature directly at the inlet so these measurements could be used as reference for determining the inlet conditions in the simulation. The same modeling process was applied to the outlet flow line. The outlet is modeled as a single point in the middle grid block of the annulus

layer between the sand column bottom and the bottom end-cap. Choosing not to model the outlet flow lines does reduce the accuracy of the model because the cumulative oil measurement and outlet pressure are measured downstream of the endcap. Therefore, the model will not capture the pressure build-ups during the initial heating period due to oil seizing in the outlet lines and any related delay in oil production from the endcap (simulation) to heated accumulator (experiment). The injection and production points were modeled with the tube-end model, which uses a linear model to calculate the flow indices. The model uses the linear block transmissibility calculation, but the separation distance is from the block center to the block face. The model is appropriate for the end of a core-face (CMG STARS User's Manual), which is a decent approximation of the set-up. The initial operating constraints are 9444 cc/min maximum injection rate (at surface conditions; 40 cc/min liquid at accumulator conditions) and 650 kPa maximum pressure for the injection point. The only production operating constraint is a minimum bottom-hole pressure of 600 psi. At 40 minutes, the injection point's primary constraint is decreased to 3452 cc/min (at surface conditions; 15 cc/min liquid at accumulator conditions) to capture the reduction in n-butane injection rate from the experiment. The butane is injected at 60 °C and 100% quality.

4.3 SENSITIVITY ANALYSIS

The above properties were used to build the base case simulation to serve as the starting point for the CMOST sensitivity analysis and history-matching efforts. Figures 4.7 and 4.8 show the comparison of the base case results for cumulative oil and oil rate with the experimental results. The red lines are simulation results; the blue dots are experimental data points. The most obvious difference is that the simulation does not have the slope change indicating the transition from liquid extraction to solvent-enhanced gravity

drainage. The simulation does accurately model the n-butane phase behavior so that the transition from liquid solvent to vapor solvent is captured. The single slope generated in the base case is closer to the behavior of the liquid extraction suggesting that that mechanism is being captured, but the parameters controlling the process do have some uncertainty. The other deviations are the initial slope of the cumulative production curve and the time it begins to plateau. The slope falls somewhere between the two experimental slopes, but because the simulation slope is steeper than the second experimental slope, the simulation plateau starts earlier. Finally, the simulation ultimate recovery is higher.

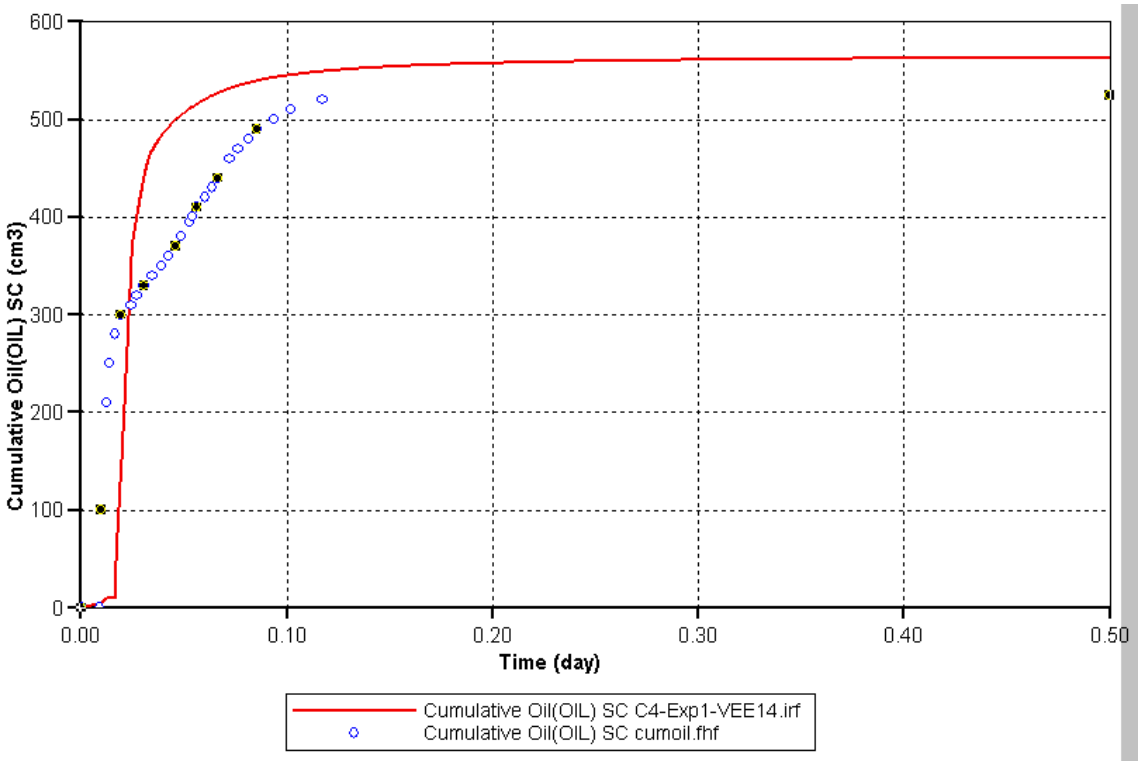

Figure 4.7. Comparison of the base case and experimental cumulative oil curves.

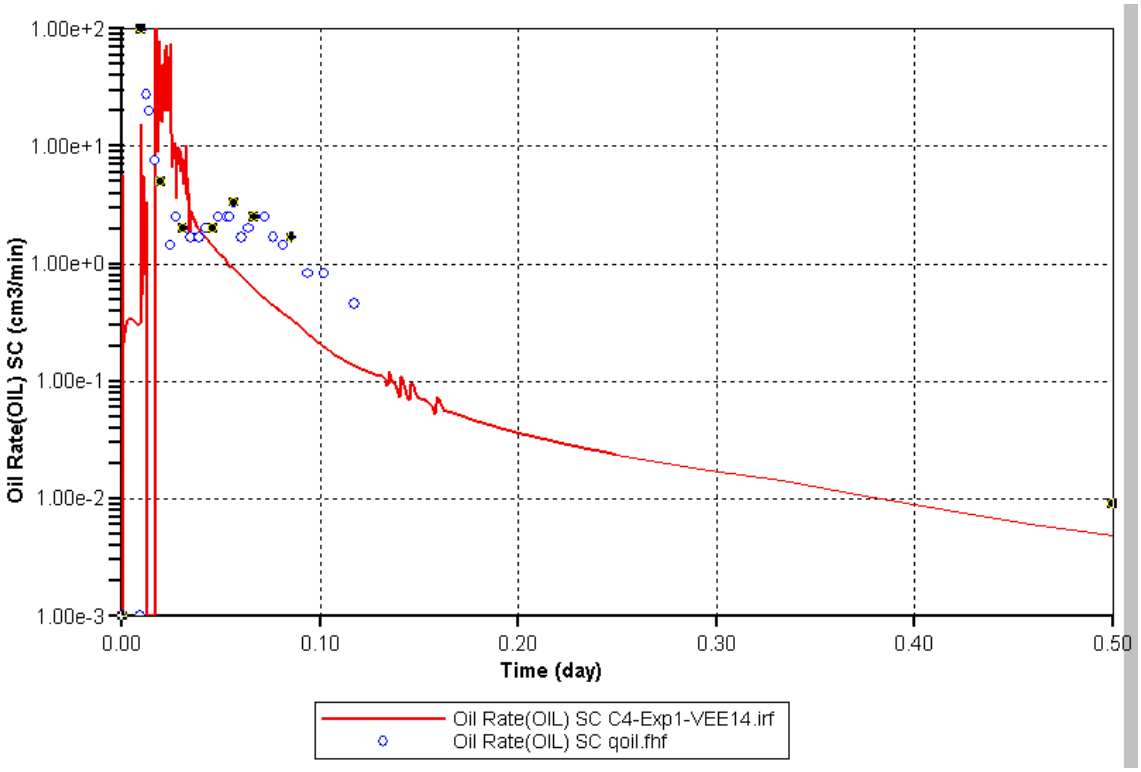

Figure 4.8. Comparison of the base case and experimental oil rate curves.

Figures 4.9 through 4.14 show the comparison of temperature at the six measurement points. The heat front arrival at the Annulus-Inlet point is correct, but all other points show a delay in arrival. The increase in temperature at the Annulus-Inlet and Column - 25 cm are not captured by the simulation. However, I do not want to match this behavior because it is a side-effect of the experimental set-up environments rather than indicative of any of the process mechanisms. The only major difference in the shape of the curves is that the outlet annulus and column – 100 cm measurements points show an trough in temperature between initial heating and stabilized temperature. These differences in the temperature profile are minor and primarily due to uncertainty in process parameters that can be refined with further study.

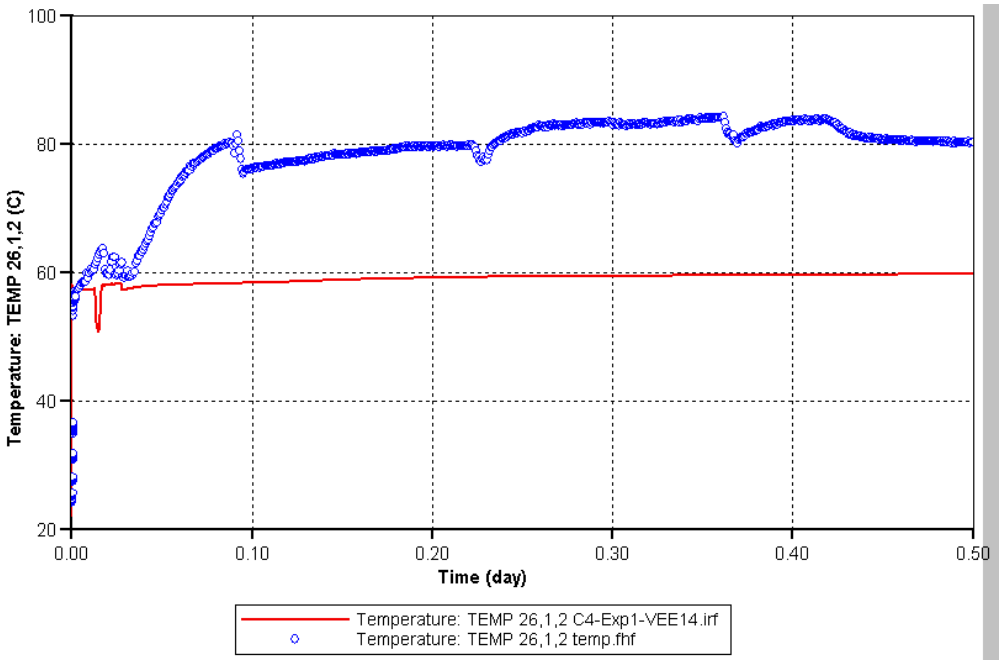

Figure 4.9. Comparison of the Annulus-Inlet temperature history.

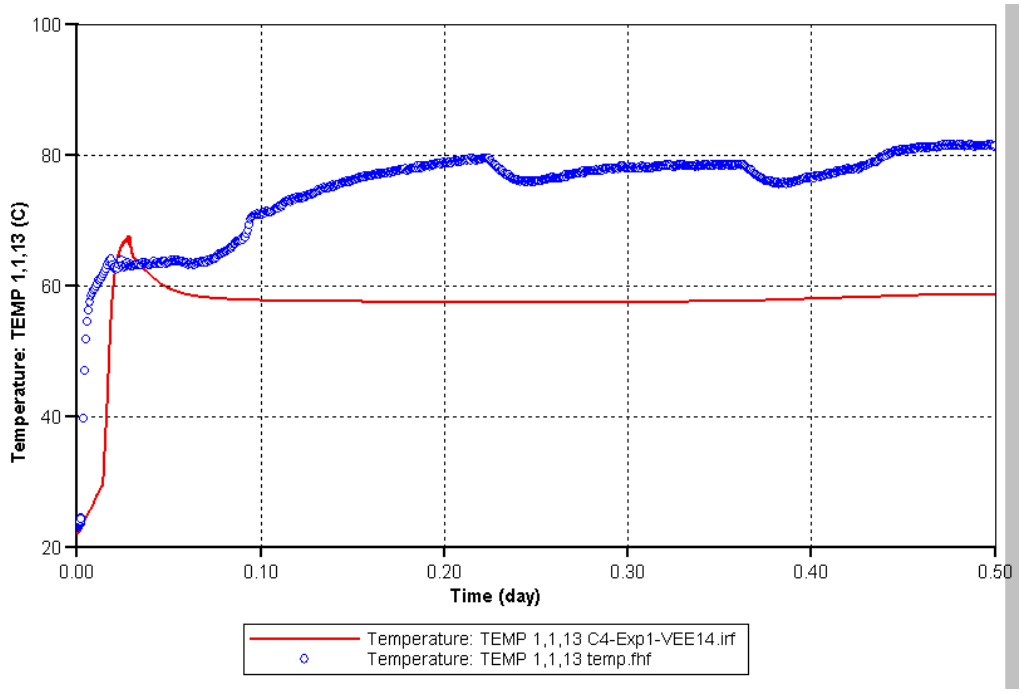

Figure 4.10. Comparison of the Column - 25 cm temperature history.

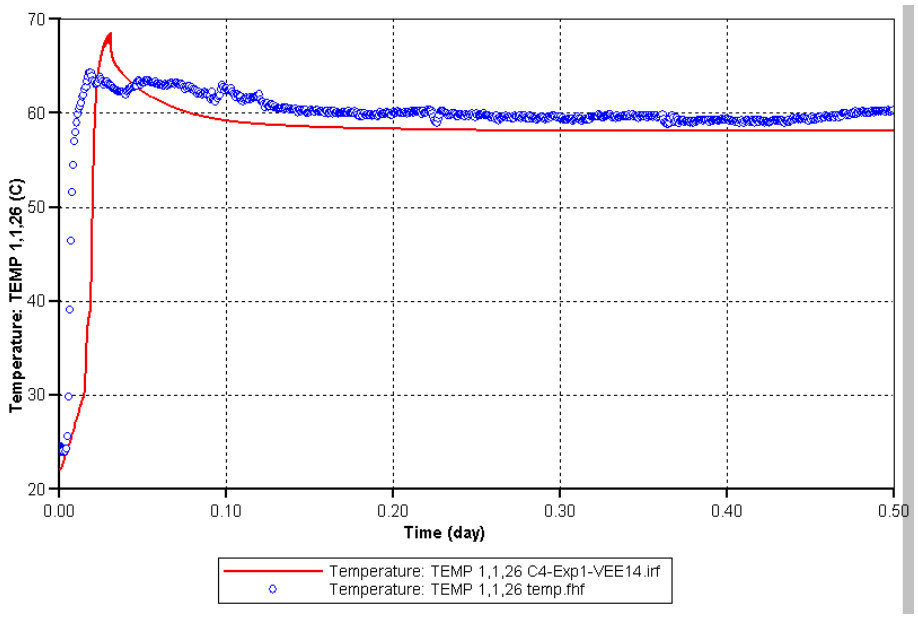

Figure 4.11. Comparison of the Column - 50 cm temperature history.

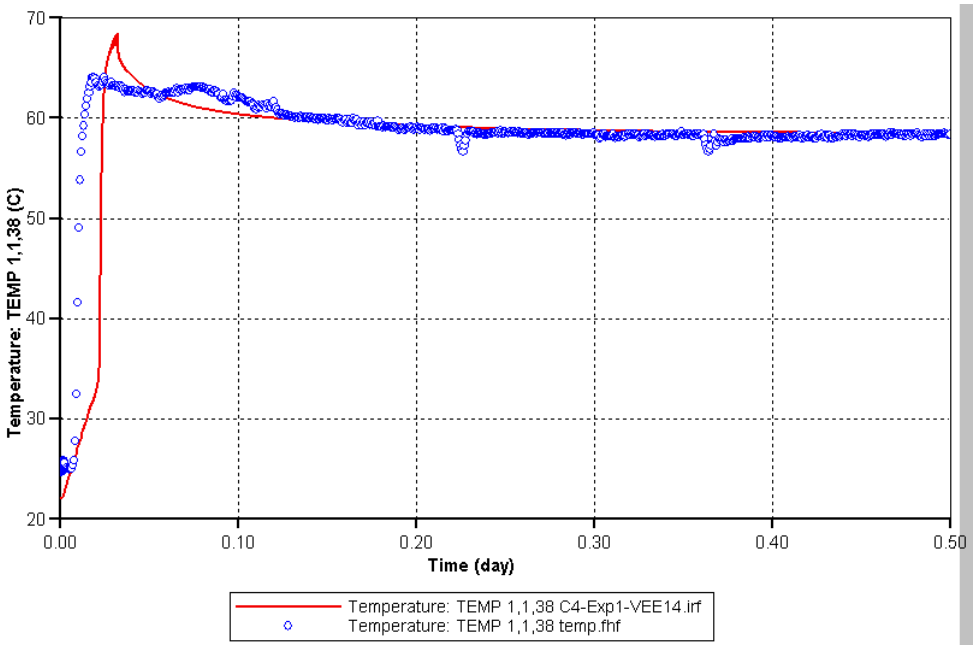

Figure 4.12. Comparison of the Column - 75 cm temperature history.

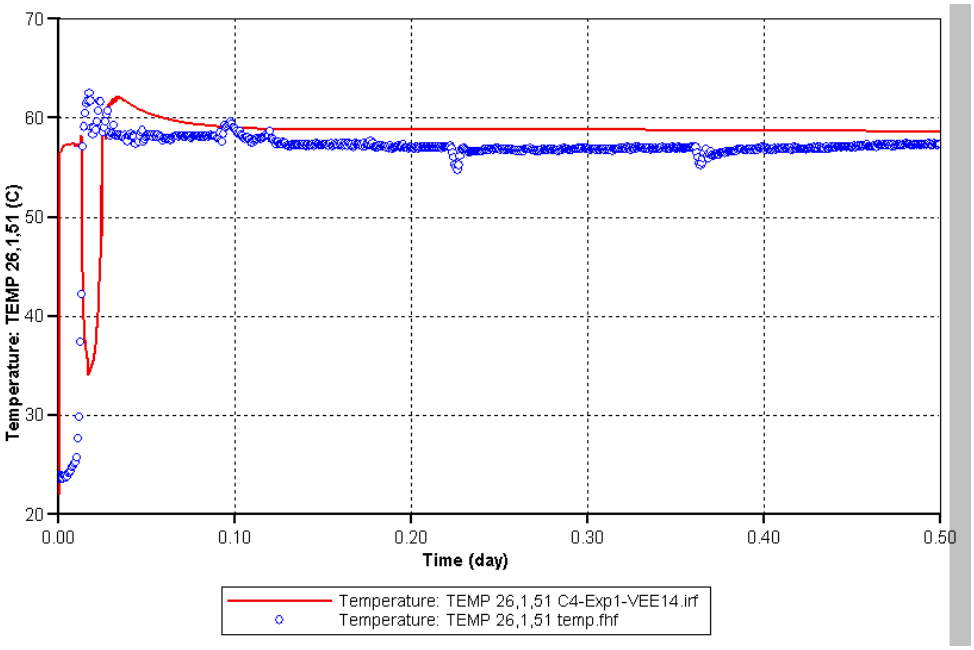

Figure 4.13. Comparison of the Column - 100 cm temperature history.

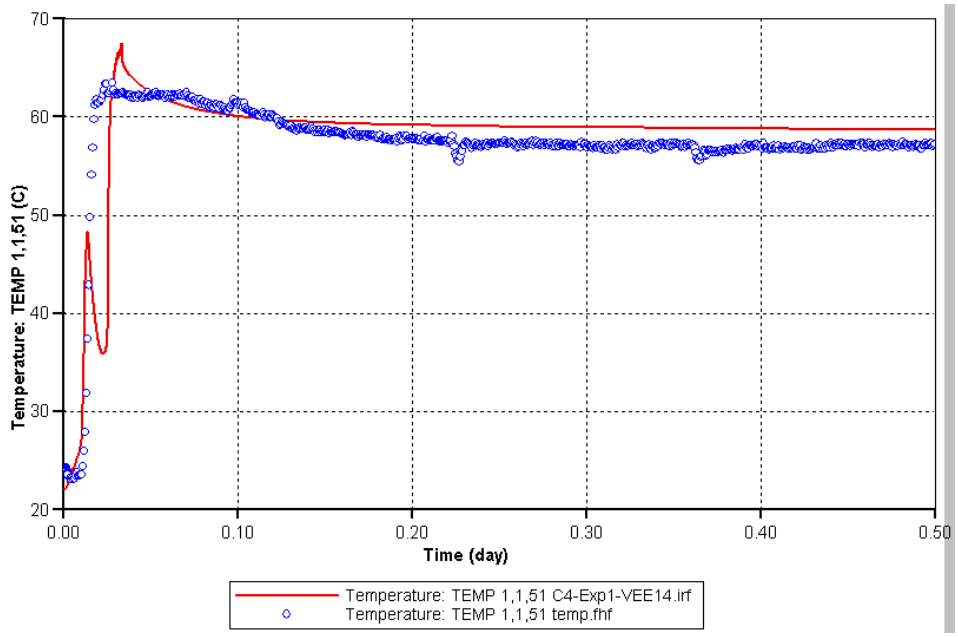

Figure 4.14. Comparison of the Annulus - Outlet temperature history.

The purpose of the sensitivity analysis was two-fold. First, parameters with the most sensitivity are those necessary to describe the two production mechanisms observed in the simulation. Second, the magnitude of sensitivity indicates how the range of uncertainty for each parameter impacts the simulation outlet. This will provide better understanding on which parameters would need further study to determine accurate values. The sensitivity analysis study was done twice. First, thirteen parameters were chosen that included experimental parameters with major uncertainty. This initial sensitivity analysis did not include n-butane partitioning coefficients (k-values) or any relative permeability parameters. Values such as porosity and viscosity, which had been directly measured, were not used during either analysis. Table 4.2 shows the 13 parameters used for the initial sensitivity analysis. The high and low values were +- 5% of the values used in the base case. The fractional factorial sampling method was used to create 128 jobs, 115 of which ran without error. The results of these jobs were used to generate tornado plot for the eight objective functions – cumulative oil, oil rate, and all six temperature measurements points. Figures 4.15 through 4.22 are the tornado plots for each objective function. The parameters are ranked in order of relative importance in regards to sensitivity of the objective function to change in the parameter. The most significant parameters for cumulative oil and oil rate are the component diffusion coefficients in the oil phase, the sand pack permeability, and the annulus permeability. The importance of oil phase diffusion coefficients suggests that the simulator is showing sensitivity to parameters that represent the liquid extraction mechanism. The importance of annulus permeability for oil rate is because the production well lies in an annular grid block, so the rate is affected by the grid block permeability as well. For the column temperature measurements, the primary parameters were the component diffusion coefficients in the oil phase, the sand and annulus permeabilities, and the thermal

conductivity of the oil in the annulus. The original analysis of the experimental results indicated that radial heat propagation was controlled by conduction rather than convection of the heat solvent. This would manifest itself as a high sensitivity to the sand column and oil thermal conductivities. For the annular temperatures, the most important parameters are the oil phase diffusion coefficients and the annular permeability. This is similar to the sand column because they will be the primary butane transport mechanisms, which is what controls temperature. The minor impact of the stainless steel thermal properties suggests that there is little uncertainty in these values beyond those being used. The gas phase diffusivities do not have a significant impact on temperature propagation because neither component is in the gas phase during heating. Finally, the overall minimal sensitivity to all thermal properties indicates only a small degree of uncertainty in the values of these parameters used for the case. Therefore, they are not used in the second phase of sensitivity analysis because their values are fairly certain.

CMOST Variable	Parameter Description
varDIFFGASC4	'C4' component diffusion coefficient in gas phase
varDIFFGASOIL	'OIL' component diffusion coefficient in gas phase
varDIFFOILC4	'C4' component diffusion coefficient in OIL phase
varDIFFOILOIL	'OIL' component diffusion coefficient in OIL phase
varPERMANN	Annular permeability
varPERMSAND	Sand pack permeability
varTHCONG1	Gas thermal conductivity in sand column
varTHCONG2	Gas thermal conductivity in annulus
varTHCONO1	Oil thermal conductivity in sand column
varTHCONO2	Oil thermal conductivity in annulus
varTHCONR1	Rock thermal conductivity in sand column
varTHCONR2	Rock thermal conductivity in annulus
varTHCONR3	Rock thermal conductivity in stainless steel

Table 4.2. Summary of sensitivity analysis parameters for the first sensitivity analysis.

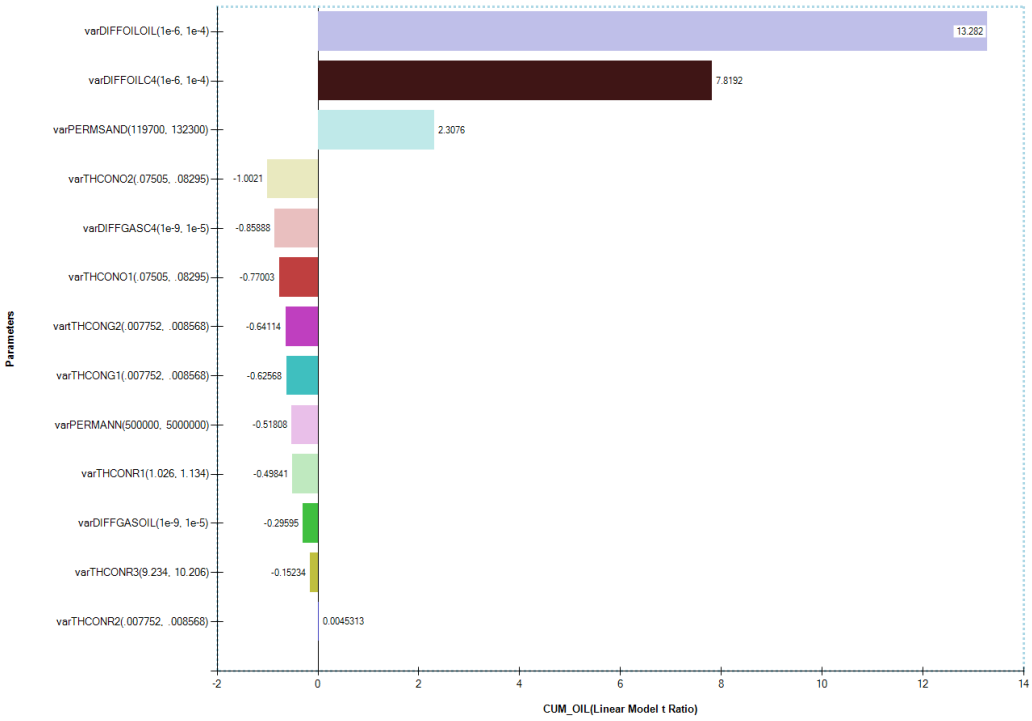

Figure 4.15. Tornado plot for the cumulative oil objective function.

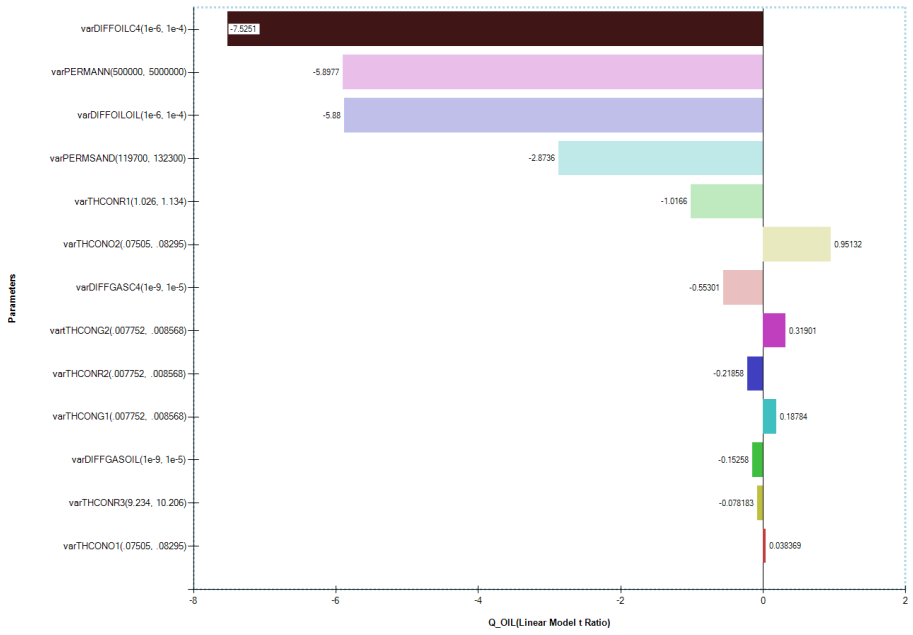

Figure 4.16. Tornado plot for the oil rate objective function.

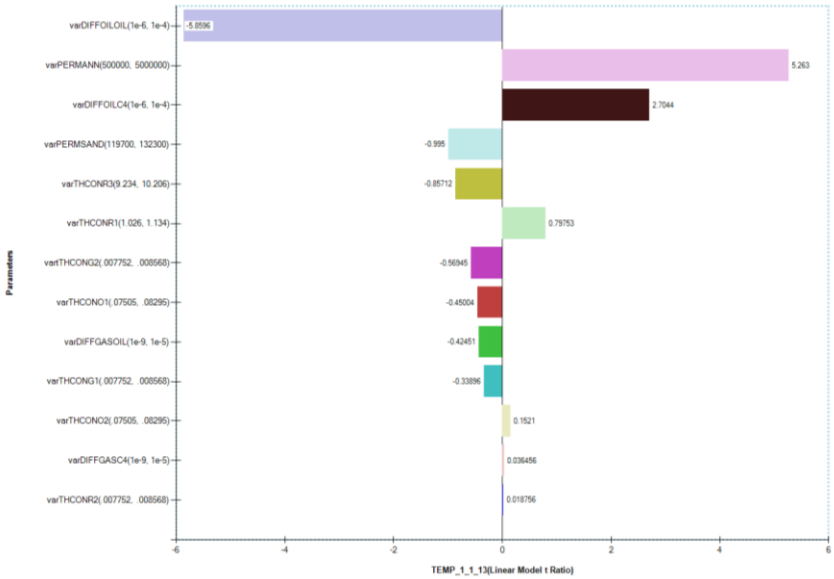

Figure 4.17. Tornado plot for the Column - 25 cm temperature objective function.

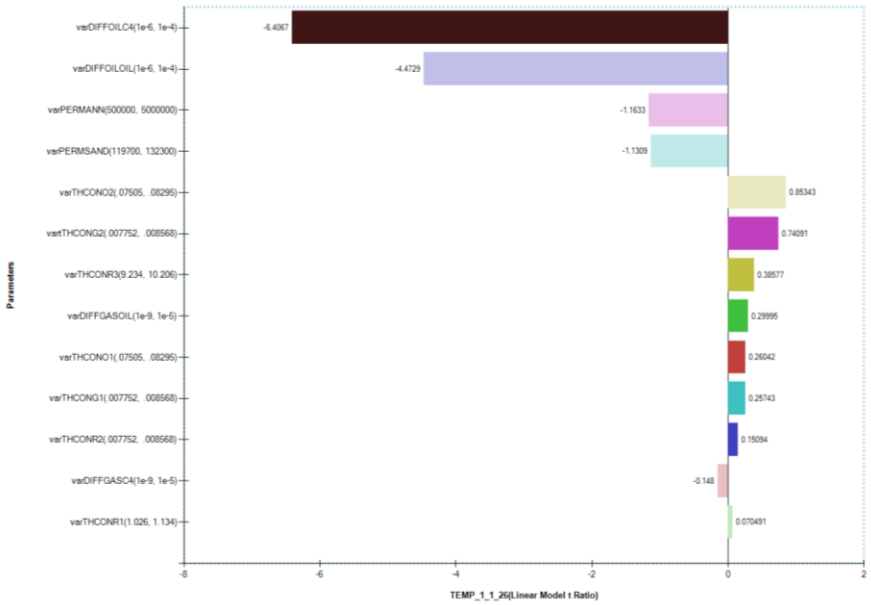

Figure 4.18. Tornado plot for the Column - 50 cm temperature objective function.

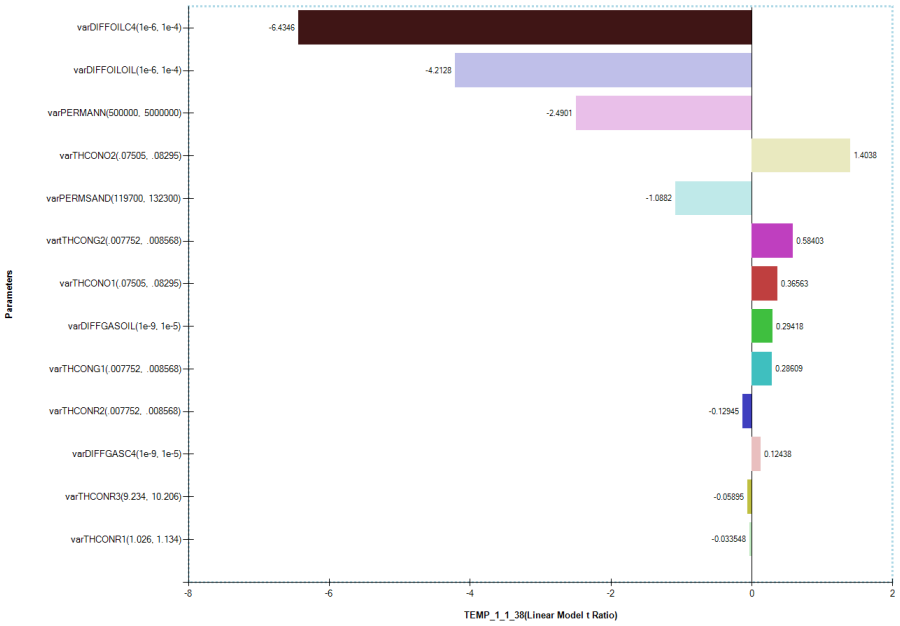

Figure 4.19. Tornado plot for the Column - 75 cm temperature objective function.

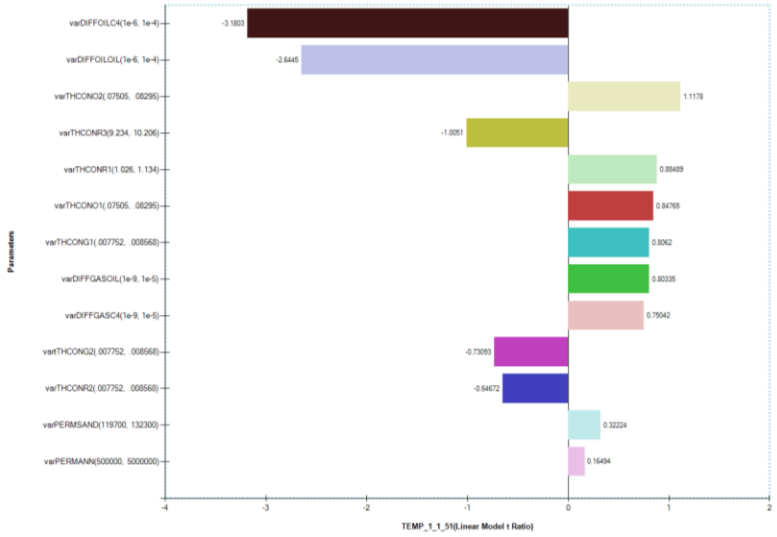

Figure 4.20. Tornado plot for the Column - 100 cm temperature objective function.

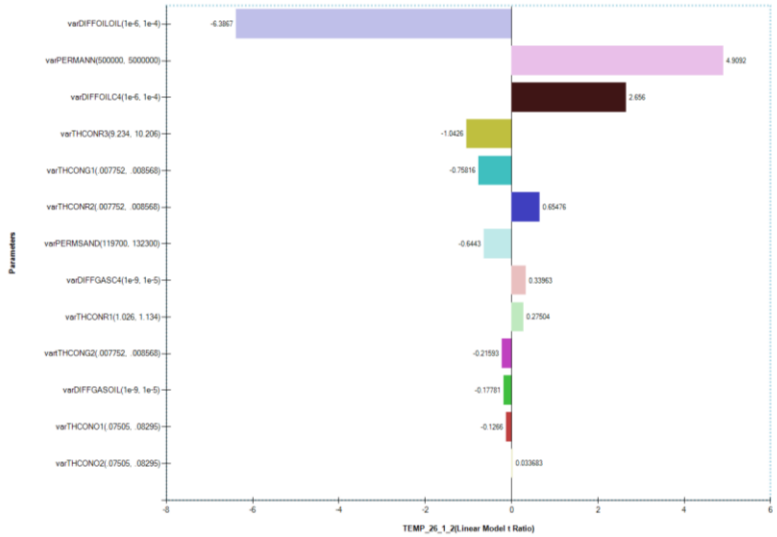

Figure 4.21. Tornado plot for the Annulus-Inlet temperature objective function.

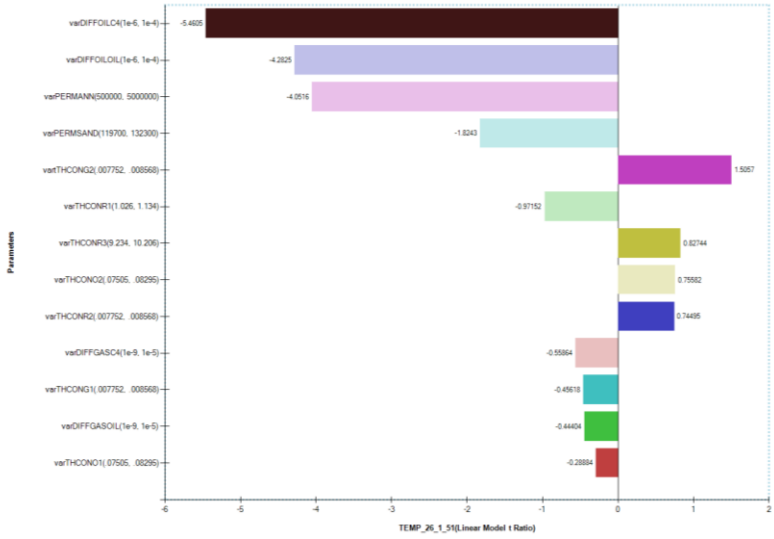

Figure 4.22. Tornado plot for the Annulus-Outlet temperature objective function.

The second sensitivity analysis focused on the key parameters controlling the process mechanisms. Possible parameters for analysis can be divided into three groups – rock properties (absolute and relative permeability), fluid properties (viscosity, k-values, and diffusion coefficients), and operating properties (heat loss and injection constraints). I did not choose to study any of the operation properties in the second analysis. Relative permeability was not included, even though it is a complete unknown and is one of the two controls on the gravity drainage process. All of the fluid properties from the first sensitivity analysis were included with the addition of an n-butane k-value. The operating properties were not included because their effect on the match was already determined. As discussed in Chapter 3, the decrease in injection rate also led to an increase in the injection temperature. This increase resulted in the overshoot behavior seen at the Annulus – Inlet and Column – 25 cm measurement points. I do not desire to match this behavior because it does not represent any mechanism active in the process. Also, the first sensitivity analysis showed that the thermal properties of the system did

not have a high significance on the model. Therefore, I chose not to include any operating properties in the second analysis. Six parameters – butane k-value at 6 bar and 60 °C, sand column permeability, and all four diffusion coefficients – were chosen for analysis. Table 4.3 shows the six parameters used with their low, base, and high values for the sensitivity analysis. The k-values, in part, describe the steady-state film gravity drainage mechanism, which occurs when the system is at equilibrium at the target operating conditions of 60 °C and 6 bar. Therefore, in a first look study, it is acceptable to study the impact of this single point value rather than all the values across the pressure-temperature domain. The oil phase diffusion coefficients describe the liquid extraction mechanism. The fractional factorial sampling method was used to create 16 jobs, 6 of which ran without error. Seven objective functions were defined – cumulative oil and all six temperature measurements points.

The most significant parameters for cumulative oil are the 'C4' component oil phase diffusion coefficient and the 'C4' k-value. These properties are the parameters underlying the two production mechanisms. Liquid extraction can be represented by diffusion of components in the oleic phase, where diffusivity is a function of temperature, pressure, and composition. Solvent-enhanced film gravity drainage can be represented by the k-value, which describes the interphase mass transfer as the butane diffuses from vapor into liquid hydrocarbon. The lack of sensitivity to the 'OIL' component oil phase diffusion coefficient is because it was only modeled as a single value with no functionality options. For the column temperature measurements, the profiles were most sensitive to the 'C4' component diffusion coefficients and k-value. While these properties do not impact the thermal behavior in a thermodynamic sense, they do have an effect on the heat transport. Heat is transferred from the hot solvent to the cold oil when the butane condenses (function of k-value). Also, the diffusion behavior of the 'C4'

component impacts the transport of the solvent into the oil, which also serves as a path to heat transport. Figures 4.23 and 4.24 show examples of the range of results achieved during the sensitivity analysis for cumulative oil and the Column – 50 cm measurement point, respectively.

CMOST Variable	Parameter Description	Units	High	Base	Low
varC4KVAL	C4' component k-value at 600 kPa, 60 °C	-	1	1.07	1.15
varDIFFGASC4	'C4' component diffusion coefficient in gas phase	m^2/sec	1.00E-04	1.00E-05	1.00E-06
varDIFFGASOIL	'OIL' component diffusion coefficient in gas phase	m^2/sec	1.00E-04	1.00E-05	1.00E-06
varDIFFOILC4	'C4' component diffusion coefficient in oil phase	m^2/sec	1.00E-08	1.00E-09	1.00E-10
varDIFFOILOIL	'OIL' component diffusion coefficient in oil phase	m^2/sec	1.00E-08	1.00E-09	1.00E-10
varPERMSAND	Sand column permeability	m^2/sec	113400	126000	138600

Table 4.3. Summary of sensitivity analysis parameters for the second sensitivity analysis.

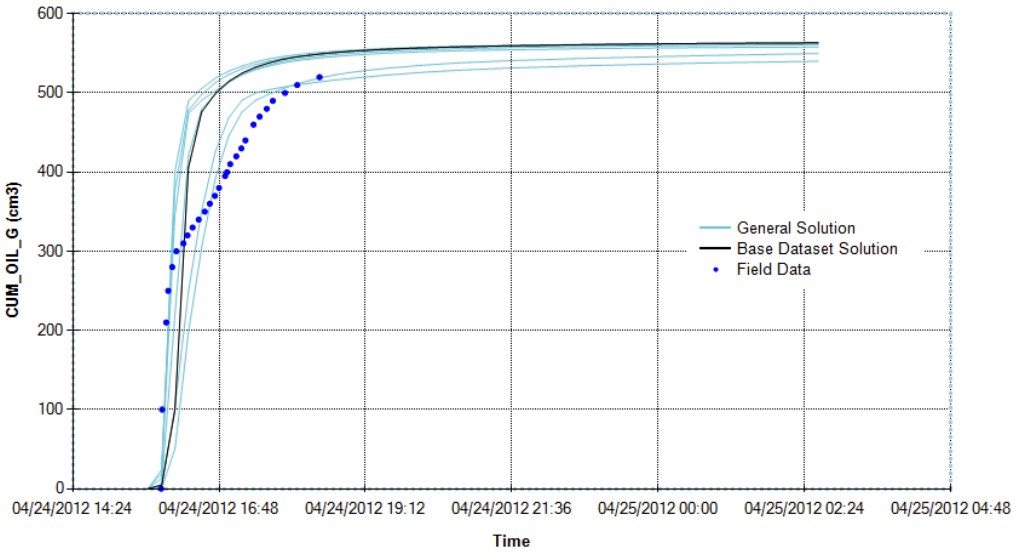

Figure 4.23. Range of results for cumulative oil during the second sensitivity analysis.

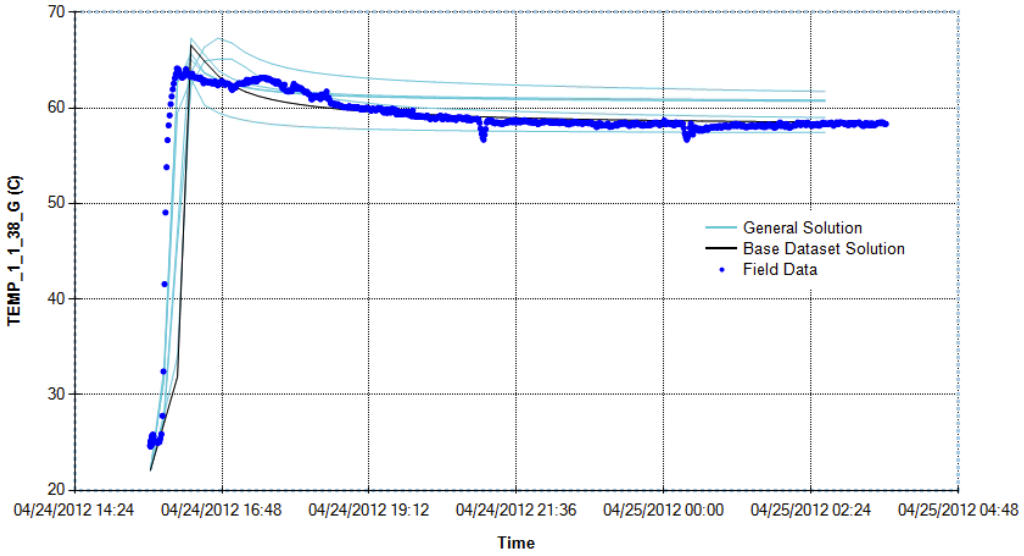

Figure 4.24. Range of results for Column - 50 cm temperature for the second sensitivity analysis.

4.4 CMOST History Match

Whereas the previous section merely looked at the range of outcomes that could be achieved given combinations of the high and low values for each parameter, this section uses the CMOST History Match tool to try to converge on an optimal set of values for the best match to the experimental data. This will determine if the chosen set of parameters with associated uncertainty are sufficient to fully model both production mechanisms. The CMOST History Match tool uses the CMG DECE Optimizer which implements CMG's proprietary optimization method: Designed Exploration (DE) and Controlled Evolution (CE). The DECE optimization can be described simply as an iterative optimization applying the DE and CE stages sequentially. The DE stage searches the parameter space in a designed random manner to obtain maximum information about the solution space. DE uses experimental design and Tabu search techniques to pick parameter values and create representative simulation datasets. CE performs statistical analyses on the DE results to determine if a better quality solution can

be achieved by banning a certain candidate value from being picked again. These values will not be used in the next CE stage. The DECE algorithm continues to routinely check these rejected values to insure the decision is still valid. The DE-CE cycle continues until an optimal solution is reached. This solution is still path dependent so that the optimal solution is non-unique.

The six parameters from the second sensitivity analysis are used as history-matching variables. The history match error for the cumulative oil and temperature profiles are used as objective functions. The global objective function, which CMOST attempts to minimize, is a weighted average of the six individual objective functions. No preferences are given to any parameter in the influence matrix. The global objective function was reduced from 21.3% for the base case to 15.9% in the optimal run. The high error even for the optimal run indicates that there is still considerable uncertainty in the values used for the match.

Figure 4.25 is the comparison of the cumulative oil from this optimal case to the experimental data. Figure 4.26 is the comparison of the temperature at the Column – 50 cm measurement point. The red lines are the simulation results; the blue dots are the experimental data. It is obvious from these graphs that the values used for the variables do not generate a good match for the cumulative oil. The early production from the liquid extraction is captured, but, as in the sensitivity cases, the transition to the film gravity drainage is missing. Additionally, the ultimate recovery exceeds the experimental result. On the other hand, the match with the temperature profile is excellent, especially for arrival of the front. This quality of match, with the exception of the temperature overshoots in the Annulus – Inlet (26, 1, 2) and Column – 25 cm (1, 1,13) points (which were not targeted for matching), is seen at all the other measurements as well.

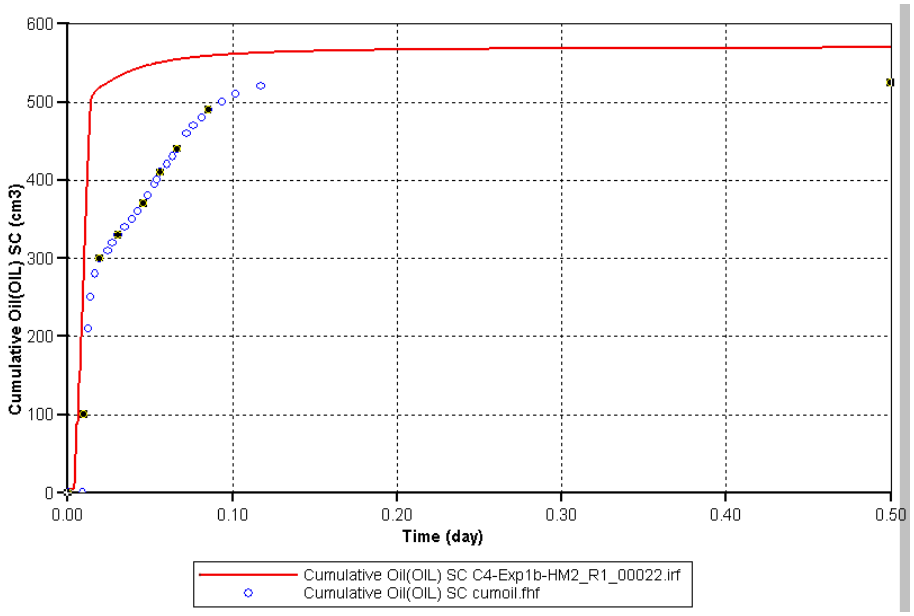

Figure 4.25. Global optimum result for cumulative oil.

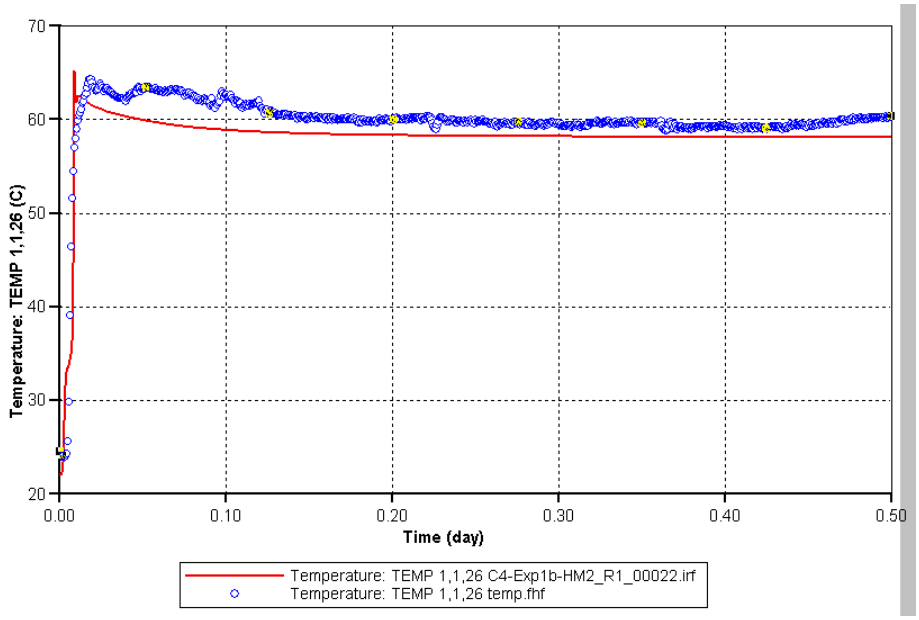

Figure 4.26. Global optimum result for Column – 50 cm temperature profile.

For the optimal global case, the cumulative oil objective function (31.9%) was higher than in the base case (23.2%), indicating a worse fit under the optimal values. Referring back to Figure 4.23 from the sensitivity analysis, better fits to the cumulative recovery can be achieved within the given parameter range than were achieved with the optimum values. Therefore, I chose to rerun the history match using only cumulative oil as the objective function. In this run, the cumulative oil objective function was decreased from 37.9% to 13.7% in the optimal case. Figure 4.27 is the comparison of the optimal result for cumulative oil to the experimental data. While the fit is much better than in the global optimum, it still does not reflect the transition from the liquid extraction phase to the film drainage phase. Figures 4.28 through 4.33 show the fit achieved for the temperature fronts. While they are not the exact match seen when temperature objective functions were considered, they are still quite good. The good fit to the temperature profiles and early cumulative oil profile in both cases mean that the liquid extraction mechanism is being adequately modeled with the parameters in this study. However, the lack of match in the film drainage region of the curve even when the other parameters are right means that a parameter underlying the film drainage process needs adjustment. This parameter is relative permeability. Because liquid extraction is a single phase process, the lack of relative permeability has no effect. However, during the two-phase flow of film drainage, relative permeability plays a significant role and its adjustment is necessary to complete our modeling efforts. Table 4.4 compares the parameter values used for each optimal case. The differences in the liquid extraction parameters are a result of the lack of relative permeability. CMOST is adjusting the available parameters in an attempt to account for the impact of relative permeability that is missing. Were relative permeability accounted for, the two sets of values should be the same. However,

even when accounting for all parameters, the solutions still might not converge on the same parameter set due to the non-uniqueness of simulation history-matching.

CMOST Variable	Global	Cumulative Oil
varC4KVAL	1.05	1.15
varDIFFGASC4	1.00E-06	1.00E-05
varDIFFGASOIL	1.00E-05	1.00E-05
varDIFFOILC4	4.21E-09	4.21E-10
varDIFFOILOIL	4.21E-09	4.21E-10
varPERMSAND	132300	113400

Table 4.4. Comparison of optimal values for the global and cumulative oil objective functions.

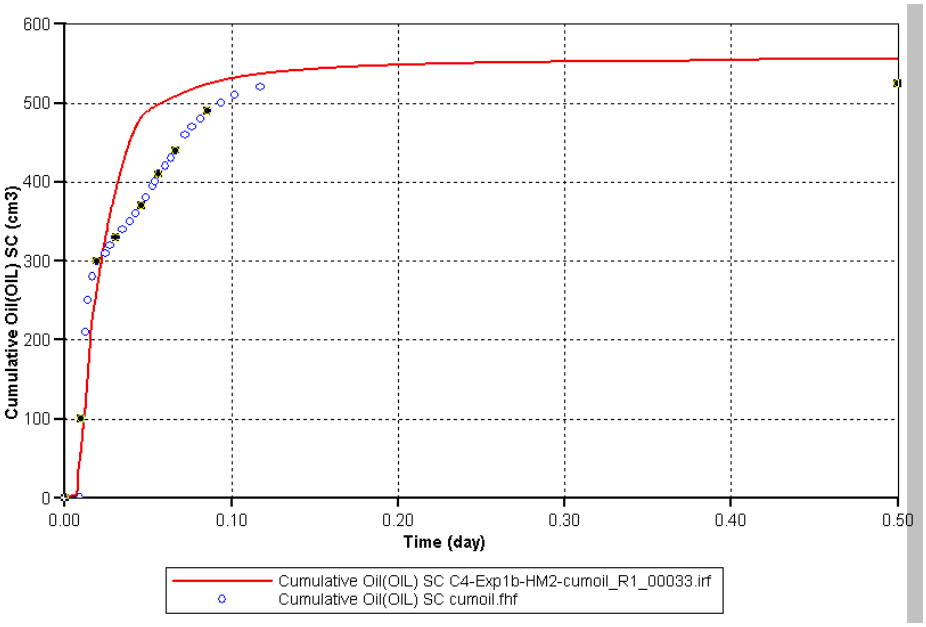

Figure 4.27. Match for cumulative oil when only using cumulative oil as objective function.

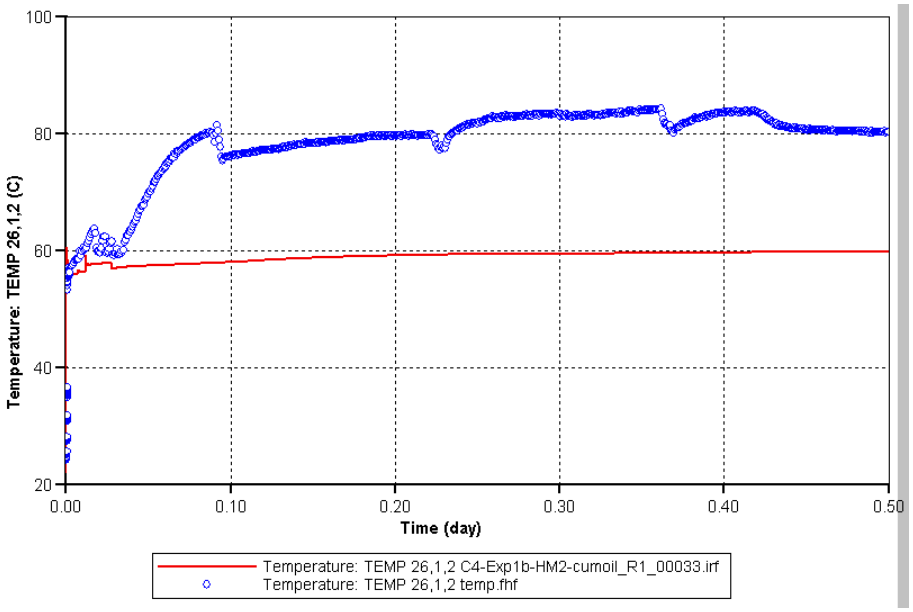

Figure 4.28. Match for Annulus - Inlet temperature profile when only using cumulative oil as objective function.

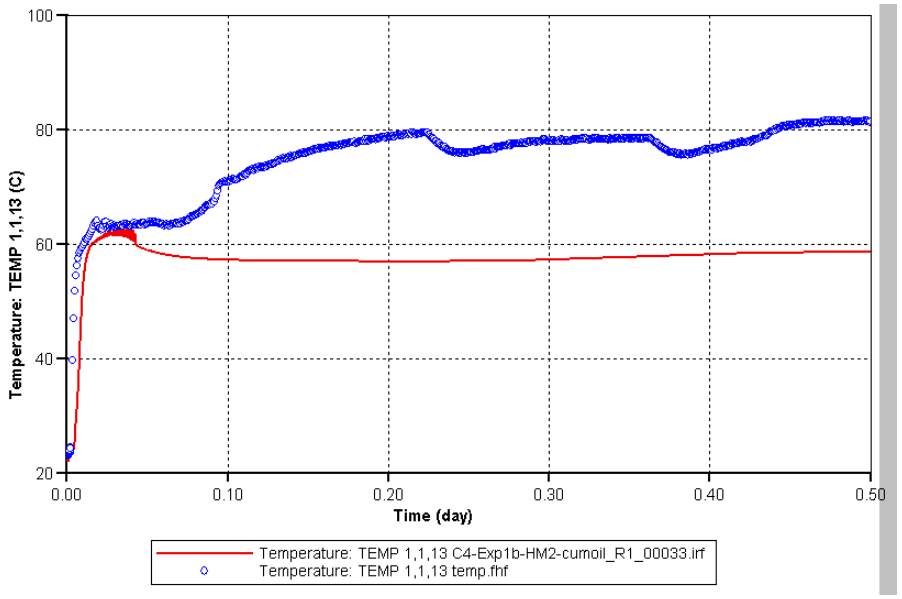

Figure 4.29. Match for Column – 25 cm temperature profile when only using cumulative oil as objective function.

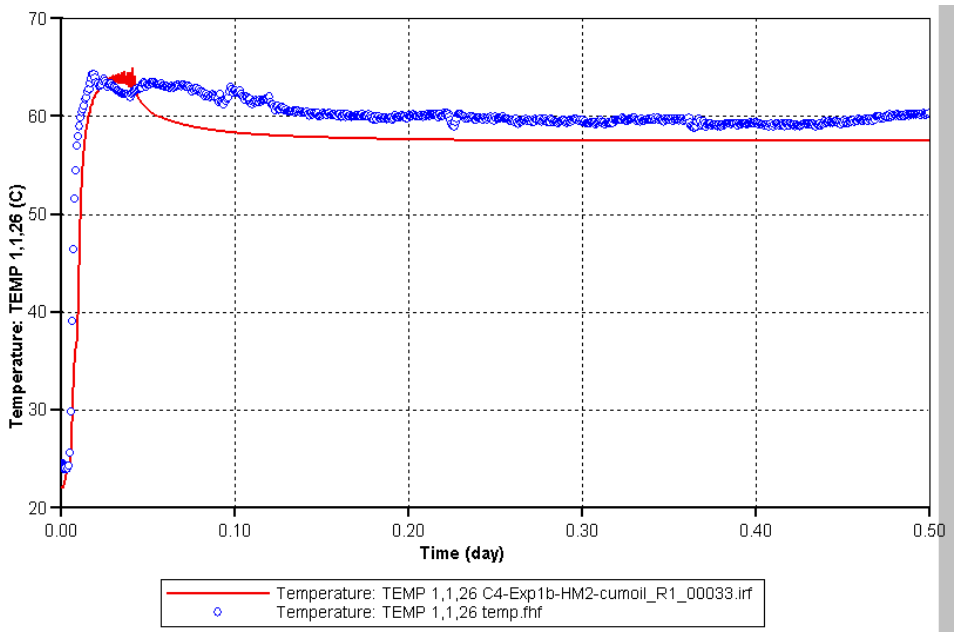

Figure 4.30. Match for Column – 50 cm temperature profile when only using cumulative oil as objective function.

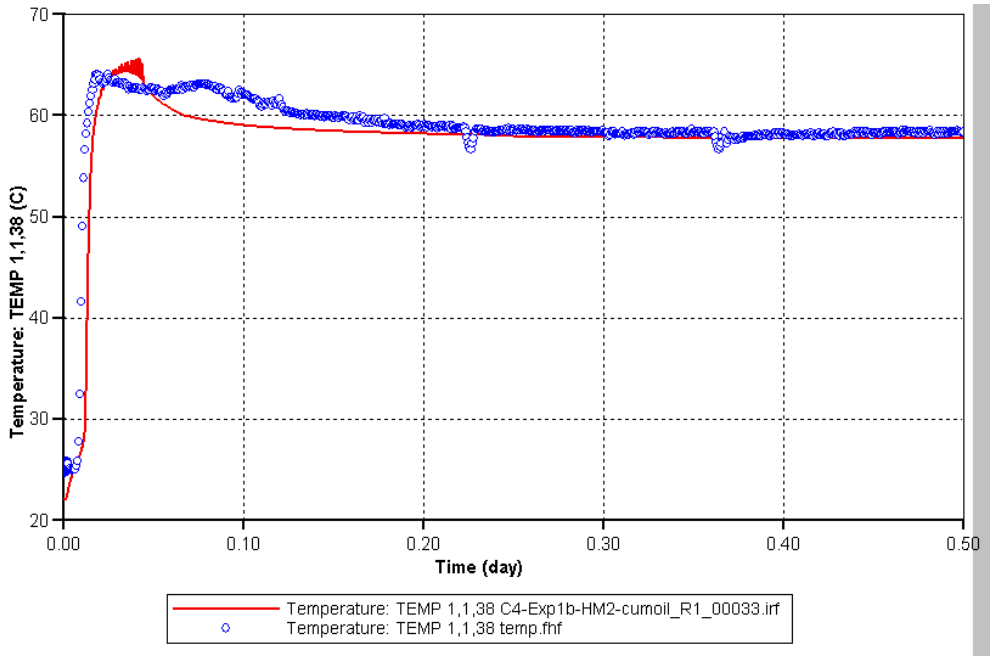

Figure 4.31. Match for Column – 75 cm temperature profile when only using cumulative oil as objective function.

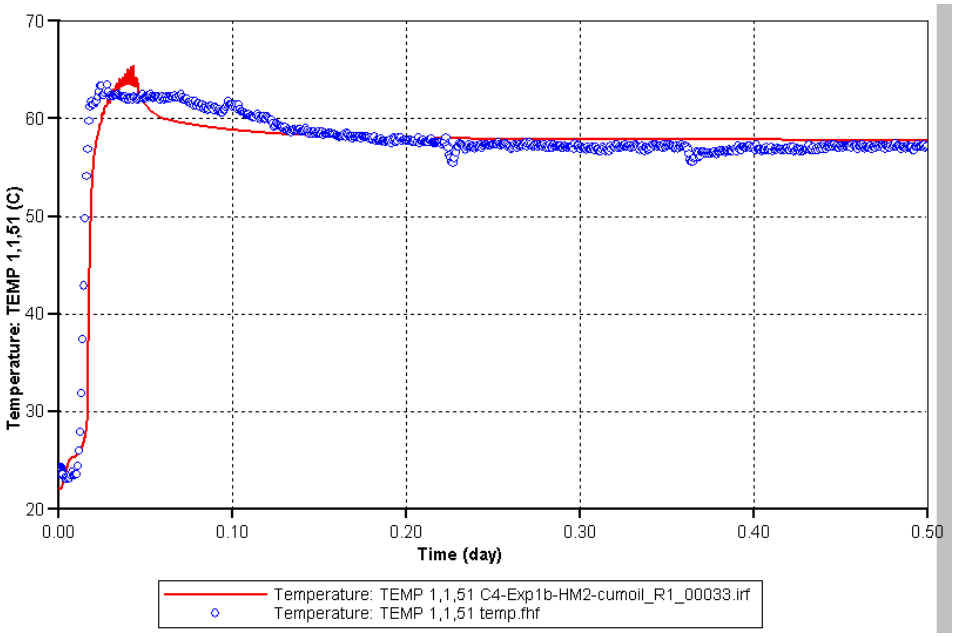

Figure 4.32. Match for Column – 100 cm temperature profile when only using cumulative oil as objective function.

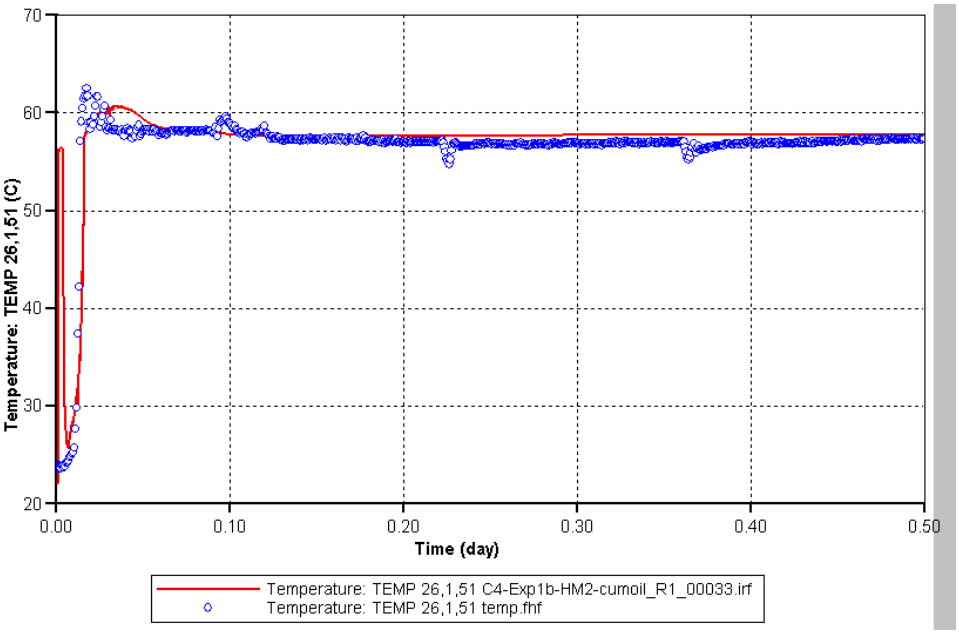

Figure 4.33. Match for Annulus – Outlet temperature profile when only using cumulative oil as objective function.

4.5 CONCLUSIONS

The purpose of this work was to identify and evaluate the significance of physical process parameters as well as the adequacy of thermodynamic and transport property models available in STARS related to the description of our process. Additionally, the impact of parameter uncertainty on process modeling was explored. An initial sensitivity analysis showed that the uncertainty in thermal properties did not significantly impact the simulation output. However, uncertainty in the parameters directly related to the production mechanisms – oil and n-butane diffusion coefficients, sand pack permeability, and butane partitioning coefficients – resulted in significant variations in simulation output. The second sensitivity analysis focusing on process parameters showed that cumulative oil was most sensitive to 'C4' component oil phase diffusivity and k-value. More data would need to be collected to reduce the uncertainty in these values for future simulation work.

The history-matching efforts were very illustrative. A first attempt using the cumulative oil and temperature profiles as objective functions produced an optimal solution that matched the temperatures well but resulted in a worse match for cumulative oil than the base case. When only the cumulative oil was used as an objective function, the cumulative oil match was greatly improved with only a small decrease in the goodness of the temperature fits. The good match for temperature indicates that the uncertainty range for the parameters representing the liquid extraction mechanism is adequate. However, the lack of fit to cumulative oil indicates that a parameter underlying the film drainage process needs adjustment. This parameter is relative permeability, which will impact the two-phase flow occurring during film drainage. If this process were to be included in the history-matching efforts, a global optimum could be found that generates a quality match for cumulative oil and temperature simultaneously. However,

this solution might not generate the true values for all parameters due to the non-uniqueness of the history matching process.

Chapter 5 – Phase Behavior and Rheological Characterization of Silica Nanoparticle Gel

5.1 Introduction

As discussed by Metin et al. (2011), in the presence of electrolytes, nanoparticle dispersions become unstable above a critical salt concentration. Over a certain range of salinities, the unstable solutions form a gel. Previous conformance control efforts with silica gels (e.g. Jurinak and Summers 1991; Burns et al. 2008; Dai et al. 2010; Stavland et al. 2011) focused on the gelation of sodium silicate solutions triggered by pH or salinity changes prior to injection and required high silica concentrations. Conformance control operations using the silica nanoparticle gels discussed in this chapter have three key differences from previously studied silica gels: the silica is in the form of colloidal silica, a suspension of fine amorphous, nonporous, and typically spherical silica particles (SiO_2) in the liquid phase, not sodium silicate powder (Na_2SiO_3); the gelation would be controlled by salinity contrasts within the reservoir rather than being triggered by changes in pH or salinity prior to injection; and gelation occurs at very low silica concentrations.

This chapter presents the equilibrium phase behavior of silica nanoparticle dispersions in the presence of sodium chloride (NaCl) and the rheology of particle dispersions in the gel region. The characteristic time for the onset of gelation as a function of silica and NaCl concentration and temperature was also determined.

5.2 Materials and Methods

The material under study is aqueous dispersions of silica nanoparticles. The nanoparticles provided by 3M, Co. (St. Paul, MN) have a mean diameter of five nm. The NexSil5 nanoparticles purchased from Nyacol have a bimodal size distribution with peaks at 3 and 18 nm. Phase behavior tests were carried out in glass vials in temperature-

controlled ovens. Phase behavior diagrams were constructed at 25 °C for both particles and at 70 and 90 °C for the NexSil5 particles.

Rheological measurements were carried out on an ARES LS-1 rheometer using a parallel plate fixture. The diameter of the parallel plate was 50 mm and the set gap between the lower and upper plate was 1 mm. The measurements were conducted at 25, 40, 55 and 75 ^{o}C. A solvent trap was used to prevent the evaporation of water from the solution. Dynamic and steady shear experiments were carried out. The nanoparticle dispersion was mixed with the NaCl solution and then placed on the lower fixture of the parallel plate. A dynamic time sweep test was first conducted at one rad/s frequency and one percent strain. The time evolution of storage and loss modulus, G' and G'', was measured for 10,000 seconds after the onset of gelation. Then, frequency sweep and strain sweep tests were carried out. After these tests, steady shear rates were applied and viscosity was recorded as a function of shear rate.

5.3 Results and Discussion

The results on phase behavior of silica nanoparticle suspensions as a function of NaCl and nanoparticle concentration are presented in this section. The rheological measurements of samples in the gel region are discussed in detail in the next section.

5.3.1 Phase Behavior

There are three phases in the nanoparticle phase diagram. Below the critical salt concentration (CSC) (Metin et al. 2011), the nanoparticle dispersion is stable and appears as a homogeneous clear liquid. Above the CSC, the suspension is unstable. The unstable suspensions have two distinct behaviors. At salinities above the CSC but below the upper gelation salt concentration, the unstable solution forms a gel phase. Many authors have proposed that gel formation is due to dynamic arrest of the particle clusters (Campbell et

al. 2005; Lu et al. 2008; de Candia et al. 2005). In colloidal suspensions, for longer separation lengths, repulsion is greater than Van der Waals attraction resulting in a long range repulsive barrier. At shorter lengths, Van der Waals attraction is still the dominating force (de Candia et al. 2005). The short range attraction is responsible for cluster growth. The long range repulsive forces lock the clusters into a cage (gel) during dynamic arrest (Campbell et al. 2005). Above the upper gelation salt concentration, the solution forms a viscous liquid. The major visual difference between the two phases is that the gel does not flow when the sample is tilted, but the viscous liquid does flow. In the viscous liquid region, the network of aggregates, which is essential for gel formation, is absent. This is supported by the theory of dynamic arrest, which requires long-range repulsive forces to suspend the clusters in a gel. Without a repulsive force, cluster growth continues which produces a viscous fluid but no gel properties. Figure 5.1 shows the total interaction potential between 5 nm diameter nanoparticles in aqueous dispersions at increasing salinities. As the salt concentration increases, the repulsive energy barrier decreases. The transition between gel and viscous liquid occurs when the repulsive force is no longer sufficient to initiate dynamic arrest.

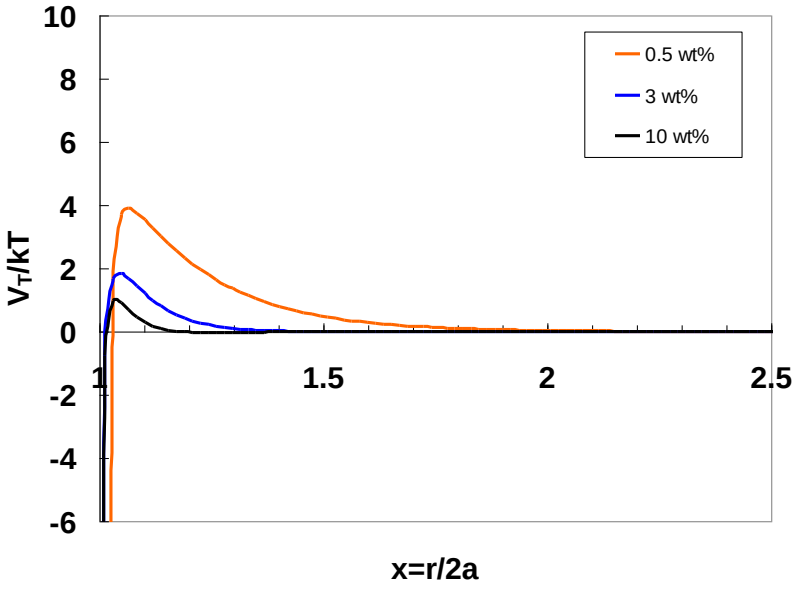

Figure 5.1. Total interaction potential for 5 nm 3M silica nanoparticles for 0.5, 3 and 10 wt% NaCl. Total interaction potential for 5 nm 3M silica nanoparticles for 0.5, 3 and 10 wt% NaCl.

It is known that strongly-aggregating colloidal suspensions form gels, whose stability depends on the volume fraction of the particles (Senis et al. 2001). Within the gel region, two types of gels are observed. At lower silica concentrations, the solution has two phases. A solid gel phase is topped by a clear supernatant liquid. At higher silica concentrations, the solution is a single-phase gel. Two-phase gels are a result of insufficient number of aggregates to incorporate the entire volume of water into the gel. Figures 5.2 and 5.3 show phase behavior diagrams for the 3M and NexSil5 particles, respectively, at 25 ^{o}C. The monodisperse 3M particles have a wider gel region with respect to salinity than the bimodal NexSil5 particles. The boundary between single-phase and two-phase gel is only a function of silica concentration for both particles.

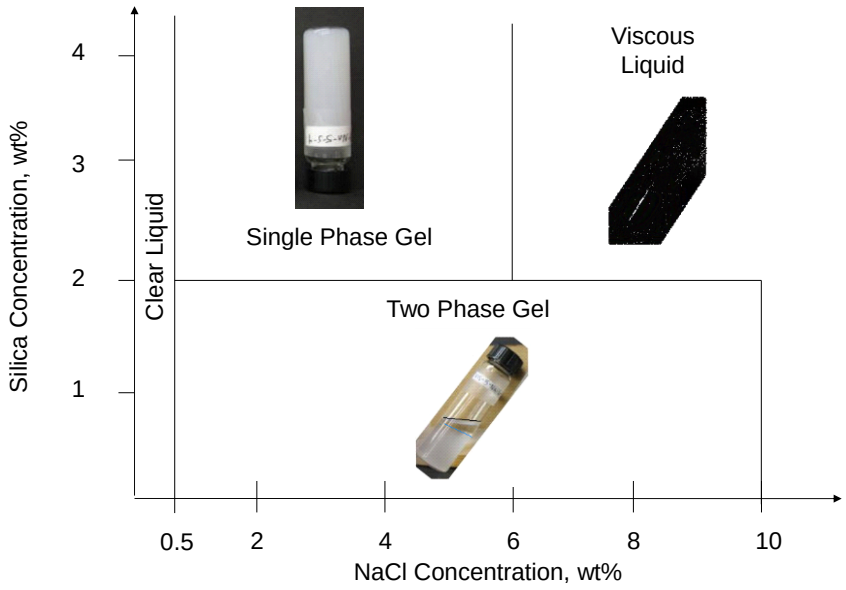

Figure 5.2. Phase behavior diagram of 5 nm 3M silica nanoparticles at 25 °C.

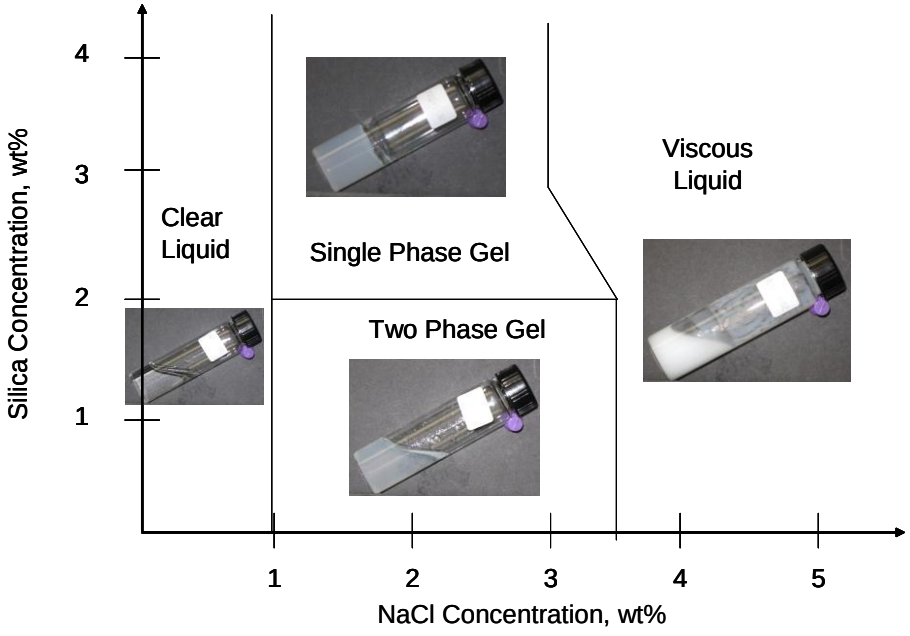

Figure 5.3. Phase behavior diagram of NexSil5 silica nanoparticles at 25 °C.

When the particle volume fraction is small, isolated large flocs, which are denser than the suspending medium, may form and can sediment under gravity. However, for large particle volume fractions, gelation usually occurs and sedimentation is then avoided unless the gel structure is so fragile that it collapses under its own weight (Larson 1999). The sedimentation phase was not observed in our gel region suggesting that the critical volume fraction for gelation must be less than one weight percent (the lowest value studied). Figure 5.4 is a schematic presentation of sedimentation and gelation of aggregates. The structure of the aggregates within the sediment, such as the solid volume fraction, is discussed based on the equilibrium approach by Metin et al. (2012). Even though both nanoparticle dispersions display the same four phase behavior regions, the extent of each region, specifically the gelation window, is different. As a consequence, the range of reservoir salinities for which each particle will gel in-situ will change depending on which particle is used. Our work suggests that the phase behavior of any given nanoparticle will have to be clearly understood before application to ensure that gelation will occur at reservoir salinity.

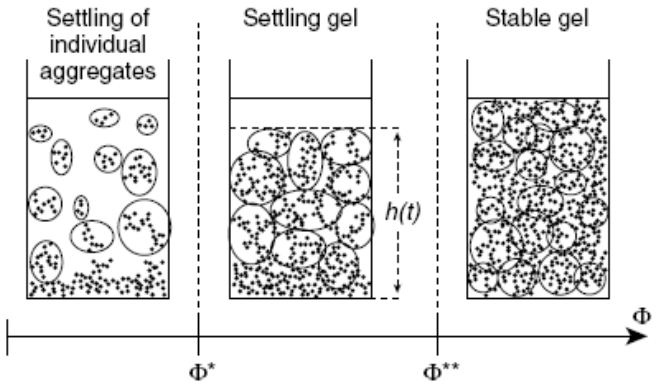

Figure 5.4. Schematic presentation of sedimentation and gel behavior of aggregates as proposed by Senis and Allain (1997).

The effect of temperature on particle phase behavior was studied for the NexSil5 particles. Figure 5.5 shows the phase diagrams for the NexSil5 particle at 25, 70, and 90 °C. The primary impact of increasing temperature is to decrease the critical salt concentration. This observation may be explained based on relative magnitude of the energy barrier and the average kinetic energy of nanoparticles. An increase of the average kinetic energy with temperature gives rise to the particle collisions that result in aggregation. As a consequence, a higher energy barrier (i.e. lower salt concentration) is required to maintain the aqueous stability of the nanoparticle dispersion.

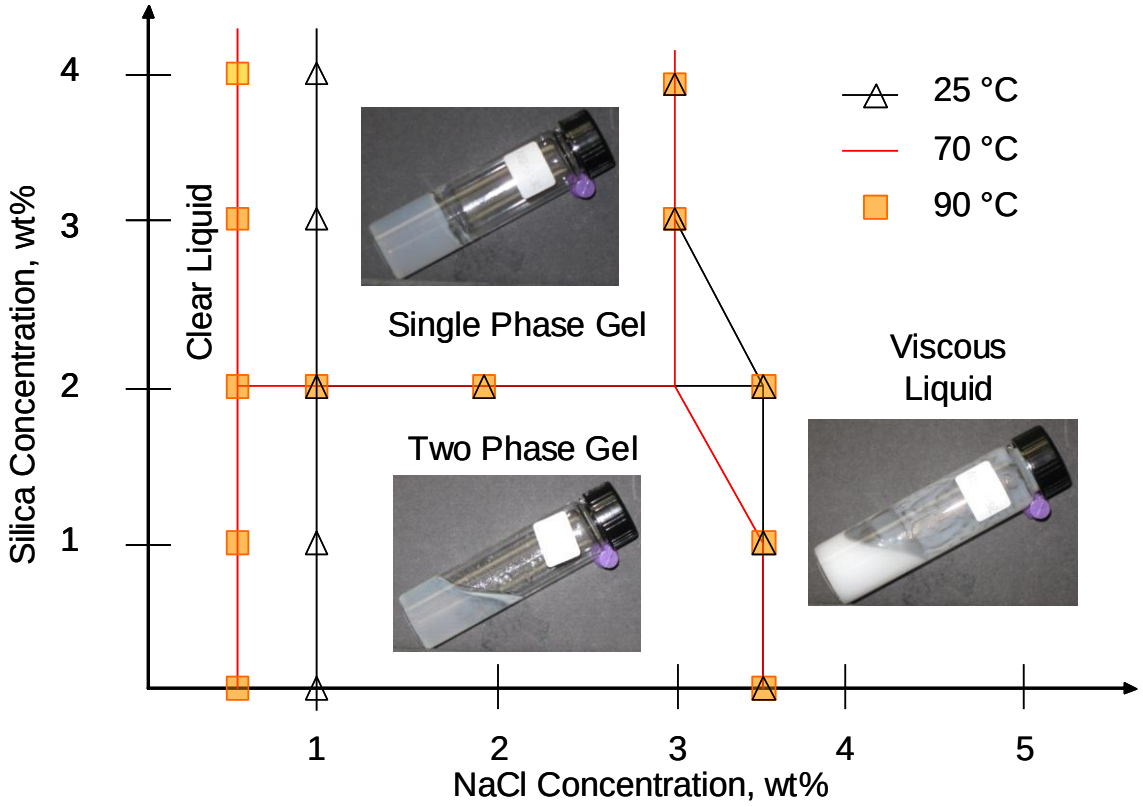

Figure 5.5. The impact of temperature on the phase behavior diagram of the NexSil5 silica nanoparticle dispersion.

5.3.2 Rheological Measurements

In addition to understanding the equilibrium behavior of the solutions to correctly identify the gelation window, it is important to understand the kinetics of the gelation. A way to explore rates of structural rearrangement within a complex fluid without significantly deforming the fluid's microstructure is to apply small-amplitude oscillatory shearing (Larson 1999). The sinusoidally varying stress can be represented as

$$\sigma(t) = \gamma_0 \left[G'(\omega)\sin(\omega t) + G''(\omega)\cos(\omega t) \right] \tag{5.1}$$

Shear stress $\omega(t)$ is proportional to the amplitude of the strain γ_0. In Equation 5.1, $G'(\omega)$ is the storage modulus and is in phase with the strain. $G''(\omega)$ is the loss modulus and is in phase with the rate of strain. The storage modulus represents storage of elastic energy, and the loss modulus represents the viscous dissipation of that energy (Larson 1999). The ratio G"/G'>>1 represents materials that are liquid-like, and the ratio G"/G'<<1 represents solid-like materials.

Early on, aggregate size grows exponentially in time until the fractal aggregates become large enough to form a network and fill the entire volume of the solution if nanoparticle concentration is sufficient. The system then crosses over to the critical growth associated with gelation (Martin and Wilcoxon 1989). Measurements taken with dynamic light scattering (DLS) and ultraviolet-visible spectrophotometer (UV-Vis) confirm the exponential growth of aggregate size in time before the onset of gelation. The UV-Vis measurements were used as a gelation time estimate. For samples with gelation times in excess of a few hours, the samples were mixed and allowed to sit in closed vials prior to placing the solution on the rheometer plate in order to reduce measurement time prior to gelation.

Dynamic time sweep tests were conducted to quantify the gelation time as a function of silica concentration, salinity, and temperature. Salinity and temperature are

reservoir properties that are constraints to the gel's application for conformance control. Silica concentration will be an operating variable that can be adjusted as necessary to ensure gelation at in-situ conditions and control project economics. The concentrations for the silica and salinity scan were chosen so that they would fall within the gelation window of both particles. A secondary silica scan was run for the 3M particle at a higher salinity outside of the NexSil5 gelation window. For the primary silica scan, the temperature was constant at 25 ^{o}C with a salinity of 3 wt% NaCl. For the secondary silica scan, the temperature was constant at 25 ^{o}C with a salinity of 5 wt% NaCl. For the salinity scan, the temperature was constant at 25 ^{o}C with a silica concentration of 4 wt%. For the temperature scan, the silica concentration was 3 wt% with a salinity of 3 wt%. The scans are overlain on the phase diagram of the 3M nanoparticle in Figure 5.6.

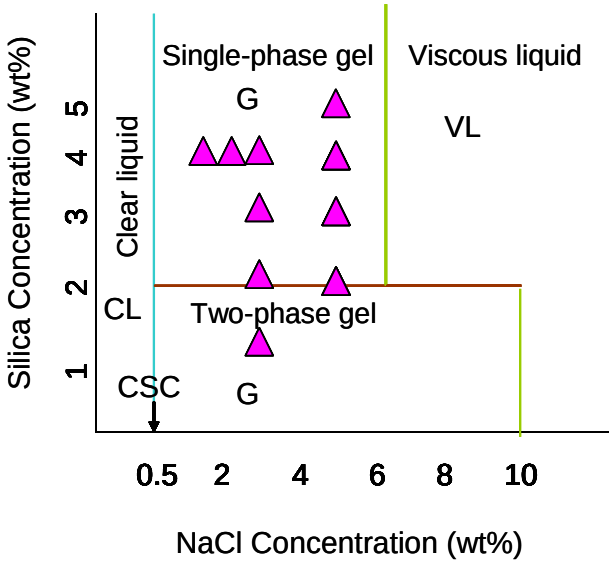

Figure 5.6. Schematic presentation of the samples studied during rheology experiments.

The onset of gelation is determined by using a UV-Vis spectrophotometer and strain-controlled rheometer. The evolution of G' and G" are recorded as a function of

time and the onset of gelation is determined based on the sudden increase of G', as shown with an arrow in Figure 5.7. The onset of gelation, estimated by evaluating the sudden change in G' in the rheology experiments, agrees well with that determined by the change in absorbance at a specific wavelength (700 nm in this case) as measured by a UV-Vis spectrophotometer. A change in aggregate size can be captured by measuring the absorbance using a UV-Vis spectrophotometer (Metin et al. 2011).

In Figure 5.7, the increase in absorbance corresponds to the increase in aggregate size, and when the network is formed, a plateau is reached. The transition corresponds to the onset of gelation as determined by G' in rheology experiments. After the gelation time, G' increases significantly, while the ratio G"/G' becomes much smaller than one indicating that the sample has a solid-like behavior. The scattered data for early G'/G" measurements is due to a lack of accuracy at smaller values. The storage modulus increases during the dynamic measurements suggesting that the gel network gets stronger and stronger over time. Maley et al. (2005) also showed that colloidal silica gels stiffen with time through light scattering and rheological measurements. The authors argued that there was no change in the gel structure but the interparticle spring constant was time-dependent and responsible for the increase in G'. According to their hypotheses, the kinetics of bond formation is reaction limited, which leads to an increase in the contact area between network forming particles.

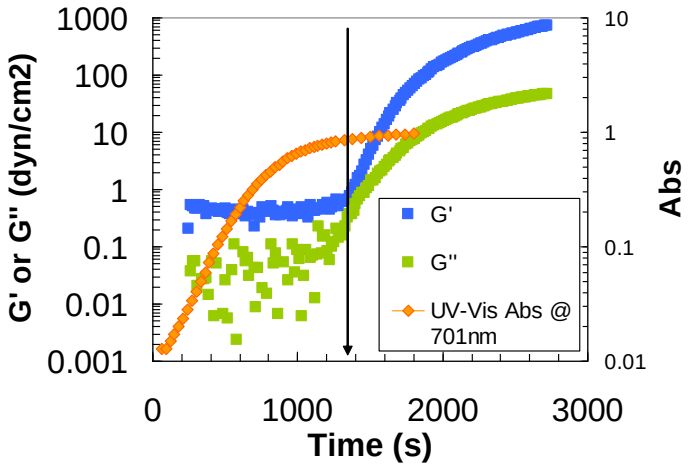

Figure 5.7. Dynamic time sweep test and UV-Vis absorbance of 4 wt% 3M silica and 5 wt% NaCl.

Gelation time decreases as silica concentration increases as shown in Figure 5.8. This observation is in agreement with the way in which the kinetics of the aggregation of silica nanoparticle suspensions change as a function of silica, as discussed by Metin et al. (2012). For the 3M particles, the change in gelation time is more significant at 3 wt% NaCl than it is at 5 wt% NaCl (Figure 5.8). The effect of particle size distribution on gelation time at constant salinity can also be seen in Figure 5.8. The polydispersivity seems to decrease the gelation time but the rate of decrease in gelation time as nanoparticle concentration increases is the same as that for monodisperse 5nm 3M particles.

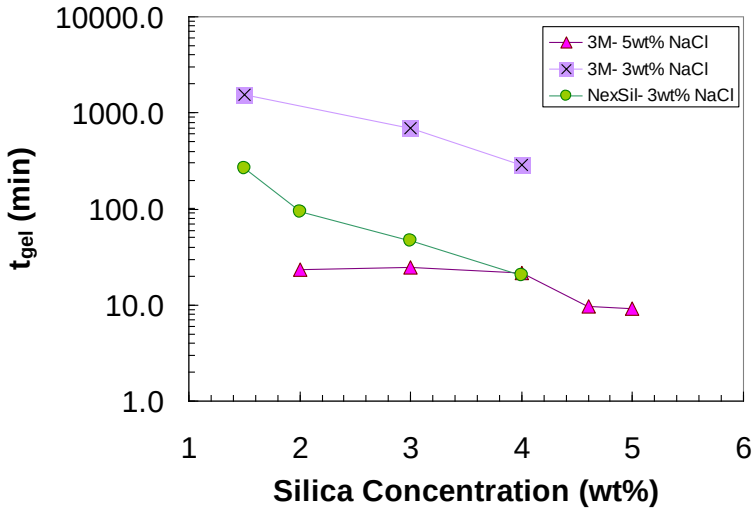

Figure 5.8. Rheometer measurement of gelation time as a function of silica concentration at 25 °C.

An increase in salinity decreases the gelation time (see Figure 5.9). This observation is also in close agreement with the way in which the kinetics of aggregation of silica nanoparticle suspensions change, as reported by Metin et al. (2012). The gelation time changes orders of magnitude as the NaCl concentration is increased. Again, the polydisperse NexSil5 particles have shorter gelation times, but for a given silica concentration show more significant decrease in gelation time with increasing salinity than for the monodisperse 3M particles (compare the slopes in Figure 5.9).

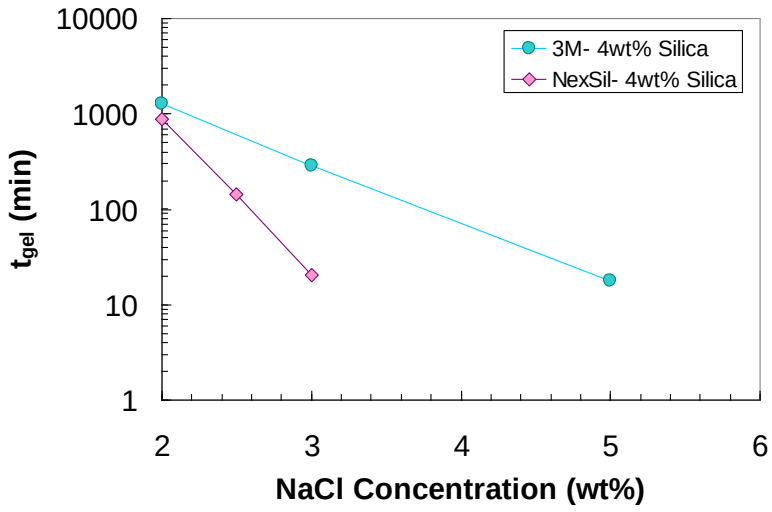

Figure 5.9. Rheometer measurement of gelation time as a function of salinity for 4 wt% silica suspensions at 25 °C.

Temperature also significantly effects the gelation time. An increase in temperature decreases the gelation time (see Figure 5.10). The activation energy (E_a) for kinetically controlled cross-linking was used by Amiri et al. (2011) to characterize the temperature dependency of the gelation time for silica suspensions (Equation 5.2).

$$\ln t_g = \frac{E_a}{RT} + A \tag{5.2}$$

where t_g is the gelation time, R is the gas constant, T is the temperature in Kelvin, and A is a constant. The activation energy is calculated using data in Figure 5.10 to be 84 and 73 kJ/mol for monodisperse 3M particles and polydisperse NexSil5 particles, respectively. These apparent activation energies for bridging of aggregates are comparable to the values reported by Silva and Vasconcelos (1999), Wang and Zhang (2009) and Amiri et al. (2011). The decrease in gelation time at high temperature was attributed to larger Brownian motion of the particles resulting in faster collisions (Metin

et al. 2011). Similar results for gelation time were reported for silica particles suspended in ethanol by Smith and Zukoski (2006).

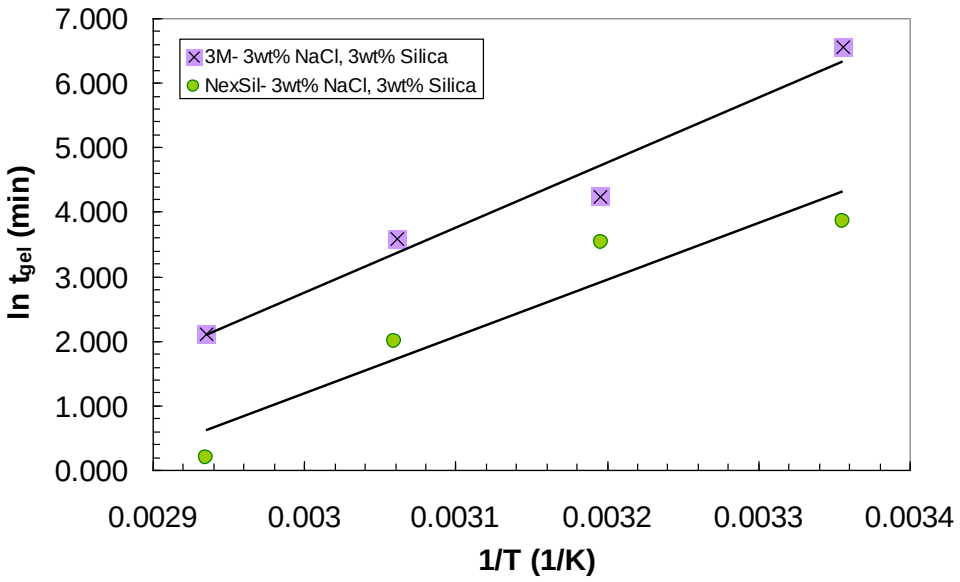

Figure 5.10. Rheometer measurement of gelation time as a function of temperature for 3 wt% silica suspensions with 3 wt% NaCl. The lines correspond to theory given in Equation 5.2.

The dependence of gelation time on silica, NaCl concentration, or temperature follows an exponential decrease (Figures 5.8 through 5.10). This means that a small change in any of the variables can result in a significant change in gelation time. The gelation time can vary an order of magnitude with changes in the primary control variables. This necessitates a thorough understanding of the gelation kinetics of the nanoparticles before designing a conformance control test. Other rheological quantities that are important for strongly flocculated gels include linear and nonlinear storage moduli at high and low frequencies and shear rate dependent viscosity (Larson 1999). The silica nanoparticle gels show solid-like behavior which is shown by the storage and

loss modulus profiles in Figures 5.11 through 5.14. Hyun et al. (2002) used large amplitude oscillatory shear (LAOS) behavior to classify polymer samples. I applied this classification to the nanoparticle samples. The decrease in G" at low shear rates was not observed by Hyun et al. (2002), so only the G" behavior after the minimum was used for interpretation. For most samples studied the G' and G'' profiles show an increase followed by a decrease as strain increases, which is classified as strong strain overshoot. For the G' profiles (Figures 5.11 and 5.13), the increase is difficult to see because of the large range on the y-axis.

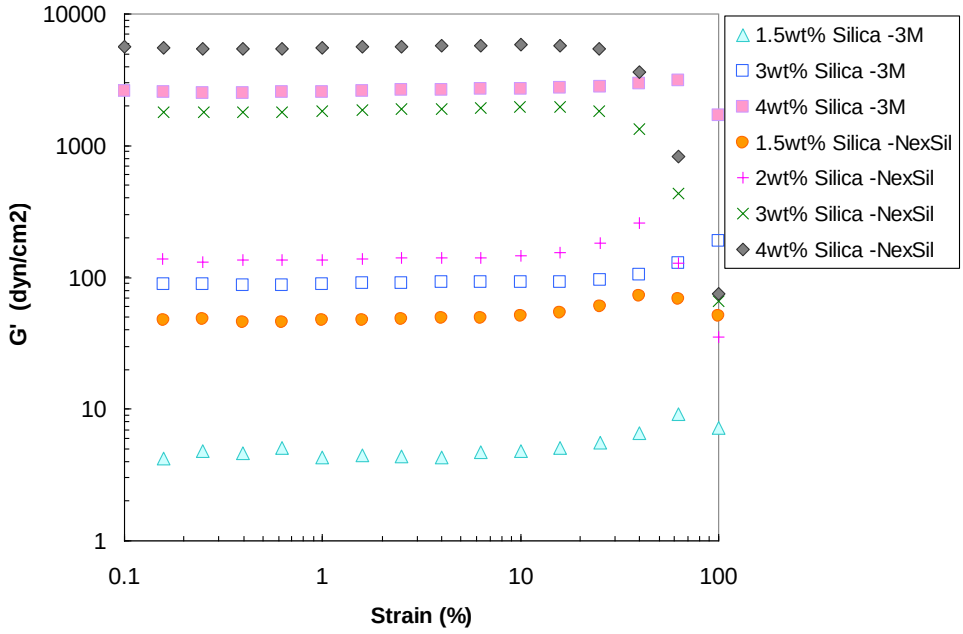

Figure 5.11. Storage modulus (G') as a function of silica concentration at 25 °C.

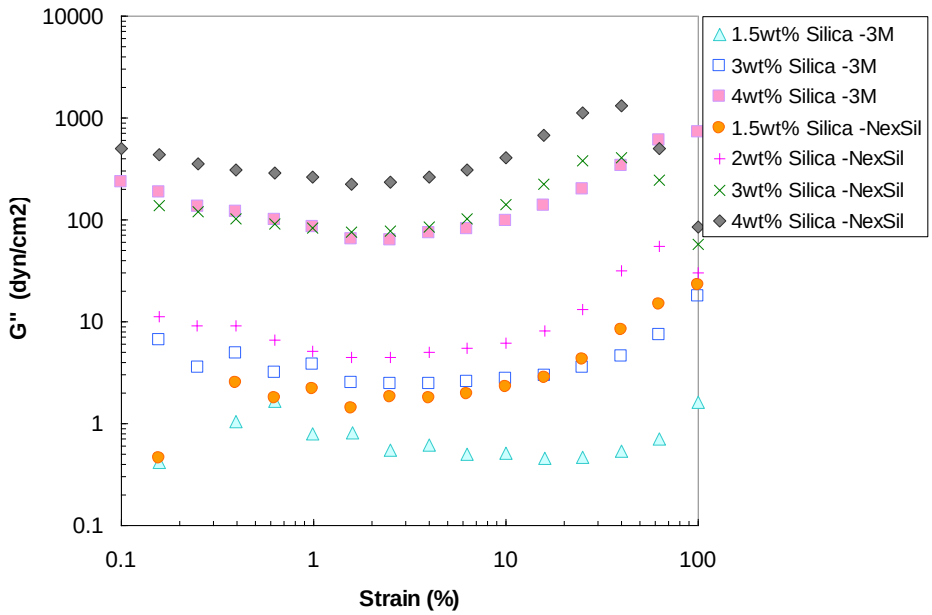

Figure 5.12. Loss modulus (G") as a function of silica concentration at 25 °C.

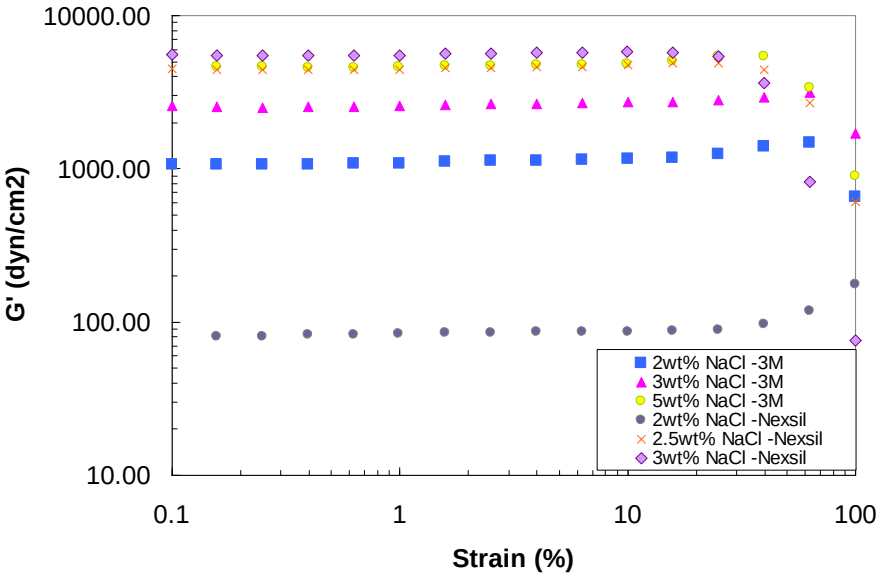

Figure 5.13.Storage modulus (G') as a function of NaCl concentration at 25 °C.

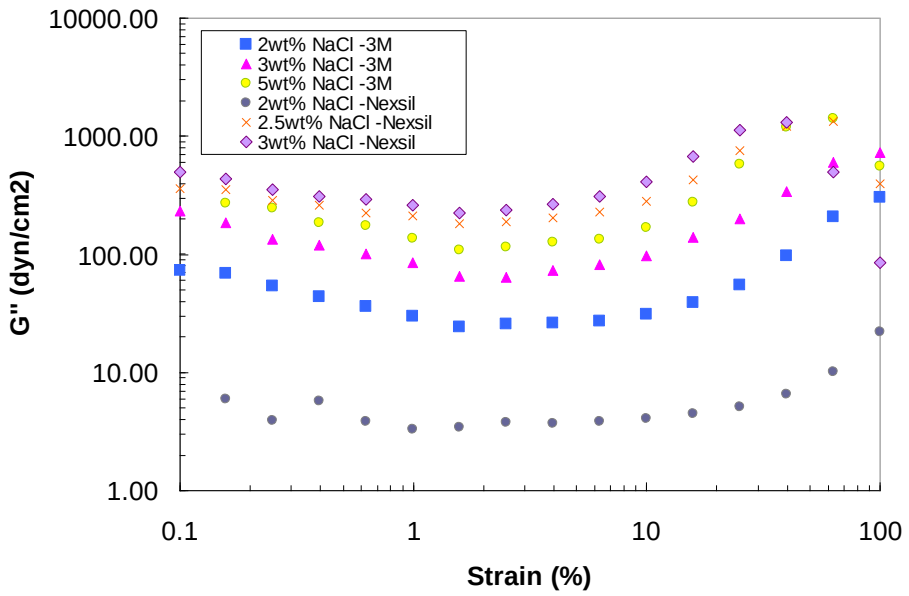

Figure 5.14. Loss modulus (G") as a function of NaCl concentration at 25 °C.

Strain hardening arises from strong secondary bonding effects, such as the formation of a shear induced network. Initial increase in loss modulus with strain is attributed to structural changes during the breakdown of agglomerates to a larger number of smaller size units which are more dissipative. Destruction of the structure or breakdown of the filler network occurs at higher strain, and the loss modulus decreases because of further breakdown of the structure (Yziquel et al. 1999). Aggregate size decreases as the silica concentration increases (Metin et al. 2012). The increase in G" as silica concentration increases is likely a result of these smaller, more dissipative aggregates at higher silica concentrations.

Martin and Wilcoxon (1989) discussed that at small strain, Brownian motion is able to restore the structure to the equilibrium value during the oscillation cycle. Therefore, the storage modulus remains constant. After a certain strain, the strain amplitude becomes significant and the Brownian motion is no longer capable of restoring

the microstructure. Above this critical strain, the storage modulus decreases, and the loss modulus continues to rise with strain amplitude. This behavior is exhibited in both silica nanoparticle gels studied. The critical strain determined from Figures 5.9 and 5.11 appears to be constant as a function of silica concentration. The samples withstand a minimum critical strain of 10% before the structure breaks. On the other hand, the critical strain does not have a clear dependency on salt concentration for both types of particles studied. Below the critical strain, G' increases with particle or NaCl concentration (Figures 5.15 and 5.16). This power law behavior was also reported by Shih et al. (1990) with boehmite alumina gels. The authors considered the structure of a gel as a collection of flocs, which are fractal objects closely packed throughout the sample. A continuous network of particles is formed before settling occurs with the resulting suspension having a very high viscosity and a finite shear modulus. The authors observed a power law behavior of G' vs ϕ^m. In our experiments, m is calculated to be 5.9 and 4.2 for 3 and 5 wt% NaCl 3M particles and 5.1 for 3 wt% NaCl NexSil5 particles. An increase in m shows that the elasticity increases more rapidly and the network becomes more resistive (Yziquel et al. 1999).

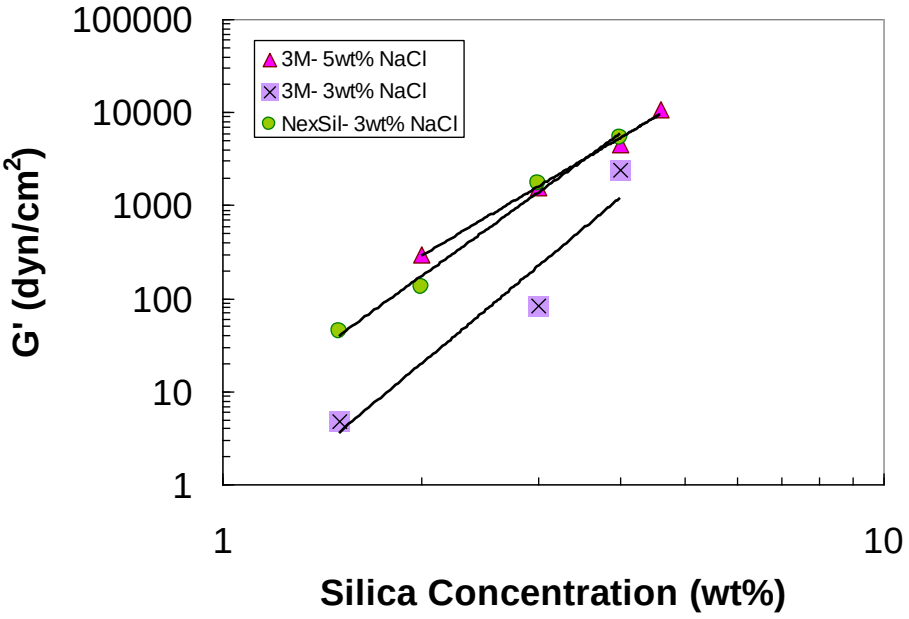

Figure 5.15. Storage modulus (G') as a function of silica concentration at 25 oC. The lines correspond to power law fit.

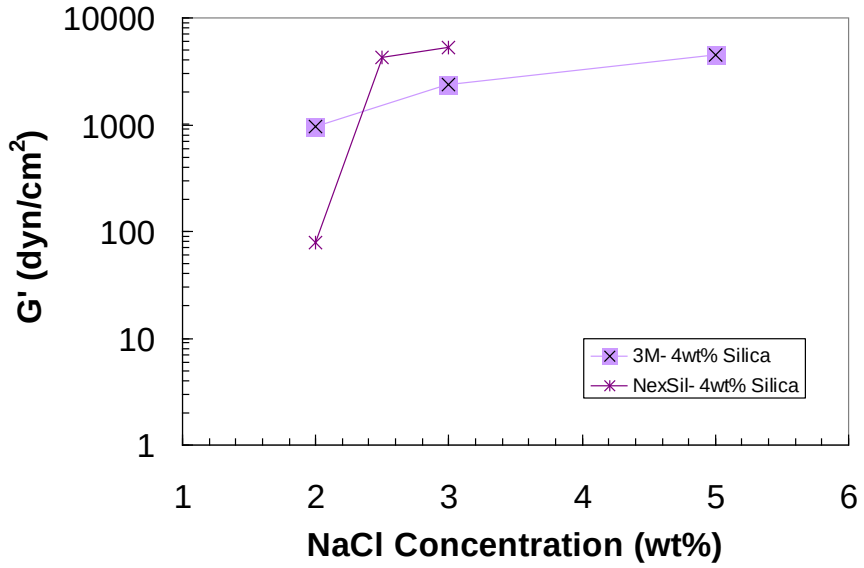

Figure 5.16. Storage modulus (G') as a function of NaCl concentration at 25 °C.

For a solid-like complex fluid, the steady shear stress is independent of shear rate, and the shear viscosity, η, decreases with increasing shear rate, $\dot{\gamma}$, as $\eta \propto \dot{\gamma}^{-1}$. A decreasing shear viscosity with increasing shear rate is called shear thinning (Larson 1999). The viscosity for each gel as a function of steady shear rate was measured 10,000 seconds after gelation. All of the gels exhibited shear thinning behavior with $\eta \propto \dot{\gamma}^{-1}$ (see Figure 5.17). Most of the samples display a power law decrease in viscosity with increasing shear rate. These samples can be modeled with the power law model (Equation 5.3). An example of power law behavior fit to the 4.6 wt% 3M silica, 5 wt% NaCl gel is shown as a solid line in Figure 5.17. The remaining samples display power law behavior at lower shear rates with a Newtonian plateau at higher rates. These samples, such as 3 wt% 3M silica, 3 wt% NaCl (dashed line in Figure 5.17), can be fit with the Carreau model (Equation 5.4). However, the Carreau model predicts a Newtonian plateau at low and high shear rates. Because this lower plateau region is missing from all samples, it is possible that the Carreau model might not be the optimal fit for all data, but it does capture the behavior recorded.

$$\eta = K\dot{\gamma}^{n} \tag{5.3}$$

where *K* and *n* are empirical parameters.

$$\frac{\eta - \eta_{\infty}}{\eta_0 - \eta_{\infty}} = \frac{1}{\left(1 + \left(K_1\dot{\gamma}\right)^2\right)^{m_1/2}} \tag{5.4}$$

where η_0 and η_{∞} are viscosities at zero and infinity shear rates, respectively, and represent the Newtonian plateau values. Other empirical parameters in Equation 5.4 are K_1 and m_1. The parameters of the Carreau model fit to the 3 wt% 3M silica, 3 wt% NaCl sample are 350000 cp, 30 cp, 20 s and 2 for η_0, η_{∞}, K_1 and m_1 respectively. This sample is the only one showing a significant plateau at high shear rates and slope steeper than -1.

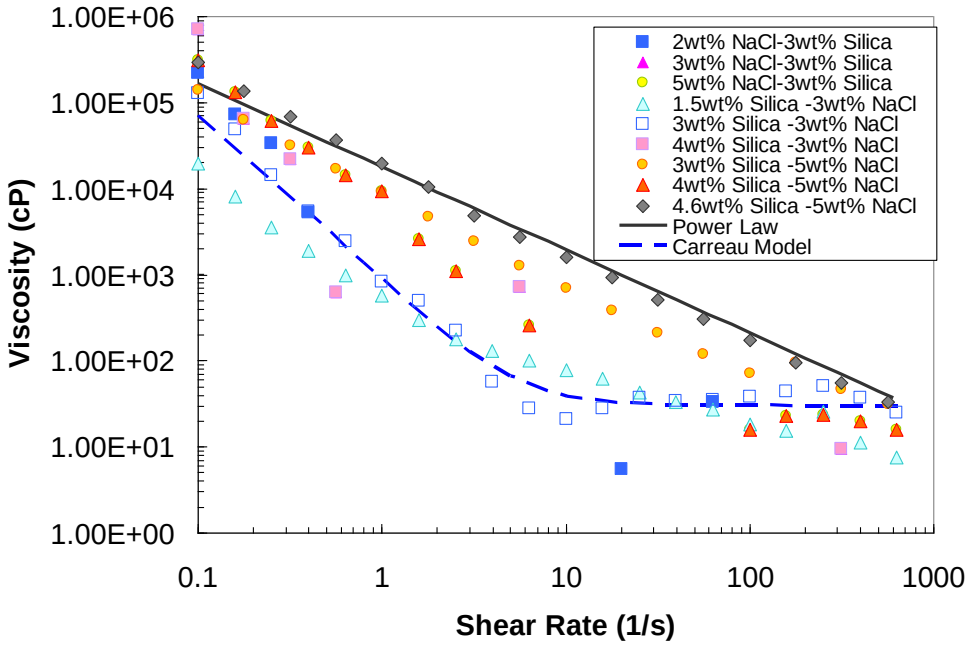

Figure 5.17. Viscosity profile for 3M nanoparticle gels at varying nanoparticle and NaCl concentrations. The solid line is a power law model fit, and the dashed line is a Carreau model fit.

5.4 CONCLUSIONS

I studied the phase behavior of silica nanoparticle suspensions as a function of silica and NaCl concentrations. Monodisperse 3M silica nanoparticles have a wider window of gelation with respect to salinity than polydisperse NexSil5 particles. The phase behavior diagrams included in this chapter will be used in future in-situ tests to determine the appropriate silica concentration and salinity gradient between injected fluid and reservoir to induce the desired degree of gelation. The gelation time decreases exponentially as a function of silica and NaCl concentration and temperature. This understanding of the gelation kinetics will determine the flow rates necessary to place the silica gel at the desired penetration depth during future experiments.

The storage modulus, G', increases with particle concentration following a power law behavior. The critical strain, 10%, is constant for the silica concentrations studied. This implies that for the two types of particles studied, single phase and two phase gels can withstand the same strain before the structure breaks. In contrast, the critical strain does not have a clear dependency on salt concentration for either of the particles studied. Steady shear measurements show that silica nanoparticle gels exhibit non-Newtonian, shear thinning behavior which could be described by the power law model or the Carreau model depending on the particle and NaCl concentration.

Chapter 6 – Conformance Control through In-situ Gelation of Silica Nanoparticle Dispersions

In a natural fracture network, the solvent injection strategy proposed in chapter three would not result in uniform injection throughout a reservoir. Preferential injection into the higher conductivity fracture areas would result in early breakthrough leaving unswept areas of high oil saturation. Conformance control would be necessary to divert subsequent solvent injection into the unswept zones. As discussed in the previous chapter, the motivation to explore the gelation properties of the nanoparticle dispersions in the presence of NaCl was to determine their scope for in-situ conformance control. The preliminary work discussed in this chapter is designed to identify the potential of this injection strategy. Once the gelation properties had been quantified, I was able to move from bulk phase study to porous media flow experiments. The hypothesis is that the gelled nanoparticle dispersions, triggered in-situ due to salinity contrasts, will be an effective conformance control process at the core scale. To do prove this, I first looked at the gelation behavior in matrix flow to gain an understanding of the mixing behavior through four core floods studying the process controls – salinity gradient and nanoparticle concentration. Then I tested the process in an artificially fractured core. All tests were done in the absence of oil.

6.1 INTRODUCTION

Due to reservoir heterogeneities, oil recovery from fluid injection during secondary and/or tertiary recovery does not occur in an ideal piston-like displacement. Rather sweep efficiency can be much lower than 100% due to heterogeneities such as high permeability control between layers (aka thief zones) and fractures. These reservoir features require the use of a conformance control agent to improve sweep. As discussed

in chapter two, current conformance control technology can be divided into four categories – polymer gels, polymer microgels, silicates, and colloidal silica. Each category has its advantages and disadvantages. Polymer gels have a history as a successful conformance control tool with the flexibility for near wellbore and in depth placement. However, they still suffer from many sort-comings including environmental safety issues, shear degradation, absorption, lack of gel time control, and poor performance under harsh reservoir conditions. Polymer microgels operate under a similar principle as polymer gels but at lower concentrations which allow deeper placement and longer gel times. However, they still have some of the same issues. Some types of microgels depend on in-situ trigger mechanisms, such as pH and temperature, which can be difficult to control/predict.

Sodium silicates and colloidal silica can better withstand harsh reservoir conditions and do not have any environmental and safety issues. Sodium silicates are silicate powder (Na_2SiO_3) dissolved in an aqueous solution. Colloidal silica is a stable aqueous dispersion of amorphous silicon dioxide particles. Both solutions behave like a Newtonian fluid before gelation, which eliminates the concern for shear degradation allowing higher injection rates to be used. Silicates, however, still suffer from lack of accurate gelation control in the field. Therefore, colloidal silica provides the best option because it has the environmental benefits of silicates with a more robust gel control and no pH limitations. Our proposed conformance control technique uses colloidal silica (aqueous silica nanoparticle dispersions) for a gelling system to address conformance control. The difference between this process and past work on colloidal silica is that no activator is used prior to injection. Rather, the salinity of the formation water is used as an in-situ activator. This eliminates the need for a preflush to condition the reservoir.

For conformance control, there can be three different objectives – permanent plugging, permanent partial permeability reduction, and temporary permeability reduction. Permanent plugging seals the injected zone completely and is very difficult, if not impossible, to remove. This type of treatment, such as cementing and chemical grouting, is meant to permanently block flow into the treated zone. Most conformance control experiments aim to permanently reduce the permeability of the treated layer. This is common in the case of thief zones. The aim of the treatment is to reduce the permeability of the thief zone to a value comparable to the unswept layer, so that injection equalizes between the two zones. Cross-linked polymer gels are the most common injection fluid used for such a treatment. The final version of conformance control is temporary permeability reduction. In these treatments, the permeability reduction can be reversed, either fully or partially. This allows for temporary diversion, but the original permeability can be regained if desired. The purpose of the proposed technology is to provide conformance control in a fracture network. The goal is to divert flow from the higher conductivity fracture networks into those that have not been swept. This control will be vital for my solvent injection strategy in the field. Despite the high permeability of the matrix of many viscous oil reservoirs, the viscosity of the oil makes it essentially impermeable to solvent flow. Without some sort of control of the fracture conductivity, the solvent will be lost down the most conductive path leaving much of the reservoir without solvent contact.

6.2 Materials and Methods

Even though the gelation behavior was studied for both the 3M and NexSil particles, only the NexSil 5 dispersion was used for the proof of concept experiments. This decision was made because the NexSil 5 dispersion is available commercially from

Nyacol whereas there was only a limited supply of the proprietary 3M dispersion. Saline solutions were made with solid NaCl from Fisher Scientific and distilled water (DI). All experiments were run using one foot long, 1.5 inch diameter Estallades limestone cores. Figure 6.1 is a schematic of the experimental set-up with 1: Isco LC-5000 syringe pump, 500 mL capacity; 2: stainless steel double-ended accumulator for brine solution; 3: stainless steel double-ended accumulator for nanoparticle dispersion; 4: Phoenix Instruments core holder – 1 ½" diameter, 1' length; and 5: Teledyne Isco Retriever 500 fraction accumulators with disposable 15 mL plastic centrifuge test tubes. Black dots are pressure measurement points. The absolute pressure is measured at the inlet (bottom dot), and differential pressures are measured over sections one, two, and three. Sections one and three are three inches long; section two is six inches long.

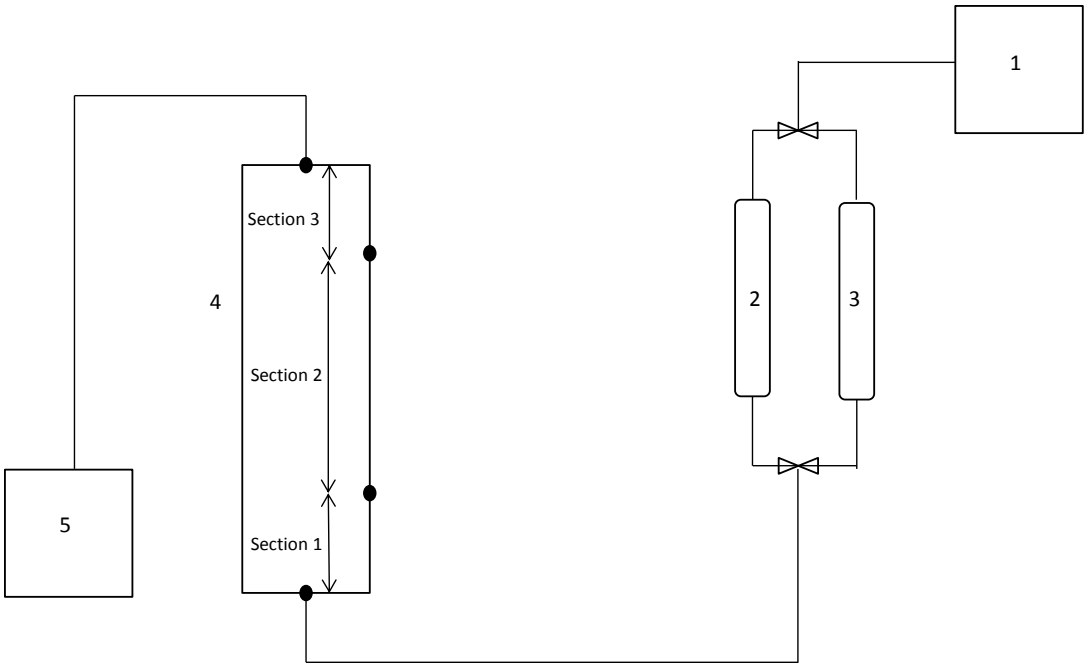

Figure 6.1. Schematic of the conformance control core-flood set-up.

The three gelling experiments had two steps – porosity and permeability measurement during initial core saturation and nanoparticle injection. For the base case a third step – tracer injection – was added between the saturation and nanoparticle injection. During the porosity measurement phase, the saturating brine solution was injected for two to three pore volumes until the pressure drop along the core was stabilized. The porosity was determined by subtracting the effluent volume collected from the injected volume. After the porosity measurement, the stabilized pressure drop was recorded for two more injection rates. These values were used to calculate the permeability of each core section. During the rate drop-down steps, the effluent was collected continuously in vials at varying time intervals dependent on injection rate. The conductivity of these samples was measured to ensure that the effluent conductivity was stable before starting the nanoparticle injection. Once the necessary measurements were completed, nanoparticle injection was started. The nanoparticle dispersion was injected for 24 to 36 hours with the effluent collected every hour. The injection rate was set so that the interstitial velocity was the same for all experiments. For the base case, a tracer test was performed after the porosity and permeability measurements. For the tracer, a low salinity solution was injected for 36 hours. Effluent conductivity was measured for each effluent sample, collected hourly. The same injection rate for the nanoparticle injection was used for the tracer injection. At the end of the experiment, the conductivity and absorbance of each sample was measured. The absorbance can be related to nanoparticle concentration through the calibration curve in Figure 6.2. The conductivity measurements were made with a conductivity probe. The absorbance measurements were done with a UV-Vis spectrometer. The absorbance was measured from 380 to 800 nm, but only the 400 nm measurements were reported. In order to eliminate any base absorbance measurement from the salt concentration, the absorbance of the saline

solutions over the applicable range was also measured (see calibration cure in Figure 6.3). There is little change in absorbance, which is expected, so an average of the values (4.8e-3) was used for a salinity baseline that was subtracted from nanoparticle solution absorbance prior to converting to nanoparticle concentration.

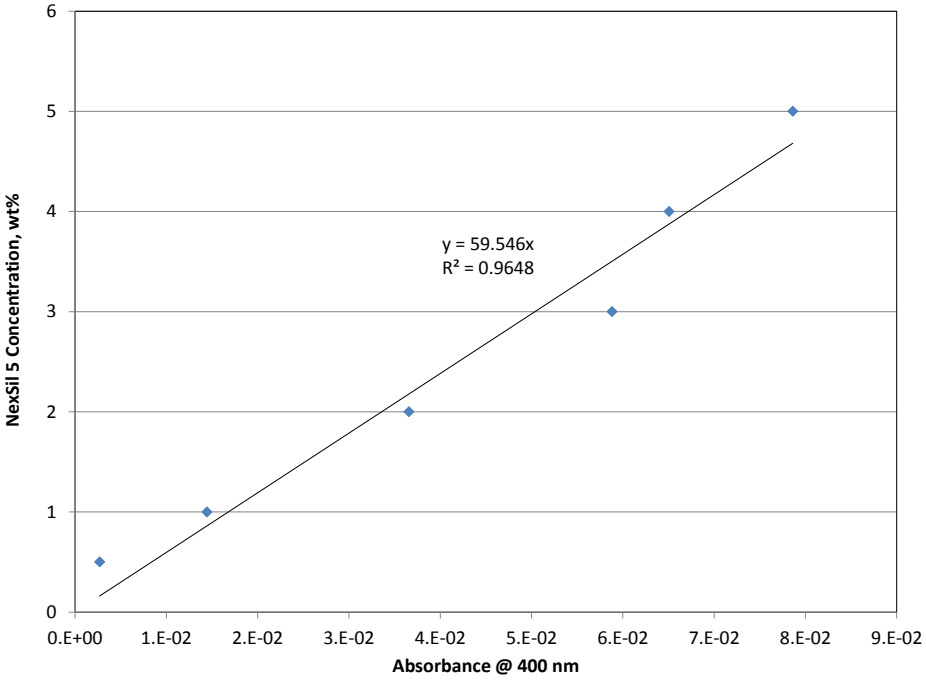

Figure 6.2. Calibration curve between absorbance and nanoparticle concentration.

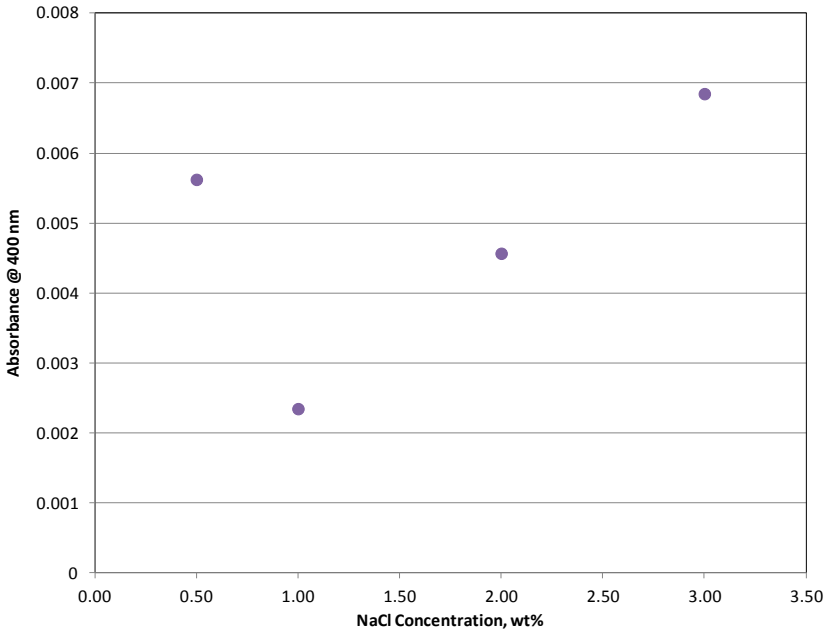

Figure 6.3. Baseline absorbance due to varying NaCl concentrations.

Under continuous injection, mixing is promoted by diffusion and convective dispersion. Convective dispersion is several orders of magnitude faster than diffusion, so the mixing zone will result in a spreading gel bank. Under this placement method, there are two different injection modes – continuous injection and slug injection. I only studied continuous injection because slug injection's only purpose is for an economic sensitivity. Many conformance control processes involve a shut-in period after injection of the gelling agent. The purpose of this shut-in is to allow the gel to reach equilibrium and maximum gel strength.

6.3 CORE FLOOD RESULTS

Five experiments were run (see Table 6.1 for experimental details). The base case consisted of a tracer test to determine the dispersion properties of the Estallades core followed by nanoparticle injection under non-gelling conditions to determine the degree, if any, to which filtration/mechanical plugging occurred from the nanoparticles

themselves. This baseline will verify that any permeability reduction observed in subsequent experiments is a result of the formation of a gel, rather than mechanical plugging. The next three experiments were designed to study the effect of salinity gradient and nanoparticle concentration on the process. The final experiment looked at the gel's performance in a fractured core, created by cutting the core in half lengthwise.

Test	Core Type	Reservoir Salinity	Nanoparticle Solution	Injection Mode
Base	Estallades	0.5 wt% NaCl	1.0 wt% NexSil 5; 0.5 wt% NaCl	Continuous
Reference	Estallades	3.0 wt% NaCl	2.0 wt% NexSil 5; 0.5 wt% NaCl	Continuous
2	Estallades	3.0 wt% NaCl	1.0 wt% NexSil 5; 0.5 wt% NaCl	Continuous
3	Estallades	2.0 wt% NaCl	1.0 wt% NexSil 5; 0.5 wt% NaCl	Continuous
Fracture	Estallades	3.0 wt% NaCl	2.0 wt% NexSil 5; 0.5 wt% NaCl	Continuous

Table 6.1. Details of proof-of-concept nanoparticle gelation experiments.

The first experiment, subsequently referred to as the Base Case, was designed to observe the salt concentration frontal movement and nanoparticle movement in the absence of gelation. Porosity and permeability measurements were made while saturating the core with 3.0 wt% sodium chloride (NaCl) brine. Table 6.2 shows the results of these measurements. Section permeabilites were calculated from measured pressure drops. Total permeability was measured by summing the sectional pressure drops (see Figure 6.4). Estallades limestone is a very homogenous rock, which suggests that the much higher section three permeability is incorrect. Therefore, only sections one and two were used for analysis. After initial saturation, the tracer test was performed by

injecting 0.5 wt% NaCl brine. The NaCl concentration history at the effluent is shown in Figure 6.5. Salt concentrations were determined from measured conductivities through a calibration cure. The concentration history was fit with the convection-diffusion equation (Equation 6.1 – solid line in Figure 6.5). The pressure drops during the tracer injection are shown in Figure 6.6. The drops are relatively flat, which is to be expected because the viscosity of the injected fluid does not change.

$$c_D = \frac{1}{2} erfc\left(\frac{1-t_D}{2\sqrt{t_D / N_{Pe}}}\right) + \frac{1}{2}\exp(N_{Pe})\, erfc\left(\frac{1+t_D}{2\sqrt{t_D / N_{Pe}}}\right) \qquad (6.1)$$

where $c_D = \dfrac{c_{disp} - c}{c_{disp} - c_{inj}}$

c_{disp} = concentration of displaced brine

c_{inj} = concentration of injected brine

c = concentration of effluent brine

t_D = pore volume injected

$N_{Pe} = \dfrac{uL}{D_l}$ = Peclet number

u = interstitial velocity

L = length of core

D_l = dispersion coefficient

	Permeability, mD	**Porosity, %**
Section 1	54.59	
Section 2	78.56	
Section 3	379.95	
Total	86.69	23.26

Table 6.2. Porosity and permeability measurements for the Base Case.

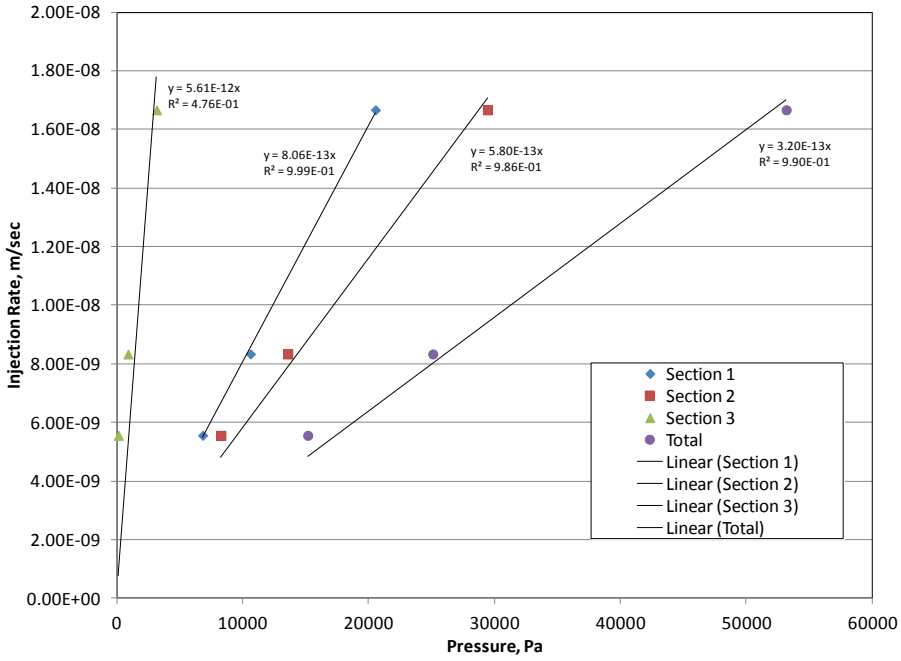

Figure 6.4. Permeability measurement curves for the Base Case.

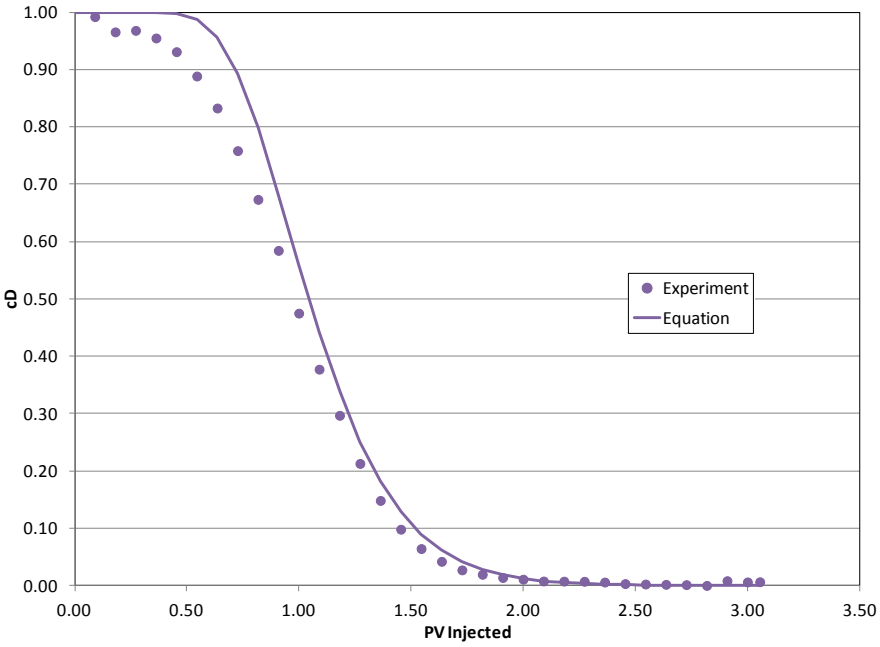

Figure 6.5. NaCl concentration history for the Base Case.

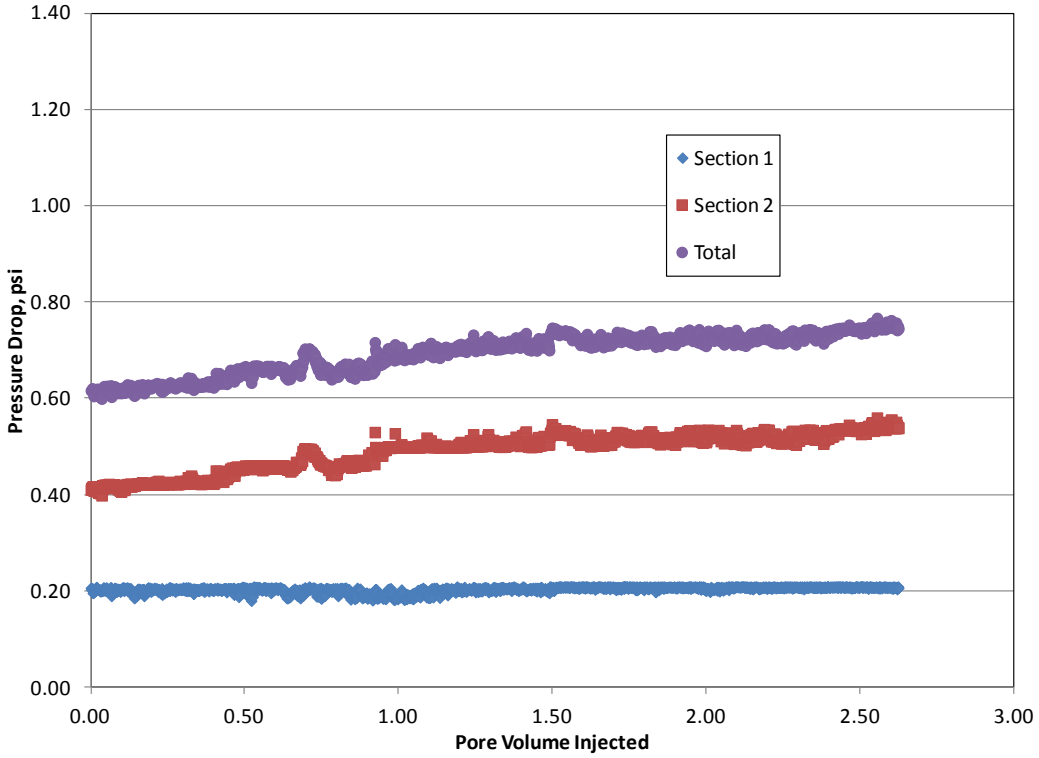

Figure 6.6. Pressure histories for the Base Case tracer test.

After the completion of the tracer test, nanoparticle injection (1.0 wt% NexSil 5 + 0.5 wt% NaCl) began. Under these conditions, no gelation should occur. Figure 6.7 shows the nanoparticle concentration history at the effluent. If no interaction between the rock and nanoparticle occurs, the curve would follow an s-shaped curve from 0 wt% to 1.0 wt%, which could be modeled using Equation 6.1. The fact that the curve does not follow this trend indicates a deviation from simple convective/diffusive transport behavior. First, nanoparticle breakthrough does not occur until ~ two pore volume (PV) injected. This suggests significant hold-up of the nanoparticles in the rock due to retention. Figure 6.8 shows the total pressure drop along the core throughout nanoparticle injection. Even though there are some fluctuations during the experiment, the net increase in pressure over the experiment is small indicating no effect on

permeability due to nanoparticle retention. Figure 6.9 shows the nanoparticle concentration during nanoparticle injection and NaCl concentration during the tracer test at the effluent overlain on the same graph as a function of PV injected. Even though these injection histories did not occur at the same time, it illustrates the delay in arrival of the nanoparticle front with respect to the salinity front. This image can be compared to subsequent data where nanoparticle and salt gradients are introduced at the same time and suggests that even in the absence of gelation there will be separation between the two fronts. Figure 6.7 also shows that after breakthrough the nanoparticle concentration increases to a value well in excess of the injected value. This is due to the later release of retained particles. If injection were to continue further, the value would eventually drop back to the injection value. The Base Case lays the foundation for the gelation cases by indicating that nanoparticle-rock interaction does occur and allowing for this baseline behavior to be excluded from the analysis of the gelation behavior.

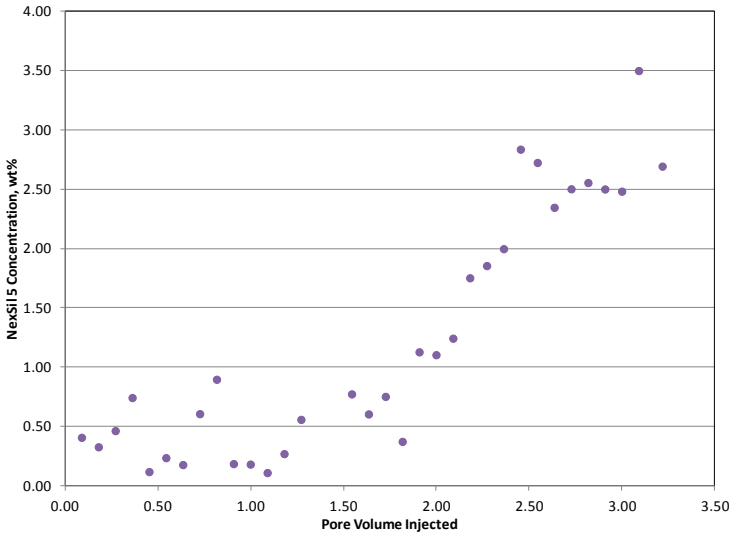

Figure 6.7. Nanoparticle concentration history at the effluent for the Base Case.

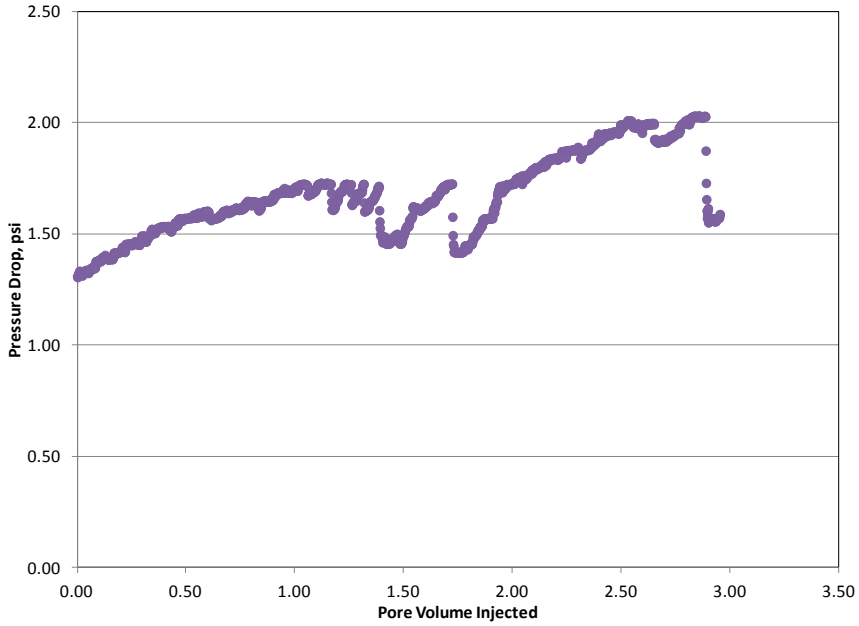

Figure 6.8. Pressure drop during nanoparticle injection.

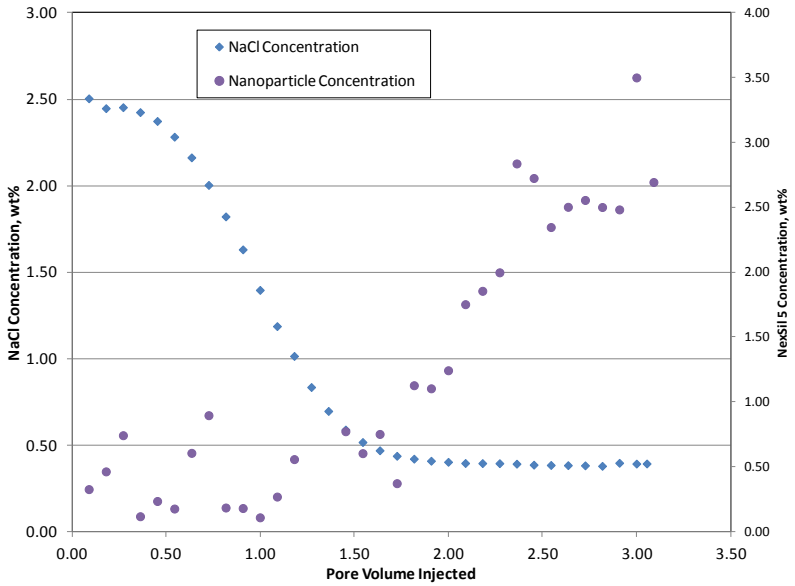

Figure 6.9. Overlay of nanoparticle and NaCl concentration histories at the effluent shows delay in nanoparticle transport.

The first gelation case was designed to serve as the reference case for comparison to the subsequent cases. The porosity and permeability measurements were done during the saturation of the core with 3.0 wt% NaCl brine. Table 6.3 shows the porosity and permeability values for the core. All of the data looks consistent so the entire core length is used for analysis. The permeabilities for this core are much higher than those of the Base Case and more in line with expected values for an Estallades limestone. The Base Case was run in an uncharacteristically low permeability plug from the Estallades core block. After initial saturation, the nanoparticle solution (2.0 wt% NexSil 5 + 0.5 wt% NaCl) was injected. From the phase behavior graph of Chapter Five (Figure 5.3), this will result in gelation with a single-phase gel at the front of the shock and a two-phase gel at the tail. Figure 6.10 shows the pressure drop during nanoparticle injection. For the first pore volume injected, the pressures stays relatively level but then shows significant increase in section one around one and two PV injected before leveling off around 2.2 psi. This is a six-fold increase from the staring pressure drop. The increase is only seen in section one (from 0.25 psi to 1.77 psi) for a seven-fold increase. This means that for this nanoparticle concentration/salinity gradient combination gelation kinetics prevent deep gel placement.

	Permeability, mD	**Porosity, %**
Section 1	172.02	
Section 2	337.26	
Section 3	182.17	
Total	233.51	22.50

Table 6.3. Porosity and permeability values for the Reference Case.

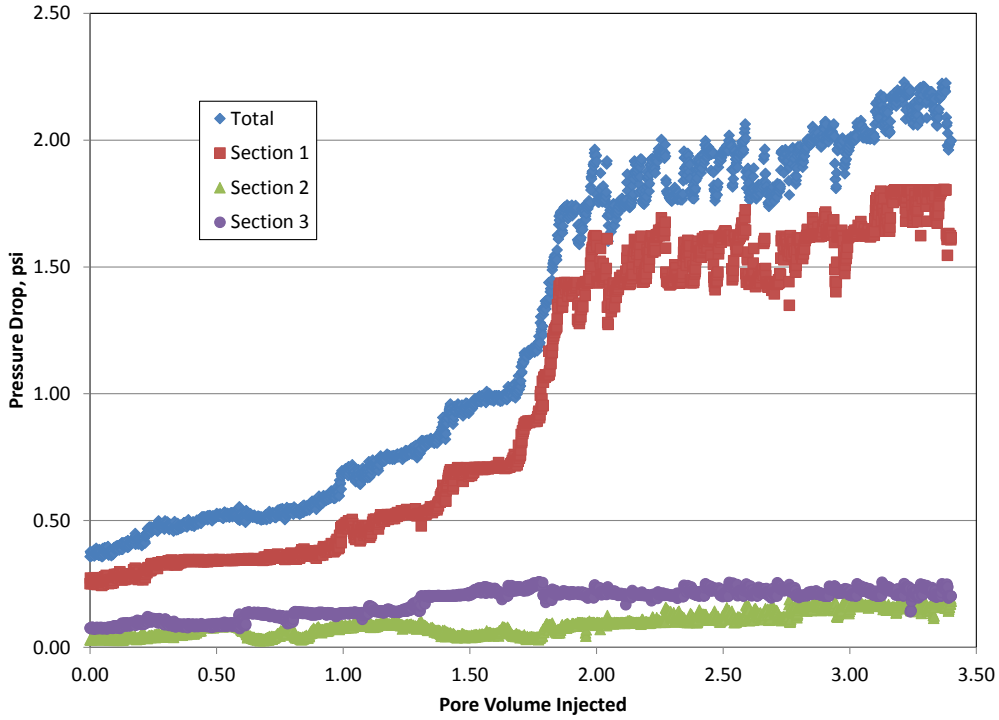

Figure 6.10. Pressure history during gelling nanoparticle injection for the Reference Case.

Figures 6.11 and 6.12 show the NaCl and nanoparticle concentration, respectively, at the effluent. Again no hold-up of the salinity front is observed. The nanoparticle concentration history does not show the same extreme delay as in the Base Case suggesting less severe retention. For this case, breakthrough occurs around 0.8 PV injected and effluent concentration increased to a maximum value of 5.8 wt% around 2.2 PV injected. There is sufficient effluent collection for this experiment to see that after peaking the concentration begins to decrease reaching a value of 2.65 wt% at termination. After the salinity front has progressed through the core, no further gelation should occur as the trigger mechanism (salinity gradient) has been removed. Gelation could be reinitiated if the nanoparticle injection was chased by high salinity brine. Figure 6.13 shows the overlay of the nanoparticle and salinity front. Gelation will occur until the

NaCl concentration falls below 1.0 wt% around 1.3 PV. This allows for sufficient mixing time in-situ under gelation conditions.

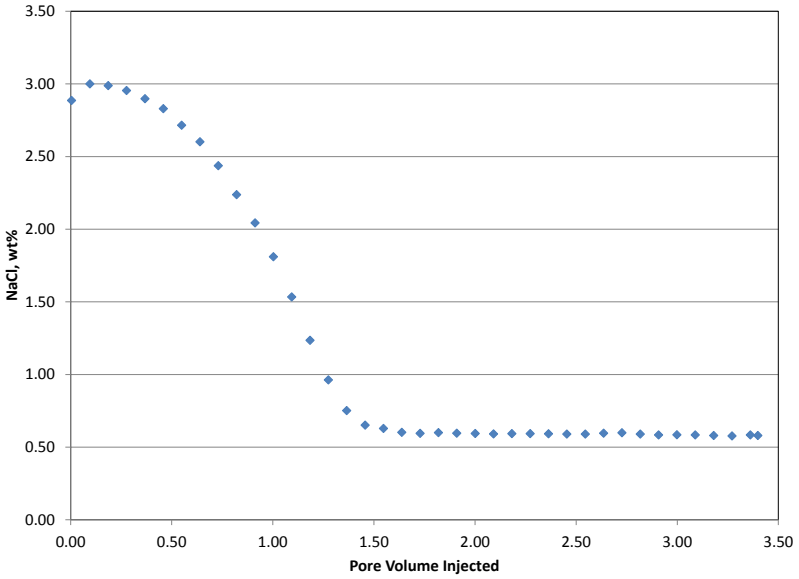

Figure 6.11. NaCl concentration history at the effluent for the Reference Case.

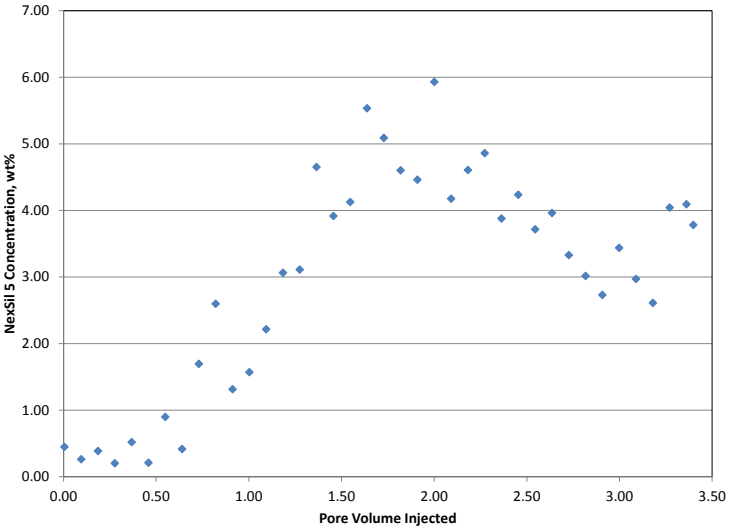

Figure 6.12. Nanoparticle concentration history at the effluent for the Reference Case.

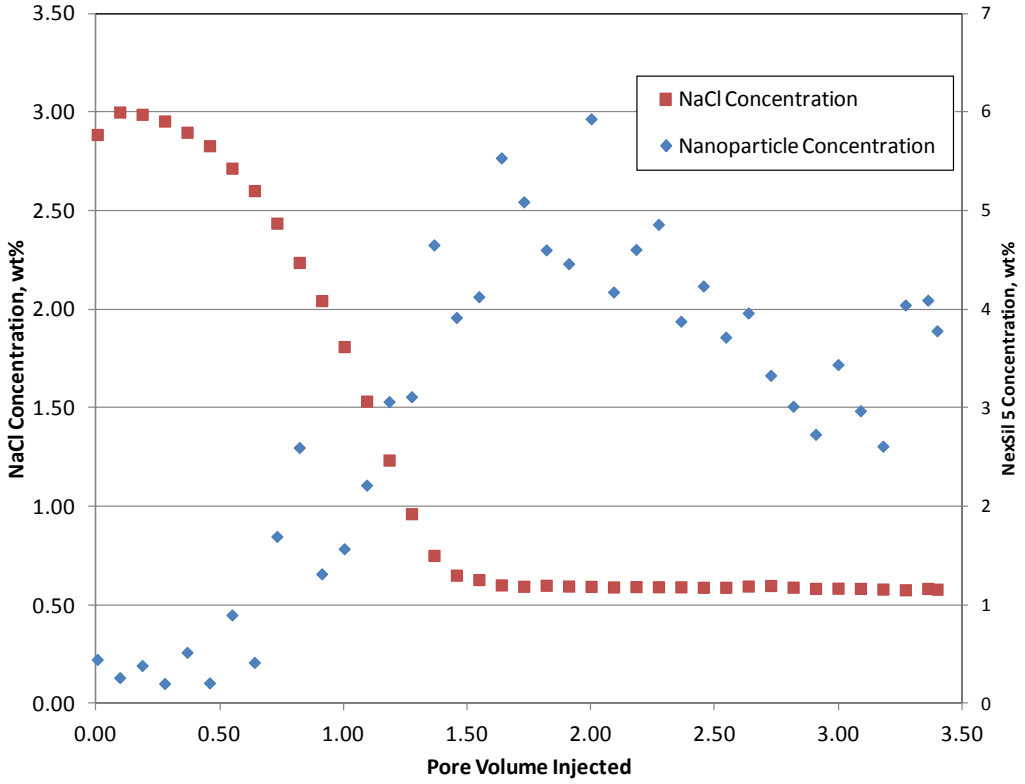

Figure 6.13. Overlay of NaCl and nanoparticle concentration effluent histories for the Reference Case.

The next experiment (Experiment 2) looks at the impact of nanoparticle concentration on the process by decreasing the concentration from 2 wt% to 1 wt%. Only two-phase gels were observed for these mixing conditions in the bulk phase analysis. Again, permeability and porosity measurements were made during the saturation with 3.0 wt% NaCl brine. Table 6.4 shows the data for these measurements, which are similar to the Reference Case. During nanoparticle injection a 1.0 wt% NexSil 5 + 0.5 wt% NaCl solution was injected. Figure 6.14 shows the pressure drop histories during nanoparticle injection. Again, the only increase in pressure occurs in section one. Over the entire experiment, section one pressure increased from 0.18 psi to 0.88 psi, a five-fold increase,

which is two-fold less than the Reference Case. This suggests that while conductivity reduction can be achieved at lower nanoparticle concentrations, it is more significant at the higher concentration, but not proportionally so. Figures 6.15 and 6.16 show the NaCl and nanoparticle concentration effluent histories, respectively. Nanoparticle breakthrough occurs around 0.5 PV injected. Then the concentration rises to a maximum of 2.3 wt% around 1.3 PV injected. After this the concentration appears to be decreasing – the same behavior as observed in the Reference Case. Figure 6.17 shows the overlay of the nanoparticle and salinity fronts. Gelation will occur until NaCl concentration falls below 1.0 wt% around 1.4 PV.

	Permeability, mD	**Porosity, %**
Section 1	178.79	
Section 2	200.46	
Section 3	451.71	
Total	226.46	24.90

Table 6.4. Porosity and permeability measurements for Experiment 2.

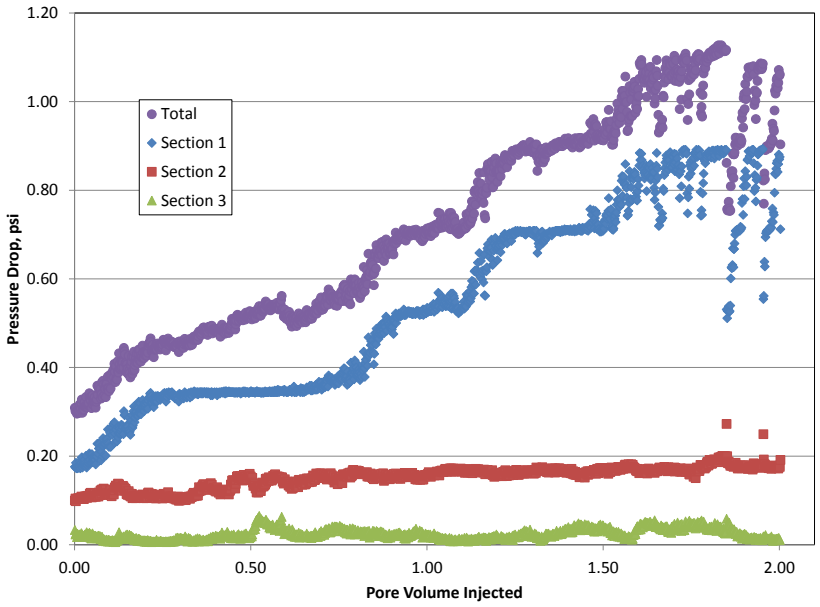

Figure 6.14. Pressure histories during gelling nanoparticle injection for Experiment 2.

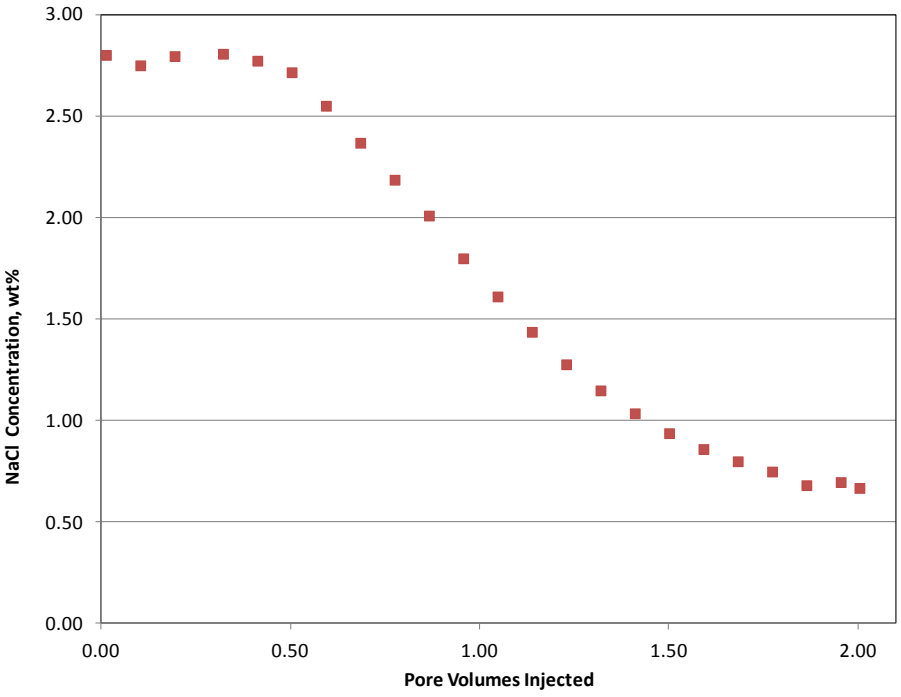

Figure 6.15. Effluent NaCl concentration history for Experiment 2.

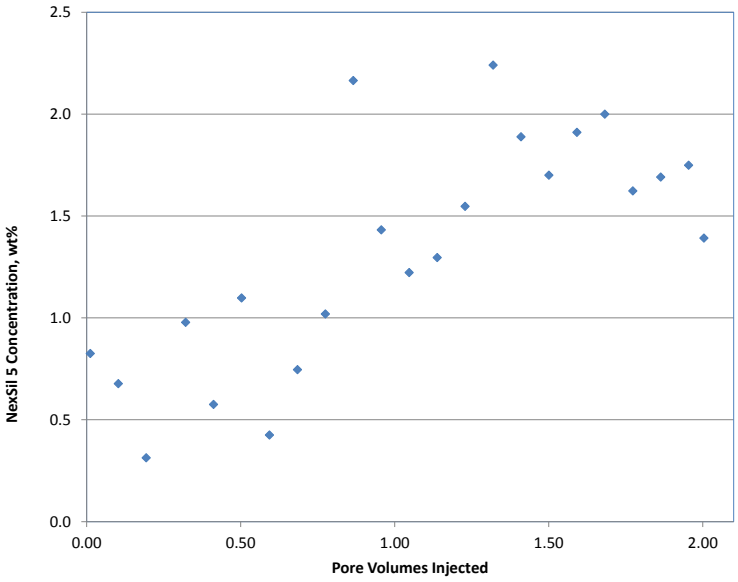

Figure 6.16. Effluent nanoparticle concentration history for Experiment 2.

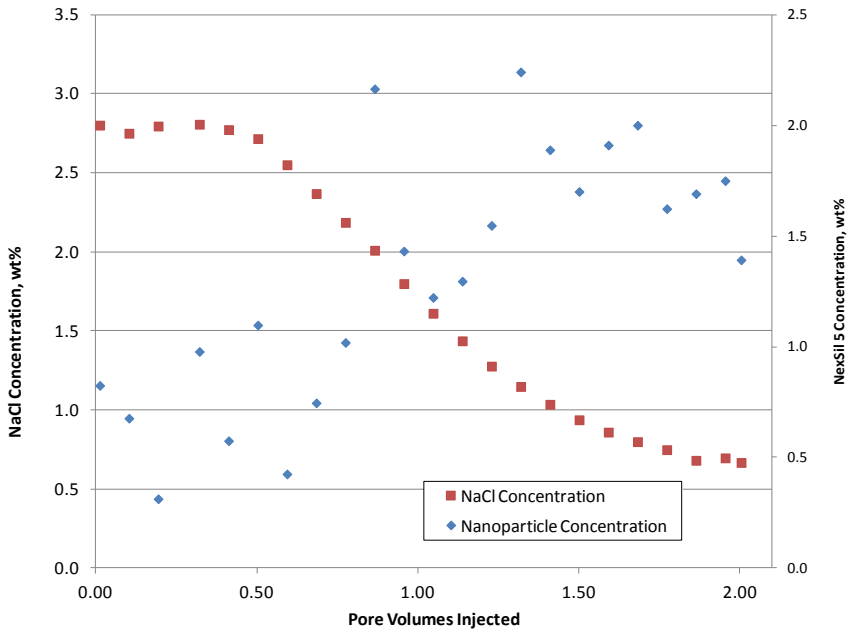

Figure 6.17. Overlay of effluent NaCl and nanoparticle concentration histories.

The final experiment (Experiment 3) looked at the impact of also decreasing the salinity gradient. From the kinetic study in Chapter Five, gelation should be retarded at lower mixing salinities. For this case, the permeability and porosity measurements were performed while saturating the core with 2 wt% NaCl brine. Table 6.5 shows the values for these measurements. The missing data for section three is due to poor data resulting in a lack of fit (see Figure 6.18). Therefore, as in the Base Case, only the first two sections will be analyzed.

	Permeability, mD	**Porosity, %**
Section 1	158.47	
Section 2	172.02	
Section 3	-	
Total	197.75	23.40

Table 6.5. Porosity and permeability measurements for Experiment 3.

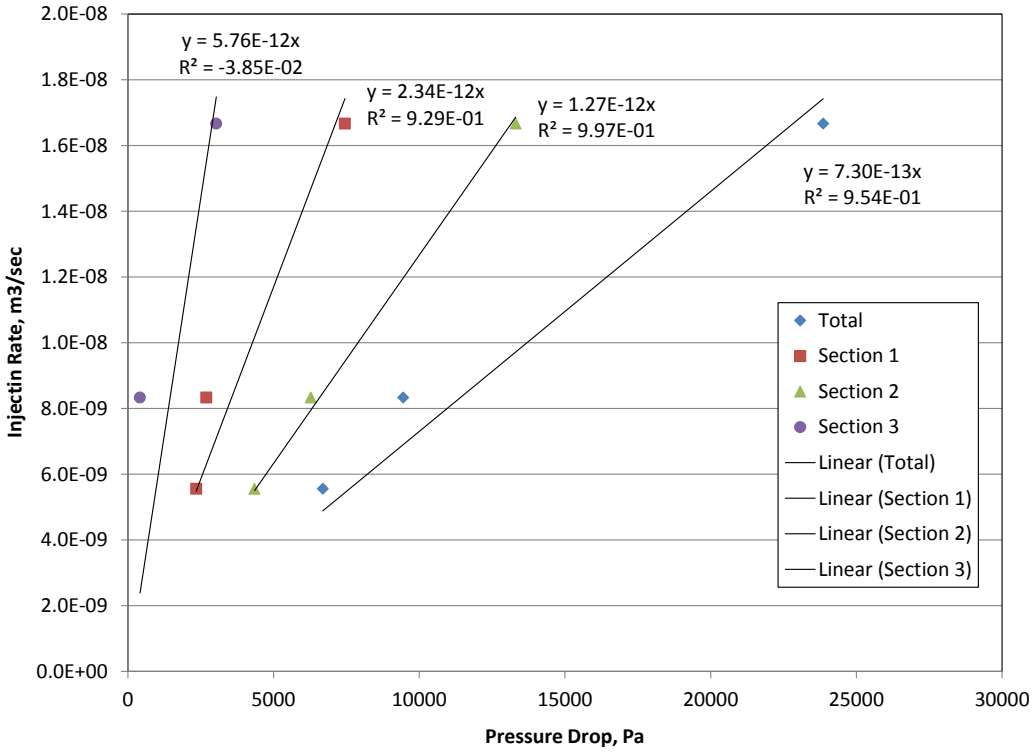

Figure 6.18. Permeability measurement data for Experiment 3.

For this case, the same nanoparticle solution (1.0 wt% NexSil 5 + 0.5 wt% NaCl) was used as in Experiment 2 so again all gels will be two-phase. Figure 6.19 shows the pressure drops during nanoparticle injection. Unlike the previous experiments, pressure increase is observed in section two as well as section one indicating deeper placement of the gel. This result is expected given the delayed gelation kinetics at the lower salinity gradient. Gelation caused an 8-fold increase in pressure for section one and a six-fold increase for section two. Even though the plugging is not as severe in section two, it would still be sufficient to divert flow and indicates the potential for deeper placement of the gel even when the gelation occurs near the inlet (section one). Figures 6.20 and 6.21 show the NaCl and nanoparticle concentration effluent histories for the experiment. Effluent collection was disturbed at ~ 2.2 PV injected so the final PV of effluent was not

collected. Fortunately, the data was still sufficient for analysis. As in all the previous experiments, no delay in the salinity front was observed. The elevated nanoparticle concentrations at the beginning are due to consistent contamination of the saturating brine. Ignoring then the quantitative analysis, qualitatively the behavior is the same as before. Breakthrough occurs at 0.8 PV. The peak nanoparticle concentration occurs around 1.7 PV injected and then begins to decrease. Figure 6.22 shows the overlay of the salinity and nanoparticle concentration histories at the effluent. In this experiment, gelation will occur as long as salinity is greater than 1.0 wt%, which last for ~ 1.2 PV injected.

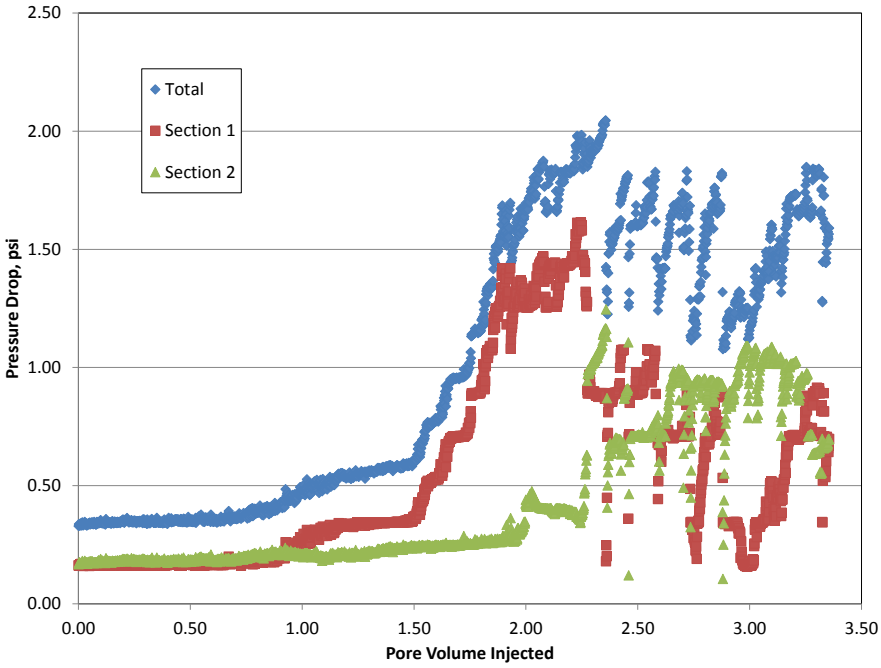

Figure 6.19. Pressure drop during gelling nanoparticle injection for Experiment 3.

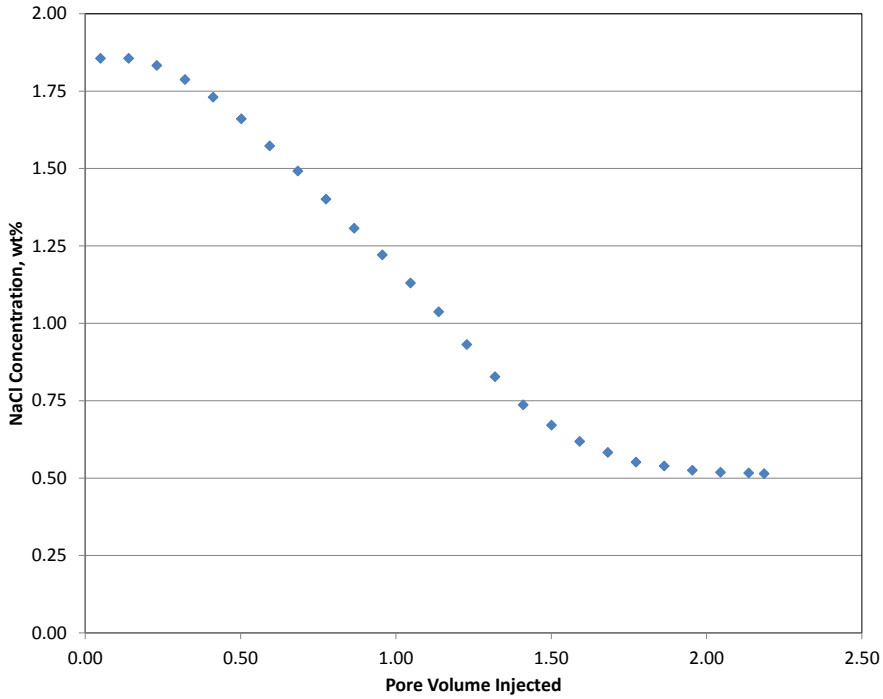

Figure 6.20. NaCl concentration effluent history for Experiment 3.

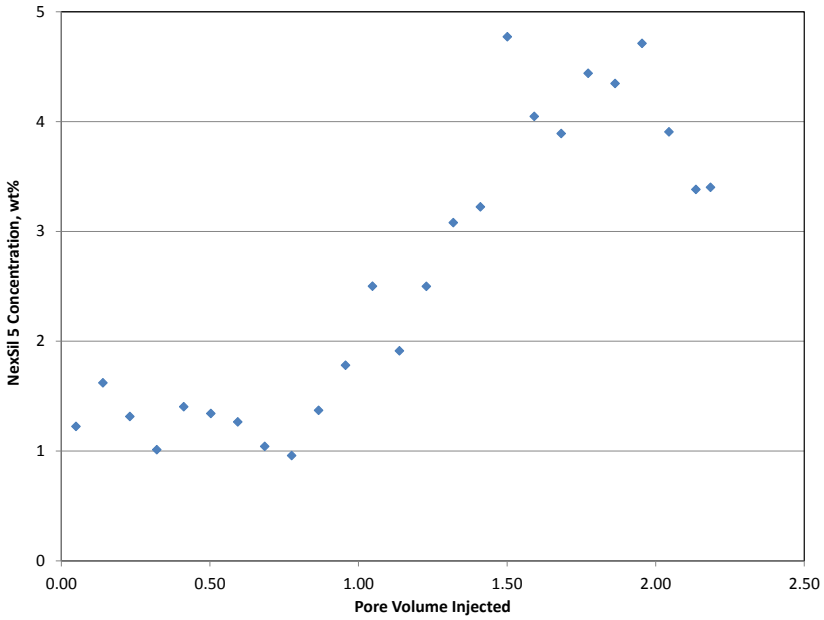

Figure 6.21. Nanoparticle concentration effluent history for Experiment 3.

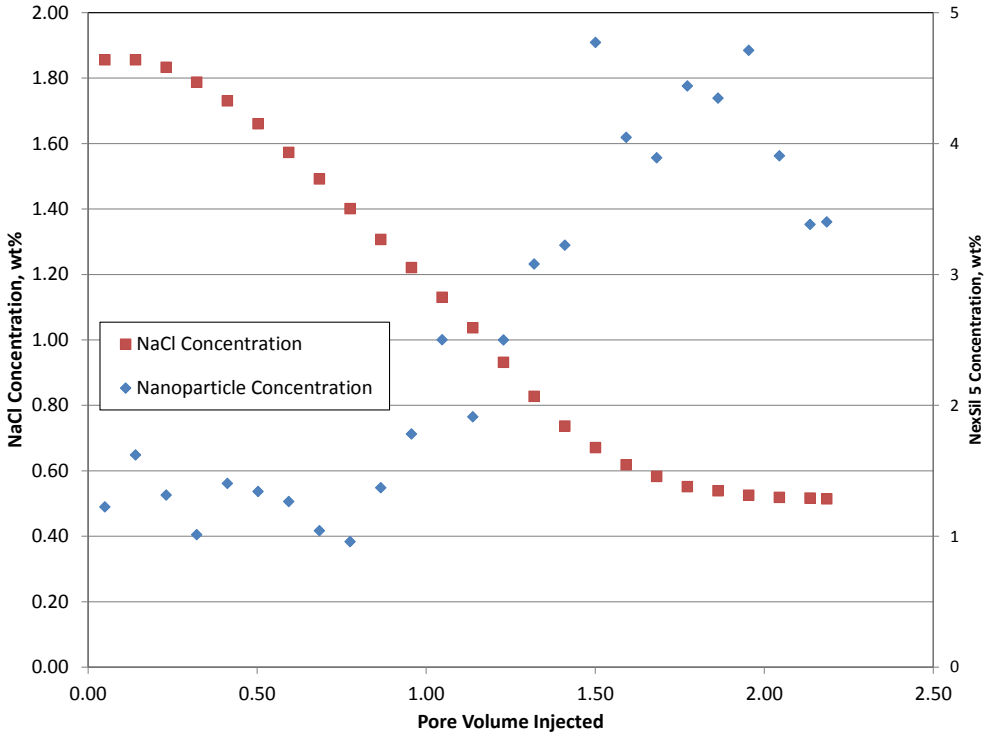

Figure 6.22. Overlay of NaCl and nanoparticle concentration effluent histories for Experiment 3.

The final experiment (Fracture Case) looks at the gel's performance in a fractured core. To create this environment, an Estallades core was cut in half lengthwise and then placed together again. The cutting process left a sufficient gap such that no spacer was necessary between the two halves to keep the fracture open inside the core holder. The same procedure was used for the porosity and permeability measurements as in the matrix cases (Table 6.6). As in some of the previous cases, the section three data was unusual, so the core was analyzed as if it were only nine inches long. The permeability is listed as apparent because it is the combination of fracture and matrix permeability and consequently much higher than in any of the previous experiments.

	Effective Permeability, mD	Porosity, %
Section 1	361.00	
Section 2	707.08	
Total	546.58	19.50

Table 6.6. Porosity and permeability data for the Fracture Case.

The same nanoparticle mixture, 2.0 wt% NexSil 5 + 0.5 wt% NaCl, was used as in the Reference Case. Figure 6.23 shows the pressure drop during injection. Section one stays fairly constant around 0.35 psi with a small jump up to 0.45 psi around 3.1 PV injected. The significant pressure increase occurs in section two from 0.07 to 0.34 psi with increases starting at 0.3 and 1.65 PV injected. These behaviors combine for a total pressure increase from 0.26 to 0.78 psi (a 3-fold increase). This is the smallest conductivity decrease of all the experiments.

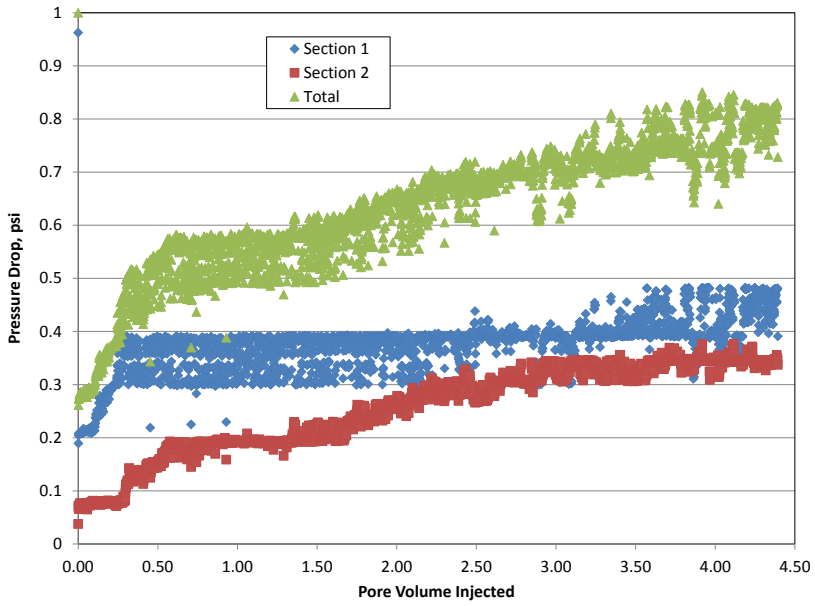

Figure 6.23. Pressure drop during nanoparticle injection for the Fracture Case.

Figures 6.24 and 6.25 show the NaCl and nanoparticle concentration effluent histories, respectively. The NaCl history is interesting because it indicates the dual fronts caused by flow through the matrix and fracture. The initial steep decline is due to fracture flow alone as the injected nanoparticle solution short-circuits through. The hump around 0.5 PV injected is when the matrix flow, still at higher salinity, starts to contribute significantly to the effluent samples. The shallower decline in the salinity profile is due to mixing of the fracture and matrix flow at the effluent. Because of the preferential flow through the fracture, matrix invasion by the low salinity nanoparticle solution is retarded thus flattening the effluent salinity gradient. The nanoparticle concentration peaks immediately and then falls until it stabilized around 5 wt% after 1 PV injected. Again the initial peak is due to early fracture flushing. The stabilization of the effluent nanoparticle concentration at a value much higher than the injected dispersion was an unexpected outcome. I believe that the higher values are due to additional particles, such as fines, that were produced and measured by the spectrometer. Future work will need to be done to verify this conclusion. Figure 6.26 shows the overlay of NaCl and nanoparticle concentration histories. The NaCl concentration remains above 1.0 wt% (thus in the gelling region) until 2 PV injected. The nanoparticle concentration history suggest that the fracture is initially swept within 0.5 PV meaning that the gelation will occur in the matrix, where sufficient salinity gradient still exists within the gelation time. On the surface these results seem to suggest that nanoparticle injection into fracture reservoirs would result in matrix, not fracture, conductivity reduction. However, matrix injection only occurred in this case because the test was performed in a core whose matrix permeability was still high enough to allow nanoparticle injectivity. In a viscous oil reservoir, the presence of cold oil would essentially prevent transport into the matrix. Instead, the nanoparticle dispersion would flow through the highly conductive fracture

pathways. Additionally, the gelation time can be adjusted, through changes in nanoparticle concentration or salinity gradient, to ensure gelation would occur within the fracture before it was swept.

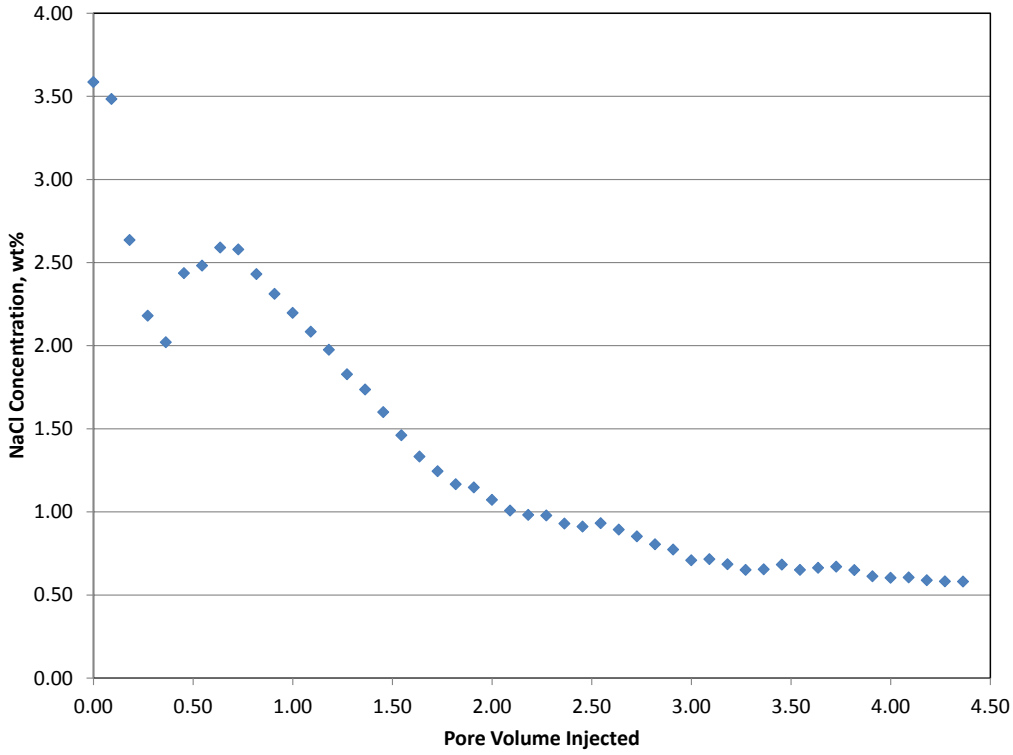

Figure 6.24. NaCl effluent concentration history for the Fracture Case.

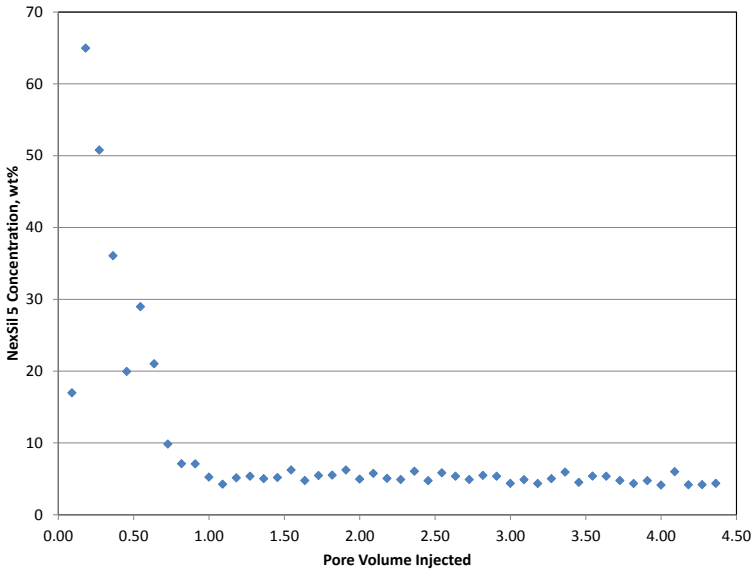

Figure 6.25. Nanoparticle effluent concentration history for the Fracture Case.

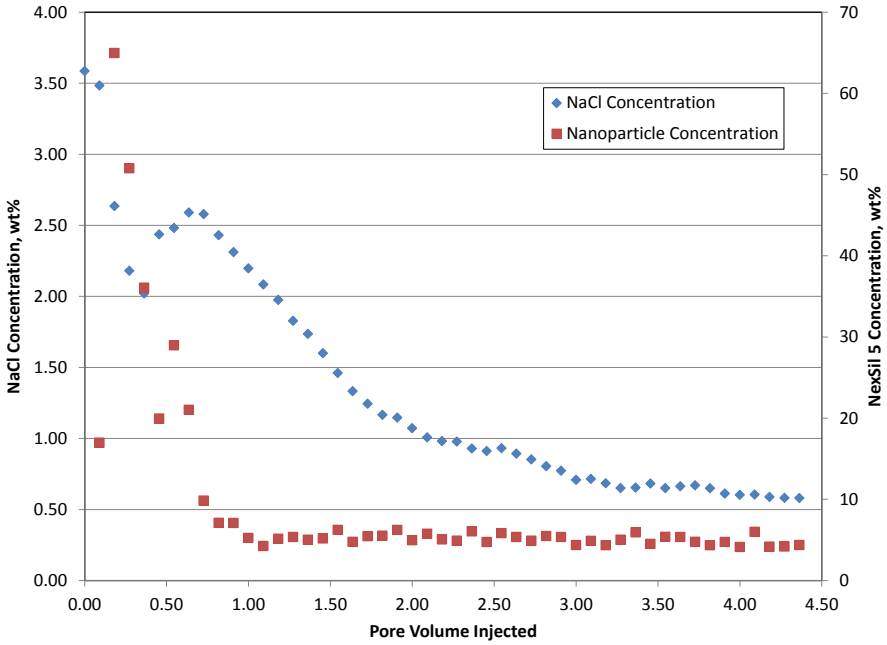

Figure 6.26. Overlay of NaCl and nanoparticle effluent concentration history for the Fracture Case.

6.4 ANALYSIS

The two major points of emphasis during analysis are the difference in gelation behavior, observed in the pressure drops, and nanoparticle retention and release, observed in the nanoparticle concentration effluent histories.

6.4.1 Gelation Behavior

For the Reference Case, the pressure first starts to increase around 0.7 PV injected (7.8 hours) with another sharp increase around 1.6 PV (17.8 hours). For Experiment 1, the pressure increases in a stair-step fashion with increases at 0.7, 1.1, and 1.4 PV injected (7.8, 12.2, and 15.6 hours). For Experiment 3, section 1 increases at 1.4 PV injected (15.6 hours), and section 2 increases at 1.9 PV injected (21 hours). The gelation time at the front of the mixing zone for the Reference Case and Experiment 1 assuming no reduction in nanoparticle concentration due to retention are 2.1 and 5.5 hours. It is clear that the effects of retention and the dilution caused by mixing slow down the gelation process as the in-situ times are significantly longer than the bulk. Additionally, the greater degree of retention in the Reference Case compared to Experiment 2 results in a quicker gelation in Experiment 2 despite the lower injected nanoparticle concentration. This suggests that the effective nanoparticle concentration available for gelation was greater for Experiment 2 than it was in the Reference Case because of a higher degree of retention in the Reference Case. The stair-step behavior in section one pressure for Experiment 2 suggests that the gelation progressively occurs in different portions of the core. Most likely, the largest pores are gelled first. When flow through these pores is impeded significantly, the nanoparticle solution is diverted to the smaller pores. The progression continues until the nanoparticles arrive at pores that are not saturated with high enough salinity to trigger gelation.

In addition to having the longest gelation time, which is expected given the reduced initial core salinity, Experiment 3 also displays loss of blockage as the pressure in section 1 drops down at 2.3 PV. This behavior supports our assertion that the gel can be partially broken upon continued injection. Because this failure was not observed in Experiment 2, the results suggest that at lower initial core salinity, the gel formed is more susceptible to failure. This is supported by the dynamic shear tests from the previous chapter that show increasing G' (storage modulus) for the gels as NaCl concentration increases (see Figure 5.16). The length of the experiment was not sufficient to see if failure caused complete reversal of conductivity decrease or if the failure would simply reduce the degree of reduction. Either behavior could be useful depending on the desire for permanent or temporary diversion.

6.4.2 Nanoparticle Retention and Release

The transport of nanoparticles in porous media has not been fully studied, but much work has been done in reference to colloid transport. Even though there are some differences in the mechanisms governing the transport of both particle types due to size differences, the work done on colloid transport can provide insight into nanoparticle behavior. I have used this source of study for analysis of the retention and release of nanoparticles observed during the experiments. Canseco, et al (2009) described colloid retention – absorption and mechanical entrainment – and release through the framework of total interaction potential between the particles and the porous medium. This potential has two minimums, which serve as attachment opportunities. The primary minimum occurs at short separation distances with a secondary minimum at larger separations. An energy barrier occurs at intermediary distances between the two. Particle can be retained via either minimum, but those attached via the secondary minimum are more likely to

release. Decreasing solution ionic strength (for my experiments, NaCl weight percentage) will decrease the depth of the secondary minimum and increase the height of the energy barrier. Therefore, most retention at lower salinities occurs in the secondary minimum. At higher salinities, deposition in both minima is common because of the reduced energy barrier. Because the release of particles trapped via the secondary minimum does not require overcoming the energy barrier, release is more common for particles trapped there. The authors studied the retention/release behavior of 780 nm surfactant-free polystyrene latex microspheres flowing through consolidated synthetic porous media. Their experiments involved initial high ionic strength saturation and flow (retention) followed by zero ionic strength flow (release).

This behavior is similar to my experiments where the nanoparticles are first exposed to the high salinity core and then flushed with continued low salinity nanoparticle injection. Therefore, the behavior discussed by the authors is an appropriate analogue to my experiments. They observed that as the initial saturating ionic strength decreases fewer particles were deposited. These principles are useful in comparing the difference between the ratios of effluent to inlet nanoparticle concentration for Experiment 3 with Experiment 2, which only differ in initial core salinity. At the lower initial core salinity, the energy barrier is higher meaning that most deposition occurred in the secondary minimum for Experiment 3. So even though more retention occurred for Experiment 2 because the higher salinity reduced the energy barrier to deposition, much of it occurred via the primary minimum. Therefore, when the retained particles were exposed to the low salinity nanoparticle injection, more release occurred for Experiment 3 because its particles were not trapped in the primary minimum where release was inhibited by the energy barrier.

Bradford and Betahar (2006) studied the influence of colloid concentration on the retention of 1 and 3.2 μm latex particles. They studied colloid attachment and straining as the two main mechanisms for colloid retention. Straining is the trapping of particle in pore throats too small to allow passage. They observed that for a given sand and colloid, retention was less for higher input concentrations, especially for smaller colloids. In order to match this observed behavior numerically, they had to supplement the straining model with a liberation term that assumed that straining was hindered at higher particle concentrations due to repulsive colloid (deposited)-colloid (aqueous) interactions. Our observations in the Reference Case and Experiment 2 are in line with this work. These two experiments only differ in injected nanoparticle concentration. Because they have the same salinity gradient history, the retention and release due to interaction potential should be similar. However, Experiment 2 has a higher ratio of effluent to inlet concentration than the Reference Case. This suggests that more particles were originally retained in Experiment 2 thus resulting in a higher produced concentration upon release. Because they both undergo the same ionic solution change, the release phase should not contribute significantly to the difference in effluent history. The above use of interaction potential to describe nanoparticle retention suggests that without the subsequent addition of high salinity brine into the core, the release of particles would reach an equilibrium. At this point, the effluent concentration would return to the inlet concentration. This means that had the experiments been run longer, the effluent concentration would have stabilized at the inlet concentration after the peak.

Nanoparticle breakthrough occurs at 0.6 PV for the Reference Case, 0.8 PV for Experiment 3 and between 0.6 to 0.8 PV for Experiment 2. The exact breakthrough for Experiment 2 is difficult because of the great degree of scatter in initial produced values. Because of the scatter in data and the inexactitude of breakthrough determination, I

would say that no significant difference existed between the three experiments in breakthrough time. However, the difference in breakthrough time between the three gelling cases and the Base Case (2 PV) is significant. The difference is due to a greater degree of straining in the lower permeability Base Case core. At lower permeabilities, smaller pore throats are more abundant making straining a more important trapping mechanism and causing the greater delay in nanoparticle breakthrough. Compared to the Reference Case and Experiment 3, the maximum nanoparticle effluent concentration for Experiment 2 occurred much sooner (1.3 v 2 PV). The delay in peak concentration for Experiment 3 is due to a wider in-situ nanoparticle distribution because the particles traveled further prior to gelation. However, for the Reference Case it is more likely that the higher concentration of nanoparticles in the injection stream slowed the release process because the negative nanoparticle (aqueous)-nanoparticle (retained) interactions created an additional barrier to release.

6.5 Conclusions and Future Work

Four matrix injection experiments were run to study the potential of nanoparticle gelation triggered in-situ by salinity gradients. The results show that permeability reduction can be achieved through the process even at low nanoparticle concentrations. For faster-gelling systems (Reference Case and Experiment 2), permeability reduction only occurs in section one. However, under retarded gelation kinetics due to lower initial salinity (Experiment 3), permeability reduction occurs in section one and two. Some nanoparticle will initially be retained due to the suppressed energy barrier to absorption in the higher salinity environment. Most of the retained particles, though, will be released upon continued exposure to the low salinity nanoparticle solution. The retention/release behavior is impacted by the initial core salinity and the injected

nanoparticle concentration. When the core salinity is initially lower, a weaker gel is formed, which allows for continued injection to break and mobilize some of the gel.

The gelation process was also explored in a fractured core. At the experimental conditions, gelation generated a three-fold pressure increase, but most of the gelation occurred in the matrix rather than the fracture. This is because the initial high salinity saturation is flushed from the fracture within 0.5 PV injection not allowing sufficient time for gelation. These results, though, are not discouraging for viscous oil applications because the conductivity contrast between the core matrix and fracture was not as high in the experiment as would be observed in a viscous reservoir. Future experiments should be run using an extremely low permeability matrix as well as an oil-saturated matrix to verify the process in high contrast situations. The salinity gradient trigger concept is still applicable in fractured reservoirs as long as a higher salinity than the injected solution is present in the fractures. Also, because gelation can be achieved at low salinities, even small salinity gradients can be used to achieve in-situ gelation.

Finally, the gelation process should be tested in a layered core to see the impact in this second important type of heterogeneity. The matrix results show that significant permeability reduction can be achieved in matrix flow, suggesting great potential for conformance control in layered reservoirs. One great area of potential would be flooded reservoirs where the nanoparticles would reduce conductivity in the high permeability layers leading to more evenly distributed injection throughout all layers. This work has shown that matrix plugging can be achieved at very low nanoparticle concentrations. So even though more injectant volume is necessary for matrix than fracture injection, the usage of nanoparticles can still be minimized. Further work would be necessary to quantify what these values would need to be.

Chapter 7: Conclusions and Future Work

This chapter summarizes the conclusions of this dissertation and recommendations for future work. The purpose of this work was two-fold: (1) develop a low temperature production process for viscous fracture reservoirs and (2) study the potential of in-situ generated silica nanoparticle gels for conformance control applications in fractured reservoirs. I used a sand column to model a single matrix-fracture interaction to study the mechanisms of the proposed low-temperature solvent injection strategy under varying experimental parameters. The experiments showed high oil recovery and within the range of parameter values studied aligned with analytic models for liquid extraction kinetics and gravity drainage. The gelation of silica nanoparticle dispersion in the presence of saline solutions was studied in both the bulk phase and during flow through porous media. The gels show potential as a conformance control technique in fractured reservoirs. While both processes showed potential at the lab-scale, the results included in this dissertation are limited by the experimental set-ups used and range of parameters studied.

7.1 CONCLUSIONS

The following sections describe the most important conclusions stemming from each research phase.

7.1.1 Novel solvent injection strategy experiments

1. The high-temperature steam injection was an efficient oil production process. At high steam temperatures, the additional viscosity reduction generated by solvent dissolution is not significant. The oil-in-water emulsions generated during steam or steam-solvent injection are not ideal and would require additional handling in the field.

2. Production during the proposed solvent injection strategy is dominated by two production mechanisms. When the injected solvent is in the liquid phase, liquid extraction occurs. Production during this phase can be described with the equation developed by Patricelli, et al (1979). When the injected solvent is in the vapor phase, solvent-enhanced gravity drainage occurs, which can be described with analytic models for gravity drainage.
3. Permeability does not have a significant impact on the liquid extraction process, but is proportionally related to oil rate during gravity drainage. Temperature affects both phases of production. Increases in temperature lead to higher mass transfer coefficients during liquid extraction. Increased temperatures lead to lower oil viscosities and higher drainage rates. The concentration gradient at the oil-solvent interface primarily affects the liquid extraction period. Higher concentration gradients lead to higher mass transfer coefficients.
4. Solvent type can have a significant impact on both processes. Solid asphaltene production was observed when n-pentane was used. Higher molecular weight alkanes will result in significant in-situ asphaltene precipitation. While this leads to in-situ upgrading, it is not desirable if the asphaltenes become mobile rather than being trapped in the residual oil. All cases showed a significant degree of in-situ upgrading.
5. The major impact of this work is introducing a new solvent injection strategy combining the best mechanisms from previously proposed techniques to achieve good production at low temperatures. The production rates, heating profiles, and solvent usage are specific to the experimental set-up used. However, the process would generate the same production mechanism at any scale as long as the injection was designed to go from liquid to vapor solvent injection.

6. The single fracture-matrix interaction is not representative of field behavior, but is sufficient to study the process mechanisms at the lab scale. In the field, there would be a small bank of condensing solvent in the matrix being pushed by vapor solvent. This large-scale feature is not captured in the set-up. Rather, the set-up is designed to study the behavior at a given point in the reservoir as it transitions from exposure to liquid to vapor solvent.
7. The best process performance can be achieved with solvents that have better solvation properties during liquid extraction. However, these solvation properties are only useful if they do not also result in asphaltene precipitation which can reduce the reservoir permeability or, if mobile, cause problems in the production lines.
8. The experiments only encompasses a small data set of variables, so there is still significant uncertainty associated with the effect of parameters on each mechanism.

7.1.2 Numerical modeling of solvent injection strategy

1. An initial sensitivity analysis showed that the uncertainty in thermal properties did not significantly impact the simulation output. However, uncertainty in the parameters directly related to the production mechanisms – oil and n-butane diffusion coefficients and sand pack permeability– resulted in significant variations in simulation output.
2. The second sensitivity analysis focusing on process parameters showed that cumulative oil was most sensitive to 'C4' component oil phase diffusivity and k-value. More data would need to be collected to reduce the uncertainty in these values for future simulation work.

3. A first history-match attempt using the cumulative oil and temperature profiles as objective functions produced an optimal solution that matched the temperatures well but resulted in a worse match for cumulative oil than the base case. When only the cumulative oil was used as an objective function, the cumulative oil match was greatly improved with only a small decrease in the goodness of the temperature fits. The good match for temperature indicates that the uncertainty range for the parameters representing the liquid extraction mechanism is adequate. However, the lack of fit to cumulative oil indicates that a parameter underlying the film drainage process needs adjustment. This parameter is relative permeability, which will impact the two-phase flow occurring during film drainage. If this process were to be included in the history-matching efforts, a global optimum could be found that generates a quality match for cumulative oil and temperature simultaneously. However, this solution might not generate the true values for all parameters due to the non-uniqueness of the history matching process.

7.1.3 Bulk phase behavior and rheology of silica nanoparticle gels

1. Silica nanoparticles exhibit four phase regions as a function of NaCl and nanoparticle concentration – clear liquid, two and single phase gel, and viscous liquid. Previous work had not identified the viscous liquid region.
2. Monodisperse 3M silica nanoparticles have a wider window of gelation with respect to salinity than polydisperse NexSil5 particles.
3. Gelation time decreases exponentially as a function of silica, NaCl concentration, and temperature.

4. The storage modulus, G', increases with particle concentration following a power law behavior. For the two types of particles studied, single phase and two phase gels can withstand the same strain before the structure breaks.
5. The silica nanoparticle gels exhibit non-Newtonian, shear thinning behavior which could be described by the power law model or the Carreau model depending on the particle and NaCl concentration.

7.1.4 Conformance control through in-situ gelation of silica nanoparticle dispersions

1. Permeability reduction can be achieved through the in-situ gelation process even at low nanoparticle concentrations. Under retarded gelation kinetics due to lower initial salinity, permeability reduction can be created deeper in the core. When the core salinity is initially lower, a weaker gel is formed, which allows for continued injection to break and mobilize some of the gel.
2. Some nanoparticle will initially be retained due to suppressed energy barrier to absorption in the higher salinity environment. Most of the retained particles, though, will be released upon continued exposure to the low salinity nanoparticle solution.
3. For the process in a fractured core, gelation generated a three-fold pressure increase, but most of the gelation occurred in the matrix rather than the targeted fracture because the fracture was flushed before the gelation time. In a viscous-oil saturated reservoir, the contrast would be great enough to keep the nanoparticle flow contained in the fracture, and the gelation time could be tailored to achieve gelation within the fracture before flushing.

7.2 FUTURE WORK

Because the research presented in this dissertation was meant only as proof-of-concept, there is further work necessary to mature the technologies. The technologies were not studied under economic injection conditions and much of the qualitative results are dependent on the experimental set-up used. This necessitates further testing under more realistic conditions. Additionally, because the tests were only done for a few values of controlling process parameters there is a high level of uncertainty on their impact. All future work is aimed to address these issues. The following list summarizes at least the first phase of these efforts.

1. Fractured core floods should be used to study the impact of residual water on the solvent injection strategy. These core floods can also be used to see the impact of asphaltene precipitation, especially with heavier solvents, on production in more realistic permeabilities. These efforts are currently underway at UT-Austin.
2. Preliminary work should be begun to consider how the solvent injection strategy will work at field conditions, including well configuration and injection rate. This will allow better decisions to be made regarding future experiments so that their set-up and injection parameters can better reflect eventual field applications.
3. Because relative permeability is a key parameter underlying the film drainage process, it must be included in future history-matching efforts in order to better capture the key parameters for process modeling.
4. Additionally, the uncertainty of the key parameters should be reduced to generate more robust simulation results.

5. Further conformance control experiments should be run using an extremely low permeability matrix as well as an oil-saturated matrix to verify the gelation process in high contrast fracture situations.
6. Finally, the gelation process should be tested in a layered core to see the impact in this second important type of heterogeneity. The matrix results show that significant permeability reduction can be achieved in matrix flow suggesting great potential for conformance control in layered reservoirs. One great area of potential would be flooded reservoirs where the nanoparticles would reduce conductivity in the high permeability layers leading to more evenly distributed injection throughout the layers.

References

Ahmadloo, F. et al. 2011. Experimental Results and Analytical Modeling of Solvent-Leaching Gravity Drainage Phenomenon in Heavy Oil Reservoirs. Paper SPE 144542 presented at Annual Technical Conference and Exhibition, Denver, Colorado, 30 October – 2 November.

Akbarzadeh, K. et al. 2004. Asphaltene Precipitation from Bitumen Diluted with n-Alkanes. Paper 2004-026 presented at Canadian International Petroleum Conference, Calgary, Alberta, Canada, 8-10 June.

Al Bahlani, A.M. and Babadagli, T. 2008. Heavy-Oil Recovery in Naturally Fractured Reservoirs with Varying Wettability by Steam Solvent Co-Injection. Paper SPE/PS/CHOA 117626 presented at the International Thermal Operations and Heavy Oil Symposium, Calgary, Alberta, Canada, 20-23 October.

Al Bahlani, A.M. and Babadagli, T. 2009. Laboratory and Field Scale Analysis of Steam Over Solvent Injection in Fractured Reservoirs (SOS-FR) for Heavy-Oil Recovery. Paper SPE 124047 presented at the Annual Technical Conference and Exhibition, New Orleans, Louisiana 4-7 October.

Al Bahlani, A.M. and Babadagli, T. 2009. Steam-Over-Solvent Injection in Fractured Reservoirs (SOS-FR) for Heavy Oil Recovery: Experimental Analysis of the Mechanism . Paper SPE 123568 presented at the Asia Pacific Oil and Gas Conference and Exhibition, Jakarta, Indonesia, 4-6 August.

Al Bahlani, A.M. and Babadagli, T. 2010. Efficiency Analysis of Steam-Over-Solvent Injection in Fractured Reservoirs (SOS-FR) Method for Heavy Oil Recovery . Paper SPE 132458 presented at the Western North America Region Meeting, Anaheim, California 26-30 May.

Al-Anazi, H.A. and Sharma, M.M. 2002. Use of a pH Sensitive Polymer for Conformance Control. Paper SPE 73782 presented at International Symposium and Exhibition on Formation Damage Control, Lafayette, Louisiana, 20-21 February.

Alkindi, A., Muggeridge, A., and Al-Wahaibi, Y. 2010. Experimental Investigation into the Influence of Convective Dispersion and Model Height on Oil Drainage Rates during VAPEX. Paper SPE 129169 presented at EOR Conference at Oil & Gas West Asia, Muscat, Oman, 11-13 April.

Allen, J.C. 1974. Gaseous Solvent Heavy Oil Recovery. Canadian Patent 1,027,851.

Allen, J.C., and Redford, A.D. 1976. Combination Solvent-Noncondensible Gas Injection Method for Recovering Petroleum from Viscous Petroleum-Containing Formation including Tar Sand Deposits. U.S. Patent 4,109,720.

Al-Rabaani, A.S., Blunt, M.J., and Muggeridge, A.H. 2008. Calculation of a Critical Steam Injection Rate for Thermally-Assisted Gas-Oil Gravity Drainage. Paper

SPE 113351 presented Improved Oil Recovery Symposium, Tulsa, Oklahoma, 19-23 April.

al-Shizawi, A., Denby, P.G., and Marsden, G. 1997. Heat-Front Monitoring in the Qarn Alam Thermal GOGD Pilot. Paper SPE 37781 presented at Middle East Oil Show, Bahrain, 15-18 March.

Amiri A., Øye G., and Sjöblom J. 2011. Temperature and Pressure Effects on Stability and Gelation Properties of Silica Suspensions. Colloids and Surfaces A 378 (1-3): 14-21.

Andersen, K.H., et al. 1946. Method of Oil Recovery. U.S. Patent 2,402,588.

ASTM D2007-80, Standard Procedure for Separating Asphaltenes from Crude Oils. 2007. West Conshohocken, Pennsylvania: ASTM International. http://dx.doi.org/10.1520/A0370-05.

Ayatollahi, S., et. al. 2005. Investigation of Thermal Gas-Oil Gravity Drainage (GOGD) in Fractured Carbonate Reservoirs. Paper SPE 93585 presented Middle East Oil & Gas Show and Conference, Bahrain, 12-15 March.

Ayub, M. and Tuhinuzzaman, M. 2007. The Role of Capillarity in the VAPEX Process. Paper 2007-075 presented at Canadian International Petroleum Conference, Calgary, Alberta, Canada, 12-14 June.

Babadagli, T. 2002. Evaluation of EOR methods for Heavy-Oil Recovery in Naturally Fractured Reservoirs. Journal of Petroleum Science and Engineering 37: 25-37.

Babadagli, T. et al. 2008. Development of Heavy-Oil Fractured Carbonate Bati Raman Field: Evaluation of Steam Injection Potential and Improving On-Going CO2 Injection. Paper SPE 115400 presented at Annual Technical Conference and Exhibition, Denver, Colorado, 21-24 September.

Bai, B., et al. 2007. Preformed Particle Gel for Conformance Control: Transport Mechanism Through Porous Media. SPE Res Eval & Eng (4): 176-184. SPE-89468-PA.

Bai, B., et al. 2008. Case Study on Preformed Particle Gel for In-depth Fluid Diversion. SPE Paper 113997 presented at 2008 SPE/DOE Improved Oil Recovery Symposium, Tulsa, Oklahoma, 19-23 April.

Behrouz, T., Kharrat, R., and Ghanzanfari, M.H. 2007. Experimental Study of Factors Affecting Heavy Oil Recovery in Solvent Floods. Paper 2007-006 presented at Canadian International Petroleum Conference, Calgary, Alberta, Canada, 12-14 June.

Bernard, G.G. 1972. Process for Recovering Oil from Heterogeneous Reservoirs. U.S. Patent 3,882,938.

Bradford, S.A. and Bettahar, M. 2006. Concentration Dependent Transport of Colloids in Saturated Porous Media. Journal of Contaminant Hydrology 82: 99-117.

Braswell, G. 2012. New Heavy Oil Solvent Extraction Pilot Plant to Test Experimental Process. JPT Online, 9-January.

Braswell, G. 2012. New Heavy Oil Solvent Extraction Pilot Plant to Test Experimental Process. JPT Online, 9-January.

Briggs, P.J., Beck, D.L., Black, C.J.J. et al. 1992. Heavy Oil from Fractured Carbonate Reservoirs. SPE Reservoir Engineering. SPE-19671-PA.

Burns L.D., et al. 2008. New Generation Silicate Gel System for Casing Repairs and Water Shutoff. Paper SPE 113490 presented at SPE/DOE Symposium on Improved Oil Recovery, Tulsa, Oklahoma, 20-23 April.

Burns, L.D., et al. 2008. New Generation Silicate Gel System for Casing Repairs and Water Shutoff. Paper SPE 113490 presented at Improved Oil Recovery Symposium, Tulsa, Oklahoma, 19-23 April.

Butler, R.M. and Mokrys, I.J. 1989. Solvent Analog Model of Steam-Assisted Gravity Drainage. AOSTRA Journal of Research 5: 17 – 32.

Butler, R.M. and Mokrys, I.J. 1991. A New Process (VAPEX) for Recovering Heavy Oil using Hot Water and Hydrocarbon Vapour. Journal of Canadian Petroleum Technology 30 (1): 97-106.

Butler, R.M. and Mokrys, I.J. 1993. Recovery of Heavy Oil using Vapourized Hydrocarbon Solvents: Further Development of the VAPEX Process. Journal of Canadian Petroleum Technology 32: 56-62.

Bychkov, A. et. al. 2008. Steam Injection into Fractured Carbonates – The Physical Recovery Mechanisms Analyzed and Upscaled. Paper SPE 117987 presented at the Abu Dhabi International Petroleum Exhibition and Conference, Abu Dhabi, UAE, 3-6 November.

Campbell A.I., et al. 2005. Dynamical Arrest in Attractive Colloids: The Effect of Long-Range Repulsion. Physics Review Letters 94: 208301-1-208301-4.

Canbolat, S., Akin, S., and Polikar, M. 2004. Investigation of steam and Gas Push Mechanism in Carbonate Medium. Paper 2004-223 presented at Canadian International Petroleum Conference, Calgary, Alberta, Canada, 8-10 June.

Canseco, V. et al. 2009. Deposition and Re-entrainment of Model Colloids in Saturated Consolidated Porous Media: Experimental Study. Colloids and Surfaces A 352: 5-11.

Castelijns, H.J., et al. 2007. Permeability Reduction in Porous Materials by In Situ Formed Silica Gel. Journal of Applied Physics 102: 114901-1 – 114901-10.

Cavallaro, A.N. et al. 2005. Laboratory Investigation of an Innovative Solvent Based Enhanced Recovery and In Situ Upgrading Technique. Paper CIP 2005-016 presented at Canadian International Petroleum Conference, Calgary, Alberta, 7-9 June.

Chang, H.L., et al. 2004. Successful Field Pilot of In-Depth Colloidal Dispersion Gel (CDG) Technology in Daqing Oil Field. Paper SPE 89460 presented at SPE/DOE Fourteenth Symposium on Improved Oil Recovery, Tulsa, Oklahoma, 17-21 April.

Chang, H.L., et al. 2006. Advances in Polymer Flooding and Alkaline/Surfactant/Polymer Processes as Developed and Applied in the People's Republic of China. Journal of Petroleum Technology (February 2006): 84-89.

Chemistry: The Central Science, Chapter 11, Section 5,

Christopher, C.A., et al. 1973. Secondary Oil Recovery Method. U.S. Patent 3,759,326.

Corrêa, A.C.F. and Firoozabadi, A. 1996. Concept of Gravity Drainage in Layered Porous Media. SPE Journal 1 (1): 101-111.

Coste, J.-P., et al. 2000. In-Depth Fluid Diversion by Pre-Gelled Particles. Laboratory Study and Pilot Testing. SPE Paper 59362 presented at 2000 SPE/DOE Improved Oil Recovery Symposium, Tulsa, Oklahoma, 3-5 April.

Cuthiell, D. and Edmunds, N. 2012. Thoughts on Simulating the VAPEX Process. Paper SPE 158499 presented at Heavy Oil Conference Canada, Calgary, Alberta, Canada, 12-14 June.

Dai C., et al. 2010. Study and Field Application of Profile Control Agent in High Temperature and High Salinity Reservoir. Paper SPE 132765 presented at Trinidad and Tobago Energy Resources Conference, Port of Spain, Trinidad, 27-30 June.

Das, S.K. and Butler, R.M. 1994. Effect of Asphaltene Deposition on the VAPEX Process: A Preliminary Investigation using a Hele-Shaw Cell. Journal of Canadian Petroleum Technology 33: 39-45.

Das, S.K. and Butler, R.M. 1995. Extraction of Heavy Oil and Bitumen using Solvents at Reservoir Pressure. Paper 95-118 presented at Petroleum Conference of the South Saskatchewan Section, Regina, Saskatchewan, Canada, 16-18 October.

Das, S.K. and Butler, R.M. 1998. Mechanism of the Vapor Extraction Process for Heavy Oil and Bitumen. Journal of Petroleum Science and Engineering 21: 43-59.

de Candia A., et al. 2005. Colloidal Gelation, Percolation and Structural Arrest. Physica A 358: 239-248.

Diaz, D., Somaruga, C., Norman, C., and Romero, J. 2008. Colloidal Dispersion Gels Improve Oil Recovery in a Heterogeneous Argentina Waterflood. Paper SPE

113320 presented SPE/DOE Improved Oil Recovery Symposium, Tulsa, Oklahoma, 19-23 April.

Dickson, J.L. et al. 2011. Design Approach and Early Field Performance for a Solvent-Assisted SAGD Pilot at Cold Lake, Canada. Paper SPE 150639 presented at Heavy Oil Conference and Exhibition, Kuwait City, Kuwait, 12-14 December.

Dovan, H.T. and Hutchins, R.D. 1987. Development of a New Aluminum/Polymer Gel System for Permeability Adjustment. SPE Reservoir Engineering (May 1987): 177-183.

Dreher, K.D., Kenyon, D.E., and Iwere, F.O. 1986. Heat Flow during Steam Injection into a Fractured Carbonate Reservoir. Paper SPE 14902 presented at the SPE Symposium on Enhanced Oil Recovery, Tulsa, Oklahoma, 20-23 April.

Dunn, S.G, Nenniger, E.H., and Rajan, V.S.V. 1989. A Study of Bitumen Recovery by Gravity Drainage using Low-Temperature Soluble-Gas Injection. Canadian Journal of Chemical Engineering 67: 978-991.

Edmunds, N. et. al. 2009. Prospects for Commercial Bitumen Recovery from the Grosmont Carbonate, Alberta. Journal of Canadian Petroleum Technology 48 (9): 26-32.

Etminan, S.R., Maini, B.B., and Kharrat, R. 2007. The Role of Connate Water Saturation in VAPEX Process. Paper CIM 2007-005 presented at Canadian International Petroleum Conference, Calgary, Alberta, Canada, 12-14 June.

Farzaneh, S.A., Kharrat, R., and Ghazanfari, M.H. 2010. Experimental Study of Solvent Flooding to Heavy Oil in Fractured Five-Spot Micro-Models: The Role of Fracture Geometrical Characteristics. Journal of Canadian Petroleum Technology 49 (3): 36-43.

Fatemi, S. M., Kharrat, R., and Vossoughi, S. 2011. Investigation of Steam Assisted Gravity Drainage (SAGD) and Expanding Solvent-SAGD (ES-SAGD) Processes in Complex Fractured Models: Effects of Fractures' Geometrical Properties. Paper SPE 150082 presented at Heavy Oil Conference and Exhibition, Kuwait City, Kuwait, 12-14 December.

Festoey, S. and van Golf-Racht, T.D. 1987. Gas Gravity Drainage in Fractured Reservoirs through New Dual-Continuum Approach. Paper SPE 16980 presented at Annual Technical Conference and Exhibition, Dallas, Texas, 27-30 September.

Festoey, S. and van Golf-Racht, T.D. 1987. Gas Gravity Drainage in Fractured Reservoirs through New Dual-Continuum Approach. Paper SPE 16980 presented at Annual Technical Conference and Exhibition, Dallas, Texas, 27-30 September.

Fielding, R.C., Gibbons, D.H., and Legrand, F.P. 1994. In-Depth Drive Fluid Diversion Using an Evolution of Colloidal Dispersion Gels and New Bulk Gels: An Operational Case History of North Rainbow Ranch Unit. Paper SPE 27773

presented at SPE/DOE Symposium on Improved Oil Recovery, Tulsa, Oklahoma, 17-20 April.

Firoozabadi, A. and Markeset, T.I. 1994. Miscible Displacement in Fractured Porous Media: Part I – Experiments. Paper SPE 27743 presented at Symposium on Improved Oil Recovery, Tulsa, Oklahoma, 17-20 April.

Frauenfeld, T., Jossy, C., and Ivory, J. 2009. Numerical Simulation and Economic Evaluation of Hybrid Solvent Processes. Paper 2009-108 presented at Canadian International Petroleum conference, Calgary, Alberta, Canada, 16-18 June.

Frauenfeld, T., Jossy, C., Jossy, E. et al. 2005. Evaluation of the N-Solv Process – Experimental Operation and Results. Technical report, Alberta Research Council (unpublished).

Gupta, S.C. and Gittins, S.D. 2005. Christina Lake Solvent Aided Process Pilot. Paper 2005-190 presented at Canadian International Petroleum Conference, Calgary, Alberta, Canada, 7-9 June.

Haghighat, P. and Maini, B.B. 2008. Role of Asphaltene Precipitation in VAPEX Process. Paper CIP 2008-087 presented at Canadian International Petroleum Conference, Calgary, Alberta, 17-19 June.

Hardy, M. et al. 1999. The First Carbonate Field Application of a New Organically Crosslinked Water Shutoff Polymer System. Paper SPE 50738 presented at SPE International Symposium on Oilfield Chemistry, Houston, Texas, 16-19 February.

http://wps.prenhall.com/wps/media/objects/3311/3391416/blb1105.html (accessed 8 March 2013).

Huang, T., Crews, J.B., and Johnson, M.H. 2009. Using Nanoparticles for Water Flow Control in Subterranean Formations. US Patent No. 8,053,397.

Huh, C., Choi, S.K., and Sharma, M.M. 2005. A Rheological Model for pH-Sensitive Ionic Polymer Solutions for Optimal Mobility-Control Applications. Paper SPE 96914 presented at Annual Technical Conference and Exhibition, Dallas, Texas, 9-12 October.

Hyun K., et al. 2002. Large Amplitude Oscillatory Shear as a Way to Classify the Complex Fluids. J. Non-Newtonian Fluid Mech 107: 51-65.

Ikwumonu, A., Rawnsley, K., Habsi, M., and Penney, R. 2007. Key Learnings from History Matching a Thermally Assisted Gas Oil Gravity Drainage Pilot in Fractured Reservoirs. Paper IPTC 11411 presented at International Petroleum Technology Conference, Dubai, UAE, 4-6 December.

Ivory, J., Frauenfeld, T. and Jossy, C. 2010. Thermal Solvent Reflux and Thermal Solvent Hybrid Experiments. Journal of Canadian Petroleum Technology 49 (2): 23-31.

James, L. and Chatzis, I. 2004. Details of Gravity Drainage of Heavy Oil during Vapor Extraction. Paper 2004-23 presented at International Symposium of the Society of Core Analysts, Abu Dhabi, UAE, 5-9 October.

James, L.A., Rezaei, N. and Chatzis, I. 2008. VAPEX, Warm VAPEX, and Hybrid VAPEX – The State of Enhanced Oil Recovery for In Situ Heavy Oils in Canada. Journal of Canadian Petroleum Technology 47 (4): 1-7.

Jiang, Q. and Butler, R.M. 1996. Experimental Studies on Effects of Reservoir Heterogeneity on the VAPEX Process. Journal of Canadian Petroleum Technology 35 (10): 46-54.

Jiang, Q., et. al. 2010. Evaluation of Recovery Technologies for the Grosmont Carbonate Reservoirs. Journal of Canadian Petroleum Technology 49 (5): 56-64.

Jurinak J.J. and Summers L.E. 1991. Oilfield Applications of Colloidal Silica Gel. SPE Prod Eng 6 (11): 406-412. SPE-18505-PA.

Jurinak, J.J. and Summers, L.E. 1989. Oilfield Applications of Colloidal Silica Gel. Paper SPE 18505 presented at International Symposium on Oilfield Chemistry, Houston, Texas, 8-10 February.

Jurinak, J.J., Summers, L.E., and Bennett, K.E. 1991. Laboratory Testing of Colloidal Silica Gel for Oilfield Applications. SPE Paper 23581 Supplement to SPE 18505.

Karmaker, K. and Maini, B.B. 2003. Experimental Investigation of Oil Drainage Rates in the VAPEX Process for Heavy Oil and Bitumen Reservoirs. Paper SPE 84199 presented at Annual Technical Conference and Exhibition, Denver, Colorado, 5-8 October.

Krumrine, P.H. and Boyce, S.D. 1985. Profile Modification and Water Control with Silica Gel-Based Systems. Paper SPE 13578 presented at International Symposium on Oilfield and Geothermal Chemistry, Phoenix, Arizona, 9-11 April.

Lalehrok, F., et al. 2008. Application of pH-Triggered Polymers in Fractured Reservoirs to Increase Sweep Efficiency. Paper SPE 113800 presented at SPE/DOE Improved Oil Recovery Symposium, Tulsa, Oklahoma, 19-23 April.

Larson G. 1999. The Structure of Complex Fluids. Oxford University Press, New York.

Leaute, R.P. 2002. Liquid Addition to Steam for Enhancing Recovery (LASER) of Bitumen with CSS: Evolution of Technology from Research Concept to a Field Pilot at Cold Lake. Paper SPE 79011 presented at International Thermal Operations and Heavy Oil Symposium and International Horizontal Well Technology Conference, Calgary, Alberta, Canada, 4-7 November.

Leaute, R.P. and Carey, B.S. 2007. Liquid Addition to Steam for Enhancing Recovery (LASER) of Bitumen with CSS: Results from the First Pilot Cycle. Journal of Canadian Petroleum Technology 46 (9): 22-30.

Li, W. and Mamora, D.D. 2010. Numerical Simulation of Thermal Solvent Replacing

Liu, Y., Bai, B., and Shuler, P.J. 2006. Application and Development of Chemical-Based Conformance Control Treatments in China Oil Fields. Paper SPE 99641 presented at Symposium on Improved Oil Recovery, Tulsa, Oklahoma, 22-26 April.

Lu P.J., et al. 2008. Gelation of Particles with Short-range Attraction. Nature 453: 499-504.

Lu, X., et al. 2000. Performance and Evaluation Methods of Colloidal Dispersion Gels in the Daqing Oil Field. Paper SPE 59466 presented at Asia Pacific Conference on Integrated Modeling for Asset Management, Yokohama, Japan, 25-26 April.

Luo, P. et al. 2008. Asphaltene Precipitation and Its Effects on the Vapour Extraction (VAPEX) Heavy Oil Recovery Process. Paper SPE 117527 presented at International Operations and Heavy Oil Symposium, Calgary, Alberta, Canada, 20-23 October.

Macaulay, R.C., Krafft, J.M., Hartemink, M., and Escovedo, B. 1995. Design of a Steam Pilot in a Fractured Carbonate Reservoir – Qarn Alam Field, Oman. Paper SPE 30300 presented at the International Heavy Oil Symposium, Calgary, Alberta, Canada 19-21 June.

Mack, J.C. and Smith, J.E. 1994. In-Depth Colloidal Dispersion Gels Improve Oil Recovery Efficiency. Paper SPE 27780 presented at SPE/DOE Ninth Symposium on Improved Oil Recovery, Tulsa, Oklahoma, 17-20 April.

Martin J.E. and Wilcoxon J.P. 1989. Spatial Correlation and Growth in Dilute Gels. Phys. Rev. A 39: 252-258.

Metin C.O., et al. 2011. Stability of Aqueous Silica Nanoparticle Dispersions. J. Nanopart. Res. 13:839-850.

Metin C.O., et al. 2012. Aggregation Kinetics and Shear Rheology of Aqueous Silica Suspensions. J. Nanopart. Res. Submitted.

Metin C.O., Rankin K.M., and Nguyen Q.P. 2012 Phase Behavior and Rheological Characterization of Silica Nanoparticle Gel. Prepr. Pap.-Am. Chem. Soc., Div. Pet. Chem. 57 (1), San Diego, California, March 2012.

Meziane, S. and Kadi, H. 2008. Kinetics and Thermodynamics of Oil Extraction from Olive Cake. Journal of the American Oil Chemists' Society 85: 391-396.

Moffitt, P.D. et al. 1996. Development and Field Testing of a New Low Toxicity Polymer Crosslinking System. Paper SPE 35173 presented at SPE Permian Basin Oil and Gas Recovery Conference, Midland, Texas, 27-29 March.

Moghadam, S., Nobakht, M., and Gu, Y. 2007. Permeability Effects in a Vapour Extraction (VAPEX) Heavy Oil Recovery Process. Paper 2007-095 presented at

Canadian International Petroleum Conference, Calgary, Alberta, Canada, 12-14 June.

Moradi-Araghi, A. Bjornson, G., and Doe, P.H. 1993. Thermally Stable Gels for Near-Wellbore Permeability Contrast Corrections. SPE Advanced Technology Series 1 (1): 140.

Morel, D.D., Bourbiaux, B., and Latil, M. 1990. Diffusion Effects in Gas-Flooded Light Oil Fractured Reservoirs. Paper SPE 20516 presented at Annual Technical Conference and Exhibition, New Orleans, Louisiana, 23-26 September.

Muruaga, E., et al. 2008. Combining Bulk Gels and Colloidal Dispersion Gels for Improved Volumetric Sweep Efficiency in a Mature Waterflood. Paper SPE 113334 presented at SPE/DOE Improved Oil Recovery Symposium, Tulsa, Oklahoma, 19-23 April.

Naderi, K. and Babadagli, T. 2011. Use of CO2 as Solvent during Steam-Over-Solvent Injection in Fractured Reservoirs (SOS-FR) Method for Heavy Oil Recovery . Paper IPTC 14918 presented at the International Petroleum Technology Conference, Bangkok, Thailand 7-9 February.

Naderi, K. and Babadagli, T. 2012. Field Scale Application of the SOS-FR (Steam-Over-Solvent Injection in Fractured Reservoirs) Method: Optimal Operating conditions. Paper SPE 154088 presented at the Improved Oil Recovery Symposium, Tulsa, Oklahoma 14-18 April.

Nakamura, S. et al. 1995. A Critical Evaluation of a Steamflood Pilot in a Deep Heavy Carbonate Reservoir in Ikiztepe Field, Turkey. Paper SPE 30727 presented at Annual Technical Conference and Exhibition, Dallas, Texas, 22-25 October.

Nasr, T.N. et. al. 2003. Novel Expanding Solvent-SAGD Process “ES-SAGD.” Journal of Canadian Petroleum Technology 42 (1): 13-16.

Nenniger, E.H. 1979. Hydrocarbon Recovery. Canadian Patent 1,059,432.

Nenniger, J. 2012. “The American Energy Initiative.” Written statement before the House Committee on Energy and commerce, U.S. House of Representatives, Washington, DC, 20 March.

Nenniger, J.E. and Dunn, S.G. 2008. How Fast is Solvent Based Gravity Drainage? Paper CIPC 2008-139, Proceedings of the Canadian International Petroleum Conference/SPE Gas Technology Symposium Joint Conference, Calgary, Alberta, Canada, 17-19 June.

Nenniger, J.E. and Dunn, S.G. 2008. How Fast is Solvent Based Gravity Drainage? Paper CIPC 2008-139, Proceedings of the Canadian International Petroleum Conference/SPE Gas Technology Symposium Joint Conference, Calgary, Alberta, Canada, 17-19 June.

Noll, M.R., Bartlett, C., and Dochat, T.M. 1992. In Situ Permeability and Chemical Fixation using Colloidal Silica. Proc., 6th Nat. Outdoor Action Conf. on Aquifer Restoration, National Ground Water Association.

Noll, M.R., et al. 1993. Pilot Field Application of a Colloidal Silica Gel Technology for In Situ Hot Spot Stabilization and Horizontal Grouting. Proc., 7th Nat. Outdoor Action Conf. on Aquifer Restoration, National Ground Water Association.

Ohms, D. et al. 2009. Incremental Oil Success from Waterflood Sweep Improvement in Alaska. SPE Paper presented at 2009 SPE International Symposium on Oilfield Chemistry, The Woodlands, Texas, 20-22 April.

Orr, B. 2009. ES-SAGD; Past, Present and Future. Paper SPE 129518 presented at International Student Paper Contest, Annual Technical Conference and Exhibition, New Orleans, Louisiana, 4-7 October.

Pathak, V., Babadagli, T., and Edmunds, N.R. 2010. Hot Solvent Injection for Heavy Oil/Bitumen Recovery: An Experimental Investigation. Paper SPE 137440 presented at Canadian Unconventional Resources & International Petroleum Conference, Calgary, Alberta, Canada, 19-21 October.

Pathak, V., Babadagli, T., and Edmunds, N.R. 2011. Mechanics of Heavy Oil and Bitumen Recovery by Hot Solvent Injection. Paper SPE 144546 presented at Western North American Regional Meeting, Anchorage, Alaska, 7-11 May.

Patil, P., Bøye, B. and Devaraj, M. 2011. Evaluation of an Environmentally Acceptable Colloidal Silica-Based Conformance Systems. Paper IPTC 15117 presented at International Petroleum Technology Conference, Bangkok, Thailand, 7-9 February.

Patricelli, A., et al. 1979. Fattori Che Influenzano l'Estrazione dei Lipidi da Semi Decorticati di Girasole. Riv Ital Sostanze Grasse 56: 136-142.

Penney, R. 2005. Steam Injection in Fractured Carbonate Reservoirs: Starting a New Trend in EOR. Paper IPTC 10727 presented at IPTC Conference, Doha, Qatar, 21-23 November.

Penney, R., et. al. 2007. First Full Field Steam Injection in a Fractured Carbonate at Qarn Alam, Oman. Paper SPE 105406 presented at Middle East Oil & Gas Show and Conference, Kingdom of Bahrain, 11-14 March.

Pritchett, et al. 2003. Field Application of a New In-Depth Waterflood Conformance Improvement Tool. SPE Paper 84897 presented at the SPE International Improved Oil Recovery Conference in Asia Pacific, Kuala Lumpur, Malaysia, 20-21 October.

Purkaple, J.D. and Summers, L.E. 1988. Evaluation of Commercial Crosslinked Polyacrylamide Gel Systems for Injection Profile Modification. Paper SPE 17331

presented at SPE/DOE Enhanced Oil Recovery Symposium, Tulsa, Oklahoma, 17-20 April.

Rahnema, H., Kharrat, R., and Rostami, B. 2008. Experimental and Numerical Study of Vapor Extraction Process (VAPEX) in Heavy Oil Fractured Reservoir. Paper 2008-116 presented at Canadian International Petroleum Conference/SPE Gas Technology Symposium, Calgary, Alberta, Canada, 17-19 June.

Ranganathan, R., et al. 1998. Experimental Study of the Gelation Behavior of a Polyacrylamide/Aluminum Citrate Colloidal-Dispersion Gel System. Society of Petroleum Engineering Journal (December 1998): 337-343.

Reis, J.C. 1990. Oil Recovery Mechanisms in Fractured Reservoirs during Steam Injection. Paper SPE 20204 presented at the SPE Symposium on Enhanced Oil Recovery, Tulsa, Oklahoma, 22-25 April.

Rezaei, N., Mohammadzadeh, O., and Chatzis, I. 2010. Improving the Performance of Vapor Extraction of Heavy Oil and Bitumen using the Warm VAPEX Process. Paper SPE 137824 presented at Canadian Unconventional Resources & International Petroleum Conference, Calgary, Alberta, Canada, 19-21 October.

Sahuquet, B.C. and Ferrier, J.J. 1980. Steam-Drive Pilot in a Fractured Carbonate Reservoir: Lacq Superieur Field. Paper SPE 9453 presented at Annual Technical Conference and Exhibition, Dallas, Texas, 21-24 September.

Sandiford, B.B. 1982. Selectively Controlling Fluid Flow through the Higher Permeability Zones of Subterranean Reservoirs. U.S. Patent 4,332,297.

Senis D. and Allain C. 1997. Scaling Analysis of Sediment Equilibrium in Aggregated Colloidal Suspensions. Phys. Rev. E 55:7797-7800.

Seright, R.S. 1992. Impact of Permeability and Lithology on Gel Performance. Paper SPE 24190 presented at Eighth Symposium on Enhanced Oil Recovery, Tulsa, Oklahoma, 22-24 April.

Seright, R.S. 1995. Propagation of an Aluminum-Citrate-HPAM “Colloidal-Dispersion” Gel through Berea Sandstone. New Mexico PRRC. <http://baervan.nmt.edu/research_groups/reservoir_sweep_improvemtn/pages/Annual%20reports/1994%20Annual/Improved%20Techniques%2094%2.05.pdf>.

Seright, R.S. 2006. Are Colloidal Dispersion Gels Really a Viable Technology?. New Mexico Petroleum Recovery and Research Center (PRRC). <http://baervan.nmt.edu/randy/>

Seright, R.S. and Liang, J. 1994. A Survey of Field Applications of Gel Treatments for Water Shutoff. Paper SPE 26991 presented at Latin American/Caribbean Petroleum Engineering Conference, Buenos Aires, Argentina, 27-29 April.

Shahin, G.T., Moosa, R., Kharusi, B., and Chilek, G. 2006. The Physics of Steam Injection in Fractured Carbonate Reservoirs: Engineering Development Options

that Minimize Risk. Paper SPE 102186 presented at Annual Technical Conference and Exhibition, San Antonio, Texas 24-27 September.

Sheng, J.J. Modern Chemical Enhanced Oil Recovery: Theory and Practice. Amsterdam: Elsevier, 2011.

Shih W.H., et al. 1990. Scaling Behavior of the Elastic Properties of Colloidal Gels. Phys. Rev. A 42:4772–4779.

Silva R.F. and Vasconcelos W.L. 1999. Influence of Processing Variables on the Pore Structure of Silica Gels Obtained with Tetraethylorthosilicate. Materials Research 2: 197-200.

Smith W.E. and Zukoski C.F. 2006. Aggregation and Gelation Kinetics of Fumed Silica–Ethanol Suspensions. J. Colloid Int. Sci. 304: 359-369.

Smith, D. 2007. The Bright Side of Technology. The BP Magazine (4): 37-40.

Smith, J.E., Lui, H., and Guo, Z.D. 2000. Laboratory Studies in In-Depth Colloidal Dispersion Gel Technology for Daqing Oil Field. Paper SPE 62610 presented at Western Regional Meeting, Long Beach, California, 19-23 June.

Smith, J.E., Mack, J.C., and Nicol, A.B. 1996. The Adon Road – An In-Depth Gel Case History. Paper SPE 35352 presented at SPE/DOE Symposium on Improved Oil Recovery, Tulsa, Oklahoma, 21-24 April.

Snell, J.S. and Close, A.D. 1999. Yates Field Steam Pilot Applies Latest Seismic and Logging Monitoring Techniques. Paper SPE 56791 presented at Annual Technical Conference and Exhibition, Houston, Texas, 3-6 October.

STARS Advanced Process and Thermal Reservoir Simulator, Version 2011 User's Guide. 2011. Calgary, Alberta: CMG

Stavland A., et al. 2011. In-depth Water Diversion using Sodium Silicate on Snorre - Factors Controlling In-depth Placement. Paper SPE 143836 presented at SPE European Formation Damage Conference, Noordwijk, The Netherlands, 7-10 June.

Stavland, A., et al. 2011. In-Depth Water Diversion using Sodium Silicate on Snorre-Factors Controlling In-Depth Placement. Paper SPE 143836 presented at European Formation Damage Conference, Noordwijk, The Netherlands, 7-10 June.

Steam under Steam Assisted Gravity Drainage (SAGD) Process. Paper SPE 133453 presented at Western North American Regional Meeting, Anaheim, California, 26-30 May.

Suat Bagci, A., Samuel, O.M., and Mackay, E. 2007. Recovery Performance of Steam-Alternating-Solvent (SAS) Process in Fractured Reservoirs . Paper CIPC 2007-040 presented at the Canadian International Petroleum Conference, Alberta, Canada, 12-14 June.

Sydansk, R.D. 1981. Process for Improving Conformance and Flow Profiles in a Subterranean Formation. U.S. Patent 4,304,301.

Thomas, L.K., Dixon, T.N., Pierson, R.G., and Hermansen, H. 1991. Ekofisk Nitrogen Injection, JPT, 151-160 (June).

Torabi, F. and Asghari, K. 2007. Performance of CO2 Huff-and-Puff Process in Fractured Media (Experimental Results). Paper 2007-119 presented at Canadian International Petroleum Conference, Calgary, Alberta, Canada, 12-14 June.

van Heel, A.P.G., et. al. 2008. Heavy-Oil Recovery by Steam Injection in Fractured Reservoirs. Paper SPE 113461 presented at Improved Oil Recovery Symposium, Tulsa, Oklahoma, 19-23 April.

van Wunnik, J.N.M. and Wit, K. 1992. Improvement of Gravity Drainage by Steam Injection into a Fractured Reservoir: An Analytical Evaluation. SPE Reservoir Engineering. SPE-20251-PA.

Vossoughi, S. 2000. Profile Modification Using In Situ Gelation Technology – A Review. Journal of Petroleum Science and Engineering 26 (2000): 199-209.

Wang G.H. and Zhang L.M. 2009. A Bio Friendly Silica Gel for Insitu Protein Entrapment: Biopolymer-Assisted Formation and Its Kinetic Mechanism. J. Phys. Chem 113: 2688-2694.

Wang, et al. 2006. Sweep Improvement Options for the Daqing Oil Field. Paper SPE 99441 presented at SPE/DOE Symposium on Improved Oil Recovery, Tulsa, Oklahoma, 22-26 April.

Xu, S. et al. 2012. Upscaling Study of Vapour Extraction Process through Numerical Simulation. Paper SPE 157784 presented at Heavy Oil Conference Canada, Calgary, Alberta, Canada, 12-14 June.

Yazdani, A. and Maini, B.B. 2005. Effect of Drainage Height and Grain Size on Production Rates in the VAPEX Process: Experimental Study. SPE Reservoir Evaluation & Engineering 8 (3): 205-213.

Yuan, J-Y., et. al. 2010. Evolving Recovery Technologies Directed towards Commercial Development of the Grosmont Carbonate Reservoirs. Paper CSUG/SPE 137941 presented at the Canadian Unconventional Resources & International Petroleum Conference, Alberta, Canada, 19-21 October.

Yziquel F., et al. 1999. Rheological Modeling of Concentrated Colloidal Suspension. J. Non-Newtonian Fluid Mech. 86 (1):133–155.

Zhao, L. 2004. Steam Alternating Solvent Process. Paper SPE 86957 presented at SPE International Thermal Operations and Heavy Oil Symposium and Western Regional Meeting, Bakersfield, California, 16-18 Mar.